THE URANIUM SERIES DIAGENESIS AND THE MORPHOLOGY OF DROWNED BARBADIAN PALEO-REEFS

by

JACOB LOUIS MEY, IV

A dissertation submitted to the Graduate Faculty in Earth and Environmental Sciences in partial fulfillment of the requirements for the degree of Doctor of Philosophy

THE CITY UNIVERSITY OF NEW YORK

2008

APPROVAL

This manuscript has been read and accepted for the
Graduate Faculty in Earth and Environmental Sciences in satisfaction of the
dissertation requirement for the degree of Doctor of Philosophy.

14 April 2008	Professor N. G. Hemming
Date	Chair of Examining Committee
14 April 2008	Professor Y. Klein
Date	Executive Officer

Prof. N. G. Hemming, Queens College (advisor, chair)

Prof. R. G. Fairbanks, Columbia University (advisor)

Prof. M. K. Weisberg, Kingsborough Community Coll.

Prof. H. Brueckner, Queens College

Supervision Committee

THE CITY UNIVERSITY OF NEW YORK

2008

ABSTRACT

THE URANIUM SERIES DIAGENESIS AND THE MORPHOLOGY OF DROWNED BARBADIAN PALEO-REEFS

Jacob Louis Mey, IV

Advisers: Professor R. G. Fairbanks (Columbia University) and
Professor N. G. Hemming (Queens College)

Paleoclimatologists rely on precise age determinations of natural materials, such as ice cores, deep ocean sediments, speleothems, and corals. Especially carbonate materials are used as proxies for past climate changes, but only if they are well preserved as closed system samples in their natural environment, and thus present ideal material for radiometric dating. It is important to understand and recognize the symptoms of diagenesis as it enables one to avoid dealing with the thus affected samples altogether. Major challenges arise, however, in that several well-established strict criteria for a priori sample selection fail to identify all affected samples, making some diagenetic effects hard to detect. In many cases, the 'hidden' effects go undetected until the end of costly and time-consuming analysis, only to yield the inconclusive open system results improper for dating corals.

The present work deals with two central questions: (i) Where do the diagenetic effects occur, and: (ii) What are the mechanisms that set their signatures? In order to answer the first question, it is necessary to understand the

second. Barbadian corals that have been exposed to fresh water diagenesis commonly show a positive correlation between $^{230}Th/^{238}U$ and $^{234}U/^{238}U$ activities in samples with elevated $\delta^{234}U_{initial}$. These trends have led authors to develop corrections to open system ages, based on the interpretation that the systematic trends are set by predictable progressive addition of excess ^{234}U and ^{230}Th. The new model developed in this study disavows the progressive addition models, and instead, contends that the trends were set early during the first freshwater exposure and that they have been preserved ever since. The model has been refined to successfully estimate 'marine residence times' for seven Barbadian paleoreefs.

In the present study, several new geospatial techniques, using GIS and 3-dimensional bathymetric digital terrain models, have been developed to improve our understanding of the sea floor morphology around Barbados and other locations with the desired paleoreefs. Our two-pronged approach, viz., unraveling the off-shore drowned paleoreefs and understanding their internal distribution of diagenetic effects, is thought to improve the possibilities for future prospecting for closed system samples to be used in paleoclimate research.

DEDICATION

This dissertation is dedicated to

my wife Rikke and my daughter Camille,

Whom without, this work

would not be!

ACKNOWLEDGEMENTS

I extend my great thanks to Rick Fairbanks and Gary Hemming as my advisers; the valuable insight gained from our discussions is immeasurable. Both of you have been paramount to my motivation and drive throughout. I also thank Rick Mortlock for his savvy knowledge, which was very beneficial and needed many times. I am indebted to my father, who through the years has taught me how to write (or at least tried to). A big thanks to the rest of my committee Mike Weisberg and Hannes Brueckner for adding insightful comments to my final draft. I am very thankful to my supervisor and colleague Lex van Geen for extending the flexibility that allowed me to complete my dissertation, but most of all, for bringing me to Lamont. To my friends and fellow graduate students Lida Teneva, Li Cao and Clara Chiu, I extend many thanks for our fruitful conversations and random rambling on all ideas. Thanks to Karrie Radloff as my office co-conspirator and co-planner to keep things running at Lamont and in the field. Also thanks to Zahid Aziz. Thanks to Daphnee Fromentin for taking care of business and Emily Hickey for helping out in the lab. I would like to thank the late Bill Haxby for introducing me to the tools necessary to study the bathymetry of the Barbados Shallows. As a token of my great appreciation, I have chosen to use the 'Haxby' color palette to portray The Shallows—a palette which by far, is the most aesthetical. I would like to thank Andrew Goodwillie for his enthusiasm and for 'more than he thinks' help from the very first time I walked into his office and asked about MB-System. Thanks also to Dale Chayes (who wrote MB-System together with Dave Caress) for technical assistance (and for writing MB-

System!). Thanks to Sidney Hemming for providing funding for crucial software. I am thankful to Juliana Maantay (Lehman College) for suggestions to the GIS aspects of the dissertation in its early stages. I also thank The Graduate Center (GC- CUNY) for the University Fellowships supporting this work throughout my tenure as a graduate student at GC. This work was also supported by NSF grants ATM03-27722, OCE05-5090 and OCE07-27696.

TABLE OF CONTENTS

COPYRIGHT ii

APPROVAL iii

ABSTRACT iv

DEDICATION vi

ACKNOWLEDGEMENTS vii

TABLE OF CONTENTS ix

LIST OF FIGURES xv

LIST OF TABLES xxv

LIST OF APPENDICES xxvi

CHAPTER 1

INTRODUCTION 1

CHAPTER 2

THE DIAGENESIS OF BARBADIAN CORAL PALEOREEFS: URANIUM SERIES DISEQUILIBRIA SYSTEMATICS AND THE EFFECTS OF REPEATED EMERGENCE HISTORIES 5

ABSTRACT 6

INTRODUCTION 8

Chemical fractionation in the uranium-series during coral diagenesis in the vadose zone 15

Radiogenic fractionation in the uranium-series 15

MATERIALS AND METHODS 17

RESULTS 19

DISCUSSION 29

$^{234}U/^{238}U$ and $^{231}Pa/^{235}U$ disequilibria in the reef profiles 29

The effect of pH change during dissolution 40

A new 'dissolution-cum-adsorption' model for uranium series trends in Barbados corals 46

CONCLUSIONS 56

ACKNOWLEDGEMENTS 58

CHAPTER 3

A NUMERICAL ANALYSIS OF THE 'DISSOLUTION-CUM-ADSORPTION' MODEL AND THE ESTIMATED MARINE RESIDENCE TIMES FOR BARBADIAN PALEOREEFS 59

ABSTRACT 60

INTRODUCTION 62

Uranium series disequilibria as expressed in the $\left[\frac{^{230}Th}{^{238}U}\right]$ versus $\left[\frac{^{234}U}{^{238}U}\right]$ activities 62

The trends in the $\left[\frac{^{230}Th}{^{238}U}\right]$ versus $\left[\frac{^{234}U}{^{238}U}\right]$ activity diagram 71

METHODS AND MATERIALS 72

Numerical Analysis of the uranium-series activity trends 72

Angles between 'closed system equal-age lines' and 'open system trend lines' 72

Calculating the slopes [a] 76

Calculating the angles [φ] 81

Calculating the length of a trend line [L] 87

RESULTS 93

DISCUSSION 106

A model of dissolution in corals 106

Estimating the time of first freshwater exposure – the 'marine residence time' 109

CONCLUSIONS 121

CHAPTER 4

OPTIMAL SCIENTIFIC DRILL POD PLACEMENTS ON THE BARBADOS' SHALLOWS

A STUDY USING SPATIAL ANALYSIS AND GEOGRAPHIC INFORMATION SCIENCE (GISC) TO IDENTIFY POTENTIAL OFFSHORE DRILLING TARGETS FOR SCIENTIFIC SAMPLING OF DROWNED PALEOREEFS OFF THE COAST OF BARBADOS. 122

ABSTRACT 123

INTRODUCTION 125

Why drill for samples offshore? - Understanding the freshwater effect 131

STUDY AREA 136

METHODS AND DATA SOURCES 136

Identification of potential drilling targets through spatial analysis using GISc. 136

Data acquisition and processing: Low resolution model data. 138

High resolution model data 141

Meta data and bathymetry data stream recording 142

Data processing facilities 142

Main data sources 143

Project work-flow chart and projected budget 144

RESULTS 148

Data processing 148

Spatial Analysis 154

DISCUSSION 155

CONCLUSIONS 170

ACKNOWLEDGEMENTS 171

Appendix 4-1 172

Appendix 4-2 174

Appendix 4-3 177

Appendix 4-4 179

CHAPTER 5

MORPHOLOGY OF THE BARBADOS SHALLOWS AND ITS CORAL HABITAT DURING THE LAST GLACIAL CYCLE 181

ABSTRACT 182

INTRODUCTION 184

METHODS AND MATERIALS 192

Processing bathymetric data 193

RESULTS 194

Map descriptions 194

Backscatter data 210

DISCUSSION 221

Spatial analysis of coral provenance 221

The Shallows morphology and the interpretation of coral provenance 227

CONCLUSIONS 248

ACKNOWLEDGEMENTS 249

CHAPTER 6

THE NERITIC EXPANSION AND THE ATMOSPHERIC pCO_2-CURVE SINCE THE LAST GLACIAL MAXIMUM: THE CORAL REEF HYPOTHESIS REVISITED WITH GIS 250

ABSTRACT 251

INTRODUCTION 253

Global sea level and atmospheric CO_2 change since the last glacial maximum 253

MATERIALS AND METHODS 259

Estimates of coral reef habitat and shallow neritic environment expansions during sea level rise since the last glacial maximum 259

Data sources 260

Atmospheric CO_2 variation and sea level rise curves since the last glacial maximum 262

RESULTS 263

DISCUSSION 283

CONCLUSIONS 291

REFERENCES 294

CURRICULUM VITAE: JACOB LOUIS MEY, IV 308

LIST OF FIGURES

CHAPTER 2

Figure 2-1: Elevation map showing uplifted coral reefs marking Pleistocene high stands 9

Figure 2-2: Barbados $^{230}Th/^{238}U_{activity}$ versus $^{234}U/^{238}U_{activity}$ from Barbadian uplifted Pleistocene reefs 22

Figure 2-3: $^{230}Th/^{234}U_{activity}$ versus $^{231}Pa/^{235}U_{activity}$ data from Barbadian reefs 24

Figure 2-4: Red Sea $^{230}Th/^{238}U_{activity}$ versus $^{234}U/^{238}U_{activity}$ plotted with Barbados activity trends 27

Figure 2-5: Diagenetic potential of Barbados reef sands 30

Figure 2-6: Oxygen isotope profile for a Barbados reef 32

Figure 2-7: $^{234}U/^{238}U$ and $^{230}Th/^{238}U$ with depth in the Salt Cave profile on Barbados' Southern Coast 38

Figure 2-8: Uranyl speciation (activity) as a function of pore water pH 41

Figure 2-9: A schematic model of the ^{238}U-^{234}U-^{230}Th uranium-series diagenesis for Barbados 47

Figure 2-10: A schematic illustration of ^{238}U-^{234}U-^{230}Th uranium series diagenesis for the Red Sea corals. 50

Figure 2-11: A schematic illustration of ^{235}U-^{231}Pa paired with the ^{234}U-^{230}Th uranium series diagenesis for Barbados 53

CHAPTER 3

Figure 3-1 Idealized uranium-series disequilibria portrayed in a $\left[\frac{^{230}Th}{^{238}U}\right]$ versus $\left[\frac{^{234}U}{^{238}U}\right]$ activity diagram 64

Figure 3-2 Distribution of the most common uranium series trends in Barbados corals that have experienced freshwater digenesis 69

Figure 3-3 Idealized activity trends based on natural observations 74

Figure 3-4 Idealized activity trends based on natural observations 74

Figure 3-4 Equal age lines computed using the derived equation (3.8) 79

Figure 3-5 Angles of trends defined as lying between the natural disequilibria trend [Z] and either the horizontal (t=zero lines) or the equal age line [Eq] 82

Figure 3-6 The evolution of the angles of the equal-age trend lines over time 85

Figure 3-7 The relationship between the lengths of two equal age trend lines representing the same age 89

Figure 3-8 The lengths of two arbitrarily chosen equal age lines calculated using the modified age equations expressing the length of a trend (see equation 3.13) 91

Figure 3-9 The relationship of the lengths of equal age lines $L[Eq]_1$ versus natural trends $L[Z]_1$, and of aged $L[Eq]_2$ versus aged $L[Z]_2$.trends 94

Figure 3-10 Data trends for Barbados: the $\left[\frac{^{230}Th}{^{238}U}\right]$ versus $\left[\frac{^{234}U}{^{238}U}\right]$ activity from Barbadian uplifted Pleistocene reefs 99

Figure 3-11 Calculated concentrations in pico-grams per gram or parts per trillion (ppt) of ^{230}Th present in corals (with a porosity of 20%) with a normalized true concentration of 3.2 ppm uranium over time, when the ^{230}Th is added to the coral by natural decay 104

Figure 3-12 Models representing the results from Table 3-2 for the dissolution trends in the Barbados reefs 107

Figure 3-13 The angle of the 60,000 year old reef was projected back to the presumed time of freshwater exposure in order to establish the original trend 110

Figure 3-14 Natural $\left[\frac{^{230}Th}{^{238}U}\right]$ versus $\left[\frac{^{234}U}{^{238}U}\right]$ activity trends for regression in the Barbados reefs 112

Figure 3-15 Functions expressing the angle change for the modeled dissolution trends shown in figure 3-12 115

Figure 3-16 Estimated 'marine residence times' for seven Barbados reefs before freshwater exposure 119

CHAPTER 4

Figure 4-1 A digital elevation model (DEM) made in ArcGIS from raw data acquired from the 90-meter resolution Shuttle Radar Topography Mission (SRTM) (1998) 126

Figure 4-2 Research vessel R/V Ranger (Picture A). The vessel deck during the 1988 Cruise 88-13 to Barbados. The heavy riser pipe (aka API pipe) is stacked on the right side (Picture B) 129

Figure 4-3 Study area showing topographical features (90 meters per pixel resolution) of the Island of Barbados and the surrounding sea bottom at various low (2 kilometers per pixel) and medium (200 meters per pixel) resolutions 134

Figure 4-4 Showing location of Multi beam bathymetric tracks acquired by the research vessel R/V Ewing on October 18, 2003 139

Figure 4-5 Work flow chart of the project and the sub-disciplines involved 145

Figure 4-6 Data stack illustrating various aspects of the data, their nature, and their processing in the MB-System 149

Figure 4-7 Low resolution (200meter per pixel) bathymetry map of the Barbados Shallows 152

Figure 4-8 A 3-D projection of the final high resolution bathymetry digital elevation model of The Shallows 156

Figure 4-9 "Target zones" in study area identified from the 3D bathymetric map 158

Figure 4-10 Results of the 3-D spatial analysis, where the multivariate regression results hover in red above the target areas 160

Figure 4-11 Result of the spatial raster calculation done in ArcGIS. The 'cut-outs' in the target areas represent the problematic zones; they are projected onto the sea-bottom, thereby displacing the green areas that failed the analysis 162

Figure 4-12 Final result of the spatial analysis, showing the target areas (green parcels) which are most likely to be successful for collecting drill samples 164

Figure 4-13 The grading of problem severity of "less problem zones" shown in 3D 166

CHAPTER 5

Figure 5-1: General topographical and bathymetric maps of the Caribbean and vicinity. The small box indicates the location of Barbados in the Caribbean Sea. 185

Figure 5-2: General topographical map of Barbados and vicinity 187

Figure 5-3A Perpendicular non-projected map of the Barbados Shallows showing the scale of the full area 190

Figures 5-3B and 5-3C: Bathymetric Map of the Barbados Shallows, made from Hydrosweep 2 sonar data processed in MB-Systems and projected in Fledermaus Pro (see the text for details on data collecting, processing, and projecting) 195

Figure 5-4 Surface analysis of the Shallows, showing variations in elevations (color coded for clarity), as well as a rough distinction between major constructional pinnacle reefs (white shades), coral sand and rubble deposits (red shades), and Pre-Pleistocene deposits (green and blue shades) 201

Figure 5-5 Contoured map of the Shallows used for spatial analysis 203

Figure 5-6 Uplift-corrected sea level data from Barbados 206

Figures 5-7A and 5-7B Slope analysis of the Barbados Shallows, whose slopes are used in the analysis of possible reef cliffs 208

Figures 5-8A(right) **and 5-8B**(left) Map of the prevailing ocean currents 8A in the Atlantic Ocean 211

Figure 5-9A (inset) **and 5-9B** Raw backscatter data of the Barbados Shallows 214

Figure 5-10 Processed backscatter data of the Barbados Shallows draped upon the digital elevation model from Figure 5-3B 217

Figure 5-11 Interpretation of the backscatter data on the Barbados shallows 219

Figure 5-12 The exposed areas of the Barbados Shallows 26,000 years ago, when the global sea level was approximately 120-125 meters below the present 222

Figures 5-13A and 5-13B Modeled coral provenance on the Barbados Shallows at 9,000 years ago 228

Figures 5-14A and 5-14B Modeled coral provenance on the Barbados Shallows at 12,000 years ago 230

Figures 5-15A and 5-15B Modeled coral provenance on the Barbados Shallows at 14,000 years ago 232

Figures 5-16A and 5-16B Modeled coral provenance on the Barbados Shallows at 18,000 years ago 234

Figures 5-17A and 5-17B Modeled coral provenance on the Barbados Shallows at 26,000 years ago 236

Figures 5-18A and 5-18B Modeled coral provenance on the Barbados Shallows at 31,000 years ago 238

Figures 5-19A and 5-19B Modeled coral provenance on the Barbados Shallows at 36,000 years ago 240

Figure 5-20A and 5-20B Modeled coral provenance on the Barbados Shallows at 62,000 years ago 242

Figure 5-21A and 5-21B Modeled coral provenance on the Barbados Shallows at 135,000 years ago 244

CHAPTER 6

Figure 6-1 Relationship between alkalinity, dissolved inorganic carbon (DIC) and surface water pCO_2 257

Figure 6-2 (plate 1 through 26) The result of our 1-minute per pixel resolution geospatial analysis delineating the areas covered by an arbitrary 30 meter deep neritic zone and how these zones expanded on the Sunda

and North Australian shelves as sea level rose since the last glacial maximum 265-272

Figure 6-2 (Plate 1) 265

Figure 6-2 (Plate 2 through 5) 266

Figure 6-2 (Plate 5 through 9) 267

Figure 6-2 (Plate 10 through 13) 268

Figure 6-2 (Plate 14 through 17) 269

Figure 6-2 (Plate 18 through 21) 270

Figure 6-2 (Plate 22 through 25) 271

Figure 6-2 (Plate 26) 272

Figure 6-3 The low resolution (3.5 minute per pixel resolution) curve for the expansion of 30 meter deep neritic zone and the area it covers 274

Figure 6-4 The higher resolution (1 minute per pixel resolution) curve for the expansion of 30 meter deep neritic zone and the area it covers. The 1st derivative is scaled artificially to fit the range of the parent curve. 276

Figure 6-5 Relative pCO_2 of the atmosphere since the last glacial maximum, as measured in the Antarctic ice core from SIPLE dome(Data from Ahn et al., 2004) and its 1st derivative curve. 278

Figure 6-6 Sea level rise and its 1st derivative curve from the last glacial maximum to present based on corals from a variety of localities 281

Figure 6-7 The three curves showing the evolution of (i) neritic expansion (red), (ii) atmospheric pCO_2 (green) and the (iii) coral based sea level (blue) since the last glacial maximum. 287

Figure 6-8 The 1st derivatives of the parent curves (illustrated in Figure 6-7) of (i) neritic expansion (red), (ii) atmospheric pCO_2 (green) and the (iii) coral based sea level (blue) since the last glacial maximum. 289

LIST OF TABLES

CHAPTER 2

Table 2-1: Barbados coral data. 20

CHAPTER 3

Table 3-1 Approximate ages, regressed data slopes and activity trend angles[φ] of 7 Barbadian paleoreefs 97

Table 3-2: Results of dissolution modeling 101

Table 3-2: Results of dissolution modeling (continued) 102

Table 3-3 A list of the reef ages, the calculated cross points of natural and modeled angle functions as shown in Figure 3-14 and also the appropriate Marine Isotope Stages. 117

CHAPTER 4

Table 4-1 Proposed budget for Barbados mapping project 147

CHAPTER 5

Table 5-1 Paleo sea level and coral habitat zones below present sea level 225

LIST OF APPENDICES

Appendix 4-1 A list of processed raw data files from the 18 October 2003, R/V Ewing cruise (leg EW0310) used for this study 172

Appendix 4-2 Example of available parameters used for processing the bathymetry data for this study. 174

Appendix 4-3 An example of a PERL script used to generate maps for this study 177

Appendix 4-4 Example of information files for data 179

Appendix A Curriculum Vitae: Jacob Louis Mey IV 308

CHAPTER 1
INTRODUCTION

Fossil corals are frequently used in paleo-climate research. Mainly, they are important in the study of past sea levels and in establishing paleo-climate proxies, such as seasonal temperature variations and pH changes in the past, but they are also used for calibrating ^{14}C data. All these studies are based on the decay of the uranium series isotopes in corals for accurate age determinations. However, the corals in question have often been exposed to freshwater thereby causing diagenesis. As a result, they may yield wrong ages and thus, any selection of coral samples for successful dating, however stringent, is not completely without ambiguity, and may after time-consuming and costly analyses yield unreliable open system ages.

The present dissertation offers a two-pronged approach to this problem: (i) by describing and modeling the major characteristics and processes involved, we aim to gain a better understanding of the freshwater diagenesis that affects the uranium series, especially by trying to identify its effects and how to avoid the affected samples; and (ii) by developing new exploration methods, based on high resolution bathymetric data. Using the 3-dimensional geospatial techniques developed in the present work, we strive to identify off-shore coral samples for high accuracy dating and to increase their successful retrieval. In addition to improving and expanding the sampling of coral data, the desired outcome of this work is a better understanding of the reef morphologies, in particular with regard to localizing and avoiding the undesirable effects mentioned above. The latter

point is of great importance in locating the desired coral samples, relying on which we can expand our paleo climatic knowledge.

Chapter 2 details the diagenesis causing the open system uranium series disequilibria that affects paleo-reefs when exposed to fresh water. It is important to understand these processes, especially since they affect the areas where we wish to prospect for pristine high quality coral samples. Next, a new 'dissolution-cum-adsorption' model is developed for the uranium series disequilibria and applied to Barbados and Red Sea corals. Based on the new model, we conclude that the diagenetic signatures, (set as trends in the uranium series activity diagrams), were most likely set early, during a relatively short-lived event when the paleo-reefs were first exposed to fresh water.

Chapter 3 deals specifically with quantifying the relationship between the individual diagenetically affected ^{238}U, ^{234}U, and ^{230}Th isotopes in the uranium series. A set of fundamental geometrical relationships, coupled with probable dissolution effects, have been developed which, when applied to the trends in the open systems, allowed us for the first time to calculate the approximate 'marine residence times' for the individual reefs. Quantifying the dissolution-cum-adsorption model in this way, we were able to successfully determine the approximate marine residence times for seven paleo-reefs, spanning back from 60,000 to 240,000 years.

Chapter 4 is a geospatial treatment of bathymetric data from the Barbados Shallows which shows how such results can aid in the technical aspects of offshore drilling for samples at 70-120 meters below the present sea level. Using

high resolution bathymetry data to identify promising reef targets containing closed system samples, may prove of paramount importance for our efforts to further improve the undertaking of prospecting, identifying, and selecting the pristine coral samples used in paleo-sea level research, paleo-temperature investigations, and paleo-ocean chemistry, as well as in efforts to establish the radiocarbon curve.

Chapter 5 builds on the work begun in chapter 4, but with a much more scientific application of the geospatial analysis, by extending it to studies of reef morphology and to likely locations of specific coral species in the drowned reefs. A better understanding and an unraveling of the distribution of reef species in a paleo-reef setting is a valuable tool in finding the suitable reef crest samples (*Acropora palmata*) that are pivotal for determining past sea levels. For example, finding the glacial low stand paleo-reefs with the aid of these new techniques may prove helpful when we try to find samples that will allow us to further constrain the duration of the last glacial maximum.

In Chapter 6, the 3-dimensional geospatial analysis, developed in this work, is applied to bathymetry models in order to explore the influence of large areas of neritic expansion (reef habitats) and CO_2 production rates during the sea level rise since the last glacial maximum. The connection between the atmospheric CO_2 rise (partial pressure CO_2 – pCO_2) and the shallow neritic expansion is explored and compared to a recently updated sea level curve based on coral data. Taking off from the Barbados coral based sea level curve, the 3-dimensional geospatial techniques developed in chapters 4 and 5 are now applied successfully to other

regions in order to unravel broader paleo-climatic questions. Based on (i) the 'coral reef hypothesis', (ii) the 1st derivatives of the *p*CO2 curve from the Antarctic ice cores, (iii) the geospatial analysis (applied in the present work) of the neritic expansion on the Sunda and North Australian shelves, and (iv) the coral-based sea level curve, a new hypothesis is suggested that explains the rise and variability of atmospheric pCO_2 since the last glacial maximum.

CHAPTER 2:
URANIUM SERIES DISEQUILIBRIA SYSTEMATICS AND THE EFFECTS OF REPEATED EMERGENCE HISTORIES ON OPEN-SYSTEM RADIOMETRIC DATES

By

Jacob L. Mey[1, 2], Richard G. Fairbanks[1, 3], Richard Mortlock[1],

[1] Lamont Doherty Earth Observatory of Columbia University, Palisades, New York 10964, USA.

[2] Graduate Center, City University of New York, New York, NY 10016, USA.

[3] Department of Earth and Environmental Sciences, Columbia University, New York, NY 10027, USA.

ABSTRACT

Fossil corals are widely used in paleo-climate research; mainly in the study of past sea levels and reconstructions of the corals' living environments, such as seasonal temperature and pH. They are also used for constructing the radiocarbon calibration curve. All of these studies rely upon uranium series isotopes in corals for accurate age determinations. However, whereas disequilibria in the uranium series are common in fossil corals exposed to fresh water, '*a priori'* screening criteria are often insufficient to reject open-system samples. Barbadian corals that have been exposed to freshwater diagenesis commonly show a positive correlation between $^{230}Th/^{238}U$ and $^{234}U/^{238}U$ activities in samples with elevated $\delta^{234}U_{initial}$.[1] Open system samples are often identified only after all the efforts to measure a uranium series age date are complete. In an effort to salvage these measurements, researchers have repeatedly attempted to develop criteria to "correct" the open system dates. This has led some researchers to develop diagenetic models of *progressive* adsorption/desorption of ^{234}U and ^{230}Th that prescribe a strict diagenetic history, of individual corals and the fossil reefs containing the corals, captured in numerical models with highly parameterized stoichiometries. Unfortunately, age corrections applied to open system corals have not been particularly successful when applied to different locations. We present new $^{230}Th/^{234}U/^{238}U$ and $^{231}Pa/^{235}U/^{230}Th/^{234}U$ data from a submerged, 60,000 year old Barbados reef, showing large offsets in activity ratios in these relatively young samples. Data from the Red Sea confirm our observations and show an occurrence of high $\delta^{234}U_{initial}$ in young Holocene

[1] $\delta^{234}U_{initial} = ((([^{234}U/^{238}U]_{measured})-1)*e^{\lambda 234t})*1000$

samples. Based on these new observations, we formulate an alternative model for the diagenesis of the uranium series, in which the correlation between the $^{234}U/^{238}U$ versus $^{230}Th/^{238}U$ and the $^{231}Pa/^{235}U$ versus $^{230}Th/^{234}U$ activities, as observed in samples from the Barbados reefs, are presumed to be *set early*, that is, during the reef's first exposure to fresh water during uplift or falling sea levels. The 'diagenetic potential' of reef-sand and rubble is highest during this event, and leads to rapid dissolution of aragonite sands and to their structural inversion to calcite. Our model clashes with the assumptions that are at the basis of most diagenesis models, inasmuch as the latter relies on the progressive addition of ^{234}U. Importantly, the slopes of the $^{230}Th/^{238}U$ versus $^{234}U/^{238}U$ and the $^{231}Pa/^{235}U$ versus $^{230}Th/^{234}U$ activities are dependent on their respective ^{230}Th and ^{231}Pa in-growth during the time span from when the living reef was buried in the marine setting to the time of initial exposure to the vadose fresh water environment. The relatively constant tectonic uplift of Barbados, combined with the cyclical sea level changes that are controlled by periodical orbital forcing (the so-called Milankovich cycles), set the lag times for daughter isotope in-growth during the period from reef formation to the initial fresh water exposure in the vadose zone. Major Barbadian constructional reefs show the same uranium series activity trends, as these are locked in by their duplicated emergence histories. Unfortunately, these findings indicate that reliable open system age corrections are not possible for fossil corals.

INTRODUCTION

$^{230}Th/^{234}U/^{238}U$ age determinations of corals from Barbados (Figure 2-1) for sea level and radiocarbon calibration have a long history, and their applications have gained wide acceptance. In the last two decades, strict criteria have been established for the *'a priori'* screening for closed system samples (Fairbanks et al., 2006); however, even a stringent criteria are often insufficient to identify and reject open-system samples, thus avoiding time-consuming analysis resulting in unreliable ages. A better understanding of uranium series diagenesis, in particular of the causes of the open system behavior that has led to elevated $^{234}U/^{238}U$ activity ratios in corals, is required in order to improve prospecting for closed-system samples.

Samples that have been exposed to freshwater frequently show open system behavior, whereas those that have remained submerged in the marine environment represent closed systems having $\delta^{234}U_{initial}$ values that are similar to those found in modern corals and in seawater (Bard et al., 1990; Fairbanks et al., 2005; Hamelin et al., 1991). Samples with elevated $\delta^{234}U_{initial}$ values typically display positive correlations of $^{230}Th/^{238}U$ versus $^{234}U/^{238}U$ activity ratios, indicating consistent synchronous addition of ^{230}Th and ^{234}U (Bender et al., 1979; Gallup et al., 1994; Hamelin et al., 1991; Thompson et al., 2003; Villemant and Feuillet, 2003).

Open system samples with $\delta^{234}U_{initial}$ values exceeding those found in modern seawater (i.e. $\delta^{234}U_{initial} = 147$, Henderson, 2002) and modern corals,

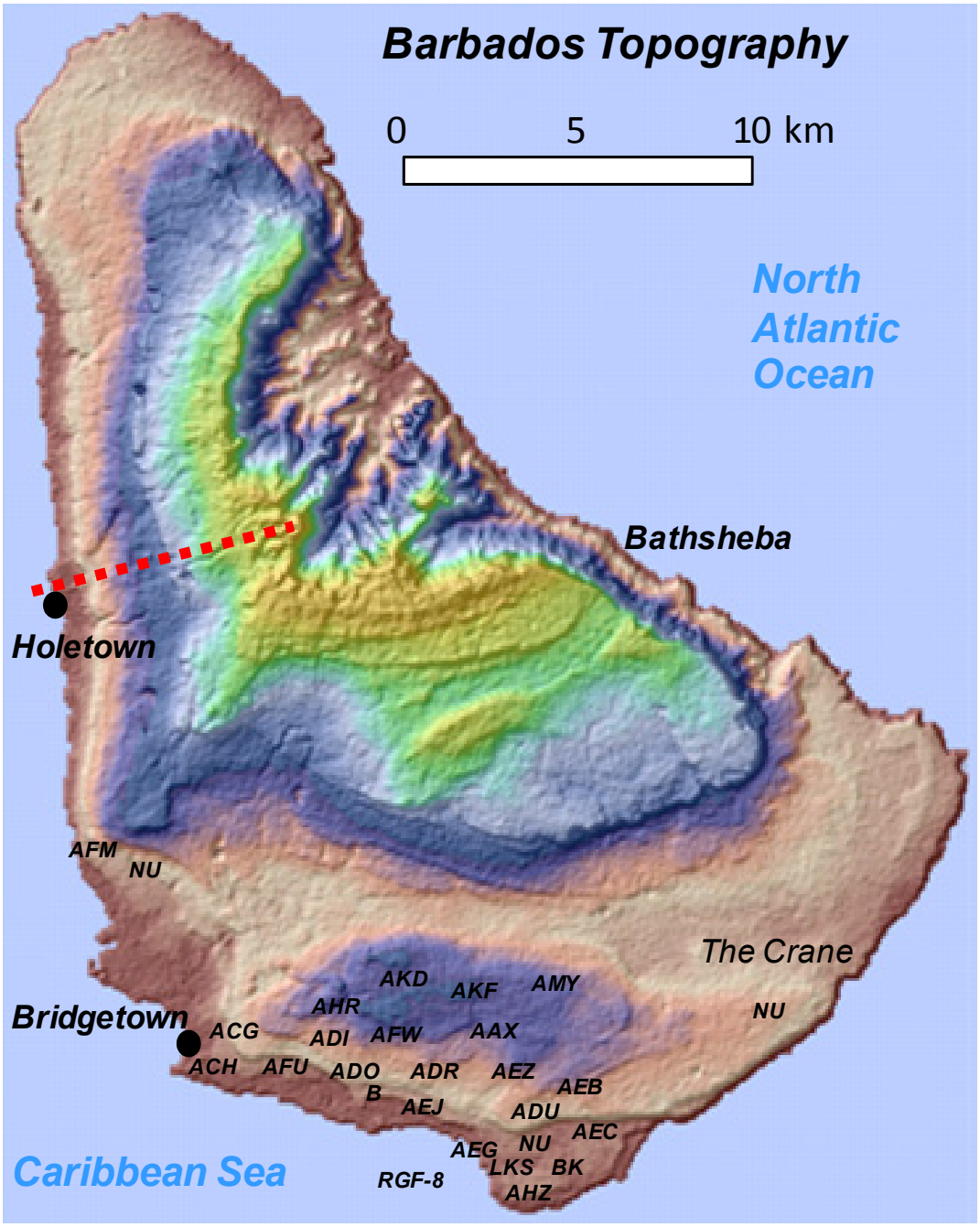
Barbados Topography
0
5
10 km
North Atlantic Ocean
Bathsheba
Holetown
AFM
NU
The Crane
AKD
AKF
AMY
AHR
NU
Bridgetown
ACG
ADI
AFW
AAX
ACH
AFU
ADO
ADR
AEZ
AEB
B
AEJ
ADU
AEC
AEG
NU
LKS
BK
Caribbean Sea
RGF-8
AHZ

Figure 2-1

Figure 2-1 Elevation map showing uplifted coral reefs marking Pleistocene high stands and location of uranium series dated samples used in this study (DEM data source: NASA Shuttle Radar Topography Mission). Color scale height dependent from 0 meters (brown) to 342 meters (orange).

have recently been used (e. g. Thompson et al., 2003, Villemant and Feuillet, 2003, Thompson and Goldstein, 2005) to challenge what has been called the Astronomical Theory of Climate Change (ATCC) (Milankovitch, 1941; Mesolella et al., 1969; Hays et al., 1976; Shackleton et al., 1983; Imbrie et al., 1984; Shackleton, 1987 and others) and have used open system samples to draw rather sensational conclusions about apparently rapid sea level changes and other climate events occurring during the last interglacial period (Thompson and Goldstein, 2005). These sensational estimates of rates of sea level change for the last interglacial have made their way into the modern debates over future Global Climate Change senarios and thus far have gone unchecked. Such challenges to the ATCC are based on uranium series ages of coral with elevated $\delta^{234}U_{initial}$ values, and rely on various age correction models that do not include a full review of the sample history and diagenesis processes (Bender et al., 1979; Gallup et al., 1994; Scholz et al., 2004; Thompson et al., 2003; Villemant and Feuillet, 2003). The majority of these studies subscribes to models that assume continuous or multiple episodic additions of ^{234}U and/or ^{230}Th to corals via adsorption, due to the low solubility of ^{230}Th and/or ^{234}Th. Several recent studies also emphasize the progressive supply of ^{234}U via α-recoil (Thompson et al., 2003; Villemant and Feuillet, 2003). The assumptions implied in such models, however, lead to over-parameterization and such models do not adequately consider the major changes in the corals' chemical environment, when the fossil reefs are first exposed to the fresh water zone.

The mobilization of the uranium-series in natural groundwater systems is very common, but the fractionation of uranium isotopes remains largely unanswered. The phenomenon is known to occur in most aquifers (Kronfeld, 1974; Kronfeld et al., 1994; Osmond et al., 1983; Rosholt et al., 1963) and depending on age of host rocks and residence time of the pore water, some continental aquifers may show extreme $^{234}U/^{238}U$ activity ratios. Old coral reefs, too, are commonly affected by uranium series disequilibrium. This is often the case for samples exposed to the percolating meteoric waters in a vadose zone, but is especially the case in the local aquifers, referred to here as the more stagnant phreatic zone.

Several models for uranium series disequilibrium in reef settings have been proposed, in order to 'correct' for the isotopic disequilibrium within the same coral sample, and also to calibrate their ages, based on the addition of ^{234}U and ^{230}Th (e.g. Anderson et al., 1973; Banner et al., 1991; Banner et al., 1990; Bender et al., 1979; Broecker, 1973; Gallup et al., 1994; Kaufman et al., 1971; Ku et al., 1990; Thompson and Goldstein, 2005; Thompson et al., 2003, Scholz et al 2004). Unfortunately, most of these studies do not distinguish between samples that have been exposed to the percolating freshwater of the vadose zone and those altered in the water saturated, phreatic zone. The degrees of alteration, as well as the characteristic development of the uranium series diagenesis, are generally very different; in particular, these phenomena occur more extensively in the phreatic zone, as compared to the vadose zone (Pingitore, 1976). For example, large variations in the total uranium content, both higher and lower, are observed in

altered phreatic zone corals (Pingitore, 1976). This study restricts itself to understanding the processes occurring in the vadose zone, as few specimens remain unaltered, once they experience extended exposure to the phreatic zone.

Published models attempt to account for the addition of ^{234}U or ^{230}Th via several mechanisms in coral reef settings. The 'continuous diagenesis model', coined by Bender et al., (1979) and used by Chen et al., (1991); Hamelin et al., (1991); Bar-Matthews et al., (1993); Henderson et al., (1993): Gallup et al., (1994) and others bases itself on a presumed continuous addition of ^{230}Th and ^{234}U over time. The 'progressive diagenesis models' used by Kigoshi, 1971; Kronfeld, 1974; Thompson et al., 2003; Villemant and Feuillet, 2003; Thompson and Goldstein, 2005) ground their explanations in the progressive addition of ^{230}Th and the preferential mobilization of α-recoiled ^{234}U and ^{234}Th. Several other studies explain the continuous addition of ^{234}U and ^{230}Th as resulting from ground water ion exchange reactions (Cherdyntsev et al., 1965; Osmond et al., 1983;; Ivanovich and Harmon, 1992; Ivanovich et al., 1992a; Kronfeld et al., 1994; Osmond and Cowart, 1992; Henderson et al., 2001).

The findings of Scholz et al. (2004), Andersen et al. (2008), Scholz et al. (2006) and Scholz and Mangini (2007) suggest that the approach of the 'progressive diagenesis model' in most cases cannot be applied regionally (and even less so globally), because the parameters in the models are based on local conditions and may show highly varying degrees of uranium series redistribution and detrital contamination (as evinced, e.g., in the Red Sea data collected by Scholz et al., 2004). Andersen et al. (2008) showed that recent α-recoil models

(e.g. Thompson et al., 2003; Villemant and Feuillet, 2003) applied to corals from Henderson Island in the Pacific, produced inconsistent results. At best, the Thompson et al (2003) model correctly predicted marine isotope stage (MIS) 15 era ages in only half the analyzed corals and the Villemant et al, (2003) model even less so (Andersen et al., 2008). Although, Scholz et al. (2006) found that several older Barbadian corals (MIS 6.5 ~ 170 ka) show open system behavior they also found samples that have their original seawater $\delta^{234}U_{initial}$ retained. Another finding were that subsamples from the same coral fragment showed trends that are different than from those found for several coral fragments of the same reef in Barbados. Scholz and Mangini (2007) published a comparative analysis estimating the compounded errors of conventional ages of several subsamples from the same coral fragment and compared them to the errors of the modeled ages of Thompson et al. (2003), Villemant and Feuillet (2003) and Scholz et al. (2004). They found that the errors on the conventional age variations among the subsamples were highly disproportionate to the modeled ages, which therefore do not reflect the true age variability. The above points stress the caution that should be exerted when attempting to 'age correct' open system ages of apparent diagenetically altered corals.

Attempts have been made to physically or chemically remove the isotopic contamination caused by the diagenetic 'additions' by stepwise leaching of the coral surfaces and subsequently analyzing the leachates and the remaining fragments so as to model a uranium-series 'cleaning' isochron (Bischoff and Fitzpatrick, 1991; Kaufman, 1993; Liang and Ku, 1984; Luo and Ku, 1991, Luo et

al., 2000; Schwarcz and Latham, 1989). However, the cleaning techniques used have generally been unsuccessful in achieving pristine samples for accurate dating.

We present new data that is inconsistent with uranium series diagenesis models invoking 'continuous' or 'progressive' addition of uranium and thorium isotopes. In direct contrast with existing models, we propose that the uranium-series diagenesis occurs in the reef setting in the short time period immediately following initial exposure to the vadose freshwater environment.

Chemical fractionation in the uranium-series during coral diagenesis in the vadose zone

The reef sands surrounding corals are composed primarily of high uranium (~3-4 ppm uranium) aragonite, which is thermodynamically less stable in freshwater than in seawater. During periods of falling sea level, the switch from marine to fresh water environments leads to rapid dissolution of aragonite and also accelerated the aragonite-calcite inversion (Winland, 1969). The uranium series isotopes are expunged to the groundwater via these two main mechanisms. Uranium substitutes readily for the divalent calcium in the calcite lattice with some distortion of the nearest-neighbor oxygen shell, but with no significant disruption of the local structure (Sturchio et al., 1998). On the other hand, the large uranyl ions (UO_2^{2+}), owing to their configuration and size, are not expected to substitute readily into either calcite or aragonite, although more readily into the latter, again without significant local disruption of the structure (Reeder et al., 2000). Dissolution of the corals will occur when the pH of the pore water is

lowered by the intruding fresh water and a new chemical equilibrium is established. During accelerated re-crystallization of aragonite, the denser calcite structure selectively resists substitution by the large uranyl (UO_2^{2+}) ions (as was observed by Eggins et al., 2005)

Radiogenic fractionation in the uranium-series

^{238}U decays to ^{234}U via one α and two β^- decays (i. e. ^{238}U [$t_{1/2}$=4.47x10^9 years] →α→ ^{234}Th [$t_{1/2}$=24.3 days] → β^- → ^{234}Pa [$t_{1/2}$=1.17 minutes] → β^- → ^{234}U [$t_{1/2}$=2.46x10^5 years]). When an α-particle emits, it causes radiation damage and the recoiled ^{234}Th nucleus causes damage to the crystal lattice over very short distances that are measured from several tens of nanometers in silicate minerals (Kigoshi, 1971), to extrapolated estimates of 80 nanometers in aragonite based on its lower density (Thompson et al., 2003). Such lattice damages, when exposed to groundwater, result in preferential weathering/leaching, releasing excess ^{234}U. Osmond and Cowart (1976; 1983) hypothesized that the loss of two β-particles from the decay process brings about a forced mobile hexa-valent state of the ^{234}U, since these are normally bound with a +4 valence in a mineral lattice. The oxidation potential around the newly recoiled ^{234}U is also believed to have an effect on this forced valence. These two conceptualizations are widely accepted as correctly representing the main causes for the isotopic fractionation of the uranium-series at the rock-water interface in a wide range of continental groundwater environments (see, e. g., Adloff and Rössler, 1991; Ivanovich et al., 1992b; Ordonez-Regil et al., 1989; Osmond and Cowart, 1976; Osmond and Cowart, 1980; Osmond and Cowart, 1985; Osmond and Cowart, 1992; Petit et al.,

1985; Rasilainen et al., 2003; Rössler, 1983; Suksi and Rasilainen, 2001a; Suksi and Rasilainen, 2001b; Suksi et al., 2006).

Whether the valence that is forced upon the $^{234}U^{6+}$ makes it more reactive during ion exchange, thereby allowing for preferential adsorption onto coral surfaces, has not been established with certainty. However, observations from various groundwater environments indicate that it does. The efficiency and timing of the $^{234}U/^{238}U$ fractionation processes is still in need of more research, but it is evident that an advanced stage of uranium disequilibrium occurred in the very young Holocene samples (Scholz et al., 2004).

In Summary, our 'early diagenesis' model, based on data presented here from the 60,000 year old MIS 3 reef around Barbados, establishes the local trend in $^{230}Th/^{238}U$ versus $^{234}U/^{238}U$ activity, as documented during the reef's very first exposure to the vadose environment. Subsequently, the slopes of the trends are maintained through the processes of systematic decay. In all likelihood, the progressive dissolution of the coral samples, rather than causing the above activity to move away from the "true age" line (and consequently exacerbate the disequilibrium), the dissolution will tend to collapse the trends involved in the $^{230}Th/^{238}U$ versus $^{234}U/^{238}U$ activity inasmuch the excess ^{234}U is gradually removed the more the affected surfaces are cleaned.

MATERIALS AND METHODS

In support of this hypothesis, we present uranium series analyses of 26 coral fragments from four Barbados reefs (see Figure 2-1 for sample localities): 6

samples from an 8 m section of a submarine core drilled offshore that penetrated the 60,000 yr. BP drowned reef (RGF-8; -59.547W, 13.046N), 8 samples taken from the 105,000 yr. BP, below the 1st high cliff reef above Salt Cave Point (SCP; -59.463W, 13.085N), 6 samples from the 125,000 yr. BP lower part of the 1st high cliff reef near Chancery Lane (AEC; -59.565W, 13.066N) and 6 samples from the 210,000 yr. BP cliff near Regency Park above Worthington (LKS; -59.565W, 13.083N).

Coral cores or fragments were cut to 4 mm thick slabs and placed in an ultrasonic bath with several Milli-Q (18 MΩ) water exchanges for 45 minutes until clear. From each sample slab, 2 concentric plugs for uranium-series dating and an archive sample (Ø = 13 mm and 5 mm, respectively) were cored while submerged in Milli-Q (18 MΩ) water. The concentric coring assures consistency and recognizes the proximal locations of several age determinations on the same slab. Such systematic sampling is important when pairing uranium series age determinations of fossil coral with results obtained using other analytical methods, such as X-ray diffraction (XRD), thin section inspection, and other isotope studies. The core's outer ring (500 mg) was used for uranium series (U-Th-Pa) dating, whereas the central pieces (50 mg each) were archived. Immediately before preparation, the samples were cleaned multiple times with the method outlined above for cleaning slabs. All samples were screened for calcite contents, using X-ray diffraction (XRD) analysis at 0.2% detection limits (Chiu et al., 2006). They were inspected for any detrital contents by examining them both under a stereo microscope and a scanning electron microscope (SEM). The

samples used in determining the uranium series were not chemically etched before dissolution All U-Th and U-Pa isotopic analyses were conducted on a FISONS Plasma-54 'Magnetic Sector – Multi Collector – Inductively Coupled Plasma - Mass Spectrometer' (MS-MC-ICP-MS) at the Isotope Laboratory of the Lamont Doherty Earth Observatory of Columbia University. The techniques used to determine $^{230}Th/^{234}U/^{238}U$ and $^{231}Pa/^{235}U$ ages in a single coral fragment by MS-MC-ICPMS are described elsewhere (Mortlock et al., 2005).

RESULTS

The new data are collectively presented in Table 2-1. U-Th dating was performed on all samples, but U-Pa dating was only performed on one set of the RGF-8 core samples. The Barbados $^{230}Th/^{238}U$ versus $^{234}U/^{238}U$ activities are shown in Figure 2-2 along with open and closed system data from Thompson et al. (2003) and also the youngest closed system data (less than 28,000 years) from Chiu et al. (2005). All data trends represent single reef units and the individual coral fragments are typically sampled over several meters within each unit. Replicates were analyzed on the six RGF-8 core samples and these results did not differ significantly from the first data set. The youngest of the open system reefs (~60,000 years) plot on a linear trend and show a higher degree of disequilibria than most of the older reefs. The activity trends for each reef are marked with dashed lines as a visual aid to recognize this phenomenon of the Barbados reef data. The$^{230}Th/^{234}U$ versus $^{231}Pa/^{235}U$ activities trend for core RGF-8 is shown in Figure 2-3 along with the closed system data from Chiu et al. (2005). The young

TABLE 2-1

BARBADOS	Latitude	Longitude	Depth[1]	Species	U-series I.D.	U (ppm)	1σ error	^{232}Th(ppt)	1σ error	^{234}U/^{238}U act.	1σ error	$\delta^{234}U_{initial}$ [2]	1σ error	^{230}Th/^{238}U act.	1σ error	^{230}Th/^{234}U act.	1σ error	U/Th age [3]	1σ error	^{231}Pa/^{235}U act.	1σ error	Pa/U age	1σ error
Sample																							
U/Th series																							
LKS-3-1	13.07N	-59.58W	na	A. palmata	an050720.004	3.48	0.001	157	0.1	1.103	0.001	205	1.8	1.009	0.001	0.915	0.001	243012	843	not analyzed	-	-	-
LKS-3-2	13.07N	-59.58W	na	A. palmata	an050721.002	3.49	0.001	76	0.1	1.095	0.000	181	1.3	0.981	0.001	0.896	0.001	227665	817	not analyzed	-	-	-
LKS-3-3	13.07N	-59.58W	na	A. palmata	an050721.003	3.28	0.001	2960	1.8	1.117	0.001	252	2.0	1.055	0.001	0.944	0.001	270017	1154	not analyzed	-	-	-
LKS-3-4	13.07N	-59.58W	na	A. palmata	an050721.004	3.26	0.000	388	0.2	1.108	0.000	214	1.4	1.014	0.001	0.915	0.001	242812	640	not analyzed	-	-	-
LKS-3-5	13.07N	-59.58W	na	A. palmata	an050721.005	3.27	0.001	194	0.1	1.100	0.001	199	1.8	1.005	0.001	0.914	0.001	242772	793	not analyzed	-	-	-
LKS-3-6	13.07N	-59.58W	na	A. palmata	an050722.002	3.29	0.001	417	0.2	1.103	0.000	202	1.4	1.004	0.001	0.910	0.001	238975	653	not analyzed	-	-	-
AEC-1	13.06N	-59.56W	na	A.Palmata	an040806.001	3.74	0.001	155	0.1	1.115	0.000	167	0.9	0.802	0.001	0.719	0.001	133954	297	not analyzed	-	-	-
AEC-2	13.06N	-59.56W	na	A.Palmata	an040806.002	3.58	0.001	144	0.2	1.117	0.001	172	1.3	0.815	0.002	0.729	0.001	137577	427	not analyzed	-	-	-
AEC-3	13.06N	-59.56W	na	A.Palmata	an040823.003	3.66	0.001	50	0.1	1.120	0.001	174	1.2	0.802	0.002	0.716	0.002	132690	552	not analyzed	-	-	-
AEC-4	13.06N	-59.56W	na	A.Palmata	an040823.004	2.91	0.001	344	0.4	1.131	0.001	196	1.1	0.841	0.001	0.744	0.001	142383	395	not analyzed	-	-	-
AEC-5	13.06N	-59.56W	na	A.Palmata	an040824.004	3.60	0.001	120	0.1	1.120	0.001	175	1.1	0.799	0.001	0.714	0.001	131842	319	not analyzed	-	-	-
AEC-6	13.06N	-59.56W	na	A.Palmata	an040824.005	3.73	0.001	74	0.0	1.120	0.001	173	1.1	0.787	0.001	0.703	0.001	128180	272	not analyzed	-	-	-
NU-1442-B	13.08N	-59.46W	na	M. annularis	na	2.32	0.001	26	na	1.108	0.001	146	2.0	0.696	0.009	0.628	0.009	1299	2200	not analyzed	-	-	-
NU-1506	13.08N	-59.46W	na	Diploria sp	na	2.49	0.001	77	na	1.113	0.001	153	2.0	0.702	0.001	0.631	0.001	106100	300	not analyzed	-	-	-
NU-1501	13.08N	-59.46W	na	Diploria sp	na	2.56	0.002	434	na	1.115	0.001	157	2.0	0.724	0.001	0.649	0.001	111700	300	not analyzed	-	-	-
NU-1505	13.08N	-59.46W	na	A. palmata	na	3.27	0.002	47	na	1.118	0.001	160	2.0	0.717	0.001	0.641	0.001	109300	300	not analyzed	-	-	-
NU-1478	13.08N	-59.46W	na	A. palmata	na	3.38	0.002	42	na	1.127	0.001	174	2.0	0.730	0.006	0.648	0.006	110800	1500	not analyzed	-	-	-
NU-1504	13.08N	-59.46W	na	A. palmata	na	3.37	0.002	89	na	1.130	0.001	181	2.0	0.756	0.001	0.669	0.001	117100	400	not analyzed	-	-	-
NU-1502	13.08N	-59.46W	na	A. palmata	na	3.04	0.002	85	na	1.141	0.001	204	2.0	0.807	0.001	0.707	0.001	129000	400	not analyzed	-	-	-
NU-1503	13.08N	-59.46W	na	A. palmata	na	3.17	0.002	49	na	1.146	0.001	207	2.0	0.795	0.001	0.694	0.001	124500	400	not analyzed	-	-	-
RGF-8-25-2 -I	13.04N	-59.54W	41.59	A. palmata	an050127.005	3.31	0.001	78	0.3	1.134	0.001	162	1.0	0.521	0.001	0.459	0.001	66130	196	not analyzed	-	-	-
RGF-8-27-1-I	13.04N	-59.54W	45.56	A. palmata	an050127.001	4.01	0.001	68	0.1	1.144	0.001	175	0.9	0.538	0.001	0.470	0.001	68307	110	not analyzed	-	-	-
RGF-8-28-1 I	13.04N	-59.54W	46.15	A. palmata	an050125.001	3.47	0.001	104	0.3	1.177	0.001	229	1.1	0.677	0.002	0.575	0.002	90922	490	not analyzed	-	-	-
RGF-8-30-1-I	13.04N	-59.54W	47.56	A. palmata	an050129.002	3.35	0.001	32	0.1	1.194	0.001	256	1.3	0.726	0.001	0.608	0.001	98937	226	not analyzed	-	-	-
RGF-8-31-3-I	13.04N	-59.54W	50.46	A. cervicornis	an050129.001	3.41	0.001	509	0.3	1.169	0.001	217	1.2	0.657	0.001	0.562	0.001	87930	184	not analyzed	-	-	-
U/Th/Pa series																							
RGF-8-25-2 -II	13.04N	-59.54W	41.59	A. palmata	an050930.004	3.32	0.001	659	0.4	1.134	0.000	162	0.7	0.516	0.002	0.455	0.001	65317	140	0.798	0.012	75586	2987
RGF-8-27-1-II	13.04N	-59.54W	45.56	A. palmata	an050930.005	4.07	0.001	299	0.3	1.141	0.000	171	0.8	0.539	0.002	0.472	0.001	68711	156	0.811	0.016	78627	4068
RGF-8-28-1 II	13.04N	-59.54W	46.15	A. palmata	an051003.003	3.39	0.001	121	0.1	1.176	0.000	227	0.8	0.669	0.002	0.568	0.001	89296	204	0.995	0.015	250644	ND
RGF-8-30-1-IIA	13.04N	-59.54W	47.56	A. palmata	an050929.003	3.46	0.001	47	0.1	1.176	0.001	228	1.6	0.680	0.001	0.578	0.002	91656	392	0.996	0.016	236488	ND
RGF-8-30-1-IIB	13.04N	-59.54W	47.56	A. palmata	an051004.002	3.40	0.001	3062	0.1	1.188	0.001	251	2.3	0.737	0.001	0.620	0.002	102144	460	1.081	0.016	no age	-
RGF-8-31-3-II	13.04N	-59.54W	50.46	A. cervicornis	an051003.004	3.55	0.001	656	0.6	1.174	0.000	225	0.8	0.674	0.001	0.574	0.001	90696	175	1.057	0.016	no age	-

na = not available *Sea Bottom Depth (m) ND = not determined

Table 2-1: Barbados coral data.

[1] Depths in meters are from the sea bottom downwards.

[2] $\delta^{234}U_{initial} = ((([^{234}U/^{238}U]_{measured})-1)*e^{\lambda 234t})*1000.$

[3] Ages are in years calculated from decay constants (Cheng et al, 2000) λ_{234} = 2.8263 x 10^{-6} and λ_{230} =9.1577 x 10^{-6} using standard U-series decay equations for daughter excess (Dickin, 2005) e.g.

$$\left[\frac{^{230}Th}{^{238}U}\right]_{Present} = \left[\left(1 - e^{-\lambda_{230}*t}\right) + \frac{\lambda_{230}}{\lambda_{230} - \lambda_{234}}\left(e^{-(\lambda_{230}-\lambda_{234})*t}\right)\left(\left[\frac{^{234}U}{^{238}U}\right]_{Present}\right)\right]$$

and

$$\left[\frac{^{234}U}{^{238}U}\right]_{Present}^{total} = \left[\left(\left[\frac{^{234}U}{^{238}U}\right]_{Initial} - 1\right)e^{-\lambda_{234}*t}\right] - 1$$

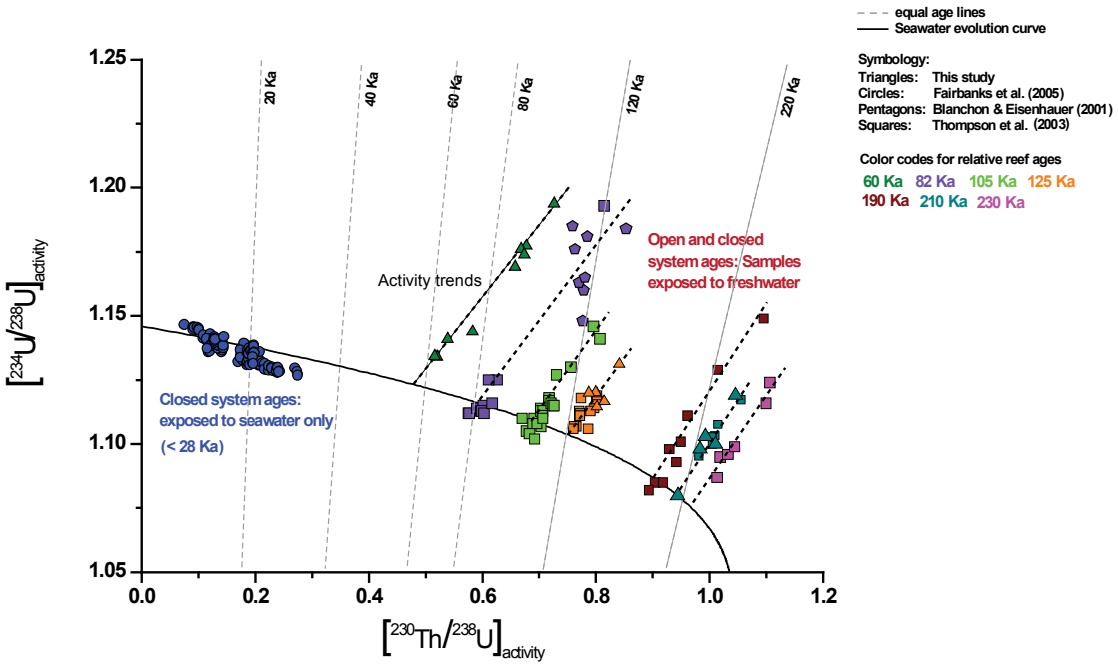
equal age lines
Seawater evolution curve
Symbology:
Triangles: This study
Circles: Fairbanks et al. (2005)
Pentagons: Blanchon & Eisenhauer (2001)
Squares: Thompson et al. (2003)
Color codes for relative reef ages
60 Ka 82 Ka 105 Ka 125 Ka
190 Ka 210 Ka 230 Ka
20 Ka
40 Ka
60 Ka
80 Ka
120 Ka
220 Ka
Activity trends
Open and closed system ages: Samples exposed to freshwater
Closed system ages: exposed to seawater only (< 28 Ka)
1.25
1.20
1.15
1.10
1.05
0.0
0.2
0.4
0.6
0.8
1.0
1.2
[234U/238U]activity
[230Th/238U]activity

Figure 2-2

Figure 2-2 Barbados $^{230}Th/^{238}U_{activity}$ versus $^{234}U/^{238}U_{activity}$ from Barbadian uplifted Pleistocene reefs. Samples with elevated $^{234}U/^{238}U$ and $^{230}Th/^{238}U$ ratios plot along trend lines which are generally similar in slope (~0.3) for all reefs. The closed system seawater evolution curve is based on $\delta^{234}U_{initial}$ =1.149. (Data from Blanchon and Eisenhauer, 2001; Thompson et al. 2003, Fairbanks et al., 2005; this study)

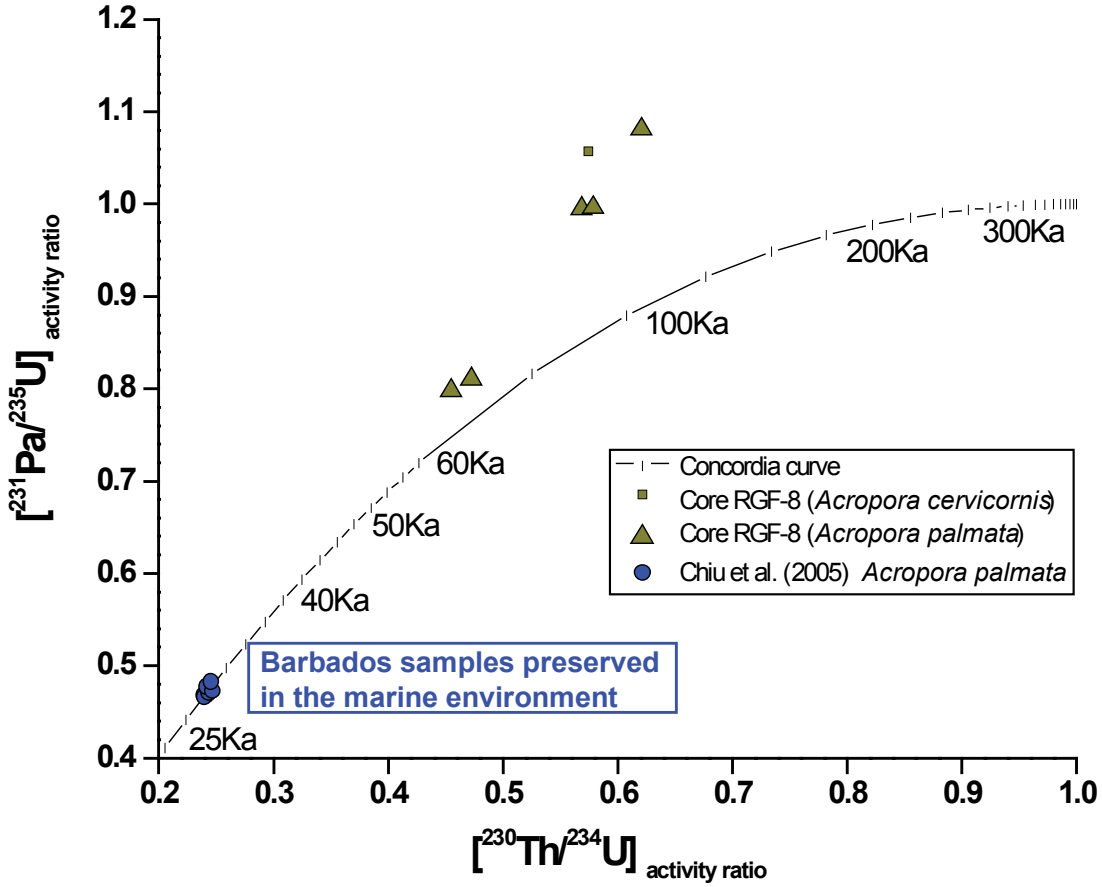
1.2
1.1
1.0
0.9
0.8
0.7
0.6
0.5
0.4
0.2
0.3
0.4
0.5
0.6
0.7
0.8
0.9
1.0
[231Pa/235U] activity ratio
[230Th/234U] activity ratio
300Ka
200Ka
100Ka
60Ka
50Ka
40Ka
25Ka
Concordia curve
Core RGF-8 (Acropora cervicornis)
Core RGF-8 (Acropora palmata)
Chiu et al. (2005) Acropora palmata
Barbados samples preserved
in the marine environment

Figure 2-3

Figure 2-3 $^{230}Th/^{234}U_{activity}$ versus $^{231}Pa/^{235}U_{activity}$ data from Barbadian reefs (this study and Chiu et al., 2005). The two pairs of data points close to one another are replicates of the same sample.

curve for the U-Th system may not lie on the Concordia of the U-Pa system and vice versa.

The Red Sea data from Aquaba reefs are shown in Figure 2-4 and their activity trends are compared with Barbados trends. The Red Sea reefs have markedly different activity trend slopes (steeper) compared to the shallower Barbados trends (Figure 2-4).

The largest $^{234}U/^{238}U$ and $^{230}Th/^{238}U$ activity anomalies are found in the *youngest reefs* (RGF-8) exposed to freshwater, indicating an early diagenetic alteration, offsetting the real ages (Figure 2-2). These results contradict the 'coming of age', radiogenic addition diagenesis models as developed by Thompson et al. (2003) and Villemant and Feuillet (2003). The striking similarity of the activity anomalies in the two series (Th/U vs. Pa/U) measured in the 60,000 year old drowned reef (as shown in Figures 2-2 and 2-3) rather support an early 'dissolution-cum-adsorption' diagenesis model, in which the reef sands surrounding the corals may supply the excess ^{230}Th, ^{231}Pa and ^{234}U. Alternatively, as the coral dissolves, the ^{238}U and ^{235}U mobilizes, but ^{230}Th, ^{231}Pa and ^{234}U adsorb onto the extant coral, thereby driving up the disequilibria for the extant fragments. The fact that ^{238}U and ^{235}U series both show elevated activity ratios, suggest that the responsible diagenetic processes causing them had strikingly similar effects (proportionate daughter additions) in both series and are not controlled by the nature of their individual decay schemes.

Another important observation is that the $^{230}Th/^{238}U_{activity}$ versus $^{234}U/^{238}U_{activity}$ trends differ regionally, as may be shown by comparing samples

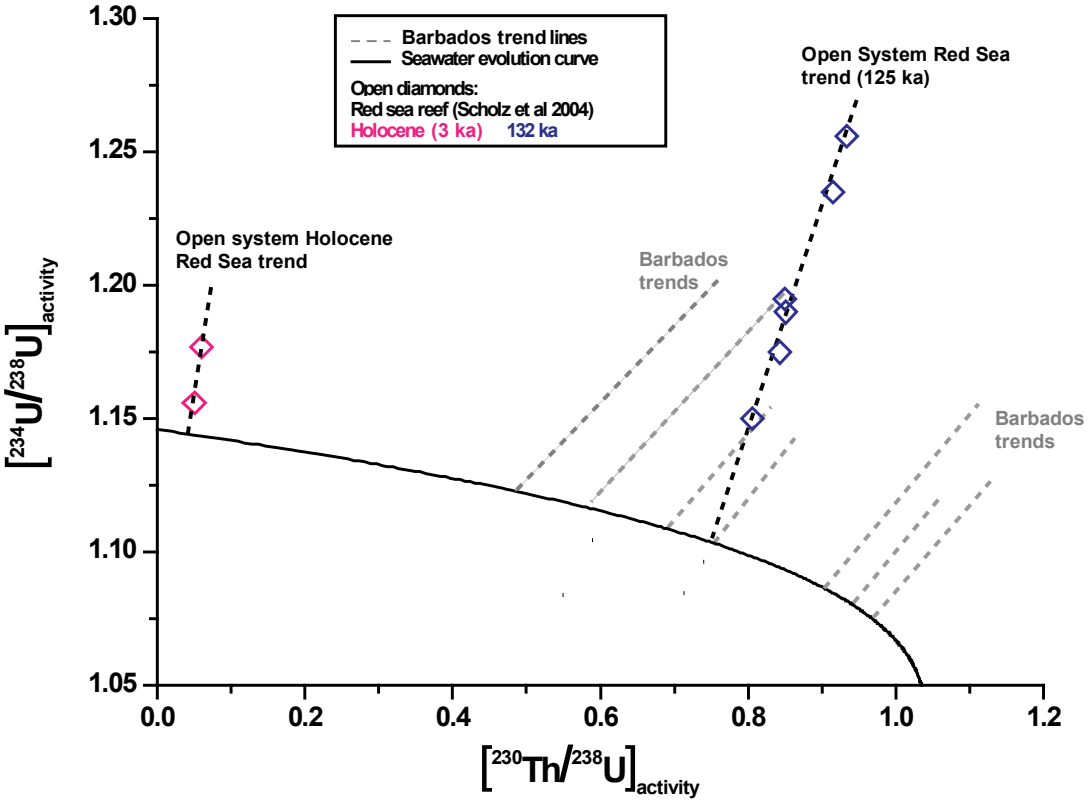
Barbados trend lines
Seawater evolution curve
Open diamonds:
Red sea reef (Scholz et al 2004)
Holocene (3 ka)
132 ka
Open System Red Sea trend (125 ka)
Open system Holocene Red Sea trend
Barbados trends
Barbados trends
1.30
1.25
1.20
1.15
1.10
1.05
0.0
0.2
0.4
0.6
0.8
1.0
1.2
[234U/238U]activity
[230Th/238U]activity

Figure 2-4

Figure 2-4 Red Sea $^{230}Th/^{238}U_{activity}$ versus $^{234}U/^{238}U_{activity}$ plotted with Barbados activity trends as plotted in Figure 2-2. Red Sea data are from Scholz et al., (2004).

(< 28.000 year) closed system samples that were preserved in the marine environment all have $^{230}Th/^{234}U$ versus $^{231}Pa/^{235}U$ activities on the Concordia curve. This is in excellent agreement with their $^{230}Th/^{238}U$ versus $^{234}U/^{238}U$ activities lying on or slightly below the seawater evolution curve and therefore displays closed system in both series for these samples. Analyzing both the U-Th and U-Pa series is useful for determining whether or not the samples are truly open or closed system, because some samples lying on the seawater evolution

from the Red Sea (Scholz et al., 2004; see Figure 2-4) with those from Barbados (Figure 2-2).

DISCUSSION

$^{234}U/^{238}U$ and $^{231}Pa/^{235}U$ disequilibria in the reef profiles

Winland (1971) observed that on Barbados, aragonite sand grains are generally absent (less than 5%) in fossil uplifted reefs older than 125,000 years (See Figure 2-5), presumably making the sands the largest source of excess ^{234}U, ^{230}Th, and also ^{231}Pa as a result of the transition to calcite. On Barbados, the age of reef sands may be contemporaneous with the extant corals or older, especially at sea cliff locations, where erosion supplies sand from reefs adjacent to the growing reefs. Thus, the $^{234}U/^{238}U$ - $^{230}Th/^{238}U$ and $^{231}Pa/^{235}U$ – $^{230}Th/^{234}U$ trend lines may very well represent mixtures of uranium series isotopes from pristine coral (closed system) and various amounts of these isotopes assumed to be derived from a dissolving sand source, and, to a much lesser degree, from the corals themselves. Technically, the trend lines in these activity diagrams are also in part due to the common denominator '^{238}U' of the ^{234}U and ^{230}Th trend line.

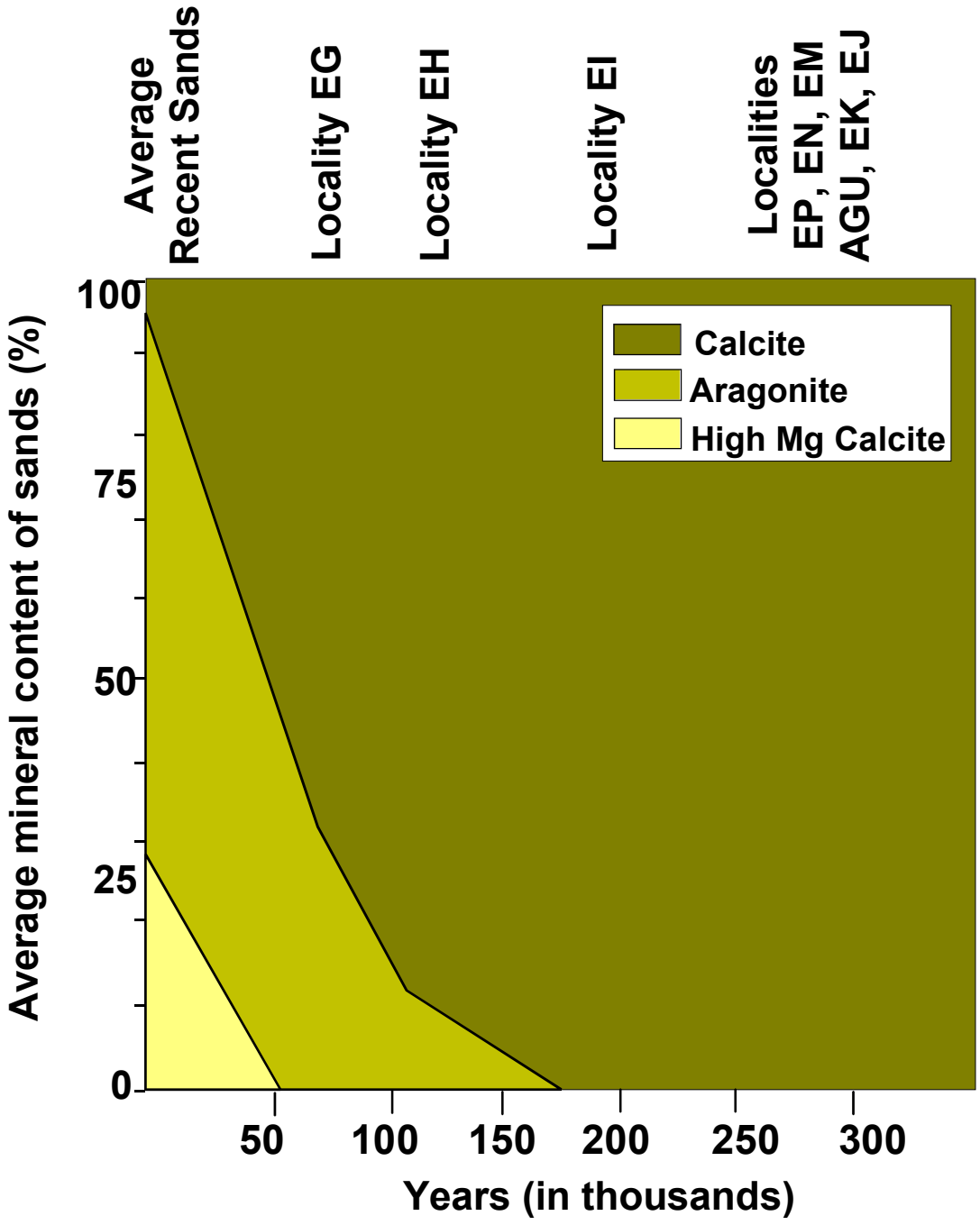
Average Recent Sands
Locality EG
Locality EH
Locality EI
Localities EP, EN, EM AGU, EK, EJ
Average mineral content of sands (%)
100
75
50
25
0
Calcite
Aragonite
High Mg Calcite
50
100
150
200
250
300
Years (in thousands)

Figure 2-5

Figure 2-5 Diagenetic potential of Barbados reef sands (redrawn from Winland, 1971). Abbreviated sample locations (e. g. EG through EJ) refer to a sampling transect (marked on Figure 2-1) eastward from Holetown.

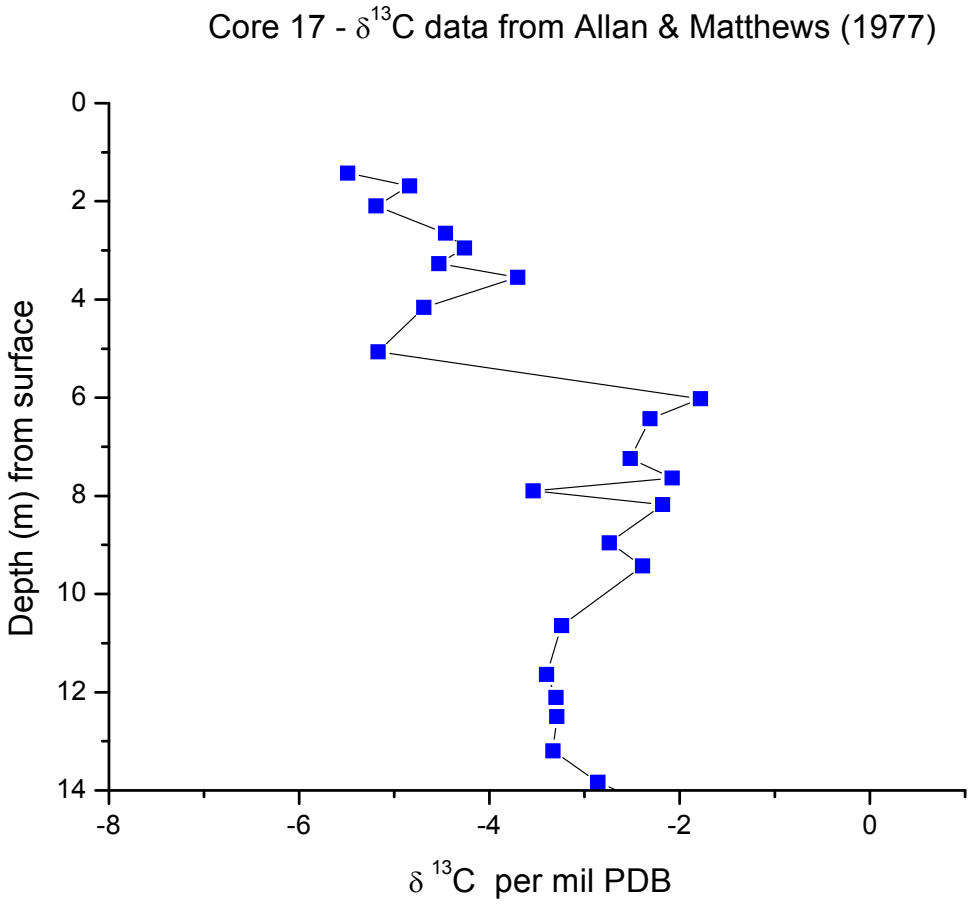
Core 17 - δ13C data from Allan & Matthews (1977)
Depth (m) from surface
0
2
4
6
8
10
12
14
-8
-6
-4
-2
0
δ 13C per mil PDB

Figure 2-6

Figure 2-6 Carbon isotope profile for a Barbados reef (Allan and Matthews, 1977) showing the depth of the altered vadose zone tagged with lower carbon isotope ratios due to the inclusion of soil gas CO_2.

For this reason, one should exercise care when interpreting these lines as representing two sources. In Figure 2-4, the Red Sea data from Scholz et al. (2004) are plotted with our Barbados data, showing that the diagenesis trend lines measured in the Barbados uplifted reefs *are not universal*. Compared with the Red Sea data, the Barbados trend lines plot with shallower slopes; in particular, the $^{230}Th/^{238}U$ versus $^{234}U/^{238}U$ trend line from the Red Sea samples indicates very little ^{230}Th addition. One explanation for this could be that the reef had been exposed to fresh water shortly after growth and burial in the contemporary sands, but before these aragonite sand grains experienced ^{230}Th in-growth. This is generally consistent with the elevated $^{234}U/^{238}U$ activity ratios in the Holocene samples from the Red Sea, which contain little or no excess ^{230}Th (Scholz et al., 2004). Even though this is not evident from Scholz et al. (2004), our prediction is that a steep $^{231}Pa/^{235}U$ activity trend would also occur in the Red Sea samples.

As for ^{234}U and ^{238}U, they are believed to have similar geochemical characteristics and mobility in their hexa-valent states under oxidizing conditions in an aqueous medium. Such similar properties would lead us to assume that these two isotopes do not fractionate once they are dissolved in ground water. However, this appears to be exactly what happens in most natural fresh water systems (Cherdyntsev et al., 1965; Ivanovich and Harmon, 1992; Ivanovich et al., 1992a; Kronfeld, 1974; Osmond and Cowart, 1992; Osmond et al., 1983; Rosholt et al., 1963, and others). According to Osmond and Cowart (1992) and Osmond et al. (1983), the $^{234}U/^{238}U$ activity in some natural aquifers could reach several tens of times the expected unity. Cherdyntsev et al. (1965) showed that a

weathering of α-recoil tracks, caused by intermediate short-lived isotopes, could pave the way for a preferential release of excess ^{234}U in the water-rock interface — a process also known as the Szilard-Chalmers effect (Petit et al., 1985) or the "hot atom effect" (Dickin, 2005). The same process is now widely cited as causing the occurrence of excess ^{234}U in natural systems. Due to natural decay, the release potential for ^{234}U increases with the age of the host rocks, especially in the case of igneous rocks with high uranium contents.

Both ^{230}Th and ^{231}Pa are tetravalent and insoluble, so if expunged into solution, their rapid adsorption onto coral surfaces is to be expected (Barnett et al., 2000; Dickin, 2005; Ivanovich and Harmon, 1992; Ivanovich et al., 1992a; Morse et al., 1984; Osmond and Cowart, 1992; van Calsteren and Thomas, 2006; von Gunten et al., 1996). It is much less clear why ^{234}U is *preferentially* adsorbed, and also how ^{230}Th and ^{231}Pa are transported from the sands and added to the fossil corals, with the disequilibrium observed today.

As for α-recoil in Barbadian corals, it is thought to play a minimal role in the redistribution of uranium series isotopes, for several reasons: (i) the spherical spatial distribution of α-recoil tracks only allows for a small fraction of bulk recoiled ^{234}U to escape from the mineral surface; (ii) the water-mineral interface required to supply recoiled ^{234}U is too limited, relatively speaking, to explain what has been observed to occur naturally in young samples (and also in some of the older ones); (iii) the water-coral interface (total surface area) is significantly reduced during dissolution, thereby lessening its effect with time; and (iv) there is no evidence of coral samples consistently showing a systematic increase of excess

^{234}U with age. In fact, our young samples display ranges from mild to severe disequilibria in the uranium-series, which clashes with the conception that this is invariably exacerbated in older samples and that the latter never are closed system For instance, Andersen et al (2008) observed that some 600 ka samples from Henderson island in the Pacific yield closed system ages. Scholz et al. 2007 reported several reliable closed system ages from MIS 6.5 (~175 ka) on Barbados). Therefore, mechanisms such as the 'coming of age' α-recoiled controlled uranium series additions cannot by themselves explain the open system signatures in Barbados corals, because the large $^{234}U/^{238}U$ activity offsets seen in the youngest samples reported here for the first time (shown in Figure 2-3), compared to those in the much older reefs, excludes the option of a constant progressive process. In other words, the uranium series data from the younger reefs (e.g. the 60,000 year old RGF-8 core) negate the 'coming of age' model. In addition, an estimate of mass-balances, based on the release-rate of α-recoiled ^{234}U in reef settings, shows an insufficient supply of ^{234}U in the corals to account for the enrichment when one takes into account their bulk uranium contents and age (Gallup et al., 1994). Instead, the explanation must be sought in uranium series fractionation and transport caused by other mechanisms, such as uranyl speciation controlled by pH or valence differences (Barnett et al., 2000; Morse et al., 1984; von Gunten et al., 1996). Alternatively, the preferential surface adsorption of $^{234}U^{6+}$, as against $^{238}U^{6+}$ bound in uranyl ions, could also provide a partial explanation.

Under oxidizing conditions in natural groundwater systems, the less mobile $^{234}U^{4+}$ is invariably oxidized to $^{234}U^{6+}$ and bonds to the uranyl ion (UO_2^{2+}), presumably becoming as mobile as its parent $^{238}U^{6+}$. This leads to increased complexing with other common anions such as CO_3^{2-}, SO_2^{2-} and Cl^- (Ivanovich and Harmon, 1992; Ivanovich et al., 1992a; Osmond and Cowart, 1992; Osmond et al., 1983). Once uranium is released in the pore water and bound to the uranyl (UO_2^{2+}) ions, it is subject, under the right conditions, to considerable adsorption. The adsorption rate may change significantly during changing environmental conditions (Morse et al., 1984). Also, changing the pH is known to have a dramatic effect on uranyl complexation with other ions (Langmuir et al 1997, Reeder et al 2000). In moderate concentration, these complexing ions (such as CO_3^{2-}) start to reduce UO_2^{2+} adsorption and may thus be responsible for much of the uranium mobility in most ground waters (Rose & Wright, 1980).

Soil gas and vertical chemical gradients in the vadose zone

Allan and Matthews (1977) have published $\delta^{13}C$ and $\delta^{18}O$ depth profiles measured in two different locations in Barbados (Figure 2-6). This profile shows the influence of soil gas on the partially recrystallized carbonate sands, where carbon isotope distributions show the effects of diagenesis in the vadose zone. The process is most pronounced in the vadose environment down to the water table, but not as much in the phreatic lens below, where the carbon isotopic signatures are less affected (not shown here). In the vadose zone, $\delta^{13}C$ values average -6 per mil (PDB). These values reflect the precipitation of diagenetic calcite containing a fraction of isotopically depleted biogenic carbon

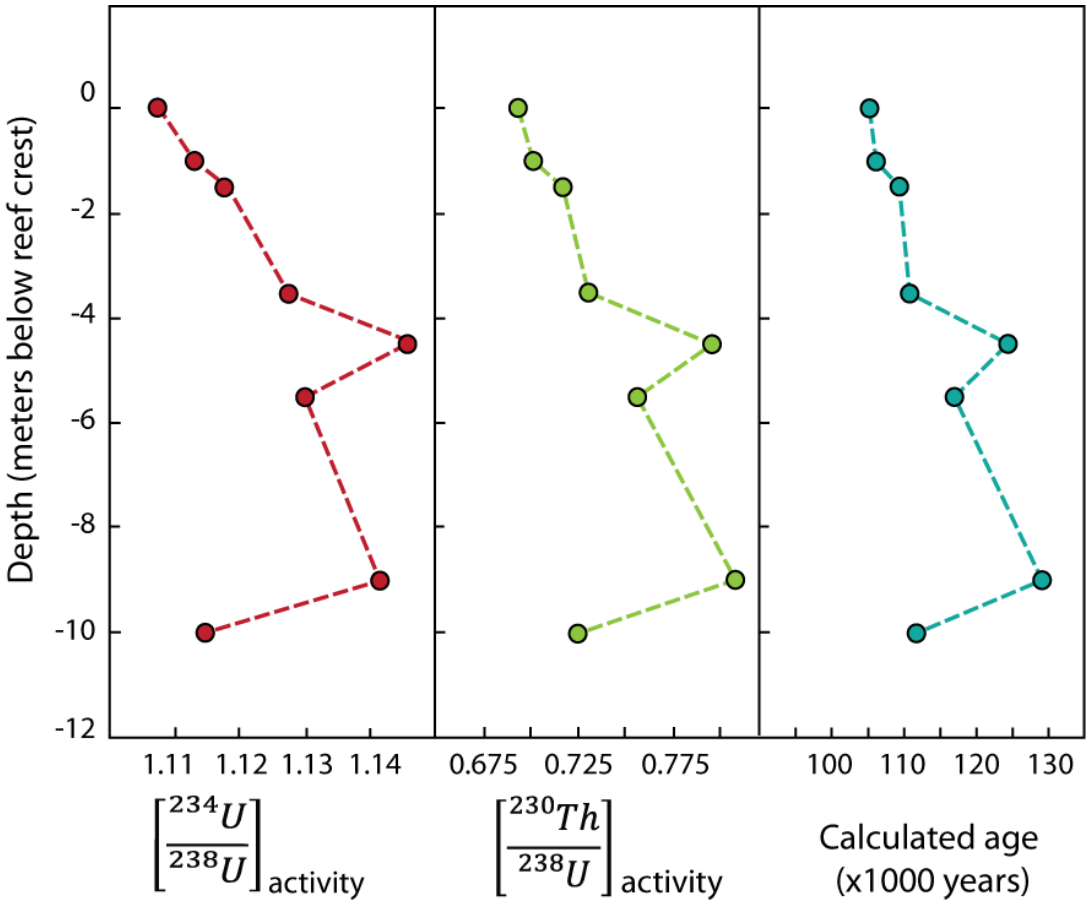
Depth (meters below reef crest)
0
-2
-4
-6
-8
-10
-12
1.11
1.12
1.13
1.14
$\left[\frac{^{234}U}{^{238}U}\right]_{\text{activity}}$
0.675
0.725
0.775
$\left[\frac{^{230}Th}{^{238}U}\right]_{\text{activity}}$
100
110
120
130
Calculated age
(x1000 years)

Figure 2-7

Figure 2-7 $^{234}U/^{238}U$ and $^{230}Th/^{238}U$ with depth in the Salt Cave reef profile on Barbados' Southern Coast (Data from Thompson, 2004).

(approximately -25 per mil $\delta^{13}C$), generated in the overlying soils. The carbon isotope data suggests that soil gas was present in the upper reef. This contributed to a reduction in pH of the percolating vadose waters, thereby increasing the CO_3^{2-} and reducing adsorption (as discussed previously), thus changing the uranyl speciation. As the 'charged' fresh water percolated down through the reefs, the dissolved CO_3^{2-} concentration dropped as calcite started to precipitate. As soon as the pH rose again, a gradual increase in uranium adsorption from the dissolved uranyls was allowed onto the coral surfaces further down into the profile (see Figure 2-7).

The effect of pH change during dissolution

Marine pore waters have a fairly constant pH of ~ 8. Consequently, one can assume (following Figure 2-8) that uranyl speciation is fixed (i.e. in equilibrium) in this environment and that little or no carbonate dissolution occurs. In the event that the pH is lowered in the reef pore water by the introduction of fresh water (such as rain water), uranium series isotopes are released by carbonate dissolution and bond in the uranyl complexes. Significant amounts of CO_3^{2-} from the dissolving sands will slow the adsorption onto the surfaces, as the pore water becomes more alkaline. The net effect of the process will be an increase in the concentration of uranium in the pore water, thereby slowing down (or hindering altogether) its adsorption back onto the extant sand grains. As the pore water migrates through the sandy matrix and further dissolves it, the pore waters may experience a continued rise in pH. When the CO_3^{2-} activity stabilizes because of saturation, and calcite starts to crystallize, uranyl adsorption onto the coral

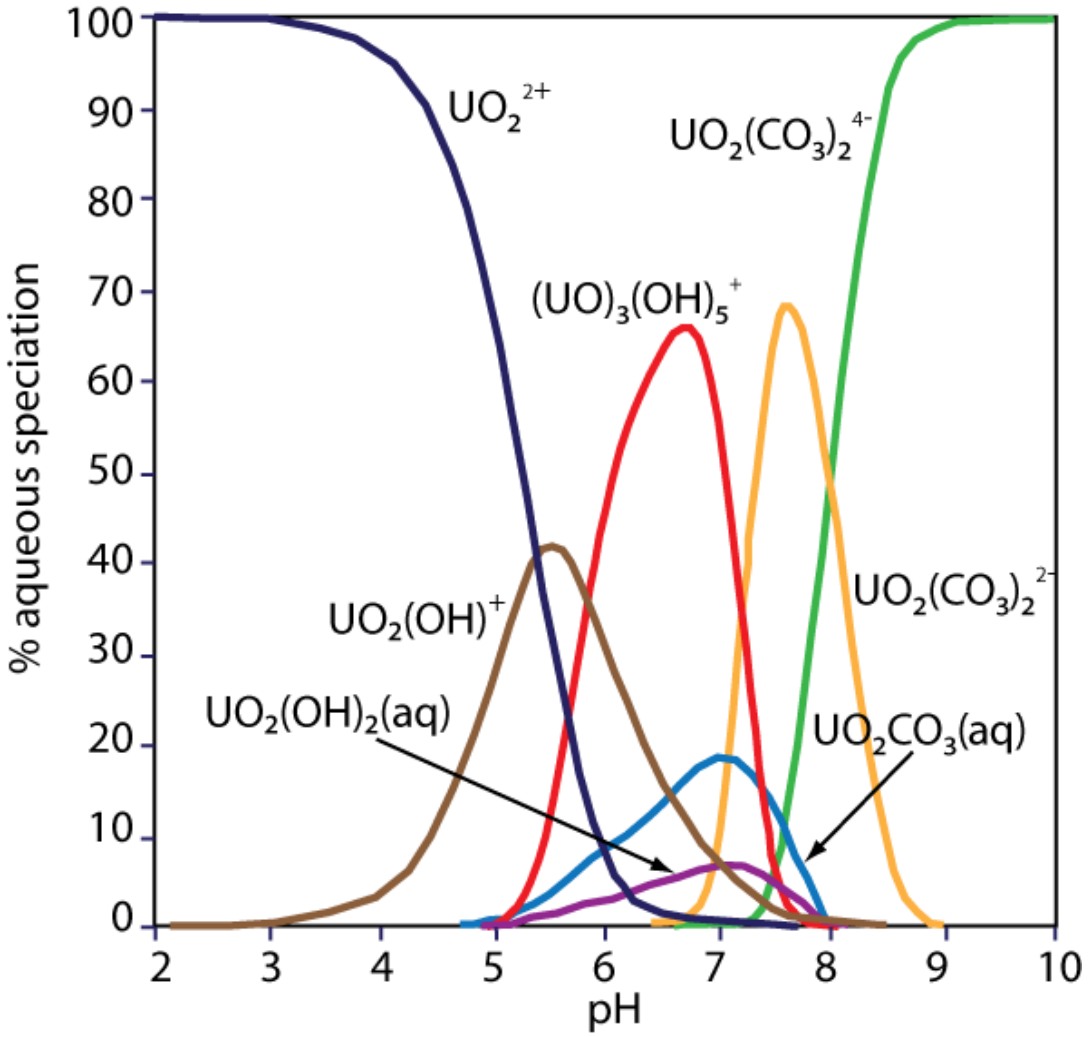
100
90
80
70
60
50
40
30
20
10
0
% aqueous speciation
2
3
4
5
6
7
8
9
10
pH
UO_2^{2+}
$UO_2(CO_3)_2^{4-}$
$(UO)_3(OH)_5^{+}$
$UO_2(OH)^{+}$
$UO_2(CO_3)_2^{2-}$
$UO_2(OH)_2(aq)$
$UO_2CO_3(aq)$

Figure 2-8

Figure 2-8 Uranyl speciation (activity) as a function of pore water pH (redrawn from Barnett et al. 2000).

surfaces will slowly increase. This may happen if uranyl laden water enters a reef structure, thus peppering the corals with uranyls by adsorption and/or surface ion exchanges. In the vadose zone, this process will have maximum effect on intact intricate coral structures, whose pore surfaces are large during the very first freshwater exposure. However, as dissolution reduces the pore surface, the process is gradually extinguished as residence time of the pore water is drastically lowered. During this dissolution-cum-adsorption process, fractionation between ^{234}U and ^{238}U may occur, since uranyl speciation is extremely sensitive to changes in the environment.

Thus, it may be controlled by processes subject to preferential kinetics whereby adsorption of one type of uranyl is favored over the other, depending on whether it hosts $^{234}U^{6+}$ or $^{238}U^{6+}$.

Kronfeld et al. (1994) observed that in the Transvaal carbonate hosted vadose aquifer, the trend towards uranium disequilibrium, with its accompanying excess ^{234}U increases, with the uranium content slightly decreasing downwards from the surface. Also, their tritium data showed that the residence time of the waters is very short; the number of years needed for the observed disequilibrium to evolve is on the order of 20. Considering this short time domain, a predominant leaching process favoring release of α-recoiled ^{234}U from damaged lattice sites on the pore surfaces must be ruled out as explanation for the uranium disequilibrium. Therefore, the dissolution-adsorption process, being much more effective in discriminating the various trends, is a preferred alternative. Since the conditions inside the aquifer are oxidizing and do not change with depth, it is unlikely that a

reducing barrier could cause uranium precipitation or change the mobility of the uranium species (Osmond et al., 1983). Relatedly, Kronfeld et al. (1994) saw no evidence of marked change in the activity ratios with increased residence time. As an explanation they argued that the aquifer's low uranium concentration (<0.5 ppm, with only little overall variation), combined with the absence of secondary sources of ^{234}U (e. g. detrital dust in the recharge water) leaves only a few candidate processes that would allow for uranium series fractionation, i.e. ion exchanges, surface adsorption or a combination of both.

Morse et al. (1984) were able to experimentally demonstrate drastic changes (within minutes) in surface adsorption of uranyls on a carbonate media with increasing carbonate saturation; conversely, desorption and exchange with other uranyl complexes occur as the alkalinity and pH change. This effect is illustrated in Figure 2-8 (from Barnett et al., 2000), which shows how uranyl speciation is strongly dependent on the pH of an aqueous solution with dissolved carbonate.

Speciation dependency on pH is similarly attested for complexes containing thorium (as observed by Langmuir and Herman, 1980). Morse et al. (1984) also observed changes in uranyl speciation with varying surface adsorption rates in an aqueous medium; also, the effect of increasing CO_3^{2-} activity in the solution was seen to reduce uranyl adsorption. Lowering the pH in coral reefs or sands by influx of fresh water will increase dissolution, thereby raising the CO_3^{2-} activity. When waters pond, or are transported to lower strata, the pH will rise again, leading to saturation lowering the carbonate activity and changes in the surface adsorption of certain uranyl species, as illustrated in Figure 2-8. What remains

enigmatic, however, is whether there is a preference, during adsorption, for uranyls containing $^{234}U^{6+}$ over ones with $^{238}U^{6+}$; in addition, there is the problem of potentially preferred ion exchanges across the water-coral interface. Luo et al. (2000) observed that the highest excess of ^{234}U is usually found in the recharge areas, where the potential for rapid environmental changes leading to dissolution and subsequent adsorption is greatest.

The above examples all support the notion that the fractionation of ^{234}U over ^{238}U onto coral surfaces may have happened during the relatively sudden changes in the chemical environment caused by the influx of fresh water into the reefs. The processes responsible for the redistribution of the uranium series are not well understood and are likely a combination of many different processes. Importantly, these processes allow the uranium series fractionation to evolve over very short time frames. The net diagenetic effect is a combination of surface dissolution along with adsorption and desorption processes in addition to a pH-controlled uranyl speciation, rather than being due to a progressive 'coming of age' of the corals.

In summary, our working hypothesis is that the first introduction of fresh water to the buried reefs has changed the pH of the extant pore waters, so as to allow for a drastic change in uranyl speciation and adsorption involving ^{234}U and ^{238}U. A significant lowering of the reefs' pore water pH may occur when the emerging reef is permeated by fresh water that has percolated through the overlying soil zone carrying organic acids and excess soil gas (CO_2). This effect is shown in Figure 2-6, illustrating the $\delta^{18}O$ variations through a reef profile and

discussed earlier in the text. Those coral samples located at the top of the reef with no overlying sands to supply ^{234}U, ^{230}Th, and ^{231}Pa are the ones that are least affected by the vadose fresh water diagenesis. These samples are predominantly affected by dissolution rather than by adsorption. Deeper in the vadose zone, samples are exposed to fresh water that has percolated though a thicker section of overlying sands and rubble and they are therefore generally more affected by adsorption as a function of depth (See Figure 2-7).

A new 'dissolution-cum-adsorption' model for uranium series trends in Barbados corals

We propose that regular trends in the Barbados uranium series activity plots (as shown in Figure 2-3) are consistent, repetitive signatures, set by recapitulated 'reef-emergence' histories. During these cycles, spanning the time from reef growth to first fresh water exposure, radiogenic isotopes ^{234}U, ^{230}Th and ^{231}Pa were added to the sands by natural decay. During a short lived event, when the reefs for the first time were exposed to fresh water, the diagenetic potential was highest causing the most significant redistribution of the uranium series isotopes and did so systematically depending on the contemporary availability in the sands and corals (Figure 2-9, 2-10 and 2-11). This is the basis of our 'Dissolution Cum Adsorption' model. Whereas the extent of dissolution of the sands supplying the excess uranium-series isotopes helps us determine the magnitude of the trend lines, it does not indicate their ratios as these were locked in by the lag-time of ^{230}Th and ^{231}Pa in-growth. Our argument in favor of these cycles (or lag-times),

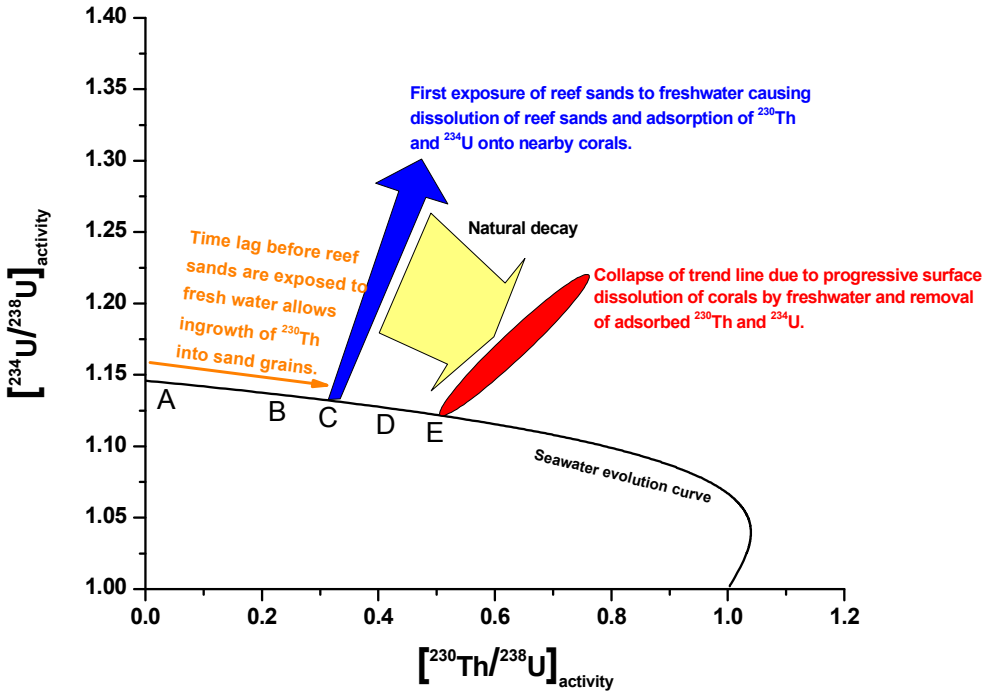
1.40
1.35
1.30
1.25
1.20
1.15
1.10
1.05
1.00
0.0
0.2
0.4
0.6
0.8
1.0
1.2
[234U/238U]activity
[230Th/238U]activity
First exposure of reef sands to freshwater causing dissolution of reef sands and adsorption of 230Th and 234U onto nearby corals.
Natural decay
Collapse of trend line due to progressive surface dissolution of corals by freshwater and removal of adsorbed 230Th and 234U.
Time lag before reef sands are exposed to fresh water allows ingrowth of 230Th into sand grains.
A
B
C
D
E
Seawater evolution curve

Figure 2-9

Figure 2-9 A schematic model of the ^{238}U-^{234}U-^{230}Th uranium-series diagenesis for Barbados. After deposition and burial in the marine environment, the reefs reflect isotopic equilibrium with sea water and follow the sea water evolution curve (A). The time lag before reef sands are exposed to freshwater allows in-growth of ^{230}Th into the aragonite grains (B). During the first exposure of reef sands to fresh water, the diagenetic potential is highest, causing major dissolution of reef sands and releasing the uranium series isotopes into the pore waters; this allows for subsequent adsorption of ^{234}U and ^{230}Th onto nearby corals. The $^{230}Th/^{238}U$ versus $^{234}U/^{238}U$ trend lines are similar for all Barbadian uplifted Pleistocene reefs, reflecting the mixing between adsorbed isotopes originally added in approximately the same proportions as the pristine coral closed-system uranium series isotopes (C). The diagenetic potential wanes relatively quickly, locking in the uranium series ratios; the latter which will now only change by natural decay, as they evolve along paths that run parallel to the seawater evolution curve (D). Over time, due to progressive surface dissolution of corals by fresh water influx and physical removal, some of the adsorbed ^{234}U and ^{230}Th will re-dissolve, causing a collapse of the trend line (E).

being roughly the same for all of the major constructional reefs on Barbados, rests mainly on two important observations: (i) the concentration of bulk uranium is constant (~3-4 ppm), so no significant U was added to the samples over time, and (ii) the setting of similar trends in the history of the reefs strictly presupposes the existence of similar amounts of ^{234}U, ^{230}Th and ^{231}Pa in-growth at the time of freshwater exposure. The significance of this latter observation becomes clear once one realizes that the regular oscillation of sea levels, coupled with a constant uplift rate, could have recorded 'like' repetitions in the histories of all the major emerged Barbados reefs, and that this process must have prevailed systematically throughout Barbados' reef-building history. Comparison of Barbados data with those from the Red Sea (Scholz et al. 2004) show significant differences, suggesting that the slopes of the uranium-series activity trends are not regionally applicable as parameters in a general progressive model. Young samples often show higher $\delta^{234}U_{initial}$ values than do older samples; therefore, diagenesis affecting the uranium series does *not* necessarily progress systematically with time. With regard to the Red Sea corals, these show an elevated ^{234}U content (due to this isotope's mobility); in contrast, we find little excess ^{230}Th, which indicates early dissolution of the reef sands, before any significant daughter in-growth of ^{230}Th and arguably also ^{231}Pa was allowed. Our explanation is that the Red Sea reefs were exposed to fresh water shortly after uplift, where sub-aerial exposition occurred approximately after 3 ka (Figure 2-10). By contrast, at Barbados the corals were first exposed after 20-40 ka (Figure 2-9). The Barbadian long 'reef-emergence' times prior to fresh

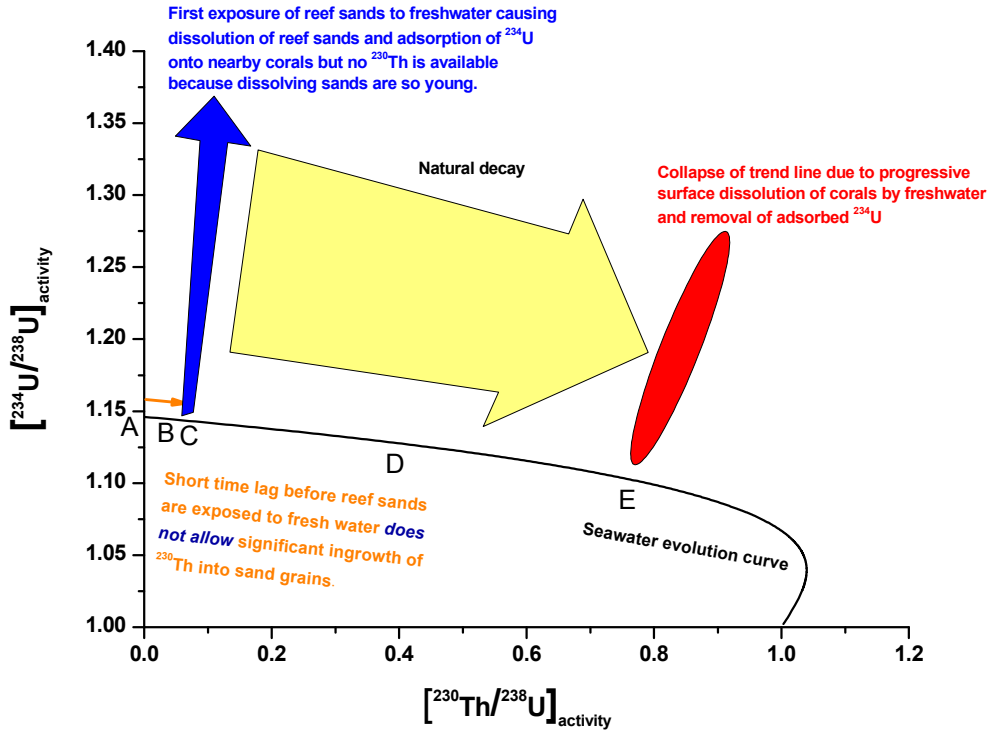
First exposure of reef sands to freshwater causing dissolution of reef sands and adsorption of 234U onto nearby corals but no 230Th is available because dissolving sands are so young.
Natural decay
Collapse of trend line due to progressive surface dissolution of corals by freshwater and removal of adsorbed 234U
A
B C
D
E
Short time lag before reef sands are exposed to fresh water does not allow significant ingrowth of 230Th into sand grains.
Seawater evolution curve
[234U/238U]activity
[230Th/238U]activity
1.40
1.35
1.30
1.25
1.20
1.15
1.10
1.05
1.00
0.0
0.2
0.4
0.6
0.8
1.0
1.2

Figure 2-10

Figure 2-10 A schematic illustration of ^{238}U-^{234}U-^{230}Th uranium series diagenesis for the Red Sea corals. After deposition and burial in the marine environment, the reefs reflect an isotopic equilibrium with sea water, which follows the sea evolution curve (A). The short time lag before the reef sands are exposed to fresh water does not allow significant in-growth of ^{230}Th into sand grains represented here by a much steeper trend line compared with the Barbadian corals; the latter experience a much longer lag time before fresh water exposure (B). During the first exposure of reef sands to fresh water, the diagenetic potential is highest, causing major dissolution of reef sands and releasing the uranium series isotopes into the pore waters, with subsequent adsorption of ^{230}Th (highly immobile) and ^{234}U (mobile) onto nearby corals, whereas ^{238}U is mobile (C). As for (D) and (E), see the description given in the preceding Figure 2-9.

water exposure resulted in more ^{230}Th and ^{231}Pa in-growth in the reef sands, tilting the activity trends to the right and away from the equal age lines (Figure 2-2). The regular trends in the activity plots of the Barbados uranium–series, as shown in Figure 2-3, are therefore signatures set by lag times that are similar from reef growth to fresh water exposure, and produce roughly the same amount of ^{230}Th in-growth for each major reef. The similar lag time that is evident for all Barbados reefs is exactly what one would expect, given that the cyclical sea level changes involved are tied to the Earth's precessional cycle and a fairly steady uplift rate. The range of ^{234}U/^{238}U and ^{230}Th/^{238}U activities overall in the reef reflects small differences in the amounts of ^{234}U and ^{230}Th that migrated from the dissolving sands onto the coral surfaces; however, the ^{234}U-^{230}Th proportions originally set depending on the main coeval sand source are retained. The excellent correlations seen in the data must reflect a relatively short-lived event, i.e. the 'locking in' of the trends in the redistribution of the uranium series at the time of the original fresh water exposure. These trends will with time tend to 'lean' to the left, due to the faster rate of decay of ^{234}U, thereby reducing the activity ratio for ^{234}U faster than is the case for ^{230}Th, as explained in Figure 2-9.

For all the open system Barbadian reefs the ^{234}U/^{238}U$_{activity}$ versus ^{230}Th/^{238}U$_{activity}$ data scatters around a main trend. The variations in magnitude reflect a natural variability in how much ^{234}U, ^{230}Th and ^{231}Pa could be transported from the dissolving extant sands onto the coral surfaces. In addition, Barbados sands may be mixed sources themselves, hosting an unknown amount of excess ^{234}U and ^{230}Th, potentially originating from older eroded reefs and sands

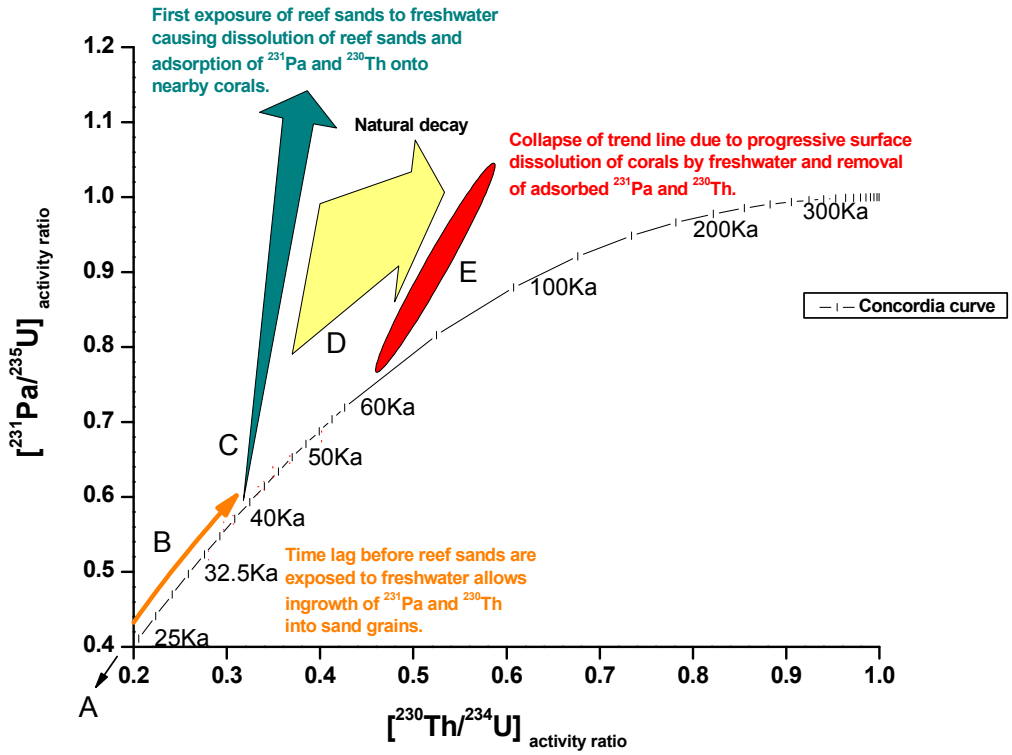
First exposure of reef sands to freshwater causing dissolution of reef sands and adsorption of 231Pa and 230Th onto nearby corals.
Natural decay
Collapse of trend line due to progressive surface dissolution of corals by freshwater and removal of adsorbed 231Pa and 230Th.
Concordia curve
Time lag before reef sands are exposed to freshwater allows ingrowth of 231Pa and 230Th into sand grains.
A
B
C
D
E
25Ka
32.5Ka
40Ka
50Ka
60Ka
100Ka
200Ka
300Ka
[231Pa/235U] activity ratio
[230Th/234U] activity ratio
1.2
1.1
1.0
0.9
0.8
0.7
0.6
0.5
0.4
0.2
0.3
0.4
0.5
0.6
0.7
0.8
0.9
1.0

Figure 2-11

Figure 2-11 A schematic illustration of ^{235}U-^{231}Pa paired with the ^{234}U-^{230}Th uranium series diagenesis for Barbados. After deposition and burial in the marine environment the reefs reflect isotopic equilibrium with sea-water and follow that of the Concordia Line (A). The time lag before reef sands are exposed to freshwater allows in-growth of ^{231}Pa and ^{230}Th into sand grains (B). During the first exposure of reef sands to freshwater the diagenetic potential is highest, causing major dissolution of reef sands, releasing the uranium-series isotopes into the pore waters, with subsequent adsorption of ^{231}Pa, ^{230}Th and ^{234}U onto nearby corals. We hypothesize that the $^{231}Pa/^{235}U$ versus $^{230}Th/^{234}U$ trend lines are similar for all Barbadian uplifted Pleistocene reefs, reflecting the mixing between adsorbed isotopes originally added in approximately the same proportions and the pristine coral, closed-system uranium- series isotopes (C). The diagenetic potential wanes relatively quickly locking in ratios which will now only change by natural decay taking parallel paths to the Concordia (D). Over time, due to progressive surface dissolution of corals by freshwater and removal, some of the adsorbed ^{234}U and ^{230}Th will re-dissolve causing a collapse of the trend lines (E).

at nearby sea cliffs. Following the argument above, the activity trends may therefore show small variations in slope due to the availability of older excess ^{234}U, ^{230}Th and ^{231}Pa sources from different settings. This older excess U-series availability could vary depending on whether the environment is characterized by high versus low energetic near-shore environment (e.g. eastern Barbados is high, western Barbados is low in this respect). In the high-erosion environment of Barbados' eastern side, the more efficient in-mixing of a much older component would tilt the trends slightly to the right because of the higher contributions by the in-grown daughters from much older sands. In contrast, on the less erosive western side of the island, the tilt would be less marked, since the sands are predominantly from younger reefs, the in-mixing less efficient and therefore the amount of ingrown ^{230}Th, ^{234}U and ^{231}Pa much less. Over time, the series with excess daughters seeks towards a secular equilibrium in their activity ratios if no extra daughters are added other than by natural decay. Combine this with continued dissolution of the coral surfaces and hence the trend lines will tend to collapse rather than showing a progressively exacerbated uranium series disequilibria. Barbados modern ground water does not contain excess ^{234}U (Banner et al. 1991), which indicates that the processes responsible for the fractionation of the uranium series are not continuous and have now been extinguished. This is a further argument that the fractionating event itself is relatively short-lived and most likely occurred after the first fresh water exposure and the extensive dissolution this caused. The dissolution process opened conduits, which caused a significant increased flow, thereby drastically reducing

the residence time for the ground water. As a result, the increased pore spaces reduced the surface areas, allowing faster transport; it may even have created isolated pockets where ground water flow and interaction were altogether stopped. This explains how certain areas of the same reef setting may display dramatic differences in severity of uranium series disequilibria, while others seem much less or not affected at all (Scholz et al., 2006).

CONCLUSIONS

A vast number of uranium series data on corals exposed to freshwater show elevated $\delta^{234}U_{initial}$ values, compared to the corresponding values found in modern corals and seawater. Barbados corals with elevated $\delta^{234}U_{initial}$, typically display positive trends $^{230}Th/^{238}U_{activity}$ versus $^{234}U/^{238}U_{activity}$ diagrams and such trends suggest a synchronous and proportional addition of ^{230}Th as well as of ^{234}U. A probable source of the excess uranium series daughters is the surrounding aragonite sands, which rapidly dissolve and invert to calcite in the vadose fresh water environment. Aragonite grains are generally absent in uplifted reefs older than 125,000 years BP (Winland, 1971). The most likely source of excess ^{234}U with subsequent preferential adsorption of ^{234}U, ^{230}Th and ^{231}Pa onto coral surfaces, is therefore from the dissolution and transformation of aragonite sands. During dissolution and aragonite-calcite transformation, the uranium series isotopes are expunged into the groundwater and, depending on the changing chemical environment (pH, CO_3^{2-} concentration etc.), are transported to, and adsorb onto, the coral surfaces. During the adsorption, the uranyl ions containing

$^{234}U^{6+}$, once in solution, may (due to a preferential chemical property) be able to adsorb more efficiently, thereby fractionating from the uranyls containing the $^{238}U^{6+}$. Such a fractionation may also be caused by selective speciation of uranyls, under the influence of the pore water pH, favoring the release of ^{234}U and the subsequent ion-exchange with ^{238}U on the coral surfaces. This mechanism would increase the amount of ^{234}U on the surfaces, while keeping the amount of bulk uranium nearly constant. In coral reefs, the existing uranium disequilibrium is therefore not a function of bulk uranium contents but is rather an effect of the significant changes in the chemical environment brought about by an initial fresh water influx, which caused a redistribution of the isotopes mainly in the coeval, but also from older sands adjacent to the emerging reefs. Coral samples displaying open system behavior were thus affected by preferential adsorption of ^{230}Th, ^{231}Pa and ^{234}U as a result of the percolating freshwater in the vadose zone.

The $^{230}Th/^{238}U$ versus $^{234}U/^{238}U$ and also $^{230}Th/^{234}U$ versus $^{231}Pa/^{235}U$ activity trends are very similar in all of Barbados' uplifted reefs, reflecting a mix between the adsorbed isotopes that were originally added (and always in approximately the same proportions) from the coeval sands, and the uranium series isotopes from the closed-system corals.

The open-system behavior of the Barbados corals resulting from exposure to fresh water is similar for both the $^{234}U/^{230}Th$ and $^{235}U/^{231}Pa$ decay suggesting a similar process. The processes that led to the fractionation of the uranium series are most likely a combination of many processes taking place during transition from a marine to a fresh water setting.

Despite the fact that ^{230}Th and ^{231}Pa are immobile, they may migrate from the sands to adsorb onto surfaces of the nearby corals. The reason that some younger Barbadian reefs show higher isotopic anomalies than is the case for the older reefs, may be that the fresh water influx happened early; subsequently, the supply of uranium-series isotopes was extinguished, as the reefs continued to dissolve in the vadose freshwater. Ultimately, the dissolution of the coral skeletons themselves progressively removed the adsorbed isotopes over time. At depths below the reef surface, a greater adsorption of ^{230}Th, ^{231}Pa and ^{234}U onto coral surfaces occurred, due to the corals' greater exposure to contamination by ^{230}Th, ^{231}Pa and ^{234}U from the dissolving sands nearby. Therefore, the surface outcrop samples have the greatest potential to yield reliable closed-system ages, whereas subsurface core samples taken deeper into the vadose freshwater environment, being commonly contaminated, provide a less reliable source of data.

The repeated reef emergence histories, made possible by a relatively constant uplift rate, coupled with the cyclical rising and falling sea levels over the last 500.000 years, set the unique uranium-series activity trends for Barbados. Other regions with constant uplift rates may show similar trends in fossil reefs, but will have different slopes depending on the rate of uplift (as shown for the Red Sea reefs). Importantly, the time lag from reef growth to emergence and exposure to fresh water, determines the amount of ^{230}Th in-growth and thus the slope of the trends. Since the slopes of the trends vary slightly around ~ 0.3 for all Barbados reefs, we imply that all Barbadian reefs experienced similar lag times from reef growth to its first freshwater exposure.

CHAPTER 3
A NUMERICAL ANALYSIS OF THE 'DISSOLUTION-CUM-ADSORPTION' MODEL AND THE ESTIMATED MARINE RESIDENCE TIMES FOR BARBADIAN PALEO-REEFS

By

Jacob L. Mey[1, 2]

1. Lamont Doherty Earth Observatory of Columbia University, Palisades, New York 10964, USA.

2. Graduate Center, City University of New York, New York, NY 10016, USA.

ABSTRACT

Fossil corals are used to estimate past sea levels and also to calibrate ^{14}C ages with the aid of U-Th and U-Pa dating methods. These coral fossils have often been subaerially exposed and thus are affected by diagenesis during their initial interaction with fresh water. In an effort to understand when such disequilibria in fossil coral reefs occurred, we have quantified our 'dissolution-cum-adsorption' model for the uranium series disequilibria using a geometrical construction, based on the evolution of the activities in a $\left[\frac{^{230}Th}{^{238}U}\right]$ versus $\left[\frac{^{234}U}{^{238}U}\right]$ diagram for closed versus open systems. The traditional age equations for the uranium-series with excess daughters have been used to construct a relationship between (i) the angles of the equal age lines in the $\left[\frac{^{230}Th}{^{238}U}\right]$ versus $\left[\frac{^{234}U}{^{238}U}\right]$ activity diagrams, and (ii) the quantified angles of the regressed lines of several uranium series disequilibria trends from Barbados. Our results indicate that the severity of the Barbados uranium series disequilibria is not only explained by ^{234}U and ^{230}Th addition, but may also reflect a loss of ^{238}U through dissolution of coral skeletal structure. The net effect is ^{238}U removal, whereas ^{234}U and ^{230}Th remain; thus, the disequilibria for the extant coral increase the excess daughters' ratio. Our results further indicate that the activity of ^{234}U is reduced (compared to ^{230}Th), as would be expected in regard to the lower mobility of trapped ^{230}Th.

It is proposed that the major dissolution that caused the uranium series disequilibria occurred during one relatively short-lived event when the paleoreefs

experienced the very first freshwater exposure. During this event, the diagenetic potential was at its maximum for redistribution of the uranium series; this then caused the ^{234}U and the ^{230}Th to behave in a systematic way, resulting in linear trends. The linear trends in the open system uranium series were set early, as shown in the $\left[\frac{^{230}Th}{^{238}U}\right]$ versus $\left[\frac{^{234}U}{^{238}U}\right]$ activity diagrams. The timing of the first exposure of the freshwater in the reefs is calculated based on the results of our new model. From the relationship between, (i) dissolution, (ii) in-grown ^{230}Th, and (iii) excess ^{234}U, we derived that the 60,000 old Marine Isotope stage 3 (MIS 3) reef was exposed to freshwater 36-38,000 years after growth in the marine environment. We have calculated these 'marine residence times' for the MIS 3 5a, 5c, 5e, 6.0, 7a and 7c reefs; our results correspond with the duration of the sea level high stand in each of the stages.

INTRODUCTION

The regular trends in the Barbados uranium series activity plots are thought to be consistent, repetitive signatures, set by recapitulated 'reef-emergence' histories (Mey et al., 2008, submitted). During these cycles, spanning the time from reef growth to first fresh water exposure, radiogenic isotopes ^{234}U, ^{230}Th and ^{231}Pa were added to the sands by natural decay. Subsequently, during a relatively short-lived event, as either the reefs were being uplifted or the sea level dropped, they were exposed to fresh water for the first time. During this event, the diagenetic potential was highest, causing the most significant redistribution of the uranium series isotopes. Remarkably, the excess isotopes were redistributed systematically depending on the available ^{234}U and ^{230}Th in the sands and corals at the time. This process has been dubbed the 'Dissolution-cum-Adsorption' diagenesis model for the uranium series in fossil coral reefs (Mey et al., 2008, submitted).

Uranium series disequilibria as expressed in the $\left[\frac{^{230}Th}{^{238}U}\right]$ *versus* $\left[\frac{^{234}U}{^{238}U}\right]$ *activities*

During diagenesis, a coral may experience several ways of gaining or losing the isotopes of the uranium series. The various theoretically possible gain or loss

scenarios, are illustrated in the $\left[\frac{^{230}Th}{^{238}U}\right]$ versus $\left[\frac{^{234}U}{^{238}U}\right]$ activity diagram of Figure 3-1.

In the following, we include a brief discussion of the respective scenarios and discuss the plausibility for each scenario to have occurred in the Barbadian paleoreef setting.

A. *^{234}U gain, but no ^{230}Th gain*. This is an unlikely scenario, because ^{238}U decays internally in the aragonite mineral structure; hence, such a scenario would only occur in very young samples with no ^{230}Th in-growth and a significant surface addition of ^{234}U from a much older source nearby. This is not believed to be the case for Barbados, because most of its reefs have experienced long 'marine residence times' with closed system ^{230}Th in-growth before being exposed to fresh water.

B. *^{234}U gain and ^{230}Th gain.* This is the most probable case for all diagenetic settings on Barbados. As ^{238}U decays, it produces ^{234}U, which decays to ^{230}Th; both these daughters are then available for redistribution during dissolution. The excess occurrence of these two isotopes in most open system corals is, according to a widely accepted theory, due to their addition to the original corals. However, if a coral fragment is dissolved causing removal of mobile ^{238}U from the dissolved mass, while the immobile ^{230}Th (and possibly also ^{234}U) is re-adsorbed to the extant coral, the effect would be the same as if these two isotopes had been subsequently added to the residual coral. This would drive up the excess ^{230}Th

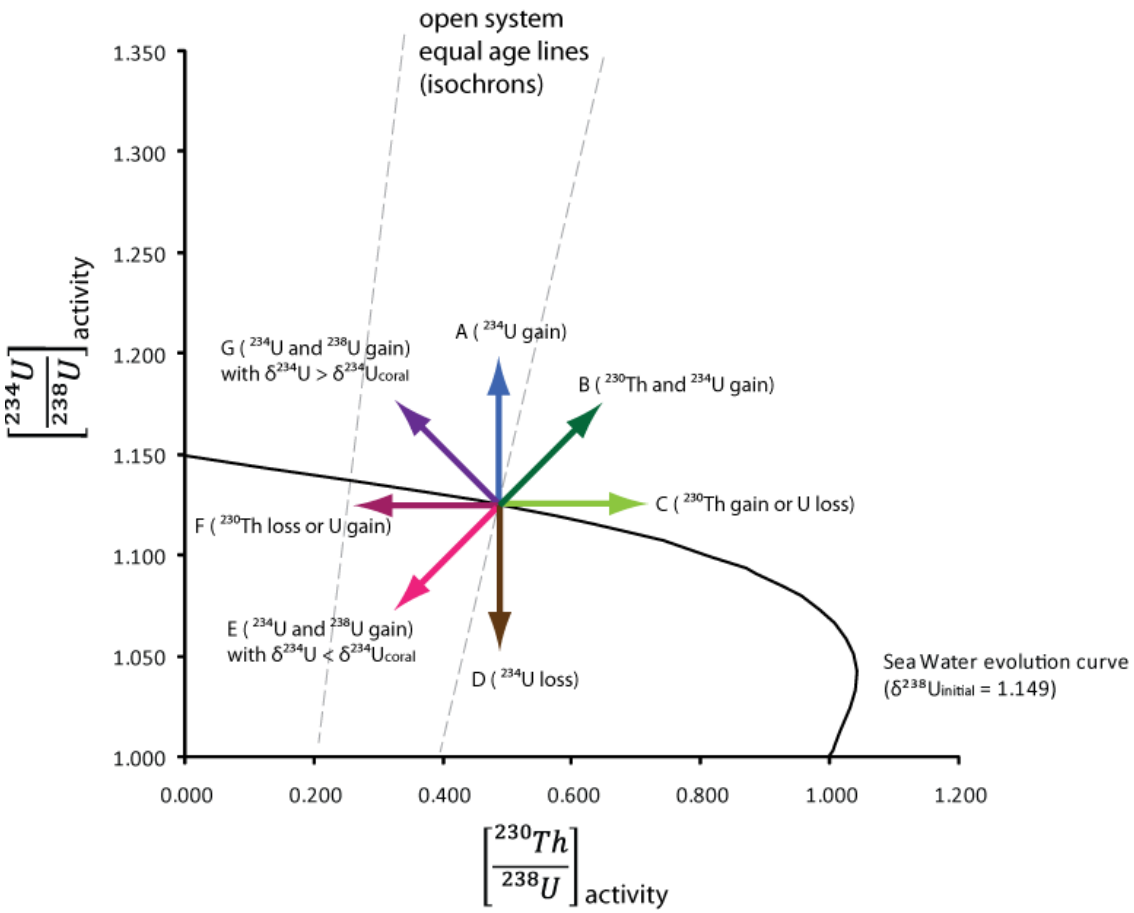
open system
equal age lines
(isochrons)
1.350
1.300
1.250
1.200
1.150
1.100
1.050
1.000
0.000
0.200
0.400
0.600
0.800
1.000
1.200
$\left[\frac{^{234}U}{^{238}U}\right]_{activity}$
$\left[\frac{^{230}Th}{^{238}U}\right]_{activity}$
A (^{234}U gain)
B (^{230}Th and ^{234}U gain)
C (^{230}Th gain or U loss)
D (^{234}U loss)
E (^{234}U and ^{238}U gain)
with $\delta^{234}U < \delta^{234}U_{coral}$
F (^{230}Th loss or U gain)
G (^{234}U and ^{238}U gain)
with $\delta^{234}U > \delta^{234}U_{coral}$
Sea Water evolution curve
($\delta^{238}U_{initial}$ = 1.149)

Figure 3-1

Figure 3-1 Idealized uranium-series disequilibria portrayed in a $\left[\frac{^{230}Th}{^{238}U}\right]$ versus $\left[\frac{^{234}U}{^{238}U}\right]$ activity diagram. Modified after Scholz et al (2006). Points A through G are explained in the text.

and possible also ^{234}U, while the original bulk ^{238}U content is kept the same (after all, the amount of added ^{234}U and ^{230}Th is on the order of parts per trillion compared to parts per million of ^{238}U). We suggest that the dissolution effect may be among the main trendsetters of uranium series disequilibria in the Barbados corals.

C. *^{230}Th gain or bulk U loss.* ^{230}Th gain beyond that of natural decay is only possible during dissolution of the coral when both ^{234}U and ^{238}U are removed and ^{230}Th is adsorbed. However, from most published data it appears that ^{234}U is not removed as efficiently as is ^{238}U; we know this because the amount of the former isotope that is present exceeds the amount that would be proportionate to the actual amount of ^{230}Th. In order for the coral to experience uranium loss across the board, a complete recrystallization, accompanied by a volume reduction, is needed so as to lower the original bulk uranium content while increasing the resident ^{230}Th content. Such samples would be easy to detect due to their high content of calcite. Lastly, within a closed system, the loss of bulk ^{238}U that is due to natural decay happens across the board, as all samples are forced to follow its specific decay curve. The excess ^{234}U is reduced by this decay, but is produced much slower from ^{238}U (half life = $4.5x10^9$). ^{230}Th is produced from ^{234}U in ratios of approximately 1:3, because the rate of decay being approximately three times slower for ^{234}U than it is for ^{230}Th. Some of the ^{234}U may be lost from the surfaces due to its mobility, but this should not change the overall ^{234}U content significantly.

D. *^{234}U loss only.* This scenario is less likely to happen because ^{234}U could not be removed without at the same time removing ^{238}U. Possibly some samples will be found to lie below the seawater evolution curve (Figure 3-1) because at the time of their formation, the seawater level was lower and the initial $\delta^{234}U$ for seawater may have been slightly lower than today (Gallup et al 1994, Henderson 2002, Ezat and Yokohama, 2006).

E. *^{234}U and ^{238}U gain with $\delta^{234}U < \delta^{234}U_{coral}$.* This scenario would presuppose a situation in which the seawater's $\delta^{234}U$ would be significantly lower than the corals'. While small variations (i.e. less than 10 ‰; Henderson, 2002) in the ocean's excess ^{234}U signature may have occurred over the last 800,000 years, variations on such timescales are small, because either considerable more time or catastrophic influx of freshwater would be needed to change the situation significantly. The coral itself would also have to gain enough ^{234}U and ^{238}U from a very young source in order to push the activity ratios 'backwards' (i.e. from right to left in figure 3-1).

F. *^{230}Th loss or U gain*. Loss of ^{230}Th is also a highly unlikely scenario, because ^{230}Th is very particle-reactive and will, once in solution, re-adsorb onto nearby coral surfaces. If the coral gains significant uranium from a younger source with a $\delta^{234}U$, close to modern seawater signatures, it may increase the ^{238}U denominators of both the $^{234}U/^{238}U$ and the $^{230}Th/^{238}U$ fractions (see figure 3-1).

G. *^{234}U and ^{238}U gain with $\delta^{234}U > \delta^{234}U_{coral}$.* This scenario is unlikely in the case of young corals, since the initial $\delta^{234}U_{coral}$ will be very close or equal to initial $\delta^{234}U_{seawater}$ (as we know, the corals faithfully record the isotopic ratios from the seawater they grow in). Over relatively short time spans (in this case 10-30,000 years), this value does not change significantly (that is, it will not exceed 10‰). Over longer spans of time, the seawater values may change slightly more; thus, $\delta^{234}U_{seawater}$ estimates range from ~132‰ to ~153‰ over glacial cycle timescales (Esat and Yokoyama, 2006; see also Henderson, 2002, Gallup et al., 1994).

If one accepts the arguments detailed above, the most likely variation of the activity trends for Barbadian paleoreefs will lie in the gray shaded area of Figure 3-2. The geometrical and quantitative analysis of the activity trends presented in this chapter are all based on the distribution of activity trends in this region; these lie between the equal age line and the seawater evolution curve. Similar trends are observed for many locations around the globe, such as the Red Sea (Scholz et al., 2004), Henderson Island (Andersen et al., 2008), Huon Peninsula, New Guinea (Ezat et al., 1999 Stein et al., 1993), Bahamas (Chen et al., 1991), Barbados (Mey et al., *in prep.*, 2005; Thompson et al., 2003; Gallup et al., 1994), Western Australia (Stirling et al., 1995), New Guinea (Ezat et al., 1999), and the southeast Pacific (Stirling et al., 2001). Although some recently published Barbados data for MIS 6.5 corals (Scholz et al., 2006) show disequilibria trends

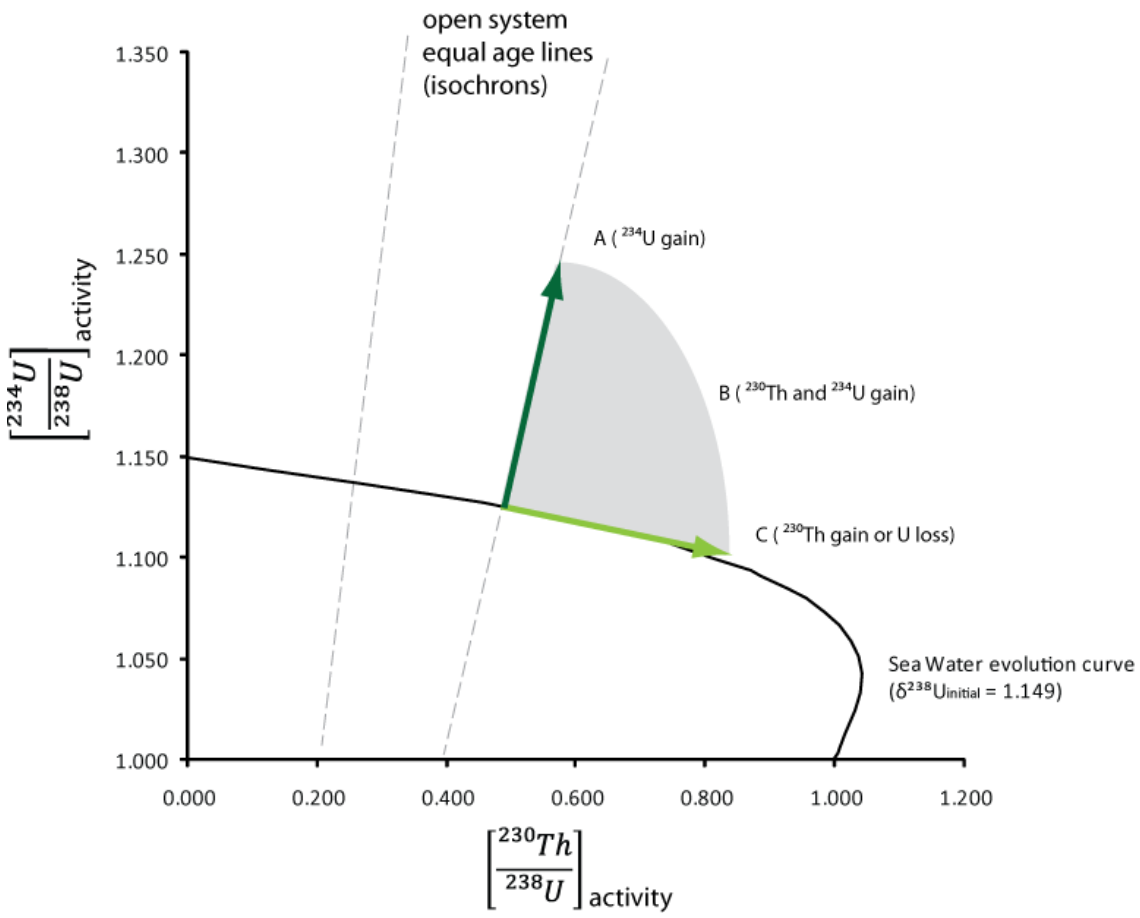
open system
equal age lines
(isochrons)
A (234U gain)
B (230Th and 234U gain)
C (230Th gain or U loss)
Sea Water evolution curve
(δ238Uinitial = 1.149)
1.350
1.300
1.250
1.200
1.150
1.100
1.050
1.000
0.000
0.200
0.400
0.600
0.800
1.000
1.200
[234U/238U] activity
[230Th/238U] activity

Figure 3-2

Figure 3-2 Distribution of the most common uranium series trends in Barbados corals that have experienced freshwater digenesis. Points A-C are explained in the text.

that are different from ours for most Barbados reefs, these corals are so old (more than 175,000 years) that they may have experienced other processes overprinting their 'first freshwater exposure' diagenetic signatures.

The trends in the $\left[\frac{^{230}Th}{^{238}U}\right]$ *versus* $\left[\frac{^{234}U}{^{238}U}\right]$ *activity diagram*

In order for uranium series disequilibria activities to set trends in the way shown by the $\left[\frac{^{230}\mathrm{Th}}{^{238}\mathrm{U}}\right]$ versus $\left[\frac{^{234}\mathrm{U}}{^{238}\mathrm{U}}\right]$ activity diagrams, one of two conditions have to be fulfilled: (i) the source of added uranium series must have been homogenous when added and must have been added to all fragments roughly at the same time, so the proportions when setting the trends are always the same, or (ii) the dissolving coral lost ^{238}U, but retained the dissolved coral's ^{234}U and ^{230}Th. If neither of these two conditions is fulfilled, the trends will not be linear. The trend lines themselves (and the data) proves that the two uranium series daughters, ^{234}U and ^{230}Th, were added or trapped in roughly the same proportions for all of the Barbados reefs.

The analyses in this study is based on the geometries of these trend lines and are used as bench marks for the uranium series disequilibria in fossil coral from Barbados and elsewhere.

METHODS AND MATERIALS

Numerical Analysis of the uranium-series activity trends

The trend lines' angles and lengths, taken together, allow for a fairly straightforward comparative analysis of; (i) of the extent of the disequilibria; (ii) of the criteria that are necessary to set these geometries as they are observed today; and (iii) the trends once set, of the subsequent evolution of the trends in the uranium series, as compared to those that follow the closed system seawater evolution curve.

In order to establish a numerical comparison between the observed natural trends of the uranium-series activity ratios from various localities, three methods are used to quantify the relationship between the closed system and the open system behaviors. These methods rely on: (i) the angles between the equal age lines and the trends; (ii) the trends' lengths (measured from the seawater evolution curve's most severe disequilibrium point on the trend line to its equal age line counterpart; and (iii) the effect of short-lived dissolution events, leading to porosity increase (mass loss) at various times.

Angles between 'closed system equal age lines' and 'open system trend lines'

Figure 3-3 is a schematic of idealized vectors, based on natural observations of trend lines within the same paleoreef unit (see the 'Results' section below for

examples of these naturally occurring trend lines from Barbados). The blue vectors represent the closed system 'equal age' trends; the red vectors are the regressed 'open system' trends of the activity data. Henceforth, [φ] is defined as the angle between the blue and red vectors (i. e. between the 'equal age system' and the 'open system' trends).

Reefs that were exposed relatively soon (1-5ka) after reef growth to vadose freshwater percolation during isostatic uplift or sea level drop and thus experienced considerable dissolution, will display a disequilibrium in the ^{234}U daughters, but less so in regard to ^{230}Th; the reason is that not enough time has passed to allow for considerable in-growth of the latter (see Figure 3-3, the blue vector). The result of this process is visible as a high angle vector lying on (or close to) the 'equal age system' trends. Such trends are set by the ^{234}U disequilibria and will through time tend to co-evolve and retain the same angle (i. e. $[\varphi] \approx 0$; see Figure 3-3, dashed blue vector) as the equal age system trends, inasmuch as (i) ^{230}Th is only added from decay, and therefore follows the equal age lines, and (ii) the diagenetic potential presumably wanes with time (Mey et al., 2008, submitted).

In contrast, when a major dissolution event occurs after several tens of thousands of years, the ^{230}Th in-growth will tilt the trend to the right (Figure 3-3, red line), and, as is the case for the equal age system trends once they are set, the trend will continue to evolve following a trend set by natural decay only.

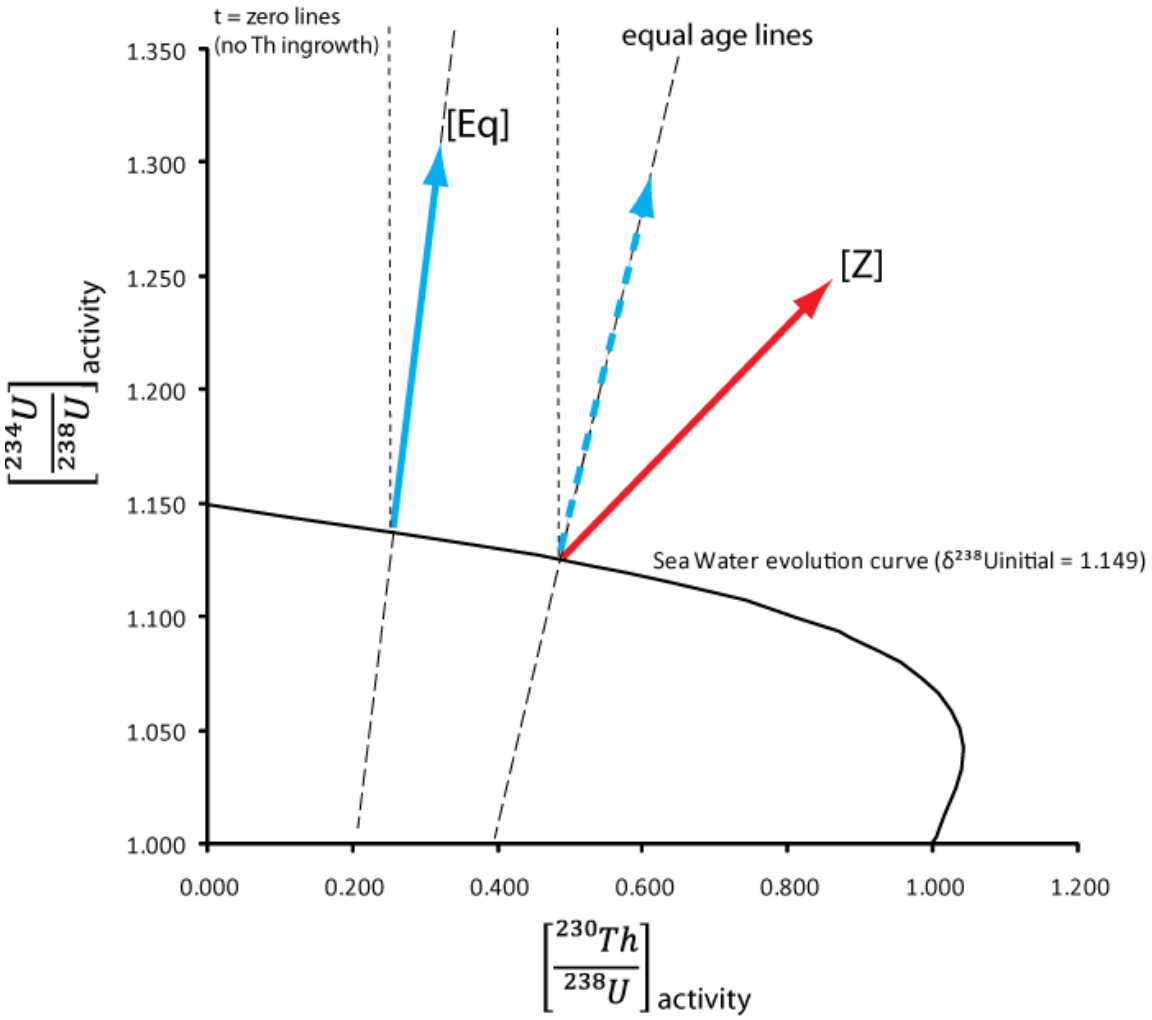
t = zero lines
(no Th ingrowth)
equal age lines
[Eq]
[Z]
Sea Water evolution curve (δ²³⁸Uinitial = 1.149)
1.350
1.300
1.250
1.200
1.150
1.100
1.050
1.000
0.000
0.200
0.400
0.600
0.800
1.000
1.200
$\left[\frac{^{234}U}{^{238}U}\right]_{activity}$
$\left[\frac{^{230}Th}{^{238}U}\right]_{activity}$

Figure 3-3

Figure 3-3 Idealized activity trends based on natural observations: Blue trends [Eq] have only experienced ^{230}Th in-growth, resulting from natural decay as well as being represented by excess ^{234}U, whereas the red trend [Z] has experienced an excess component of ^{230}Th as well as of ^{234}U.

Calculating the slopes [a]

Based on the expression for a straight line, we can derive an expression for slopes of the equal age lines [Eq] and the open system trends [Z] in Figure 3-3.

Let

(3.1) $$y = ax + b$$

where a is the slope of the lines; its value can be found from the expression

(3.2) $$a = \frac{(x_2 - x_1)}{(y_2 - y_1)}$$

At any given point in the $\left[\frac{^{230}Th}{^{238}U}\right]$ versus $\left[\frac{^{234}U}{^{238}U}\right]$ activity diagram displayed in Figure 3-3, we can choose two arbitrary equal ages on the evolution curves and obtain the values of $\{y_2, y_1, x_2, x_1\}$. For example, we could take the starting and end points of the blue vector in Figure 3-3, using the seawater evolution [SW] based on an initial activity ratio $\left[\frac{^{234}U}{^{238}U}\right]_{SW}^{INIT} = 1.149$ (aka $\delta^{234}U_{initial}$ of seawater = 149) and an arbitrary higher [HIGH] initial activity ratio $\left[\frac{^{234}U}{^{238}U}\right]_{HIGH}^{INIT} = 1.300$, with super- and subscript suffixes INIT and HIGH respectively. In this case, the values $\{y_2, y_1\}$ at equal ages and at time *t* on the evolution curve are found from the age equations that are used to derive the activity ratios, as expressed in the following formulae ((3.3 and 3.4; equations rearranged from Dickin, 2005):

(3.3) $$y_2 = \left[\frac{^{-234}U}{^{238}U}\right]_{HIGH}^{Present} = \left(\left(\left[\frac{^{-234}U}{^{238}U}\right]_{HIGH}^{INIT} - 1\right)e^{-\lambda_{234}*t}\right) - 1$$

(3.4) $$y_1 = \left[\frac{^{-234}U}{^{238}U}\right]_{SW}^{Present} = \left(\left(\left[\frac{^{-234}U}{^{238}U}\right]_{SW}^{INIT} - 1\right)e^{-\lambda_{234}*t}\right) - 1$$

Similarly, using the age equations to allow for excess daughters, we can derive the values for $\{x_2, x_1\}$ (3.5 and 3.6; equations rearranged from Dickin, 2005):

(3.5) $$x_2 = \left[\left(1 - e^{-\lambda_{230}*t}\right) + \frac{\lambda_{230}}{\lambda_{230}-\lambda_{234}}\left(e^{-(\lambda_{230}-\lambda_{234})*t}\right)\left(\left[\frac{^{-234}U}{^{238}U}\right]_{HIGH}^{Present}\right)\right]$$

(3.6) $$x_1 = \left[\left(1 - e^{-\lambda_{230}*t}\right) + \frac{\lambda_{230}}{\lambda_{230}-\lambda_{234}}\left(e^{-(\lambda_{230}-\lambda_{234})*t}\right)\left(\left[\frac{^{-234}U}{^{238}U}\right]_{SW}^{Present}\right)\right]$$

Consequently, any equal age line in the activity diagram described by coordinates $\{y_2, y_1, x_2, x_1\}$ may be expressed by the following five variables:

$$\left\{\left[\frac{^{234}U}{^{238}U}\right]_{HIGH}^{Present}, \left[\frac{^{234}U}{^{238}U}\right]_{SW}^{Present}, \left[\frac{^{234}U}{^{238}U}\right]_{HIGH}^{INIT}, \left[\frac{^{234}U}{^{238}U}\right]_{SW}^{INIT}, t\right\}$$

For simplicity, the *t*s are chosen in 1000 or 5000 year multiples; the values for $\left[\frac{^{234}U}{^{238}U}\right]_{HIGH}^{Present}$ and $\left[\frac{^{234}U}{^{238}U}\right]_{SW}^{Present}$ are found by using the equations for y_2 (equation 3.4) and y_2 (equation 3.3).

The following equation (3.7) expresses the slope of the equal age lines [Eq] using the age equations (3.3, 3.4, 3.5, and 3.6) and substituting them into equation 3.2, as described above.

(3.7)

$$a[Eq] = \frac{\left[\left(\left(\left[\frac{^{234}U}{^{238}U}\right]_{HIGH}^{INIT} - 1\right)e^{-\lambda_{234}*t}\right) - 1\right] - \left[\left(\left(\left[\frac{^{234}U}{^{238}U}\right]_{SW}^{INIT} - 1\right)e^{-\lambda_{234}*t}\right) - 1\right]}{\left[\left(1 - e^{-\lambda_{230}*t}\right) + \frac{\lambda_{230}}{\lambda_{230}-\lambda_{234}}\left(e^{-(\lambda_{230}-\lambda_{234})*t}\right)\left(\left[\frac{^{234}U}{^{238}U}\right]_{HIGH}^{Present}\right)\right] - \left[\left(1 - e^{-\lambda_{230}*t}\right) + \frac{\lambda_{230}}{\lambda_{230}-\lambda_{234}}\left(e^{-(\lambda_{230}-\lambda_{234})*t}\right)\left(\left[\frac{^{234}U}{^{238}U}\right]_{SW}^{Present}\right)\right]}$$

This expression is then reduced to:

(3.8)
$$a[Eq] = \frac{e^{-\lambda_{234}*t}\left(\left[\frac{^{234}U}{^{238}U}\right]_{HIGH}^{INIT} - \left[\frac{^{234}U}{^{238}U}\right]_{SW}^{INIT}\right)}{\frac{\lambda_{230}}{\lambda_{230}-\lambda_{234}}\left(e^{-(\lambda_{230}-\lambda_{234})*t}\right)\left(\left[\frac{^{234}U}{^{238}U}\right]_{HIGH}^{Present} - \left[\frac{^{234}U}{^{238}U}\right]_{SW}^{Present}\right)}$$

Using this equation, we can compute a matrix of any number of equal age lines, plotting them in the activity diagram, as shown in Figure 5-4. The equal

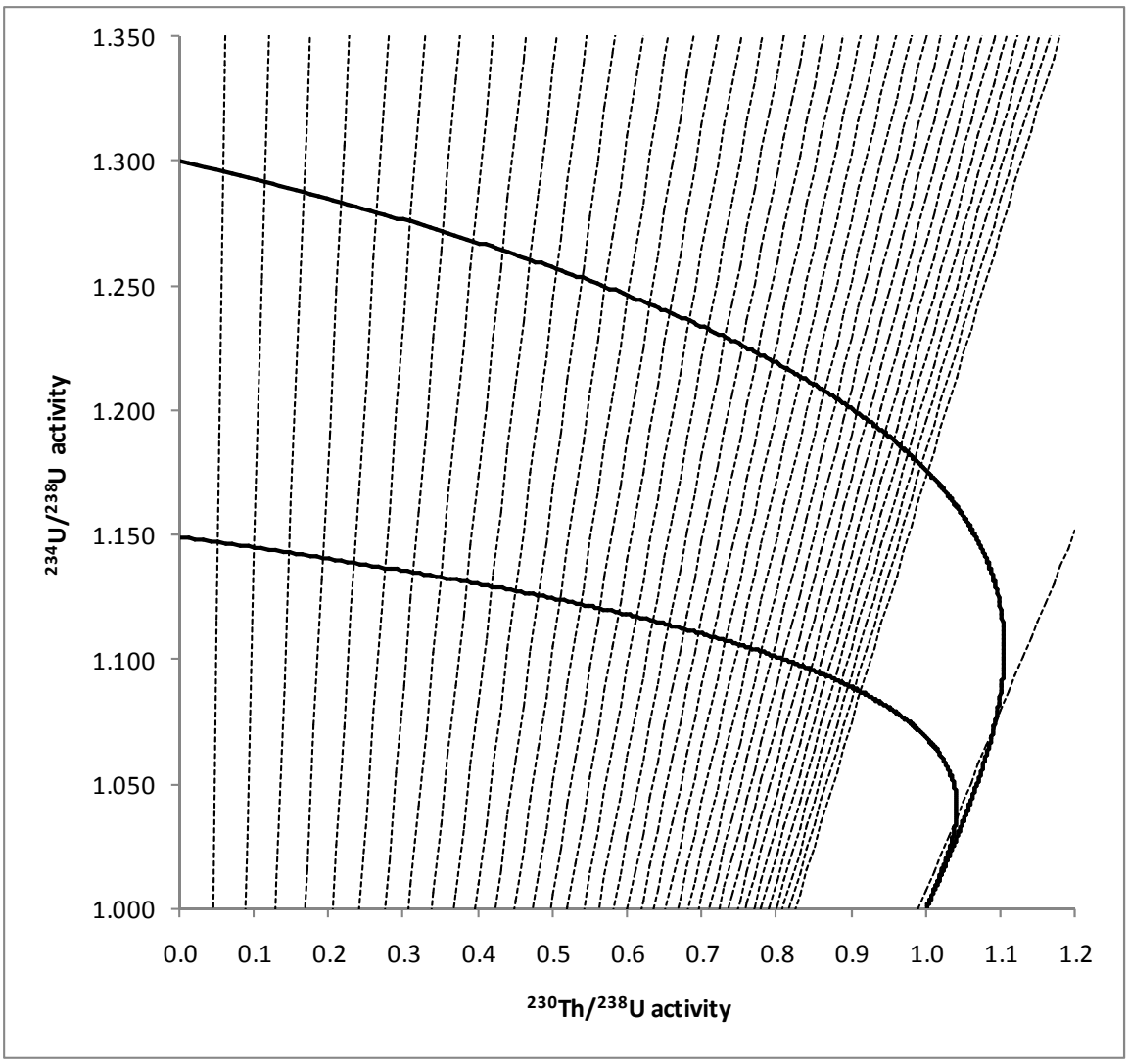
1.350
1.300
1.250
1.200
1.150
1.100
1.050
1.000
$^{234}U/^{238}U$ activity
0.0
0.1
0.2
0.3
0.4
0.5
0.6
0.7
0.8
0.9
1.0
1.1
1.2
$^{230}Th/^{238}U$ activity

Figure 3-4

Figure 3-4 Equal age lines computed using the derived equation (3.8).

age lines are plotted with 5,000 year intervals from 5,000 -200,000 years; in addition, there is one equal age line for the 500,000 years' equal age line. The slopes of the natural coral trend lines are found by calculating a 'least sum square of residuals' regression line for the data set. The slopes are read from the linear expression outputted by the software (in this case OriginLab).

Calculating the angles [φ]

The angle between two lines with slopes (a_1 and a_2) is defined as

(3.9) $$\tan\varphi = \frac{a_1+a_2}{1+a_1*a_2}$$

Therefore, the angle [φ] (in degrees) between the equal age line defined by the slope $a[Eq]$ and that of the data regression line $a[Z]$ of the actual Barbados coral data (see Figure 3-5), can be derived from the expression:

(3.10) $$\varphi = \frac{180}{\pi}\left[arctan\left[\frac{a[Z]+a[Eq]}{1+a[Eq]*a[Z]}\right]\right]$$

Substituting the values for *a*[Eq] derived from equation (3.8) results in the following equation (3.11), which allows us to calculate the angles between the equal age lines [Eq] and the actual reef disequilibria trend lines [Z].

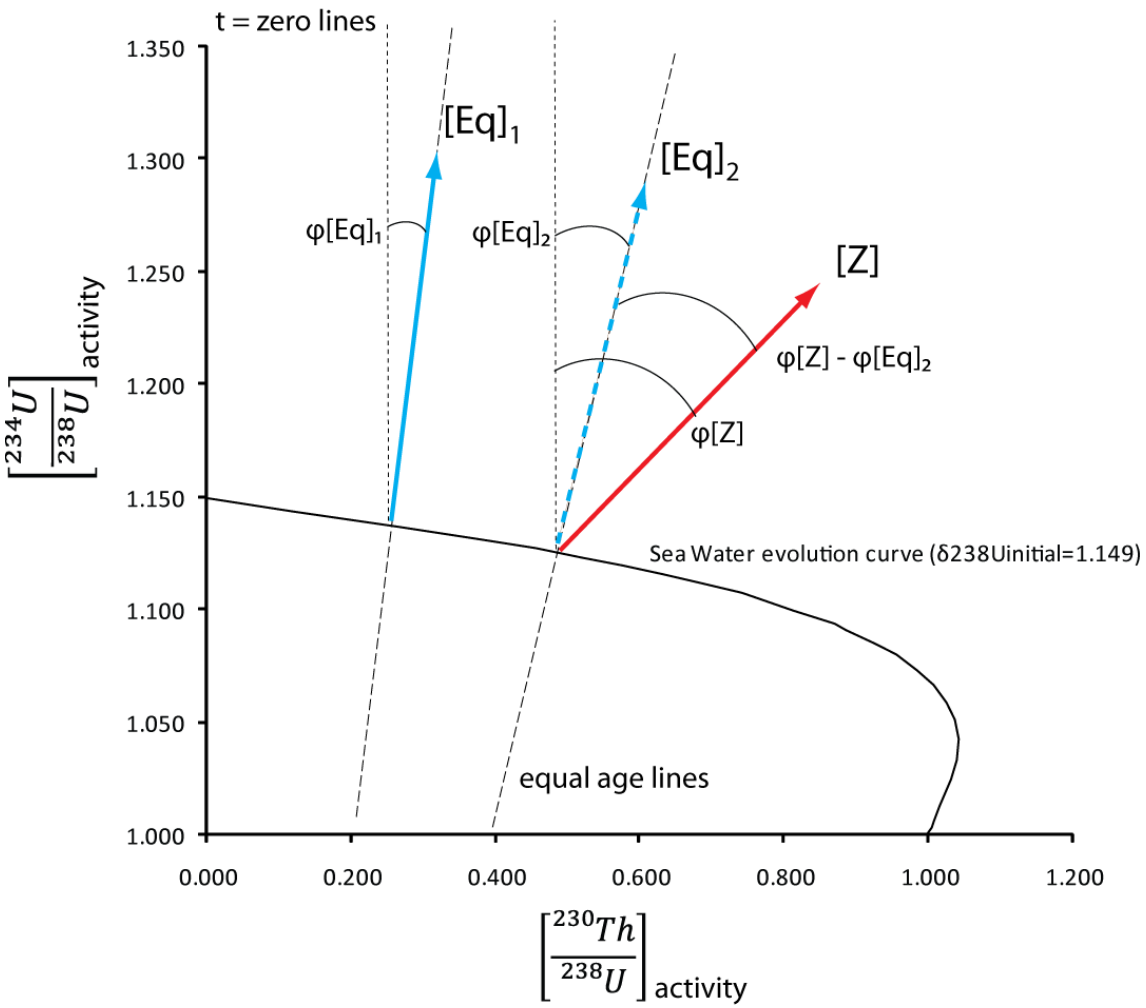
t = zero lines
[Eq]1
[Eq]2
φ[Eq]1
φ[Eq]2
[Z]
φ[Z] - φ[Eq]2
φ[Z]
Sea Water evolution curve (δ238Uinitial=1.149)
equal age lines
1.350
1.300
1.250
1.200
1.150
1.100
1.050
1.000
0.000
0.200
0.400
0.600
0.800
1.000
1.200
[234U/238U] activity
[230Th/238U] activity

Figure 3-5

Figure 3-5 Angles of trends defined as lying between the natural disequilibria trend [Z] and either the horizontal (t=zero lines) or the equal age line [Eq]. The former of the mentioned angles is designated as φ[Z] and the latter as φ[Z]-φ[Eq].

(3.11)

$$\varphi[\mathrm{Eq}] = \frac{180}{\pi}\left[arctan\left[\frac{a[Z]+\frac{e^{-\lambda_{234}*t}\left(\left[\frac{^{234}U}{^{238}U}\right]_{HIGH}^{INIT}-\left[\frac{^{234}U}{^{238}U}\right]_{SW}^{INIT}\right)}{\frac{\lambda_{230}}{\lambda_{230}-\lambda_{234}}\left(e^{-(\lambda_{230}-\lambda_{234})*t}\right)\left(\left[\frac{^{234}U}{^{238}U}\right]_{HIGH}^{Present}-\left[\frac{^{234}U}{^{238}U}\right]_{SW}^{Present}\right)}}{1+\frac{e^{-\lambda_{234}*t}\left(\left[\frac{^{234}U}{^{238}U}\right]_{HIGH}^{INIT}-\left[\frac{^{234}U}{^{238}U}\right]_{SW}^{INIT}\right)}{\frac{\lambda_{230}}{\lambda_{230}-\lambda_{234}}\left(e^{-(\lambda_{230}-\lambda_{234})*t}\right)\left(\left[\frac{^{234}U}{^{238}U}\right]_{HIGH}^{Present}-\left[\frac{^{234}U}{^{238}U}\right]_{SW}^{Present}\right)}*a[Z]}\right]\right]$$

Figure 3-6 shows angle evolution over time for the equal age lines shown in the $\left[\frac{^{230}Th}{^{238}U}\right]$ versus $\left[\frac{^{234}U}{^{238}U}\right]$ activity diagram. The evolution in question is predicated on decay in a closed system, where any excess ^{234}U is added to the system before any significant in-growth of ^{230}Th and where ^{230}Th is immobile within the system. The usefulness of the notion of angle evolution is in that it allows us (i) to calculate an approximation of the disequilibria severity by quantifying the difference between the data found and what should be expected within a closed system; (ii) to estimate the time-interval it takes to produce the current angles, starting from reef growth to first fresh water exposure when the initial uranium-series disequilibria occurred (this process is described in more detail in the 'Discussion' section below); and (iii) to approximate the ratio of the relationship between the ^{234}U and ^{230}Th as either added or trapped in the same proportions as those defining the trends.

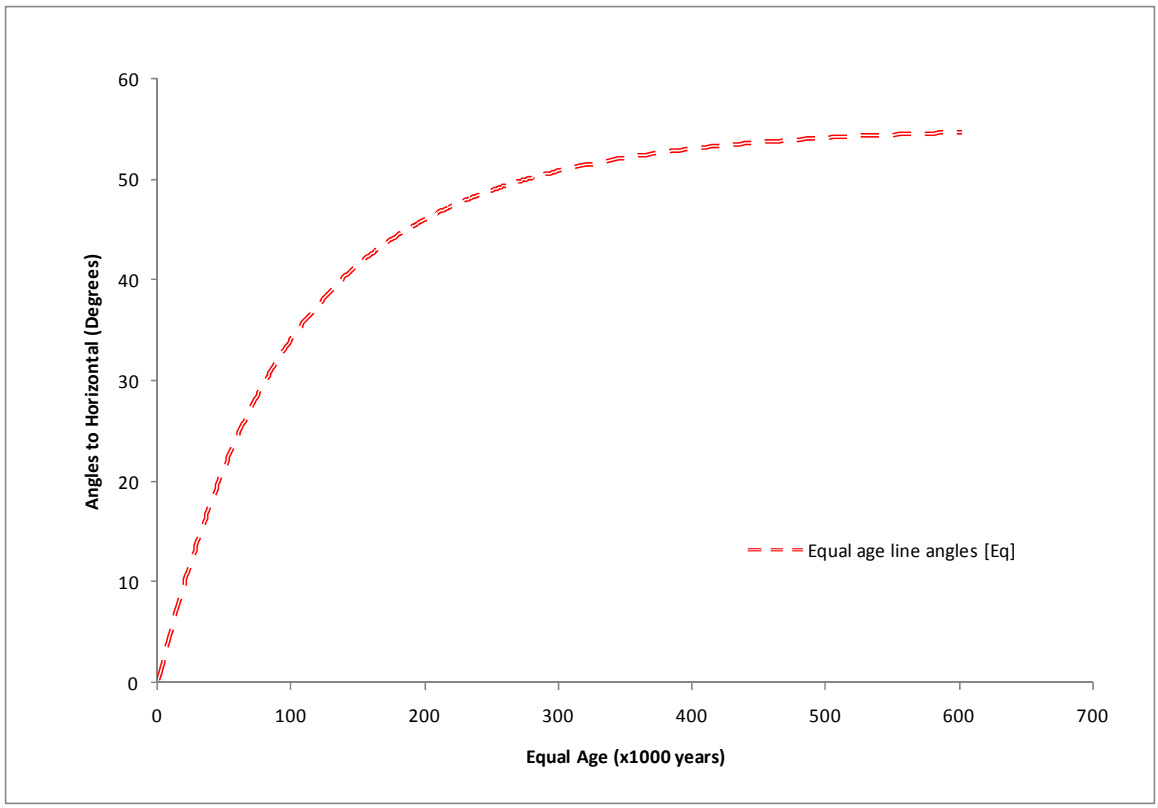
60
50
40
30
20
10
0
Angles to Horizontal (Degrees)
0
100
200
300
400
500
600
700
Equal Age (x1000 years)
Equal age line angles [Eq]

Figure 3-6

Figure 3-6 The evolution of the angles of the equal-age trend lines over time. The angles are calculated using the modified age equations described earlier (cf. equation 3.11). In a closed system, the evolution is predictable as long as the system stays closed after the trend has been set. Likewise, the modified age equations, expressed as angles, allow us to calculate the evolution of the natural trends both forward and backwards in time.

Calculating the length of a trend line [L]

The second parameter used to describe the vectors representing the disequilibria trends is trend line length.

The length of a line segment is defined as

(3.12) $$d = \sqrt{(x_2 - x_1)^2 + (y_2 - y_1)^2}$$

Inserting the $\{y_2, y_1, x_2, x_1\}$ (as defined above in equations 3.3, 3.4, 3.5 and 3.6) gives us the expression determining the length of the lines L[Eq], at time *t*, between the seawater evolution curve ($\delta^{234}U_{initial}$ =1.149) and the [HIGH] curve ($\delta^{234}U_{initial}$ = 1.300). (See equation 3.13).

(3.13)

$$L[Eq] = \sqrt{\left(\left[(1 - e^{-\lambda_{230}*t}) + \frac{\lambda_{230}}{\lambda_{230} - \lambda_{234}}(e^{-(\lambda_{230}-\lambda_{234})*t})\left(\left[\frac{^{234}U}{^{238}U}\right]_{HIGH}^{Present}\right)\right] - \left[(1 - e^{-\lambda_{230}*t}) + \frac{\lambda_{230}}{\lambda_{230} - \lambda_{234}}(e^{-(\lambda_{230}-\lambda_{234})*t})\left(\left[\frac{^{234}U}{^{238}U}\right]_{SW}^{Present}\right)\right]\right)^2 + \left(\left[\left(\left(\left[\frac{^{234}U}{^{238}U}\right]_{HIGH}^{INIT} - 1\right)e^{-\lambda_{234}*t}\right) - 1\right] - \left[\left(\left(\left[\frac{^{234}U}{^{238}U}\right]_{SW}^{INIT} - 1\right)e^{-\lambda_{234}*t}\right) - 1\right]\right)^2}$$

Equation 3.13 has been used to calculate the relationship between the lengths of one hypothetical equal age line $L[Eq]_1$ and another hypothetical equal age line $L[Eq]_2$ (See Figure 3-7).

As expected, due to the nature of the system, the individual lengths do not evolve linearly during decay; however, the ratio between them is constant over time (see Figure 3-8). This constant relationship through time that exists between the lengths of any two equal age lines in a closed system, does not obtain in an open system: here, the ratio between the lengths of excess ^{234}U series disequilibria trends and the lengths of trends of equal age is not constant. However, once an angle between the age appropriate pairs of an equal and an open system trend is set (as shown in Figure 3-9), and any further development is only by natural decay, their non-linear ratios will evolve in a predictable way that can be modeled based on the age equations (not shown here).

The relationship in question is also used to predict how much the uranium series disequilibria trend in fossil coral reefs will tend to 'collapse' during natural decay. The severity (also called the 'effect cap') of the uranium-series disequilibria established earlier can be calculated backwards in time for older reef trends; it is similarly estimated based on this predictable relationship, as the ratio between the length of an old equal age line and that of a younger equal age line does not change with increasing initial ^{234}U disequilibria. Thus, this ratio is also a good estimator of how much the ^{234}U disequilibria trend will 'shrink' due to natural decay, as illustrated in Figure 3-9 (cf. the $\left[\frac{^{230}Th}{^{238}U}\right]$ versus $\left[\frac{^{234}U}{^{238}U}\right]$ space). All relationships found in this way can be converted back to ratios if necessary.

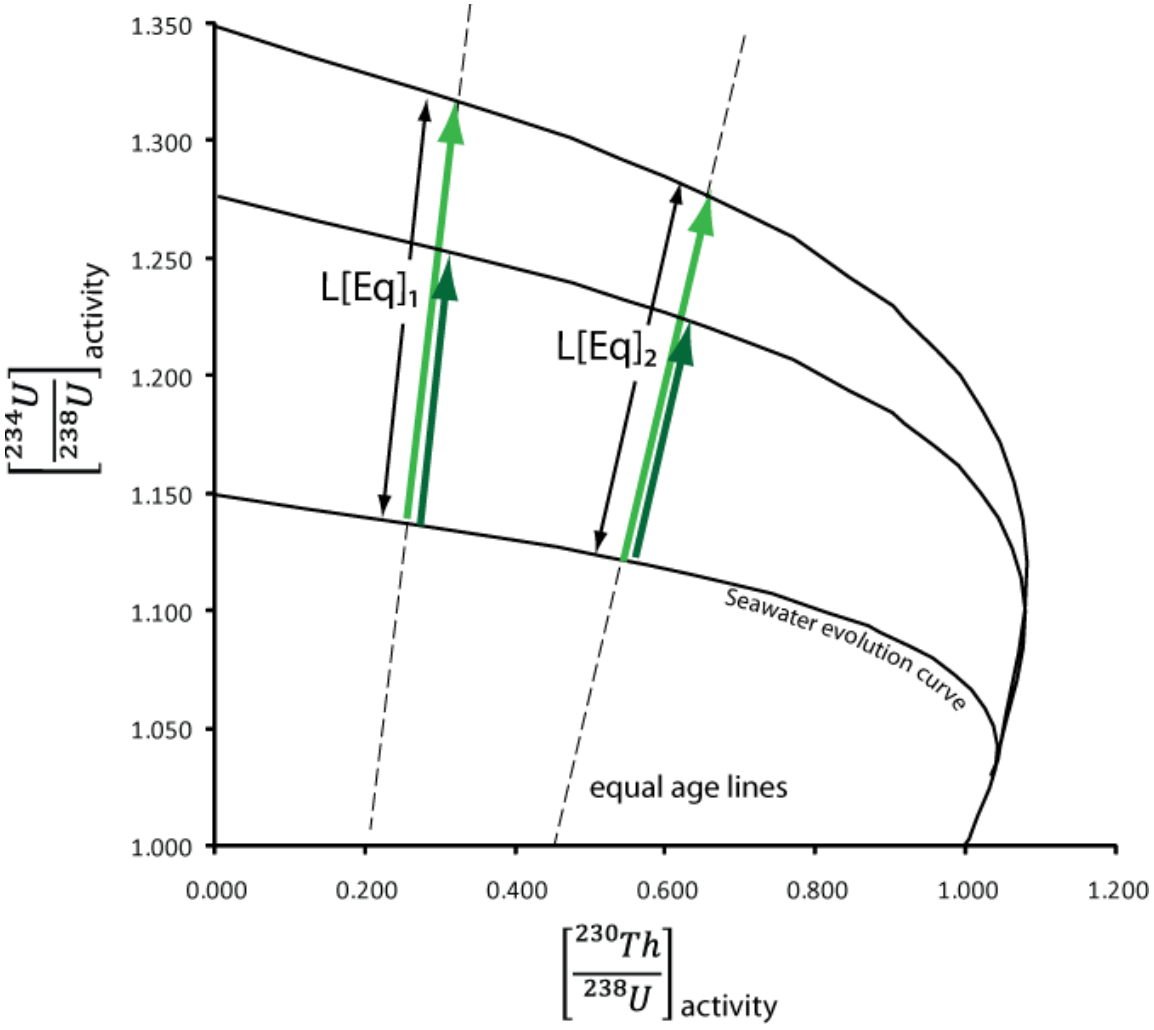
1.350
1.300
1.250
1.200
1.150
1.100
1.050
1.000
0.000
0.200
0.400
0.600
0.800
1.000
1.200
$\left[\frac{^{234}U}{^{238}U}\right]_{activity}$
$\left[\frac{^{230}Th}{^{238}U}\right]_{activity}$
L[Eq]1
L[Eq]2
Seawater evolution curve
equal age lines

Figure 3-7

Figure 3-7 The relationship between the lengths of two equal age trend lines representing the same age (pairs of dark and light green vectors). This relationship stays constant in a closed system (see Figure 3-8 and the caption there). Natural trend lines with angles that differ from those of the appropriate equal age lines will not have this constant ratio, because their angles no longer evolve synchronously. (See also Figure 3-9).

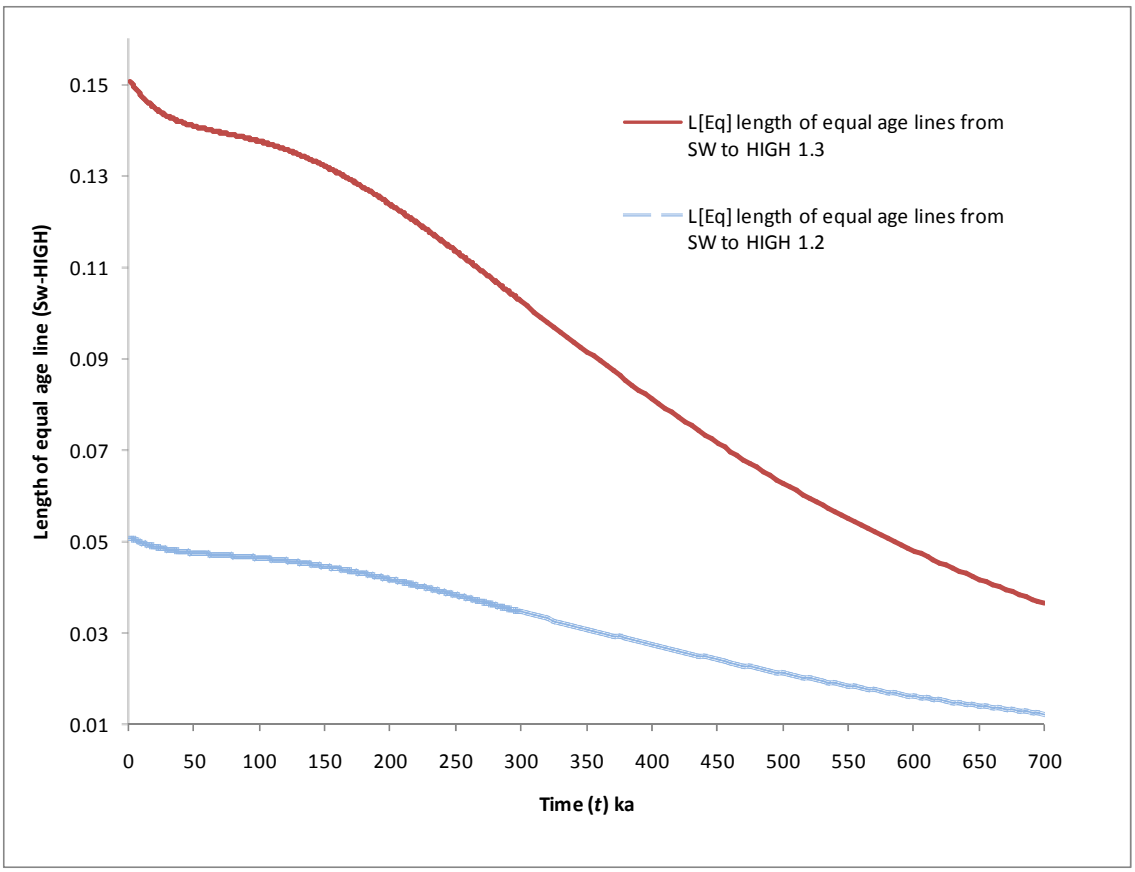
0.15
0.13
0.11
0.09
0.07
0.05
0.03
0.01
Length of equal age line (Sw-HIGH)
0
50
100
150
200
250
300
350
400
450
500
550
600
650
700
Time (t) ka
L[Eq] length of equal age lines from SW to HIGH 1.3
L[Eq] length of equal age lines from SW to HIGH 1.2

Figure 3-8

Figure 3-8 The lengths of two arbitrarily chosen equal age lines calculated using the modified age equations expressing the length of a trend (see equation 3.13). Note that the lengths of a trend do not evolve linearly, but display a variable rate of length reduction in the first 200,000 years. Despite this, the ratios between these two equal age trend lengths are always constant.

Summarizing what has been said so far about this model, ^{234}U is typically always in excess, because during dissolution, its supply from the surrounding sands is presumably infinite. After the paleoreefs are subaerially exposed and freshwater percolates through them, ^{230}Th is particle-reactive and stays behind, whereas ^{238}U is mobile and will move through the system, as will ^{234}U. What remains enigmatic is why some of the ^{234}U that was released during dissolution sticks to the corals in excess amounts (but apparently only in amounts that are proportional to the amounts of ^{230}Th—themselves strictly fixed, or at least fixed enough to set regular and proportional trends in the data). Such considerations form the very premise for our explanation of the developing disequilibria trends; we seek to use these fundamental notions as the basis for quantifying our 'disequilibria-cum-adsorption' model (see also Chapter 2).

RESULTS

Table 3-1 contains the result of the least squared sums regression analysis of the $\left[\frac{^{230}Th}{^{238}U}\right]$ versus $\left[\frac{^{234}U}{^{238}U}\right]$ activity data points for each of the seven reefs (i. e. the ~60,000 year old MIS 3, the ~82,000 year old MIS 5a, the ~105,000 year old MIS 5c, the ~125,000 year old MIS 5e, the ~190,000 year old early MIS 6 or late 7a, the ~210,000 year old MIS 7a, and the ~240,000 year old MIS 7c reef). Figure 3-10 plots all of the activity data and the regression lines for these coral reefs. The slopes vary from 0.226 (an angle of 77.4 degrees) to 0.463 (an angle of 61.4 degrees). (See Table 3-1). The angles vary due to two factors: (i) the age of the

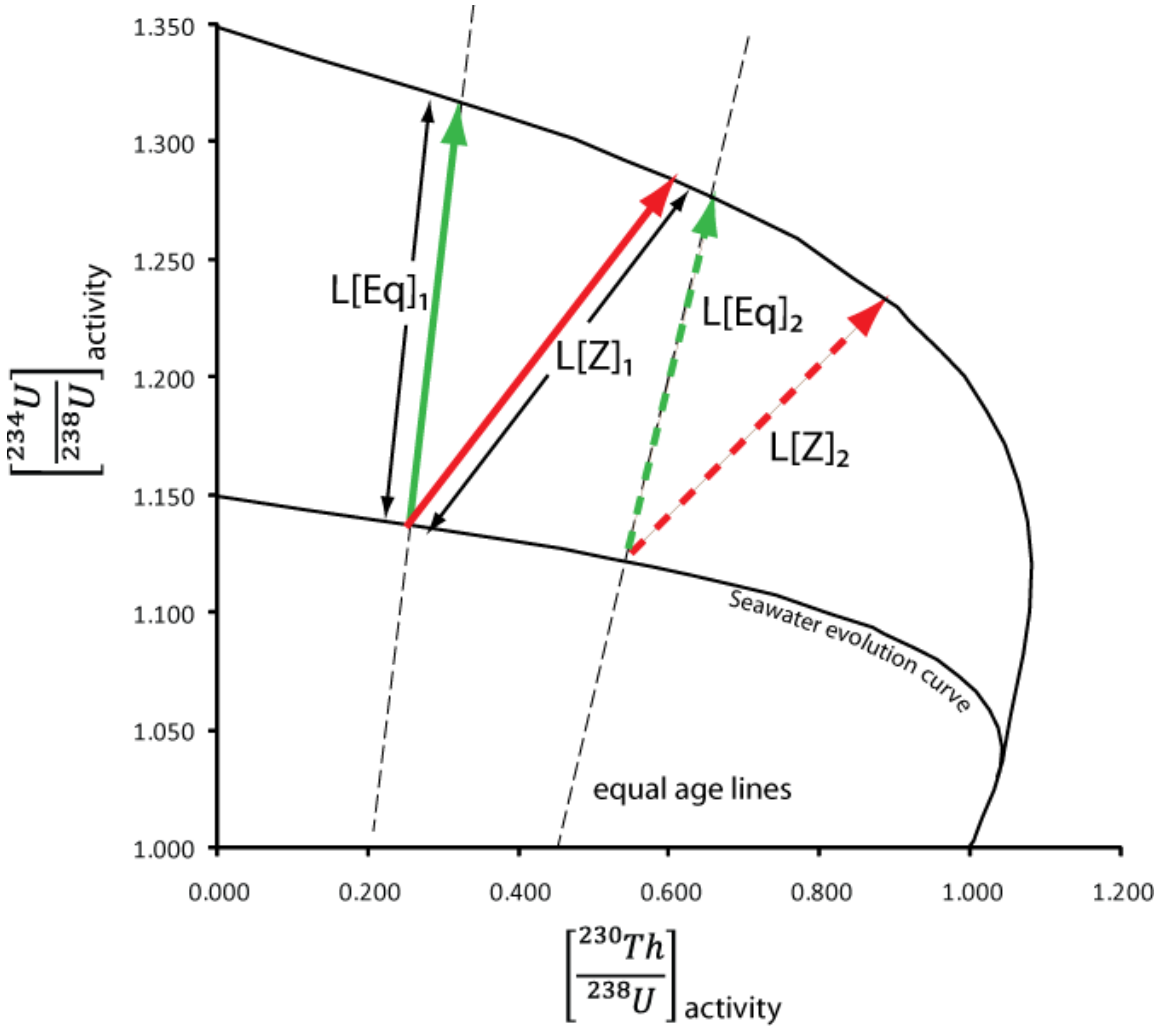
1.350
1.300
1.250
1.200
1.150
1.100
1.050
1.000
0.000
0.200
0.400
0.600
0.800
1.000
1.200
$\left[\frac{^{234}U}{^{238}U}\right]_{activity}$
$\left[\frac{^{230}Th}{^{238}U}\right]_{activity}$
L[Eq]1
L[Z]1
L[Eq]2
L[Z]2
Seawater evolution curve
equal age lines

Figure 3-9

Figure 3-9 The relationship of the lengths of equal age lines $L[Eq]_1$ versus natural trends $L[Z]_1$, and of aged $L[Eq]_2$ versus aged $L[Z]_2$.trends. In this scenario, the ratios of the lengths between them are not constant, but evolve in a predictable fashion which can be modeled using the modified age equations provided above.

reef determines a natural decay component of the slopes (angles) and becomes larger with time; and (ii) the angles become larger the more time is allowed for ^{230}Th in-growth to occur prior to the reefs' exposure to fresh water. Due to the latter factor, a young reef may have a larger angle than does an older reef, since this aspect of the evolution is controlled by the amount of dissolution of the reef, not by its decay. In this case, the young reefs exhibit a much longer 'marine residence time' than do the older ones. For example, in the activity diagram (Figure 3-10), the angle of the 60,000 year old MIS 3 reef is nearly identical to that of the 190,000 year old early MIS 6 reef (Table 3-1); yet when the reefs are modeled back, taking into account the elapsed time, one sees that they were quite different at the time of initial subaerial exposure. This is so, because the in-growth time of ^{230}Th was much longer for the MIS 3 reef, thereby compensating for the smaller, 'coming of age' component of the decay process (this notion is discussed in more detail in the 'Discussion' section below).

The results in Table 3-2 are based on a modeled dissolution of an idealized 1 cm^3 of coral with an original density of 2.3 g/cm^3, an initial porosity of 20%, and a fixed uranium concentration of 3.2 ppm in the aragonite. Concentrations of ^{230}Th are calculated using modified age equations to estimate the ^{230}Th production rate through time. The calculated production rate was compared to measured data, which were normalized to a standard uranium content of 3.2 μg/g (ppm). The calculated and normalized measured data are compared and plotted in Figure 3-11.

Table 3-1

Reef locality	Approx. reef age	Regressed data slope	Angle
RGF-8 (offshore reef)	60000	0.298	72.4
NU (Thompson et al., 2003)	82000	0.333	70.2
SCP (Salt Cave Point)	105000	0.305	72.0
AEC (Chancery Lane)	125000	0.223	77.4
NU (Thompson et al., 2003)	190000	0.345	71.0
LKS (Regency Park)	210000	0.305	69.4
NU (Thompson et al., 2003)	240000	0.463	61.4

Table 3-1 Approximate ages, regressed data slopes and activity trend angles[φ] of 7 Barbadian paleoreefs

1 The approximate age of the reef is determined by analyzing closed system samples from contemporary reefs nearby (see Schellman and Radtke (2002), Blanchon and Eisenhauer (2001), Gallup et al. (1994), Fairbanks (1989) and other references therein).

2 Regressed data slopes are calculated from the least squares sum regression of the data arrays for each reef (see also Figure 3-10).

3 Angles of the regression slopes are determined in accordance with equation 3.11 and with what has been detailed elsewhere in the text.

4 Thompson et al. (2003) refer to the Barbados reef units as Terrace 1, 2 and 3; localities are not given specifically

All other samples in the present study's sample localities are shown in Chapter 2 (Figure 2-1). There, we refer to 6 samples from an 8 m section of a submarine core drilled offshore that penetrated the 60,000 year old before present (yr. BP) drowned reef (RGF-8; -59.547°W, 13.046°N), 8 samples taken from the 105,000 yr. BP, below the 1st high cliff reef above Salt Cave Point (SCP; -59.463°W, 13.085°N), 6 samples from the 125,000 yr. BP lower part of the 1st high cliff reef at Chancery Lane (AEC; -59.565°W, 13.066°N), and 6 samples from the 210,000 yr. BP cliff close to Regency Park above Worthington (LKS; -59.565°W, 13.083°N). All other data are from Thompson et al. (2003), Blanchon and Eisenhauer (2001).

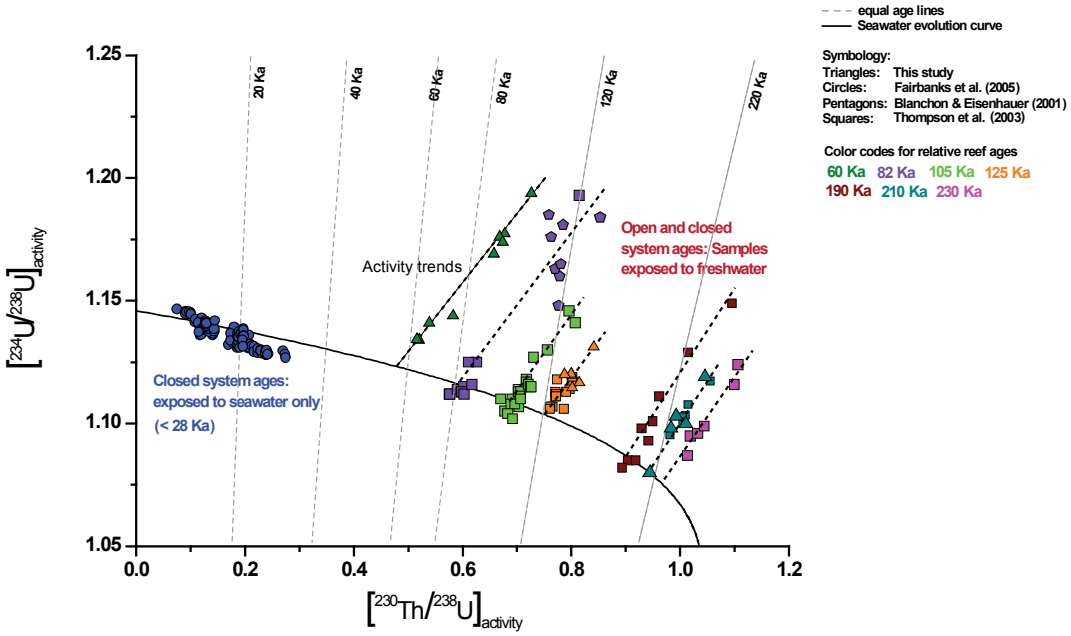
equal age lines
Seawater evolution curve
Symbology:
Triangles: This study
Circles: Fairbanks et al. (2005)
Pentagons: Blanchon & Eisenhauer (2001)
Squares: Thompson et al. (2003)
Color codes for relative reef ages
60 Ka 82 Ka 105 Ka 125 Ka
190 Ka 210 Ka 230 Ka
20 Ka
40 Ka
60 Ka
80 Ka
120 Ka
220 Ka
Activity trends
Open and closed system ages: Samples exposed to freshwater
Closed system ages: exposed to seawater only (< 28 Ka)
1.25
1.20
1.15
1.10
1.05
0.0
0.2
0.4
0.6
0.8
1.0
1.2
[234U/238U]activity
[230Th/238U]activity

Figure 3-10

Figure 3-10 Data trends for Barbados: the $\left[\frac{^{230}Th}{^{238}U}\right]$ versus $\left[\frac{^{234}U}{^{238}U}\right]$ activity from Barbadian uplifted Pleistocene reefs. Samples with elevated the $\left[\frac{^{230}Th}{^{238}U}\right]$ versus $\left[\frac{^{234}U}{^{238}U}\right]$ activity ratios plot along trend lines which are generally similar in slope (~0.3) for all reefs.

Table 3-2

original coral	[1] Total mass loss 0% loss	5% loss	10% loss	15% loss	20% loss	25%loss	30% loss	35% loss	40% loss
[2] bulk Porosity	20%	25%	30%	35%	40%	45%	50%	55%	60%
[3] density (t=0) (g/cm ^{3})	2.30	2.07	1.93	1.79	1.66	1.52	1.38	1.24	1.10
[4] conc. U ppm (ug/g)	3.20	3.20	3.20	3.20	3.20	3.20	3.20	3.20	3.20
[5] bulk U (µg/cm^3)	7.36	6.62	6.18	5.74	5.30	4.86	4.42	3.97	3.53
Dissolution occurring at 15000 years:									
[6] conc.^{230}Th (pg/g)	7.6	7.6	7.6	7.6	7.6	7.6	7.6	7.6	7.6
[7] bulk^{230}Th (pg/cm ^{3})	17.5	17.5	17.5	17.5	17.5	17.5	17.5	17.5	17.5
[8] ^{230}Th/^{238}U (pg/ug)	2.4	2.6	2.8	3.0	3.3	3.6	4.0	4.4	4.9
[9] eqv. conc ^{230}Th (pg/g)	7.6	8.4	9.0	9.7	10.6	11.5	12.7	14.1	15.8
[10] Age equivalent	**14899**	**16693**	**17983**	**19512**	**21318**	**23489**	**26162**	**29363**	**33627**
^{234}U/^{238}U	1.143	1.158	1.168	1.180	1.195	1.212	1.232	1.257	1.288
^{230}U/^{238}U	0.147	0.163	0.175	0.189	0.204	0.223	0.245	0.272	0.306
Dissolution occurring at 20.000 years:									
conc. ^{230}Th (pg/g)	9.92	9.92	9.92	9.92	9.92	9.92	9.92	9.92	9.92
bulk ^{230}Th (pg/cm ^{3})	22.81	22.81	22.81	22.81	22.81	22.81	22.81	22.81	22.81
^{230}Th/^{238}U (pg/ug)	3.10	3.44	3.69	3.97	4.30	4.70	5.16	5.74	6.46
eqv. conc. ^{230}Th (pg/g)	9.92	11.02	11.80	12.71	13.77	15.02	16.53	18.36	20.66
Age equivalent	**19899**	**22364**	**24162**	**26123**	**28596**	**31590**	**35289**	**39977**	**46120**
^{234}U/^{238}U	1.141	1.155	1.166	1.178	1.192	1.209	1.229	1.253	1.284
^{230}U/^{238}U	0.192	0.213	0.228	0.246	0.266	0.290	0.319	0.355	0.399

Table 3-2 Continued

Dissolution occurring at 30.000 years:									
conc. ^{230}Th (pg/g)	14.26	14.26	14.26	14.26	14.26	14.26	14.26	14.26	14.26
bulk ^{230}Th (pg/cm ^{3})	32.79	32.79	32.79	32.79	32.79	32.79	32.79	32.79	32.79
^{230}Th/^{238}U (pg/ug)	4.46	4.95	5.30	5.71	6.19	6.75	7.43	8.25	9.28
eqv. conc. ^{230}th (pg/g)	14.26	15.84	16.97	18.28	19.80	21.60	23.76	26.40	29.70
Age equivalent	**29625**	**33446**	**36256**	**39586**	**43596**	**48525**	**54731**	**62795**	**73709**
^{234}U/^{238}U	1.137	1.151	1.161	1.173	1.187	1.203	1.222	1.246	1.276
^{230}U/^{238}U	0.274	0.305	0.327	0.352	0.381	0.416	0.457	0.508	0.572

Dissolution occurring at 36.000 years:									
conc. ^{230}Th (pg/g)	16.69	16.69	16.69	16.69	16.69	16.69	16.69	16.69	16.69
bulk ^{230}Th (pg/cm ^{3})	38.38	38.38	38.38	38.38	38.38	38.38	38.38	38.38	38.38
^{230}Th/^{238}U (pg/ug)	5.21	5.79	6.21	6.69	7.24	7.90	8.69	9.66	10.86
eqv. conc. ^{230}th (pg/g)	16.69	18.54	19.87	21.39	23.18	25.28	27.81	30.90	34.76
Age equivalent	**35443**	**40151**	**43640**	**47802**	**52857**	**59132**	**67146**	**77771**	**92592**
^{234}U/^{238}U	1.135	1.149	1.159	1.171	1.185	1.201	1.220	1.244	1.274
^{230}U/^{238}U	0.321	0.356	0.382	0.411	0.445	0.486	0.534	0.594	0.668

Dissolution occurring at 40.000 years:									
conc. ^{230}Th (pg/g)	18.24	18.24	18.24	18.24	18.24	18.24	18.24	18.24	18.24
bulk ^{230}Th (pg/cm ^{3})	41.94	41.94	41.94	41.94	41.94	41.94	41.94	41.94	41.94
^{230}Th/^{238}U (pg/ug)	5.70	6.33	6.78	7.31	7.92	8.63	9.50	10.55	11.87
eqv. conc. ^{230}th (pg/g)	18.24	20.26	21.71	23.38	25.33	27.63	30.39	33.77	37.99
Age equivalent	**39298**	**44631**	**48597**	**53349**	**59150**	**66442**	**75822**	**88433**	**106426**
^{234}U/^{238}U	1.133	1.147	1.157	1.168	1.181	1.197	1.216	1.239	1.268
^{230}U/^{238}U	0.350	0.389	0.416	0.448	0.486	0.530	0.583	0.648	0.729

Table 3-2: Results of dissolution modeling

1. 'Total mass loss' = the mass lost by the original coral structure during the dissolution event. Solids lost during this event may lead to an increase of ^{230}Th and ^{234}U while leaving the ^{238}U constant
2. 'bulk porosity' = the total pore space (by weight) not occupied by aragonite.
3. 'density (t=0) (g/cm^3)' = weight of 1 cm^3 of coral at the time before dissolution occurs.
4. 'conc. U ppm (ug/g)' = the overall concentration of uranium.
5. 'bulk U ($\mu g/cm^3$)' = the amount of uranium present (or left after dissolution) in a 1 cm^3 of coral.
6. 'conc. ^{230}Th (pg/g)' = the expected amount of ingrown ^{230}Th in 1 cm^3 of coral containing 3.2 ug/g U at the time of dissolution.
7. 'bulk ^{230}Th (pg/cm^3)' = the total amount of ingrown ^{230}Th in 1 cm^3 of coral at the time when dissolution occurs.
8. $^{230}Th/^{238}U$ (pg/ug) = the ratio in total weight between 'bulk ^{230}Th (in picograms)' and total weight of 'bulk ^{238}U (in micrograms)' (1000x) in 1 cm^3 of coral.
9. 'eqiv. conc. ^{230}Th (pg/g)' = the equivalent ^{230}Th concentration of a coral that has been partially dissolved retaining all ^{230}Th, but losing the entire fraction of U that was mobilized during dissolution.
10. Age equivalent = the equivalent ages in years of the modeled $\left[\frac{^{230}Th}{^{238}U}\right]$ and $\left[\frac{^{234}U}{^{238}U}\right]$ activity ratios, calculated by iteration of standard age equations.

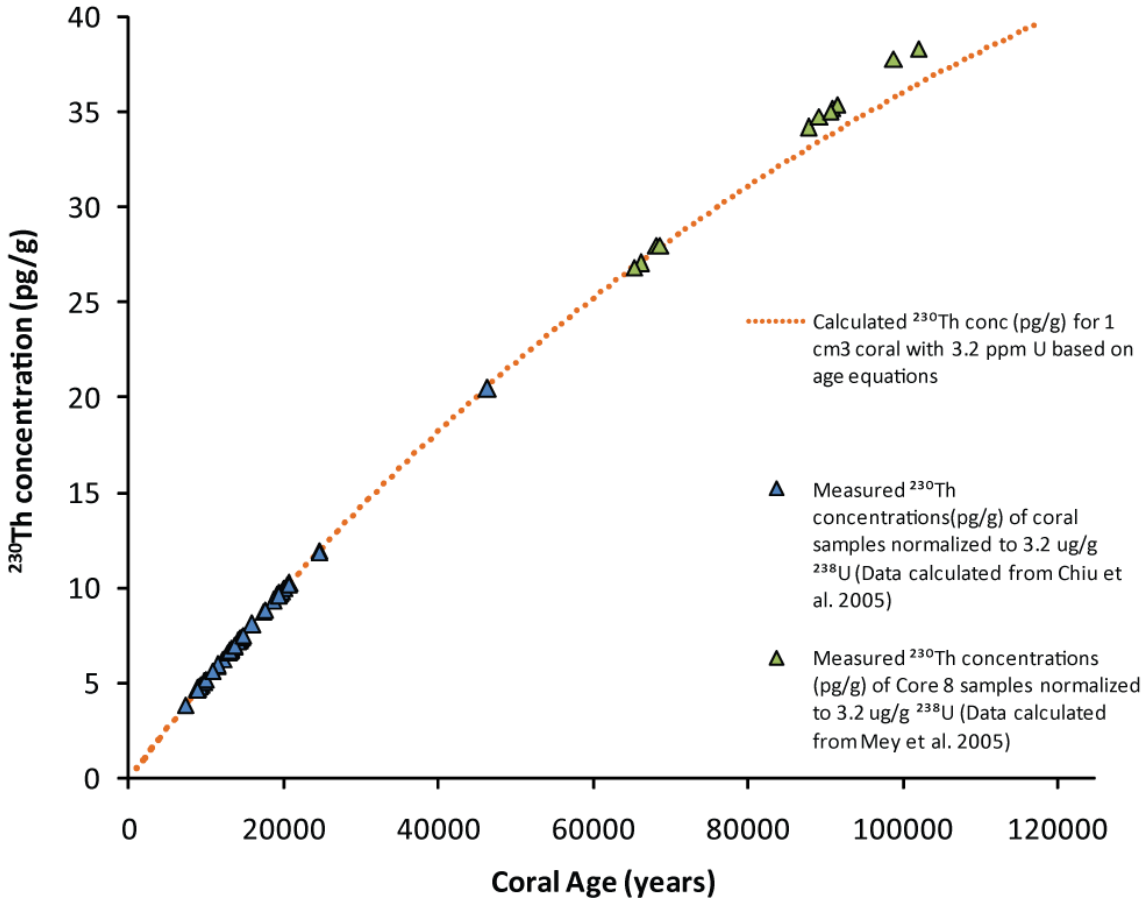
40
35
30
25
20
15
10
5
0
^{230}Th concentration (pg/g)
0
20000
40000
60000
80000
100000
120000
Coral Age (years)
Calculated ^{230}Th conc (pg/g) for 1 cm3 coral with 3.2 ppm U based on age equations
Measured ^{230}Th concentrations(pg/g) of coral samples normalized to 3.2 ug/g ^{238}U (Data calculated from Chiu et al. 2005)
Measured ^{230}Th concentrations (pg/g) of Core 8 samples normalized to 3.2 ug/g ^{238}U (Data calculated from Mey et al. 2005)

Figure 3-11

Figure 3-11 Calculated concentrations in pico-grams per gram or parts per trillion (ppt) of ^{230}Th present in corals (with a porosity of 20%) with a normalized true concentration of 3.2 ppm uranium over time, when the ^{230}Th is added to the coral by natural decay. The calculated curve is compared to the values measured in closed system (blue triangles) and open system (green triangles) corals. All samples have been normalized to assume 3.2 ppm uranium.

DISCUSSION

A model of dissolution in corals

Figure 3-12 shows various models of coral dissolution relative to time. The time spans of the models dissolution were chosen by estimating the longest and the shortest times from reef growth to first freshwater exposure. For example, MIS stage 3 lasted approximately 40,000 years (Porter et al., 1989), whereas stage 7c lasted only approximately 15,000 years. The test intervals from growth to first freshwater exposure were therefore chosen relative for the 15,000, 20,000, 30,000, 36,000 and 40,000 year marine residence times for the reefs. The modeled trends are then compared with results representing core 8 data from the MIS 3 reef, which is believed to have grown 60,000 years ago. The comparison of the data from core 8 with the appropriate model produced a good match and thus confirms our hypothesis that the process of dissolution offers a plausible influence for the activity trends in the corals.

The calculated activities as postulated by the $\left[\frac{^{230}\text{Th}}{^{238}\text{U}}\right]$ ratio are indicated in Table 3-2; the $\left[\frac{^{234}\text{U}}{^{238}\text{U}}\right]$ activity ratios themselves are estimated on the basis of the maximum length of the trends seen in the Barbados corals, in this case, the high $\delta^{234}U_{initial} = 1.300$. When we vary the ^{234}U component, the slope of the trend lines will change. In the model, we assume that the corals can have any amount of ^{234}U available as long as the initial trends remain on the equal age lines. However, from the data there appears to be a close relationship between the amount of ^{230}Th and the amount of ^{234}U added or trapped in the corals; as we have seen, this relationship is constant and sets the trends for all the open

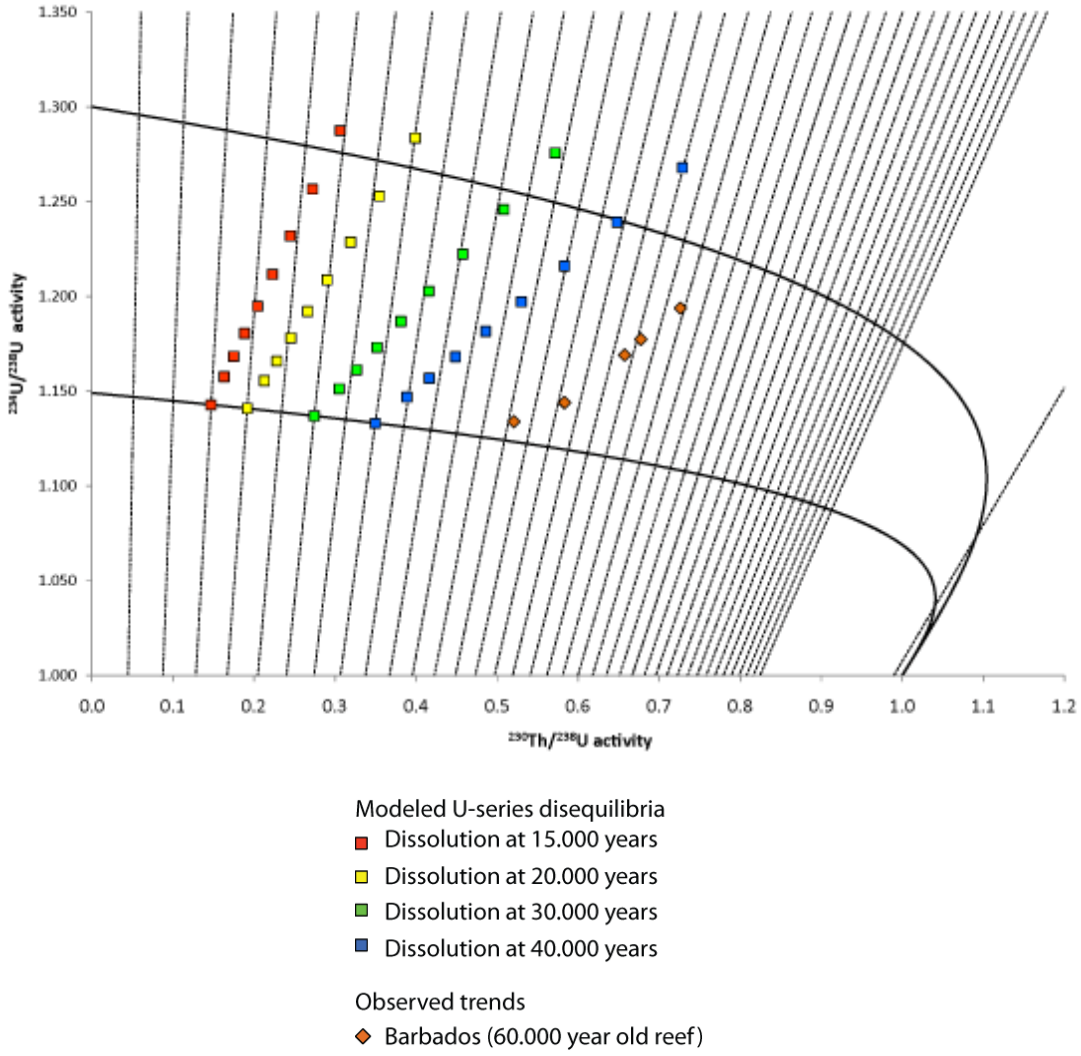
1.350
1.300
1.250
1.200
1.150
1.100
1.050
1.000
0.0
0.1
0.2
0.3
0.4
0.5
0.6
0.7
0.8
0.9
1.0
1.1
1.2
234U/238U activity
230Th/238U activity
Modeled U-series disequilibria
Dissolution at 15.000 years
Dissolution at 20.000 years
Dissolution at 30.000 years
Dissolution at 40.000 years
Observed trends
Barbados (60.000 year old reef)

Figure 3-12

Figure 3-12 Models representing the results from Table 3-2 for the dissolution trends in the Barbados reefs. Each model represents the time when the dissolution occurred: after 15,000 years (red squares), after 20,000 years (yellow squares), after 30,000 years (green squares), and after 40,000 years (blue squares). The percentages listed alongside the blue 40,000 year trend indicate the amounts of lost coral mass due to dissolution. When the coral loses mass through dissolution, the bulk $^{230}Th/^{238}U$ ratio goes up as uranium is lost and the particle-reactive ^{230}Th is adsorbed onto the extant corals. The orange squares, representing core 8 data from the 60,000 year old reef drilled off shore (see Chapter 2, Figure 2-1 for location of reef), are plotted in for comparison.

system reefs. This observation provides a strong argument for using the corals' own preference for ^{234}U versus ^{230}Th as it is reflected in the model. The estimated value of the ^{234}U component is likewise confirmed by calculating the reef trends back to time zero, so as to estimate the 'residual' which expresses a ^{234}U addition that did not come from decay in the coral following dissolution.

Estimating the time of first freshwater exposure – the 'marine residence time'

The time from reef growth to fresh water exposure, called here the 'marine residence time', is estimated by comparing the modeled trend angles (Figure 3-12) with the trends calculated back to the respective intervals (15,000 to 40,000 years). Figure 3-12 provides an example, calculated for the 60,000 year old MIS 3 reef; the procedure is repeated for all the other reefs. Following this procedure, the actual trends measured today are calculated back in time to 'match' the modeled trends. When a modeled trend parallels the 'back projected data trend', as in Figure 3-13, the model trend and the real trend represent the same particular slope. That slope reflects the time passed (as per ^{230}Th in-growth) since the growth of the reef till its first exposure to freshwater, which is when the trend for the reef was set. Figure 3-13 shows the back-projected angles of all the reefs for intervals of 40,000 years and 15,000 years. Note that none of the angles are shallower than the equal age lines, which means that excess ^{234}U (beyond that due to natural decay and seawater influence) was either trapped or adsorbed onto the coral during dissolution.

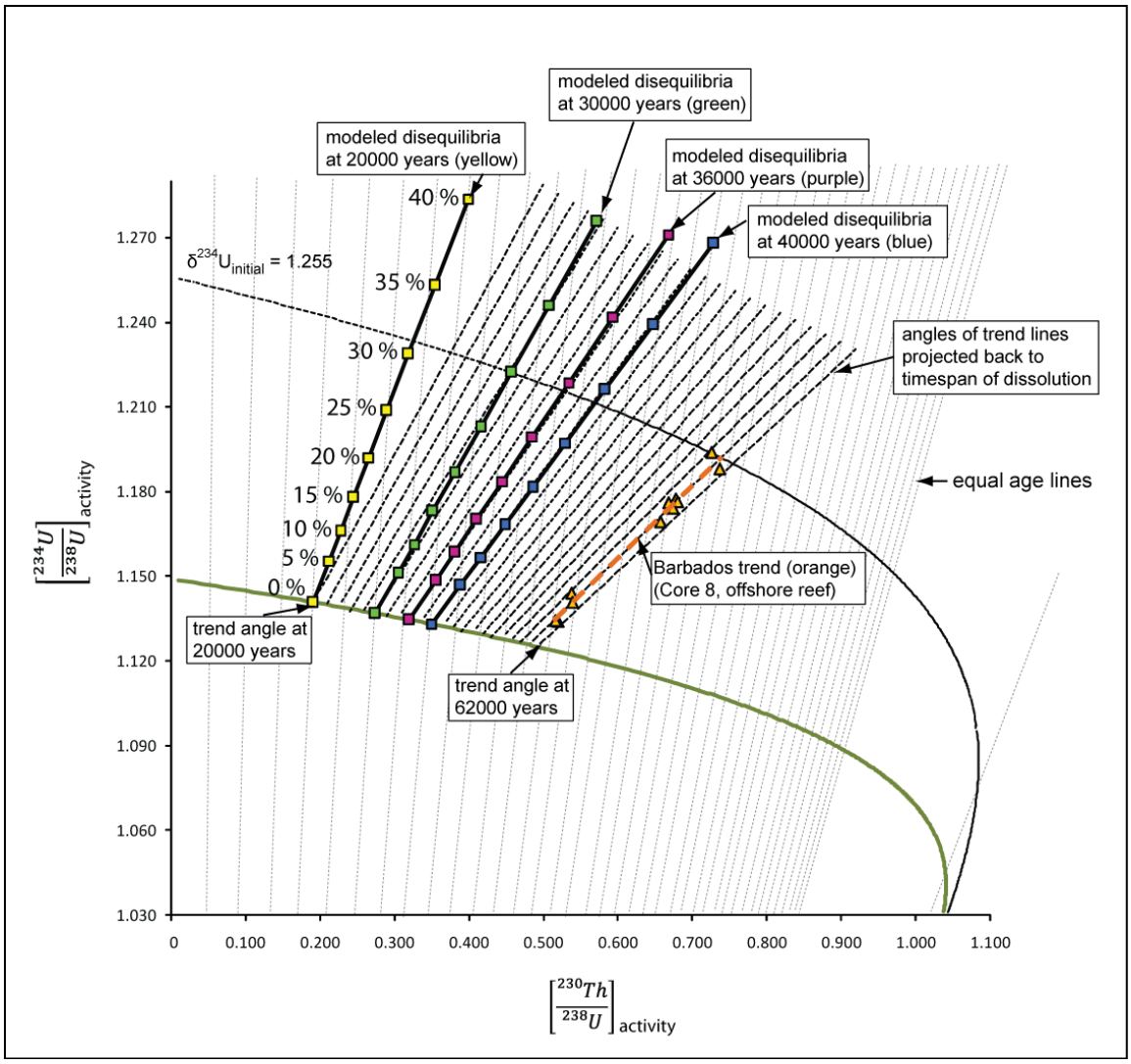
modeled disequilibria at 30000 years (green)
modeled disequilibria at 20000 years (yellow)
modeled disequilibria at 36000 years (purple)
modeled disequilibria at 40000 years (blue)
40 %
35 %
30 %
25 %
20 %
15 %
10 %
5 %
0 %
δ234Uinitial = 1.255
angles of trend lines projected back to timespan of dissolution
equal age lines
Barbados trend (orange) (Core 8, offshore reef)
trend angle at 20000 years
trend angle at 62000 years
1.270
1.240
1.210
1.180
1.150
1.120
1.090
1.060
1.030
0
0.100
0.200
0.300
0.400
0.500
0.600
0.700
0.800
0.900
1.000
1.100
[234U/238U] activity
[230Th/238U] activity

Figure 3-13

Figure 3-13 The angle of the 60,000 year old reef was projected back to the presumed time of freshwater exposure in order to establish the original trend. The 'model trends' each represent a time when the dissolution may have occurred; after 20,000 years (yellow squares), after 30,000 years (green squares), after 36,000 years (purple squares) and after 40,000 years (blue squares). The percentages listed alongside the yellow 20,000 year trend represent the amount of coral mass lost to dissolution. When the coral loses mass, the bulk ratio $^{230}Th/^{238}U$ goes up as uranium is lost, whereas the particle-reactive ^{230}Th is adsorbed onto the extant corals. The core 8 data from the drowned 60,000 year old reef (orange squares) drilled and sampled off shore are plotted in comparison (see Chapter 2, Figure 2-1 for location of reef).

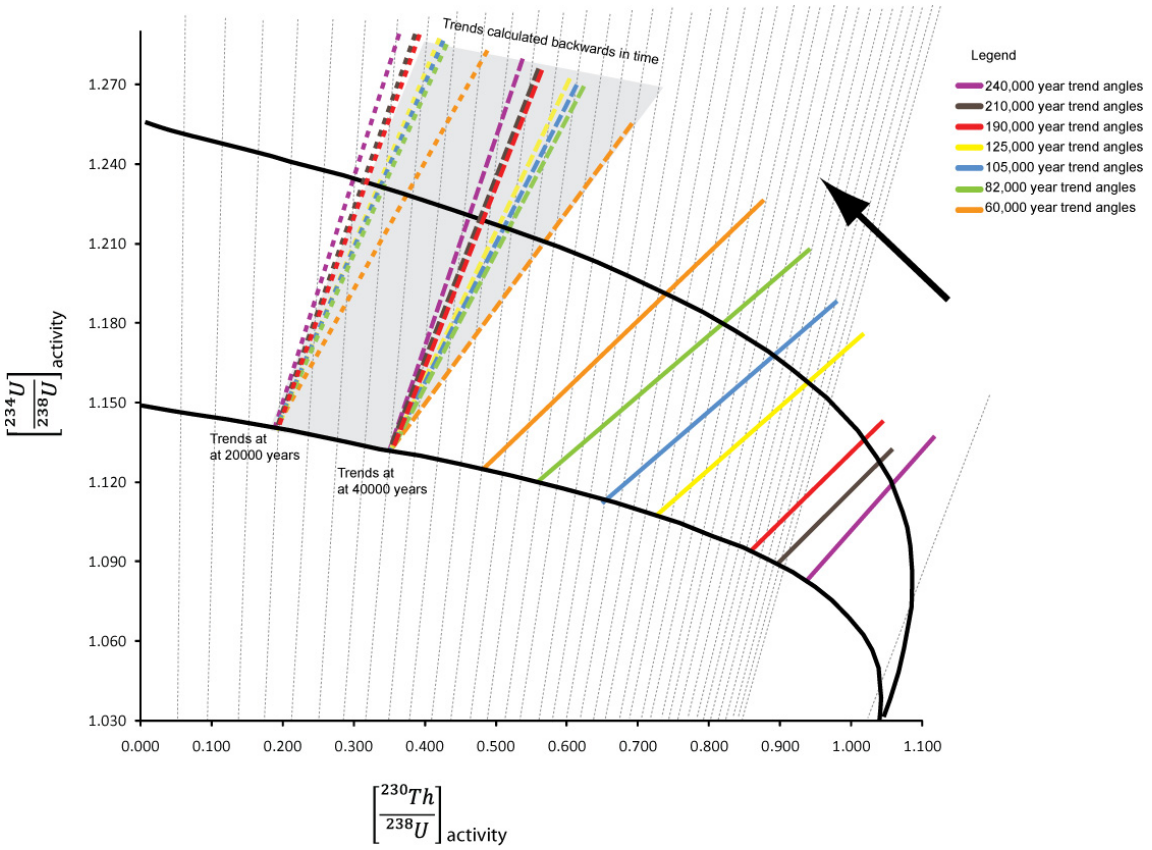
Trends calculated backwards in time
Legend
240,000 year trend angles
210,000 year trend angles
190,000 year trend angles
125,000 year trend angles
105,000 year trend angles
82,000 year trend angles
60,000 year trend angles
Trends at
at 20000 years
Trends at
at 40000 years
1.270
1.240
1.210
1.180
1.150
1.120
1.090
1.060
1.030
0.000
0.100
0.200
0.300
0.400
0.500
0.600
0.700
0.800
0.900
1.000
1.100
$\left[\frac{^{234}U}{^{238}U}\right]_{\text{activity}}$
$\left[\frac{^{230}Th}{^{238}U}\right]_{\text{activity}}$

Figure 3-14

Figure 3-13 Natural $\left[\frac{^{230}Th}{^{238}U}\right]$ versus $\left[\frac{^{234}U}{^{238}U}\right]$ activity trends for regression in the Barbados reefs, as based on the data shown in Figure 3-10 (the trend for each reef is color-coded according to age; see the legend in Figure 3-10). The trends are calculated back in time in order to estimate their original angles at times t=40,000 and t=20,000 years. The calculation follows the reversed closed system evolution, using the modified age equations expressed as trend angles (equation 3.11) and lengths (equation 3.13). Note that the presumed original angles, set at the time of freshwater exposure, are not the same, which indicates that the reefs were exposed at variable intervals after reef growth. Reefs showing similar angles are consequently presumed to have been exposed following similar time intervals.

It should also be noted that all the back-calculated angles of the reefs fall within the 15,000 to 40,000 year window. In other words, the angles of the back-calculated slopes are not larger than the 15,000 year angle $[\varphi]_{15k}$ nor are they smaller than the 40,000 year angle $[\varphi]_{40k}$. This means that for every actual reef trend there is an exactly parallel model trend indicating a 'marine residence time' that lies within the trend's range. Figure 3-15 represents this relationship as a function describing how the model trend angles evolve, as the dissolution progresses; this function is plotted against the functions describing how the angles of the reef trends change. As these trends are calculated back to younger ages, using the age equations (angles [φ] derived as in equations 3.11 and 3.13), the trends will intersect with the model function when they have identical slopes (i. e. same angle [φ]). Therefore, the crossing points between the model curve and the reef trend curve from Figure 3-15 represent the model estimates of the 'marine residence times', as listed in Table 3-3.

In Figure 3-16, the modeled 'marine residence times' are plotted with other climatic data such as marine $\delta^{18}O$ records (Shackleton, 1987; Porter et al., 1989), sea-level curves (Waelbroeck et al., 2002; Cutler et al., 2003) and the 65°N summer insolation curve (Berger, 1978). The modeled 'marine residence times' are relatively accurate in that the estimates predict the approximate time periods or full cycles of several of the Marine Isotope Stages in which the reefs grew. Likewise, relying on the published sea level curves, the 'marine residence times' seem to match closely for all reefs except for some offsets in MIS 5c and 7a2.

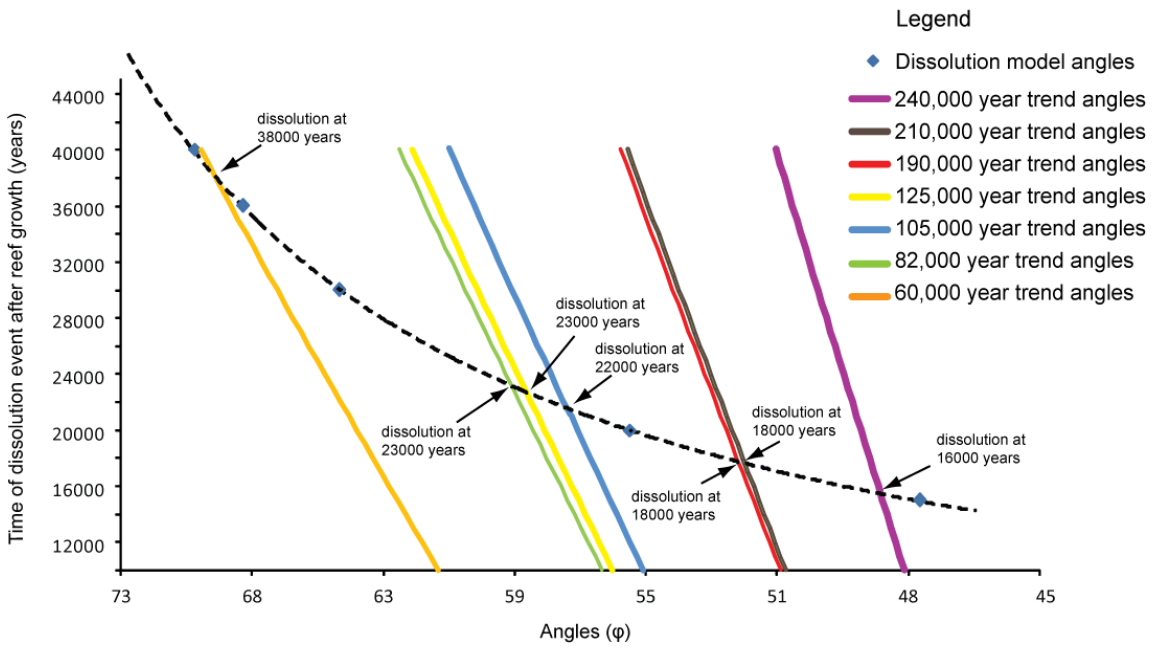
Legend
Dissolution model angles
240,000 year trend angles
210,000 year trend angles
190,000 year trend angles
125,000 year trend angles
105,000 year trend angles
82,000 year trend angles
60,000 year trend angles
Time of dissolution event after reef growth (years)
44000
40000
36000
32000
28000
24000
20000
16000
12000
73
68
63
59
55
51
48
45
Angles (φ)
dissolution at 38000 years
dissolution at 23000 years
dissolution at 22000 years
dissolution at 23000 years
dissolution at 18000 years
dissolution at 18000 years
dissolution at 16000 years

Figure 3-15

Figure 3-15 Functions expressing the angle change for the modeled dissolution trends shown in figure 3-13. The functions for the angle change for seven natural Barbados reef trends are also shown; these are color coded according to the legend in Figure 3-14. At points where the natural angle functions crosses the modeled angle function, the natural trends are parallel to a modeled trend. As shown in figure 3-13 this represents a time interval available for ^{230}Th in-growth before the freshwater disturbed the isotopic equilibrium. The results are shown in Table 3-3.

Table 3-3

Reef locality	Approx. reef age (years)	Approx. 'marine residence time' (years)	Marine Isotope Stage (MIS)
RGF-8 (offshore reef)	60,000	36,000-38,000	3
NU (Thompson et al.,2003)	82,000	22,000-23,000	5a
SCP (Salt Cave Point)	105,000	21,000-22,000	5c
AEC (Chancery Lane)	125,000	22,000-23,000	5e
NU (Thompson et al., 2003)	190,000	17,000-18,000	6.1
LKS (Regency Park)	210,000	17,000-18,000	7a.2
NU (Thompson et al., 2003)	240,000	15,000-16,000	7c

Table 3-3 A list of the reef ages, the calculated cross points of natural and modeled angle functions as shown in Figure 3-15 and also the appropriate Marine Isotope Stages. The cross points express an approximate 'marine residence time' before the reefs where exposed to freshwater.

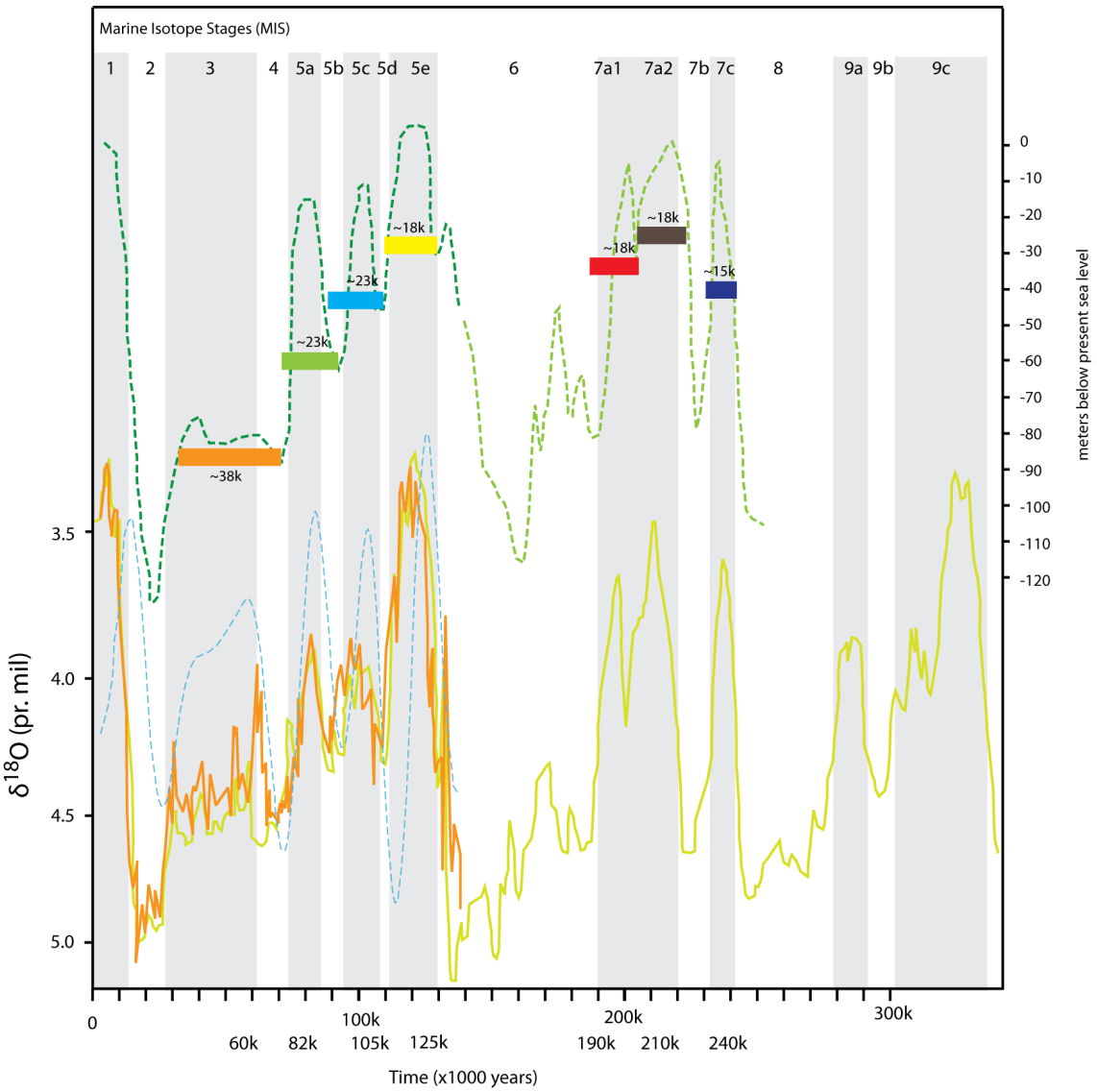
Marine Isotope Stages (MIS)
1
2
3
4
5a
5b
5c
5d
5e
6
7a1
7a2
7b
7c
8
9a
9b
9c
~38k
~23k
~23k
~18k
~18k
~18k
~15k
δ18O (pr. mil)
3.5
4.0
4.5
5.0
0
-10
-20
-30
-40
-50
-60
-70
-80
-90
-100
-110
-120
meters below present sea level
0
60k
82k
100k
105k
125k
190k
200k
210k
240k
300k
Time (x1000 years)

Figure 3-16

Figure 3-16 Estimated 'marine residence times' for seven Barbados reefs before freshwater exposure. The ages of the reefs are plotted below the ordinate axis. The 'marine residence times' from Table 3-3 are plotted with color codes in accordance with the legend provided in Figure 3-15. The dark green dashed line represents sea level estimates from Cutler et al. (2003). The light green dashed line corresponds to the sea level as derived from marine $\delta^{18}O$ (Waelbroeck et al., 2002). The solid orange line indicates marine $\delta^{18}O$, as measured by Porter et al. (1989), while the light curry solid line indicates marine $\delta^{18}O$, as measured by Shackleton (1987). The light blue line is the 65°N summer insolation curve (from Berger 1978).

CONCLUSIONS

The data trends in the $\left[\frac{^{230}\text{Th}}{^{238}\text{U}}\right]$ versus $\left[\frac{^{234}\text{U}}{^{238}\text{U}}\right]$ activity diagrams for seven Barbadian paleoreefs have been used to model 'marine residence times' for individual reefs, spanning from the times of MIS 3 to 7c. The modeled marine residence times are calculated from ^{230}Th in-growth and based on the angles of the trends, modeled in accordance with the effects of bulk mass loss during dissolution. After initial subaerial exposure, when freshwater percolated through the reefs and partially dissolved them, the resident ^{230}Th stayed in the coral structure, while ^{238}U and ^{234}U were removed with the exception of some ^{234}U, which was trapped in a similar fashion to what happened to the ^{230}Th; this trapping occurred in systematic proportions to the ^{230}Th trapping, so as to produce the unique trends observed today. From these trends, we have derived modified age equations, expressing the geometries that we have used to predict the trends' evolution through time. These equations have allowed us to model the marine residence times as the periods during which the reefs where fully submerged in the marine environment, before being exposed either due to isostatic uplift, regressing sea levels, or both. The modeling shows that the 'dissolution-cum-adsorption' model for the Barbadian reefs provides a realistic description of the diagenetic effects in the uranium series which occurred in the Barbadian paleoreefs during the first freshwater exposure, when the dissolution potential was at its highest.

CHAPTER 4:
OPTIMAL SCIENTIFIC DRILL POD PLACEMENTS ON THE BARBADOS' SHALLOWS

A STUDY USING SPATIAL ANALYSIS AND GEOGRAPHIC INFORMATION SCIENCE (GISc) TO IDENTIFY POTENTIAL OFFSHORE DRILLING TARGETS FOR SCIENTIFIC SAMPLING OF DROWNED PALEOREEFS OFF THE COAST OF BARBADOS.

By:

Jacob L. Mey[1, 2]

1. Graduate Center, City University of New York, New York, NY 10016, USA

2. Lamont Doherty Earth Observatory of Columbia University, Palisades, New York 10964, USA.

ABSTRACT:

Barbadian corals have long been a target for scientific sampling of both elevated and drowned paleoreefs. Such studies of the coral fossils have led to a greater understanding of the rate and magnitude of sea level change and how these changes tie into past global climate change and the waxing and waning of the ice ages throughout the last several hundred thousand years. Building on experience of the last several decades, researchers have discovered that the best samples to conduct such analysis on are those from paleoreefs that have not previously been exposed to fresh water, but remained preserved in the marine environment. These samples are available from reefs that grew during sea level rises as the northern hemisphere ice volume decreased and global temperatures rose. Depending on the time of growth in the period since the last glacial maximum, these drowned reefs are now submerged 30-120 meters below the present sea level.

During a drilling cruise of the R/V Ranger (Cruise 88-13) in 1988, the vessel was multi-anchored off the coast of Barbados and several drowned reefs were successfully penetrated and sampled. During the last two decades, attempts to repeat this success have been hampered by technical problems and unfavorable weather conditions with no or miniscule core recovery. Modern drill ships are capable of maneuvering a heavy 8-ton drill pod (Temporary Guide Cage –TGC) and lower it to rest on the sea bottom, acting as a guide and anchor for its massive riser pipe and in this way reduce the chance of the riser pipe breaking free of the bottom. The device will, at the same time, allow for more slack on the drill pipe ,

thus, less tight positioning of the mother-ship without hampering the drill operations. To increase the chances of successful drilling, the drill pod footprint cannot vary in slope of more than 10-15 degrees in any direction of its four corners.

Many of the best drilling sites from a scientific point of view are located on the ridges of ancient reef tracts, but unfortunately, these areas also show the most rugged variability in seafloor topography. High resolution bathymetric maps and topographic maps have been used to identify likely successful targets for drilling. In addition, three-dimensional GIS based spatial analysis techniques were employed to ensure successful placement of the drill pod on the sea bottom. Conducting this kind of analyses prior to drilling will reduce cost, save time, and enhance the chances of successful retrieval of high quality scientific samples.

INTRODUCTION

The timing of past sea level beyond 50,000 years is mainly based on the analysis of corals, using ^{230}Th-^{234}U-^{238}U and ^{231}Pa-^{235}U series for accurate age determinations (see Mortlock et al., 2005 for detailed description of techniques). Corals are used to calibrate the ^{14}C scale (Fairbanks et al., 2005). In addition, they are employed to accurately determine ages for reef corals as indicators for past sea level in the last 50,000 years. The most detailed sea level record constructed from such data comes from Barbados (Figure 4-1) and nearby Caribbean islands. The relatively simple relationship between coral distribution and depth in the Caribbean (as compared to the Pacific), coupled with the dominance of the reef crest species *Acropora palmata* in the shallowest five meters, provides a reliable sea level indicator (Mesolella, 1970; Fairbanks, 1989; Fairbanks et al., 2005 and references there). For the corals to be reliable proxies for past sea level, their original unchanged isotopic fingerprint, which allows us to determine their ages, has to be intact. Once the corals are exposed to freshwater, the U-Th and U-Pa isotopes used in age determination are brought out of equilibrium and yield wrong results. Therefore, the most promising coring targets are the drowned coral reefs that have grown in the time elapsed since the last glacial low-stand and during intervals of rising sea level and thus have not been exposed to freshwater. These drowned reefs typically make up prominent submerged ridges off many tropical islands that can be mapped accurately offshore. These ridges may have formed when sea

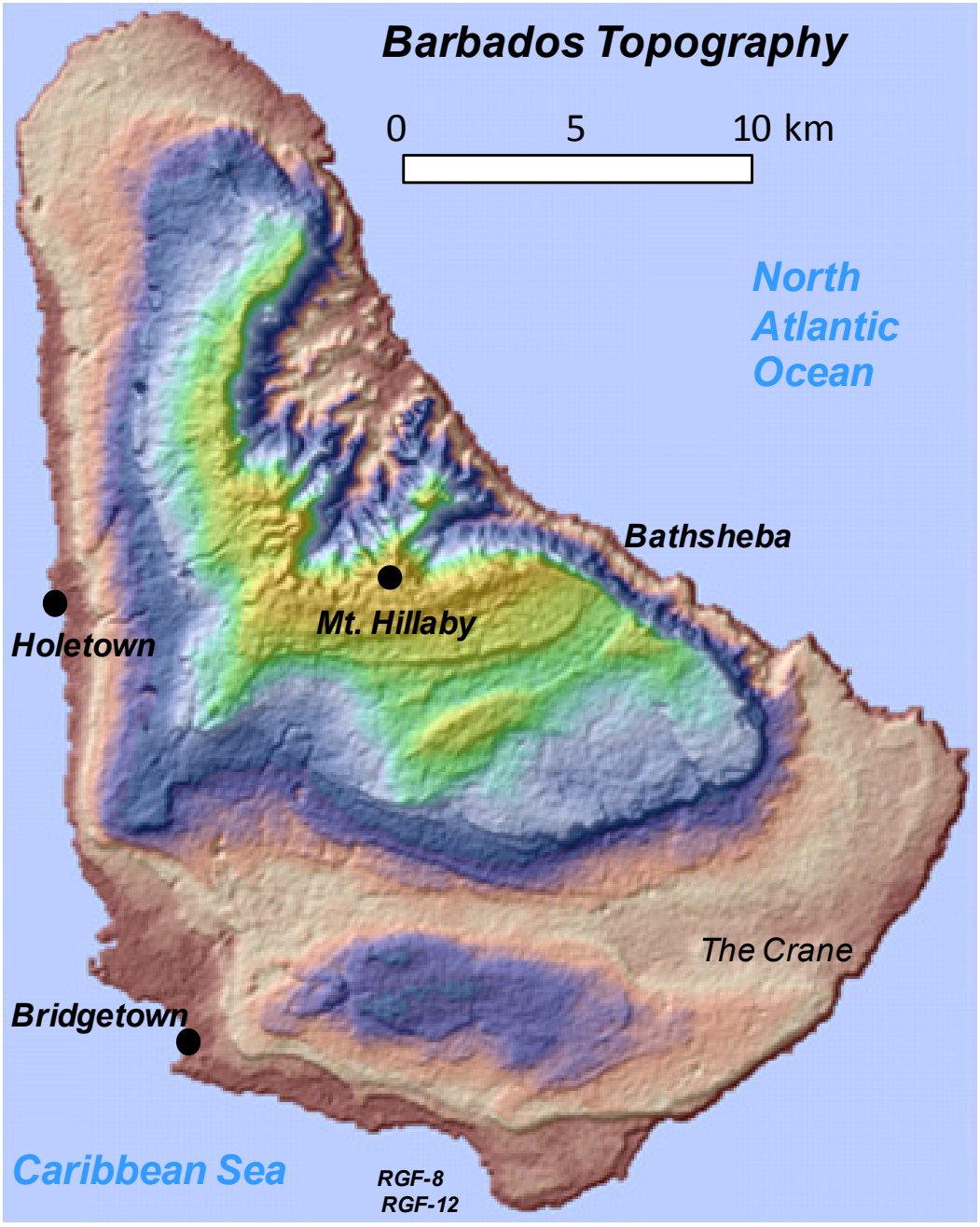
Barbados Topography
0
5
10 km
North
Atlantic
Ocean
Bathsheba
Mt. Hillaby
Holetown
The Crane
Bridgetown
Caribbean Sea
RGF-8
RGF-12

Figure 4-1

Figure 4-1 A digital elevation model (DEM) made in ArcGIS from raw data acquired from the 90-meter resolution Shuttle Radar Topography Mission (SRTM) (1998). Data source: NASA. (See the section for Data sources for more information). Color scale height dependent from 0 meters (brown) to 342 meters (orange).

levels rose relatively fast and only species like *Acropora palmata* and *Montastrea annularis* were able to accommodate the lateral expansion of the reef habitat. Several drowned reefs around Barbados indicate that on occasion, even these species were overcome by a fast rising sea level and thereby drowned. Using multi-beam echo sounder surveys and side-scan sonar images, we mapped and attempted to core many drowned reefs immediately off the southern coast of Barbados (see Figure 4-1, Sample sites RGF-8 and RGF-12). Several of these drowned Barbados reefs were cored more than a hundred meters below the sea floor in over 100 meters water depth during the 1988 R/V Ranger Cruise 88-13 (Figure 4-2). Later attempts have only been partially successful, although on a recent cruise with the R/V Knorr in April-May, 2007, the success of the 1988 R/V Ranger cruise coring depth and sample return was not only matched, but even surpassed by stunning 3-D mapping of these drowned reefs around Barbados (Mey et al., *in prep.*).

The successes obtained during both the above-mentioned cruises for offshore coring in sea conditions with up to 2-meter swells and in water depths up to 100 meters were to a large extent due to the modification of a commercial ACKER "Bushmaster" hydraulic wire-line coring rig and to the design of a hydraulic heave compensator for the 8000 lbs heavy and protective riser pipe. The coring rig is capable of coring more than 1000 meters below the sea floor, although typically only coring 100 meters below the sea floor is needed for retrieving samples for studies of sea level.

Picture A

Picture B

Figure 4-2

Figure 4-2 Research vessel R/V Ranger (Picture A). The vessel deck during the 1988 Cruise 88-13 to Barbados (Fairbanks, 1988). The heavy riser pipe (aka API pipe) is stacked on the right side (Picture B).

Why drill for samples offshore? - Understanding the freshwater effect

In order to exclude coral samples that yield wrong ages, a better understanding is required of the uranium-series diagenesis and where it occurs. This is especially the case for processes leading to excess $^{234}U/^{238}U$ (high $\delta^{238}U_{initial}$) in those corals that were exposed to the vadose and the phreatic freshwater environments. Disequilibrium in the uranium-series is expected in corals exposed to fresh water, but unfortunately '*a priori'* screening methods are generally insufficient to reject samples prior to time consuming analyses for precise U-Th age determination. As a result, a vast number of uranium series dates reported in the literature are 'open system' and numerous authors subscribe to various correction models (Bender et al., 1979; Gallup et al., 1994; Thompson et al., 2003; Villemant and Feuillet 2003; and Scholz et al., 2004). The majority of these studies assume or model continuous or episodic addition of ^{234}U and/or ^{230}Th over time, in that they rely on the low solubility of ^{230}Th and/or ^{234}Th. Several recent studies emphasize progressive production of ^{234}U via alpha-recoil (Thompson et al., 2003; Villemant and Feuillet 2003). However, the assumptions underlying these models may lead to over-parameterization, and according to Scholz et al., 2004, could be idiosyncratic to host sample locations. In general, they may not be applicable to young samples with high $\delta^{234}U_{initial}$. Some studies have already resorted to model corrections for ages based on open-system calculations. Such corrections have resulted in critical conclusions about sea level change (e. g. Scholz et al., 2004, Thompson and Goldstein, 2005).

A characteristic of the phenomenon under consideration is the general correlation, among samples within a reef unit, between the $^{234}U/^{238}U$ activity ratio and the $^{230}Th/^{238}U$ activity ratio. As to the samples, the largest collection of coral dates comes from the Barbadian reefs. In a previous study (Mey et al., 2005), samples of a 60,000 year old reef that were drilled and collected off-shore showed, upon dating, that the largest activity ratio offsets appear in these relatively young Barbadian samples; this finding is just the opposite of what is expected according to most diagenesis models. On the other hand, our measurements are consistent with what Scholz et al. (2004) observed in their samples from the Red Sea that high activity ratios occur even in young Holocene samples.

The greatest addition of ^{234}U, ^{230}Th, and ^{231}Pa in the Barbados samples occurred during the early stages of reef alteration by fresh water. In this case, we are dealing with the early Marine Isotope State 3 (MIS3) time period, when ^{234}U, ^{230}Th, and ^{231}Pa are added to corals in similar proportions, but varying amounts (Mey et al., *in prep.*; see further chapter 2, above). The bulk of reef sands and rubble is aragonite, which has a potential to release uranium series isotopes during transformation to calcite relatively soon after exposure to fresh water.

In a study of alteration rates of Barbados sands, Winblad (1969) observed that reef sands are inverted to calcite within 100,000 years. Upon completion of this process, reef corals are generally in a state of partial dissolution. We propose (cf. chapter 2) that the correlation between the $^{234}U/^{238}U$ and $^{230}Th/^{238}U$ activity ratios seen in coral samples from the same reef or within individual samples is <u>set early</u>

during fresh water exposure. This is when the "diagenetic potential" of reef sand and rubble is highest, since the unstable aragonite sands are rapidly inverted to calcite. Subsequently, the progressive dissolution of corals reduced the adsorbed ^{234}U and ^{230}Th, while preserving the initial trend in the $^{234}U/^{238}U$ and $^{230}Th/^{238}U$ ratios and, in effect, conveying back information on the 'true' age. We propose (Mey et al., *in prep*.) a new model in which ^{234}U is preferentially leached from dissolving aragonite sands and subsequently adsorbed onto coral skeletons. Dissolving sands likewise released ^{230}Th and ^{231}Pa, which also adsorbed onto nearby corals, as vadose groundwater percolated through the emergent reef. The open-system $^{234}U/^{238}U$ and $^{230}Th/^{238}U$ trend decayed through time, maintaining their activity *proportions* as evidenced by the trend lines.

The purpose of trying to understand these mechanisms is to be able to recognize reef profiles in which these diagenetic phenomena are prevalent. The drowned coral reefs off the coast of Barbados are excellent targets, because many of these have not been exposed to a fresh water influx. Our practical approach is to use 3-D spatial analysis based on high resolution multi-beam bathymetry and side-scan sonar data as an effective means of identifying drowned reefs. The special analysis will also aid the search for small spots in the otherwise rugged surrounding areas on the seafloor that are suitable for placing an 8-ton drill pod.

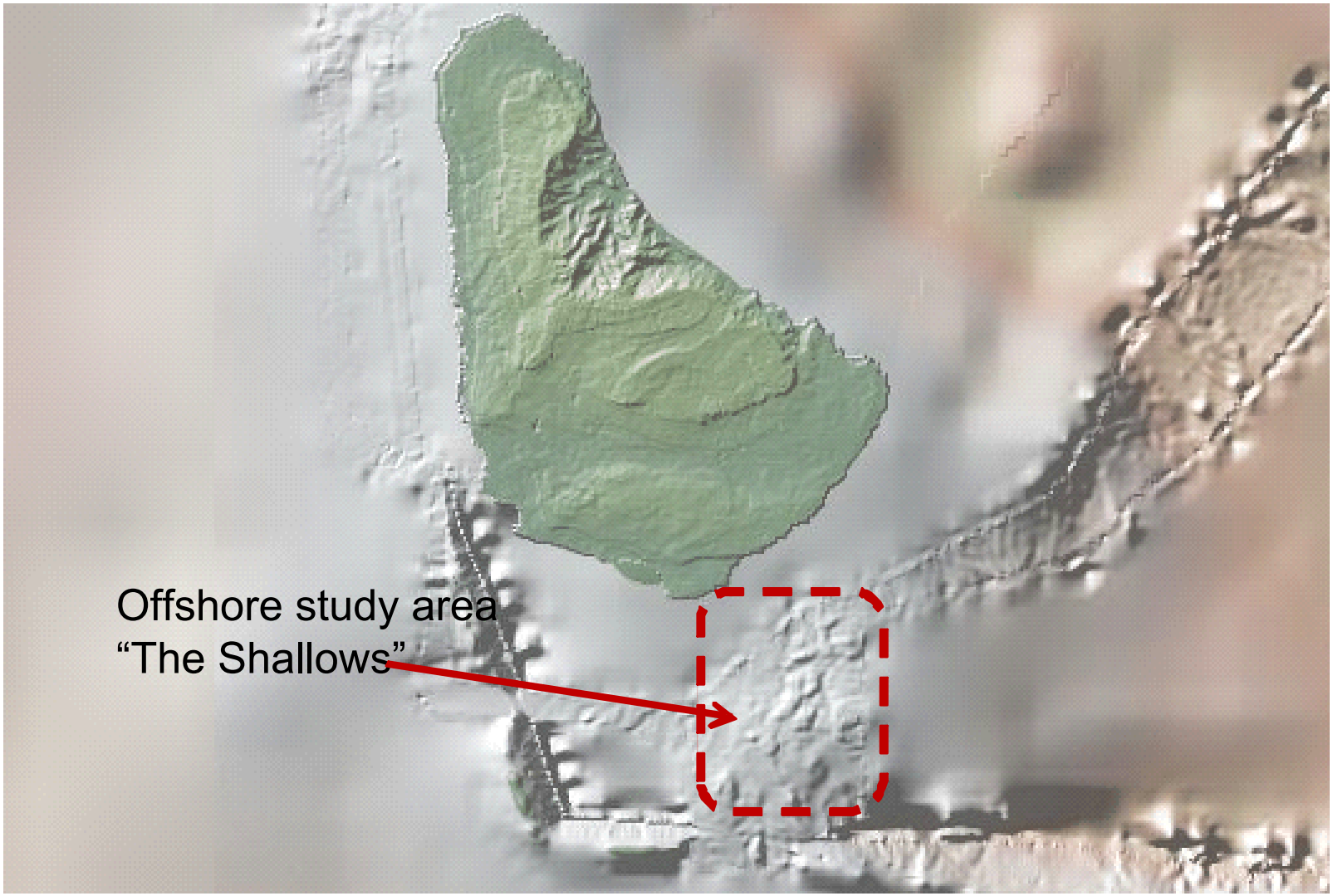

Figure 4-3

Figure 4-3 Study area showing topographical features (90 meters per pixel resolution) of the Island of Barbados and the surrounding sea bottom at various low (2 kilometers per pixel) and medium (200 meters per pixel) resolutions. The Image contains several artifacts which are not real (i. e. unedited bad bathymetry data), especially in the SW corner of the map. These artifacts are embedded in the data from the source and must be manually removed. See text for further information on data used to make this image. Map source: GeoMapApp (2006). For scale: Barbados is 24 km across at the widest part of the Island. See also Figure 4-4 for more geographical information.

STUDY AREA

The island of Barbados is located in the eastern Caribbean Sea, approx. 150 km east of the Lesser Antilles. The island extends from latitude 13º02'N to 13º10'N and from longitude 59º25'W to 59º39'W. The island stretches 32 km from north to south and 24 km from west to east with a total coast-line length of approx. 95 km and a total area of 430-km^2 (Figure 4-1). Mount Hillaby is the highest elevation on Barbados, rising 342 meters above sea level (Figure 4-1). The new potential targets for off shore drilling are located further off shore than previous sites to avoid the older component of eroded reefs. This new site is located about 5 miles south of the island in an area named "The Shallows", an area covering from latitude 12º56'N to 13º02'N and longitude 59º26'W to 59º32'W (Figure 4-3). Multi-beam bathymetric survey track and coordinates are shown in Figure 4-4.

METHODS AND DATA SOURCES

Identification of potential drilling targets through spatial analysis using GISc.

The potential drilling targets are identified through several spatial analyses, using Geographic Information Science (GISc) methods. A spatial multivariate regression analysis was conducted in ArcGIS. The set of criteria used is defined below. The first criterion identifies areas, which satisfies a 'maximum slope criterion' of less than 10-15 degrees from horizontal in any direction of a 5 by 5

meter wide footprint. This type of analysis was also conducted on larger foot print areas (e. g. 15 meters by 15 meters and 20 meters by 20 meters) to allow for errors is GPS positioning. The second criterion is based on whether the sub-bottom features are identifiable as paleoreefs or not. This identification is done by a qualitative visual inspection of the morphology of possible reef structures. The results were then lined up with side scan sonar images, before being compared to known reef structures. Because of the qualitative nature of this visual inspection, it is accorded less weight in the quantitative regression model. The third criterion is based on sea bottom depth (depth below the seafloor). This criterion has to do with whether the drill targets (i.e. the paleoreefs) are buried under thick or thin layers of overburden in the sea floor, or if the reefs are eroded, thereby exposing deeper parts of the reef as opposed to the crest. When identified, the targets are then compared to stratigraphic information from drill cores of other drowned reefs in order to estimate the plausible location of the reef crest. In the case of suspected overburden, we will also perform an analysis of how deep one needs to drill before penetrating the favorable strata in the buried reefs. Adding to our work the previous sea level studies in Barbados (Bender et al., 1979; Fairbanks, 1989; Gallup et al., 1994; Peltier and Fairbanks, 2006), and using our knowledge of tectonic uplift rate (see Bender et al., 1979; Speed et al., 2004 and references therein), we are able to construct a model predicting the depth of the sea floor the desired paleoreef(s) may be located. This kind of analysis was performed by Mesolella et al. (1970) for the Barbados reefs above sea level, but not for the drowned reefs offshore. The latter criterion, known as

'isostasy', is the least precise of the three; consequently, it was weighted with larger errors in the regression analysis. The final multivariate regression model is constrained by the final resolution of the digital elevation model of the sea floor (bathymetric map), which means that the final resolution also constrains the sizes of features resolved on the sea bottom.

Data acquisition and processing: Low resolution model data.

The low resolution (119 meters per pixel) processed data (see Figure 4-3) are readily downloaded from the GeoAppMap special "geo-tiff" format (GeoMapApp, 2006) and imported into ArcGis. The advantage of this format is the full attribute table, containing pixel depths for any region of interest for which such data exist. The land based data from the 1998 Shuttle Radar Topography Mission (http://www2.jpl.nasa.gov/srtm/; Shuttle Radar Topography Mission, 1998) has a slightly higher resolution (90 meters per pixel). The digital elevation model data are available from USGS (US Geological Survey) http://seamless.usgs.gov/Website/Seamless/viewer.php in USGS-DEM formats (Digital Elevation Model) for any area of interest. The low resolution data were used to determine if the spatial analyses would be suitable for the preliminary target zones. The advantage of using smaller data sets in the preliminary analysis is that they allow for a much faster processing time. The data were imported directly as raw DEM raster data such that the analysis protocols in ArcGis could be evaluated fairly quickly.

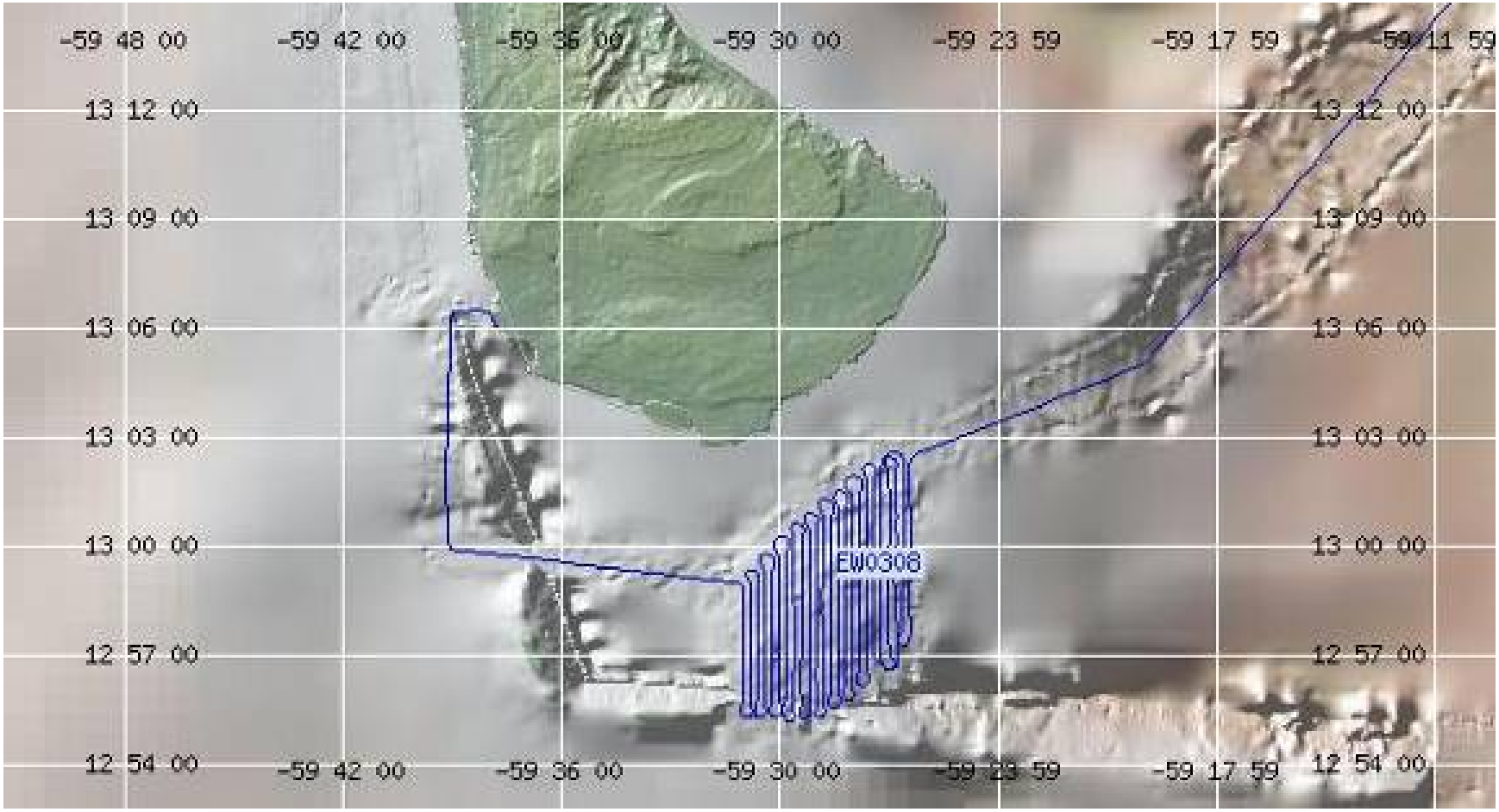
-59 48 00
-59 42 00
-59 36 00
-59 30 00
-59 23 59
-59 17 59
-59 11 59
13 12 00
13 09 00
13 06 00
13 03 00
13 00 00
12 57 00
12 54 00
EW0308

Figure 4-4

Figure 4-4 Showing location of Multi beam bathymetric tracks acquired by the research vessel R/V Ewing on October 18, 2003. Data are from http://www.marine-geo.org/mapserv

One minute center beam data of the study area are listed in Appendix 4-3.

High resolution model data

The high resolution (less than 5 meters per pixel) multi beam bathymetric raw data were acquired by the research vessel R/V Ewing during October 2003 (Cruise leg EW0308). The data are now in the public domain and available in unprocessed form through the Lamont Doherty Earth Observatory (Columbia University) data repository under the subtopic http://www.marinegeo.org/link/entry.php?id=EW0308. The continuous bathymetry data (see Figure 4-4) were acquired with a Krupp Atlas Hydrosweep−DS2 sonar. The 25-track (Figure 4-4) data was collected in 2355 files with total data set size of 964.7 MB. The file id's are: hb (center beam), hs (swath). The hydro sweep (hs) full swath data were continuously logged for the whole cruise and the center beam data was extracted and processed separately. The center beam logging frequency is dependent on water depth, because of the varying travel time of ping returns through the water column as the seafloor changes. The full swath data from transect cruises are not routinely processed (as in the case of the data set employed), therefore we employed the MB−System software available at: http://www.ldeo.columbia.edu/res/pi/MBSystem/html/mbsystem_how_to_get.html The MB-System software runs on a UNIX or LINUX platform and considerable time is used processing and combining the raw data into a complete raster file that can be read by ArcGIS. The final raster file was very large, therefore it was processed on a high-end custom built 64-bit PC-system with 8 Giga-bytes of memory and 1.5 Tera-bytes of storage.

Meta data and bathymetry data stream recording

The R/V Maurice Ewing data logging systems run on a Sparc Ultra Enterprise Server with 48 serial ports. Three 16−port Digi International SCSI Terminal Servers are attached to this system. Generally, all data logged by the Ewing Data Acquisition System (DAS) are time stamped with the CPU time of the server, and broadcast to the Ewing network by the use of UDP packet broadcasts. The CPU time of the server is synchronized once every half hour to a Datum UTC GPS time clock. GPS times are also time−tagged with CPU time, while the time of the GPS position is derived from the GPS fix itself. (More information about the onboard systems is available online (see list of data sources); it contains a full report with tables describing the data instruments which performed logging during this cruise. The tables associated with the instruments contain information on logging periods and data losses for those instruments as well. For this cruise (leg EW0308) there was no loss of data for the study area. For further details on data acquisition and cruise details refer to the technical report "EW0308" available online at http://www.marine-geo.org/link/ado_swath.php?id=EW0308).

Data processing facilities

All the equipment and software necessary to perform the type of analysis suggested in this study was available at Lamont Doherty Earth Observatory. This includes the software (ArcGIS, FledermausPro, Excel, MatLab, and MB-System),

the hardware (powerful PC's and Silicon Graphics (UNIX) machines) in addition to external devices such as large format printers used to produce the final survey maps brought onboard to aid the drilling operation and drill-pod positioning.

Main data sources

The following data sources were used in the study:

- 90-meter resolution radar data of the Barbados surface from the1998-Shuttle Radar Topography Mission (SRTM) (http://www2.jpl.nasa.gov/srtm/).
- 119 meter DEM (digital elevation model) data of Barbados available from USGS (US Geological Survey) http://seamless.usgs.gov/Website/Seamless/viewer.php or from http://www.marine-geo.org/mapserv via GeoMapApp (2006)
- High resolution (less than 5 meter) raw data of bathymetric survey of target area available from the data repository of Lamont Doherty Earth Observatory, Columbia University via http://www.marine-geo.org/link/ado_swath.php?id=EW0308 while the UNIX software "MB-System" needed to compile the raw data is available for free at http://www.ldeo.columbia.edu/res/pi/MB-System/html/mbsystem_how_to_get.html
- Among the data sources that were desired but not found affordable, were digital topographic maps of Barbados and digital bathymetric maps of the waters around Barbados. Some data were scanned from existing printed maps, using the scanning and rendering facilities in the GIS lab of the

Department of Biodiversity, American Museum of Natural History, New York. High resolution (1-meter per pixel) lidar data, while likewise desirable for this type of survey, were not available at this time.

Project work-flow chart and projected budget

The work flow and a detailed list of all the project subcategories are listed in the work flow chart (Figure 4-5). This chart summarizes the structure of the various disciplines needed to carry out this project optimally. The work schedule is summarized below:

Month 1	Download and organize all 2355 high resolution data streams.
Months 1-3	Compile data in MB-system, make master-raster file and several sub-raster files of the off-shore study area.
Months 3-4	Perform spatial analysis at various resolutions to identify drilling targets. Perform multivariate regression analysis to assess likely target success based on spatial and visual characteristics using ArcGIS.
Month 5-6	Inspection and follow-up survey of drill targets
Month 6	Select positive drill targets and plan drilling operation.

All projected cost and expenses are listed in the budget (Table 4-1)

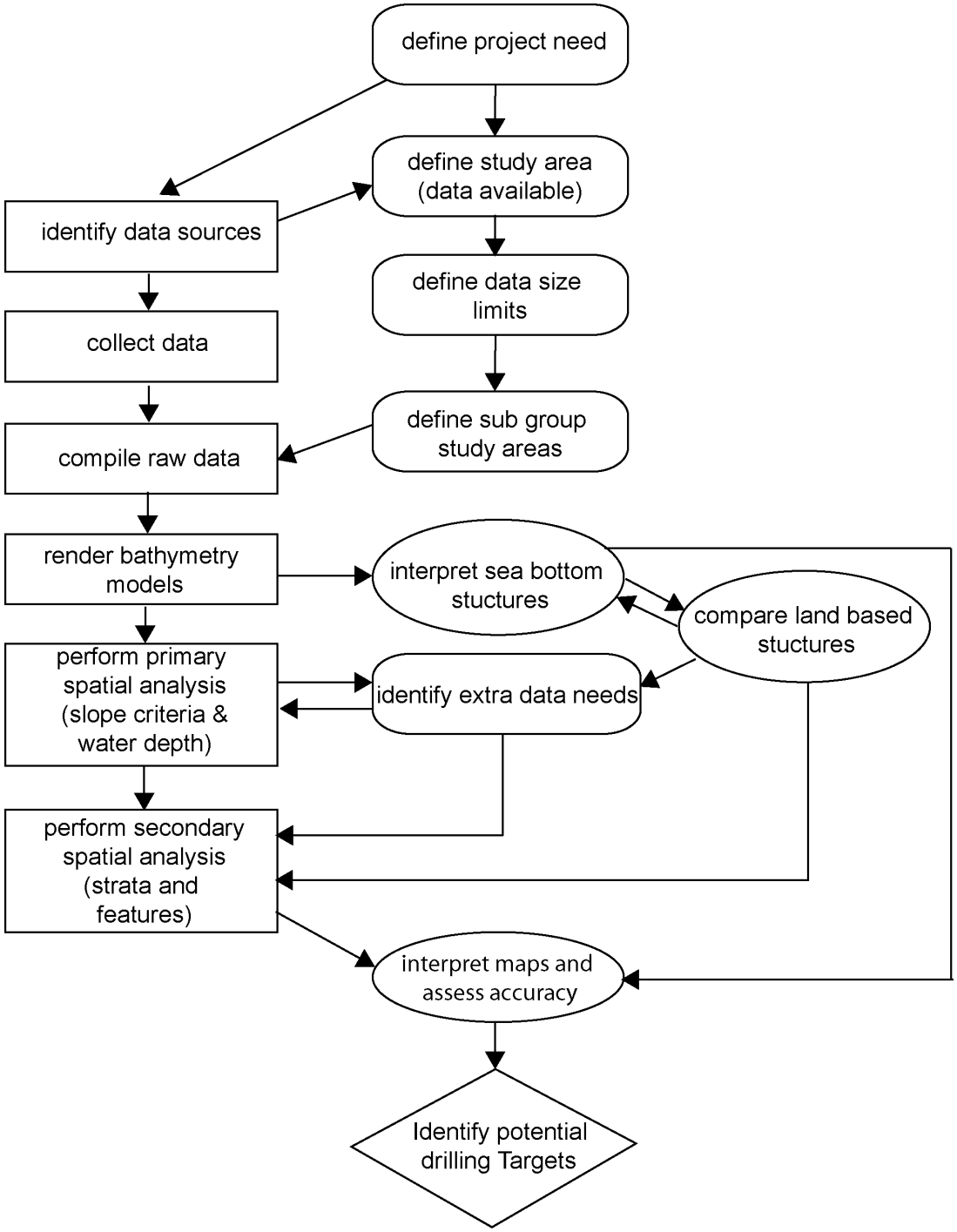
define project need
define study area (data available)
identify data sources
define data size limits
collect data
define sub group study areas
compile raw data
render bathymetry models
interpret sea bottom stuctures
compare land based stuctures
perform primary spatial analysis (slope criteria & water depth)
identify extra data needs
perform secondary spatial analysis (strata and features)
interpret maps and assess accuracy
Identify potential drilling Targets

Figure 4-5

Figure 4-5 Work flow chart of the project and the sub-disciplines involved.

Table 4-1 Proposed budget for Barbados mapping project

Budget:	
Salaries:	
Lamont faculty (15 hrs)	$ 500.00
Graduate student salary	
(10 hrs pr week Jan-May)	$2400.00
Undergraduate field assistant (2 weeks)	$1200.00
Consumables:	
Maps, printing, laminating etc	$ 500.00
Travel (Barbados, 2 weeks)	
Field work expenses: (boat rentals etc)	$2000.00
Transportation	$1500.00
Car rental	$ 350.00
Lodgings (McGill Research Facility)	
& Meals	$1100.00
Total:	$9950.00
Overhead:	
58% of salaries:	$2378.00
Total requested:	$12328.00

RESULTS

Data processing

The list of data files used for the final Bathymetric maps is included in Appendix 4-1. All bathymetric data have been processed in MB-System; an example of the data processing parameters is shown in Appendix 4-2. The 'gridding' of data sets for particular areas was done by executing PERL-scripts, which use the MB-System data formats and processes and output grid-formats used and plotted in Generic Mapping Tools (GMT) in the same process. An example of such a PERL-script is included in Appendix 4-3. An 'mbinfo' command output, listing the types of information available in the mb183 file format, is included in Appendix 4-4.

Bathymetry data collection on board a ship is subject to the ship's movements in three dimensions while receiving ping returns from a stationary sea floor. To correct the effects of these movements during the processing of multi-beam swath sonar data, the ship's three gyroscopes help to compensate for undesired variations in the data. In particular, these variations include, but are not limited to, real time variables such as speed, GPS-offset, roll, pitch, heave, tilt, yaw, and tide. These variations, furthermore, need correction parameters that are not dependent on real time collection, such as salinity, temperature, sound velocity profile, water depth, grazing angles, etc. All of these corrections are gathered in a set of parameter files (see the example in Appendix 4-2), which are then

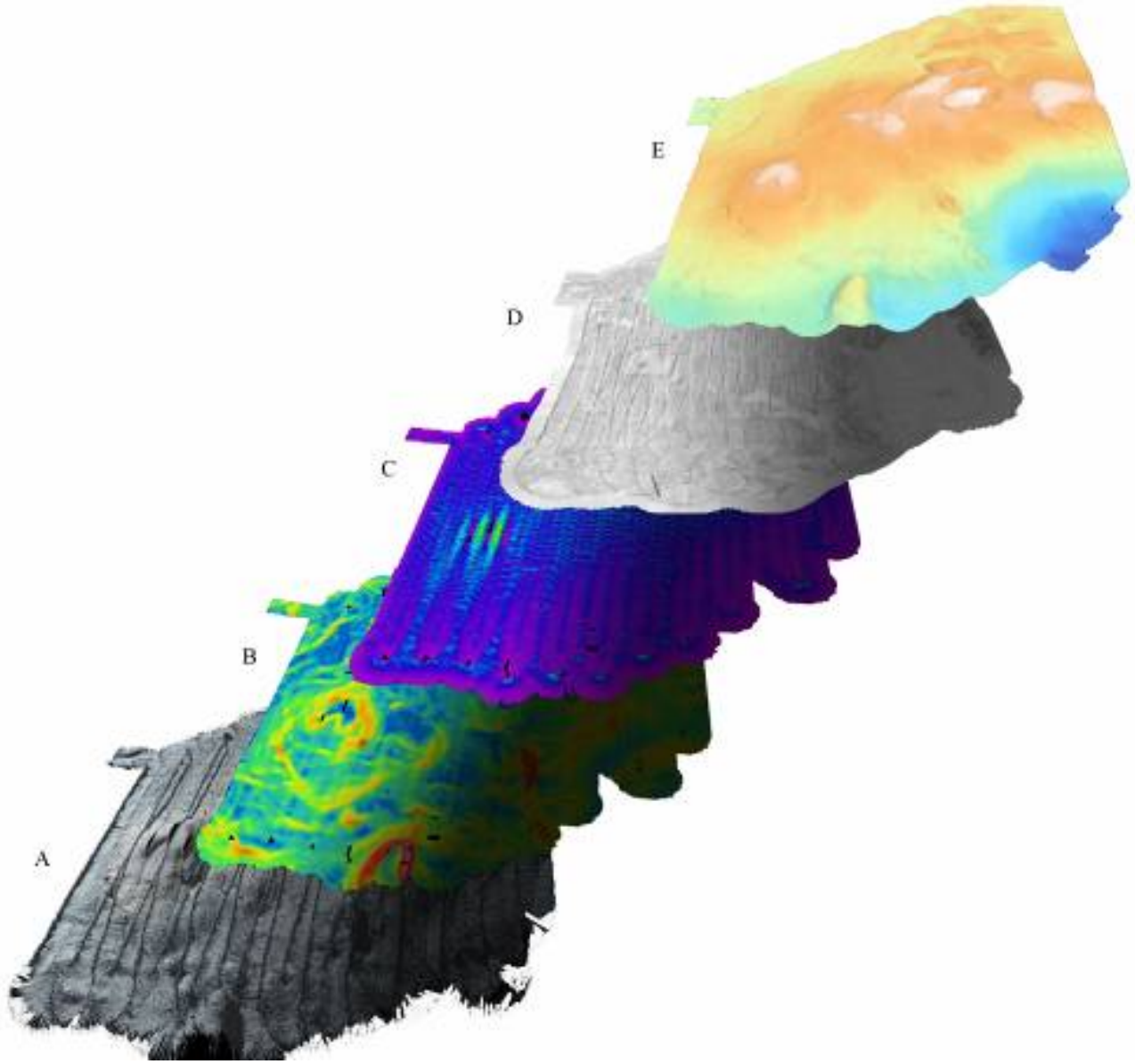

Figure 4-6

Figure 4-6 Data stack illustrating various aspects of the data, their nature, and their processing in the MB-System. The bathymetric data are projected in a 3D space viewed from south to north.

processed for each data file using the MB-System command ‘mbprocess’. The five data stacks illustrated in Figure 4-6 represent from bottom to top:

A. Raw unprocessed data.

B. Standard deviation of slopes as an example of correction parameter.

C. Data density (pings).

D. Side scan sonar data.

E. Final bathymetric map projected in 3-D viewed from south to north.

The final map resolution was lower than expected, because the HydroSweep DS2 on this transect was run in deep water mode. Also, the ship-speed was high during data acquisition (10 knots as opposed to the ideal 4 knots). The final resolution is estimated to be 4-6 meters per pixel in the ship track direction (along track) and less than 1 meter in the sonar swath direction (across track) close to the center beam. lower resolutions are obtained towards the outer pings of the swath. This directional difference in resolution was expected to occur for shallow water. Nevertheless, the swath direction data yielded adequate information on the “roughness” of the sea-bottom, resolving features that are less than 5-10 meters. An overview map (Figure 4-7) shows the extent of the study area, the depths, the precise ship track, as well as the sampling points for each ping swath. This overview map has been produced with a 200 meters per pixel resolution. The final processed digital elevation model with a resolution of 11 meters per pixel is shown in 3-D perspective in figure 4-8. The color shades are depth dependent grading from shallow (white) to deep (blue). See Figure 4-7 for further depth information.

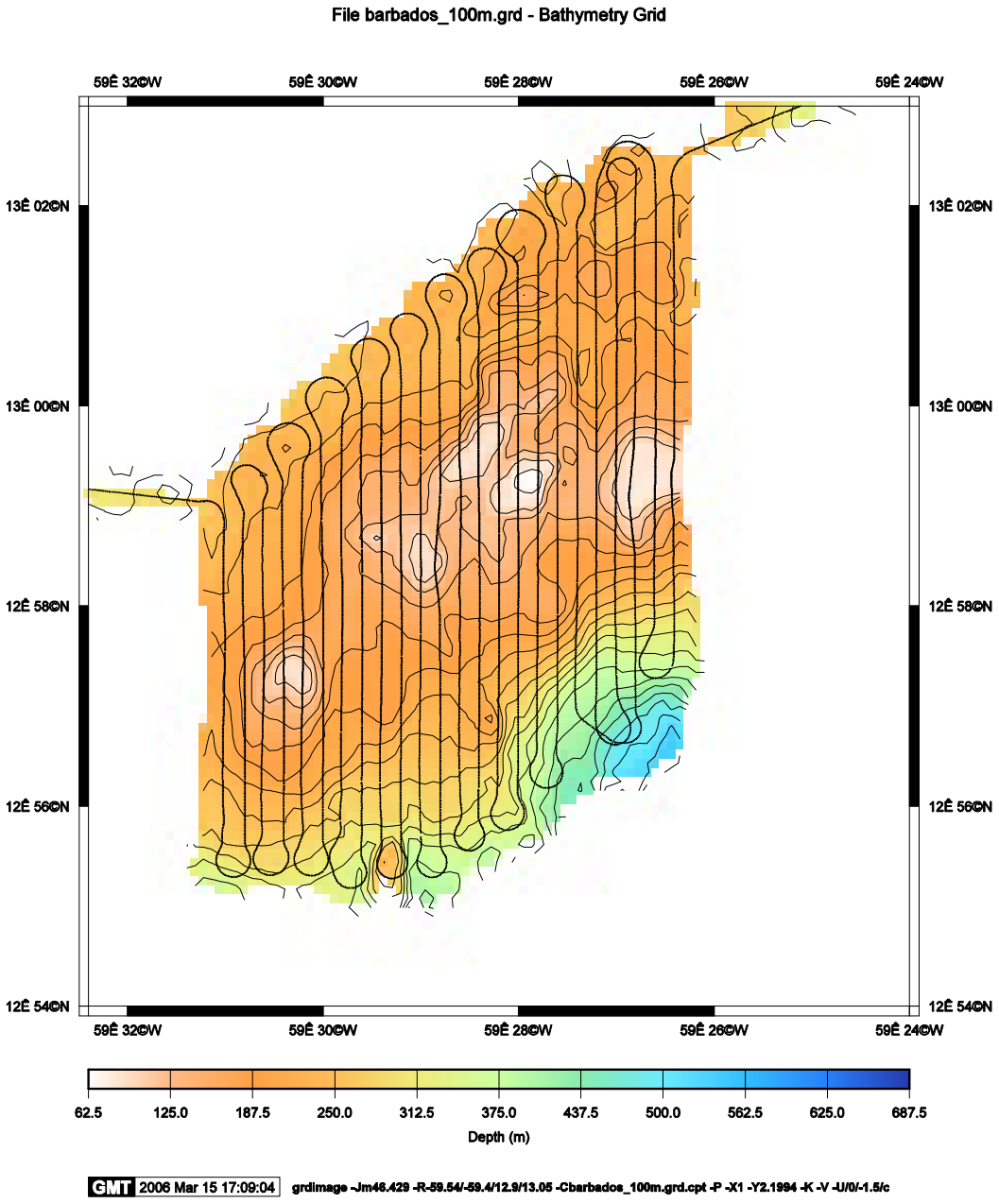
File barbados_100m.grd - Bathymetry Grid
59Ê 32ÐW
59Ê 30ÐW
59Ê 28ÐW
59Ê 26ÐW
59Ê 24ÐW
13Ê 02ÐN
13Ê 00ÐN
12Ê 58ÐN
12Ê 56ÐN
12Ê 54ÐN
62.5
125.0
187.5
250.0
312.5
375.0
437.5
500.0
562.5
625.0
687.5
Depth (m)
GMT 2006 Mar 15 17:09:04
grdimage -Jm46.429 -R-59.54/-59.4/12.9/13.05 -Cbarbados_100m.grd.cpt -P -X1 -Y2.1994 -K -V -U/0/-1.5/c

Figure 4-7

Figure 4-7 Low resolution (200meter per pixel) bathymetry map of the Barbados Shallows. The covered data area measures 10 km east-west and 14 km north-south.

Spatial Analysis

All spatial data processing was done in ArcGIS. Bathymetric data were extracted and processed in the MB-system. The output was netCDF grid-formatted before importing it into ArcGIS. The target areas were chosen based on depth and on the general likelihood of their containing desired reef samples (so-called 'target zones'). As outlined earlier, several criteria were used in a multivariate weighted regression (see Figure 4.7), which identifies target zones with high or low probabilities of drilling success (i. e. 'problem' and 'fewer problem' zones)

The final parameters used in the regression were:

A. Overall slope (less than 15 degrees for a 5 by 5 meter footprint)

B. Distance to steep slopes (50 meter buffer zones)

C. Water depth inside target zones (less than 150 meters)

The areas that initially satisfy the criteria for 'zones of interest' are marked in green in Figure 4-9. These zones are chosen based on a high probability of reefs growing in these areas (as will be discussed in chapter 5), due to the fact that in the past, there were shallow waters around these large, pinnacle-shaped 'sea hills'. The ArcGIS spatial analysis results used to identify 'problem zones' (e. g. areas that failed the multivariate regression discussed above), are shown in red in the 3-D projection in Figure 4-10. These red 'problem zones' are areas above the seafloor where one should avoid altogether positioning the ship for drilling. The problem zones are projected directly onto the sea floor, thereby displacing the

now inappropriate ‘green’ zone pixels (Figure 4-11). The analysis results indicating which of the remaining green areas are suitable for drilling are shown in Figure 4-12. The severity gradient of the problematic zones, ranging from least severe (red) to moderate severe (orange) to very severe (yellow) are projected in 3-D in Figure 4-13.

DISCUSSION

Acquiring and processing bathymetric data is both costly and demands considerable effort in planning and post-processing. Employing a large research vessel, such as the R/V Ewing, is logistically complicated, and even when the ship’s resources are made available for the range of smaller science budgets, more narrow projects such as detailed bathymetry surveys are often down-prioritized in favor of other types of studies employing a broader range of the ship’s capabilities (e. g. direct sampling).

One aspect of bathymetric studies has been the challenges raised by the enormous data sets produced even for very small surveys. In recent years, however, sophisticated and more powerful systems, capable of efficient and faster post-processing of these large data sets, have become readily available at much lower cost. But even under these improved conditions, all large data sets still require in-depth scrutiny. This makes the data preparation very time consuming in terms of manual inspection and editing, which can easily take months. In spite of all this, bathymetric surveys done for practical and scientific purposes present a

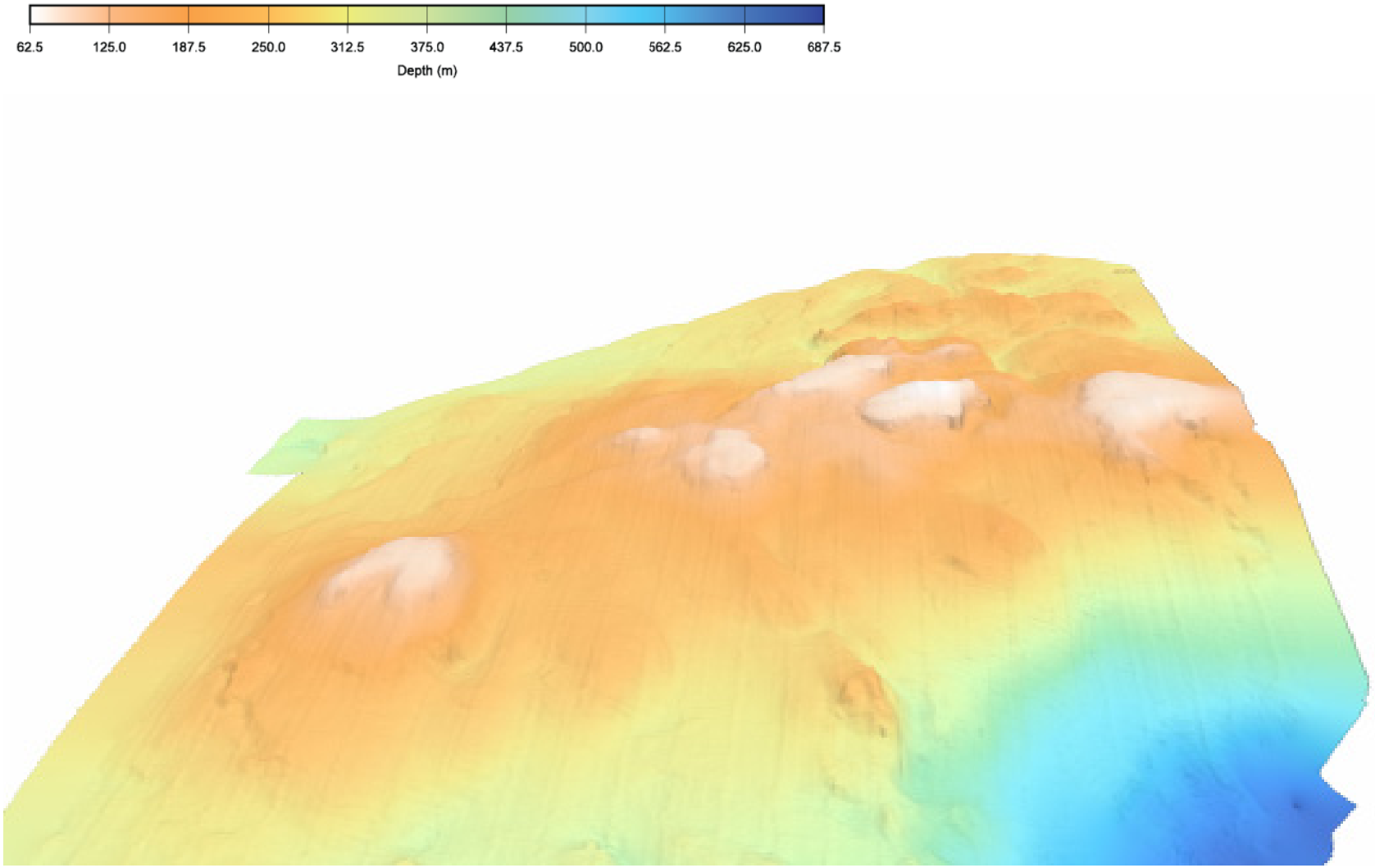

Figure 4-8

Figure 4-8 A 3-D projection of the final high resolution bathymetry digital elevation model of The Shallows. Scale as in Figure 4-7.

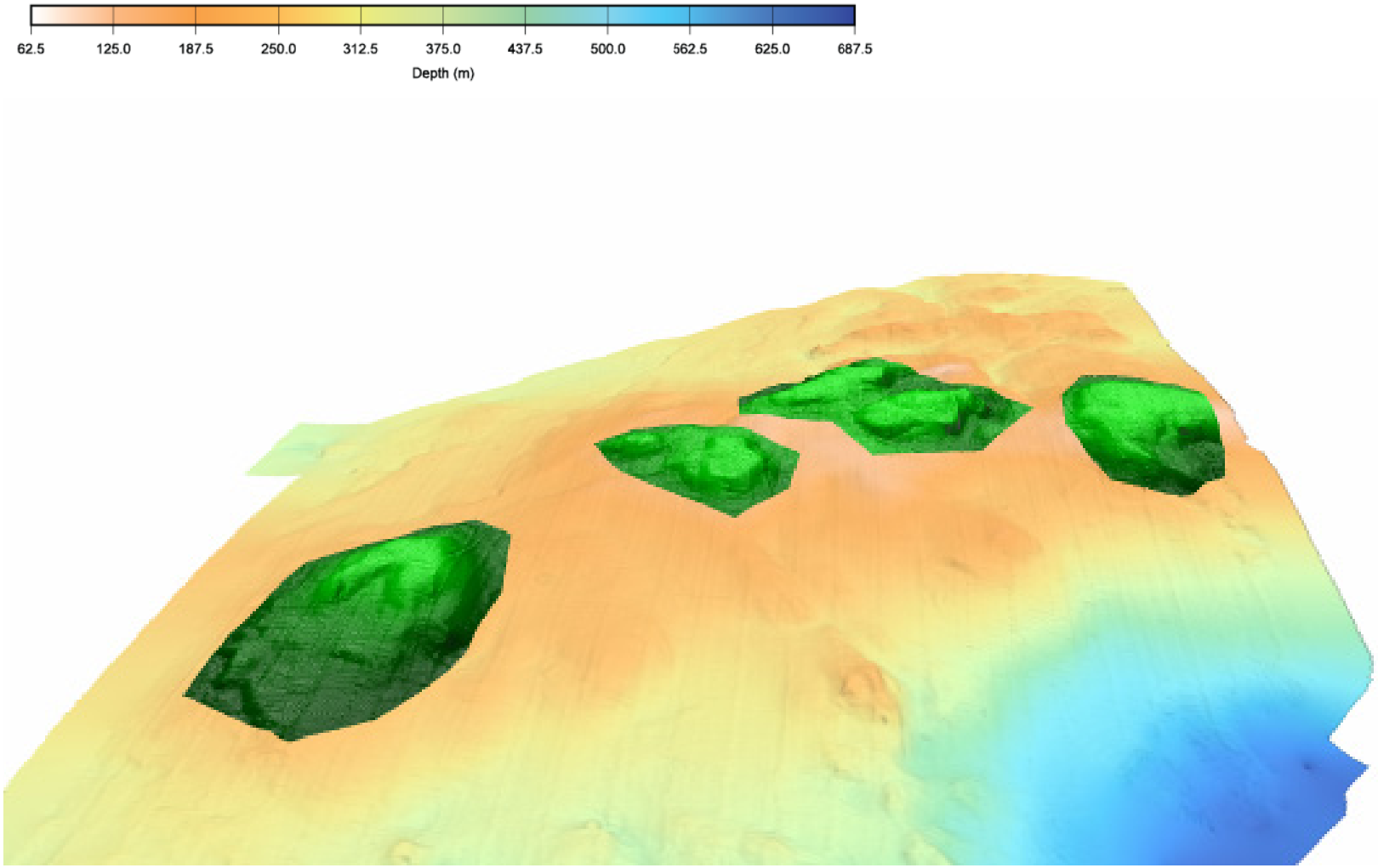

Figure 4-9

Figure 4-9 "Target zones" in study area identified from the 3D bathymetric map. Scale as in Figure 4-7.

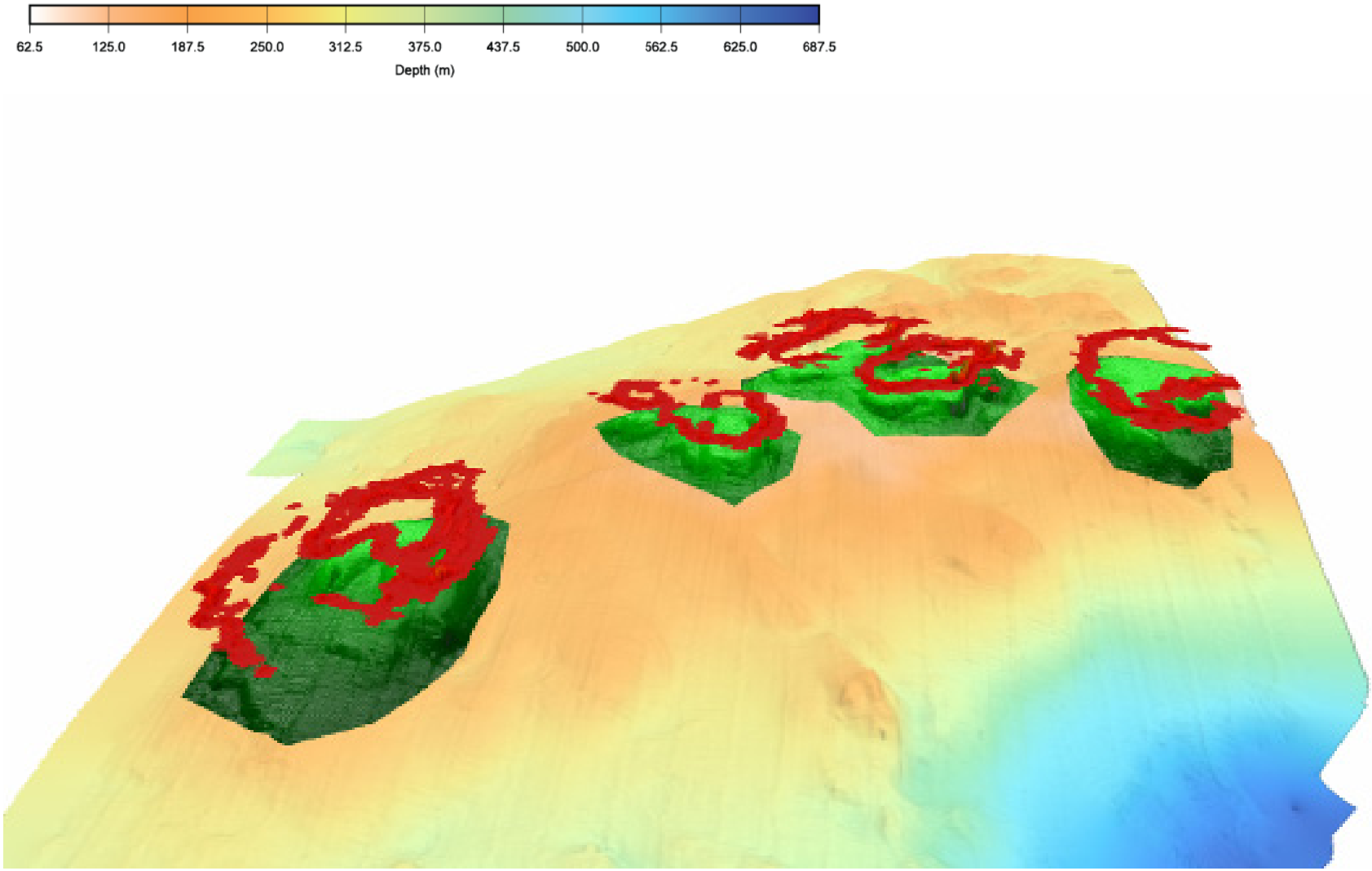

Figure 4-10

Figure 4-10 Results of the 3-D spatial analysis, where the multivariate regression results hover in red above the target areas. These red areas represent problem zones which should be avoided in drilling. Scale as in Figure 4-7.

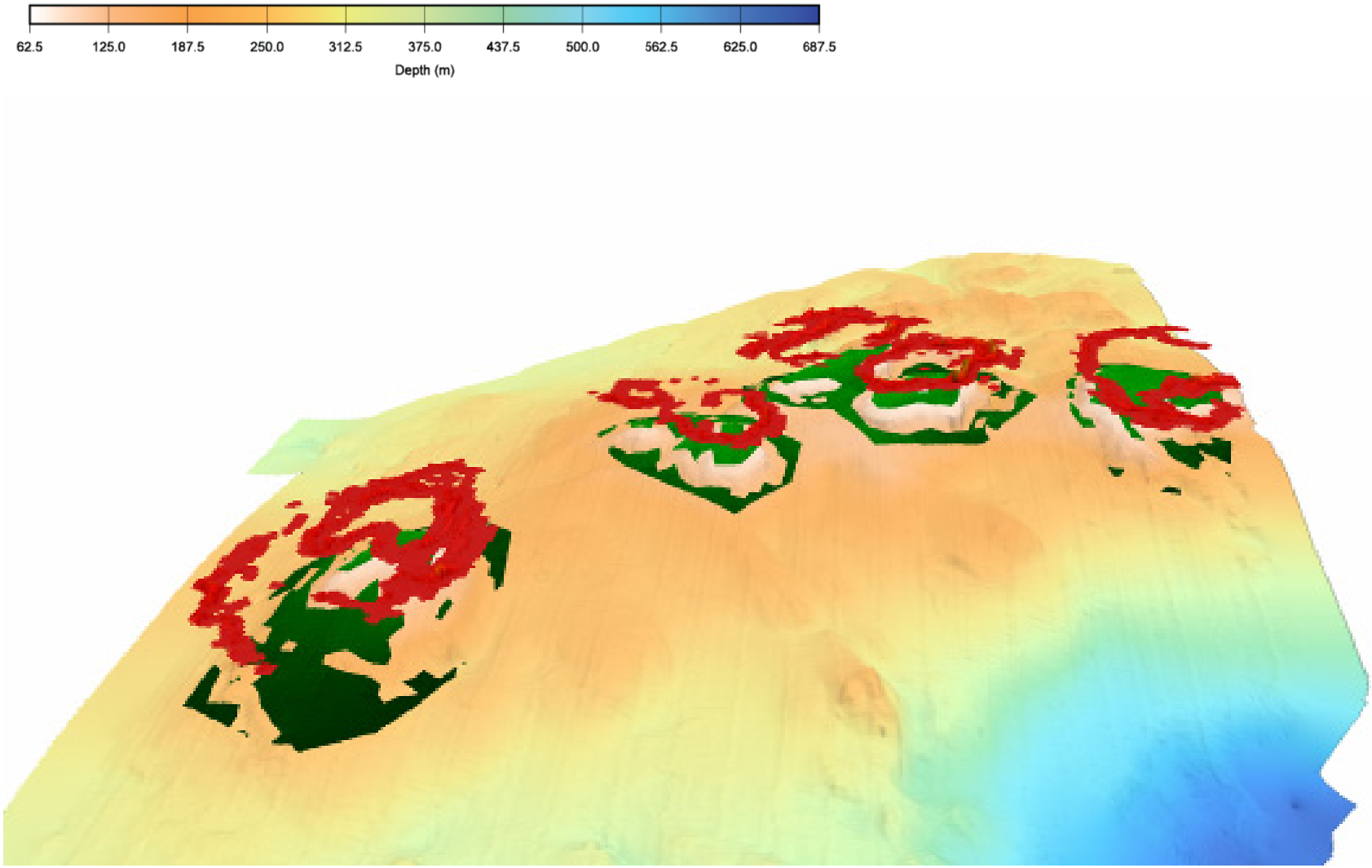

Figure 4-11

Figure 4-11 Result of the spatial raster calculation done in ArcGIS. The 'cut-outs' in the target areas represent the problematic zones; they are projected onto the sea-bottom, thereby displacing the green areas that failed the analysis. Scale and depth legend as in Figure 4-7.

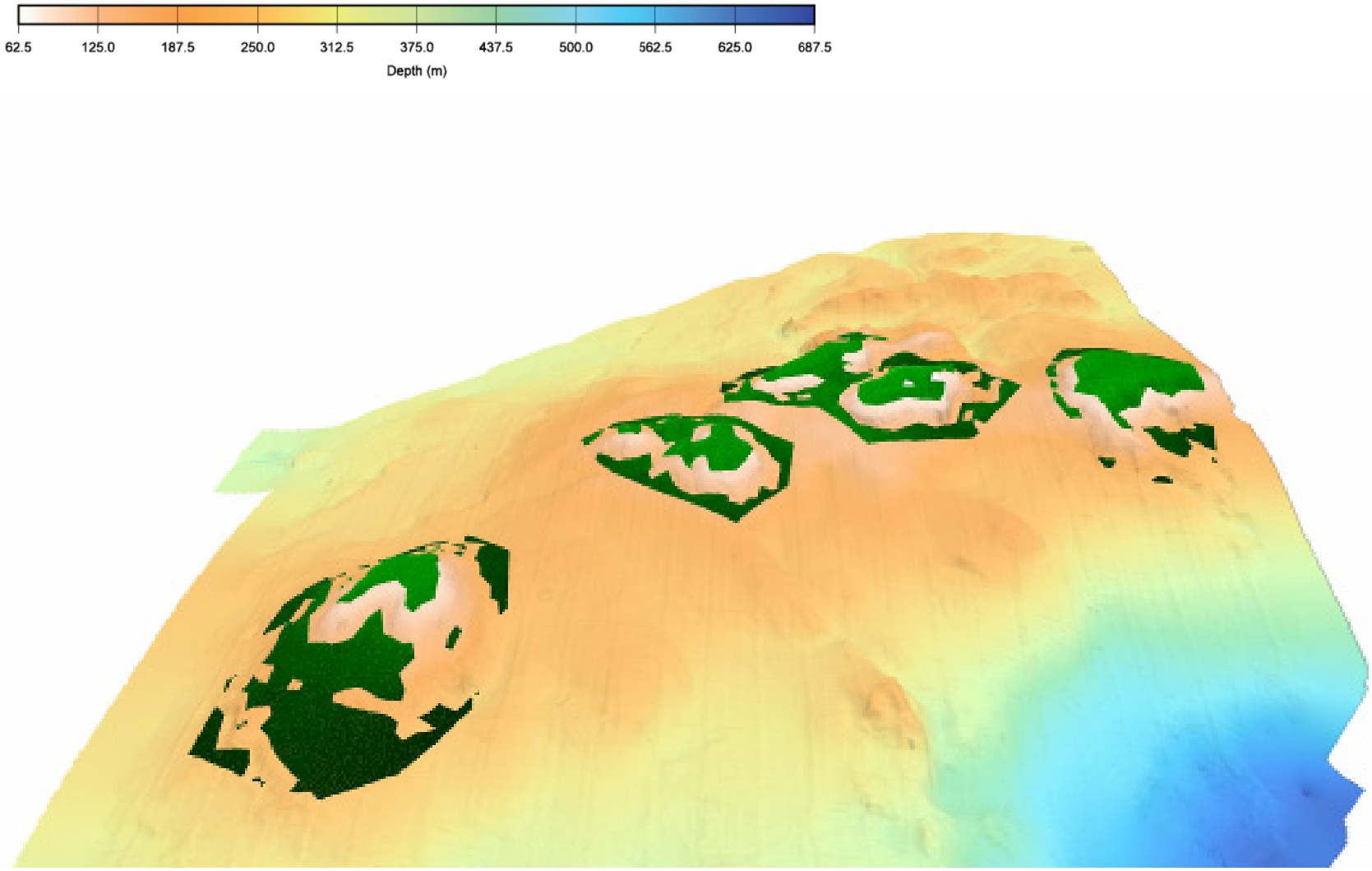

Figure 4-12

Figure 4-12 Final result of the spatial analysis, showing the target areas (green parcels) which are most likely to be successful for collecting drill samples. Scale as in Figure 4-7.

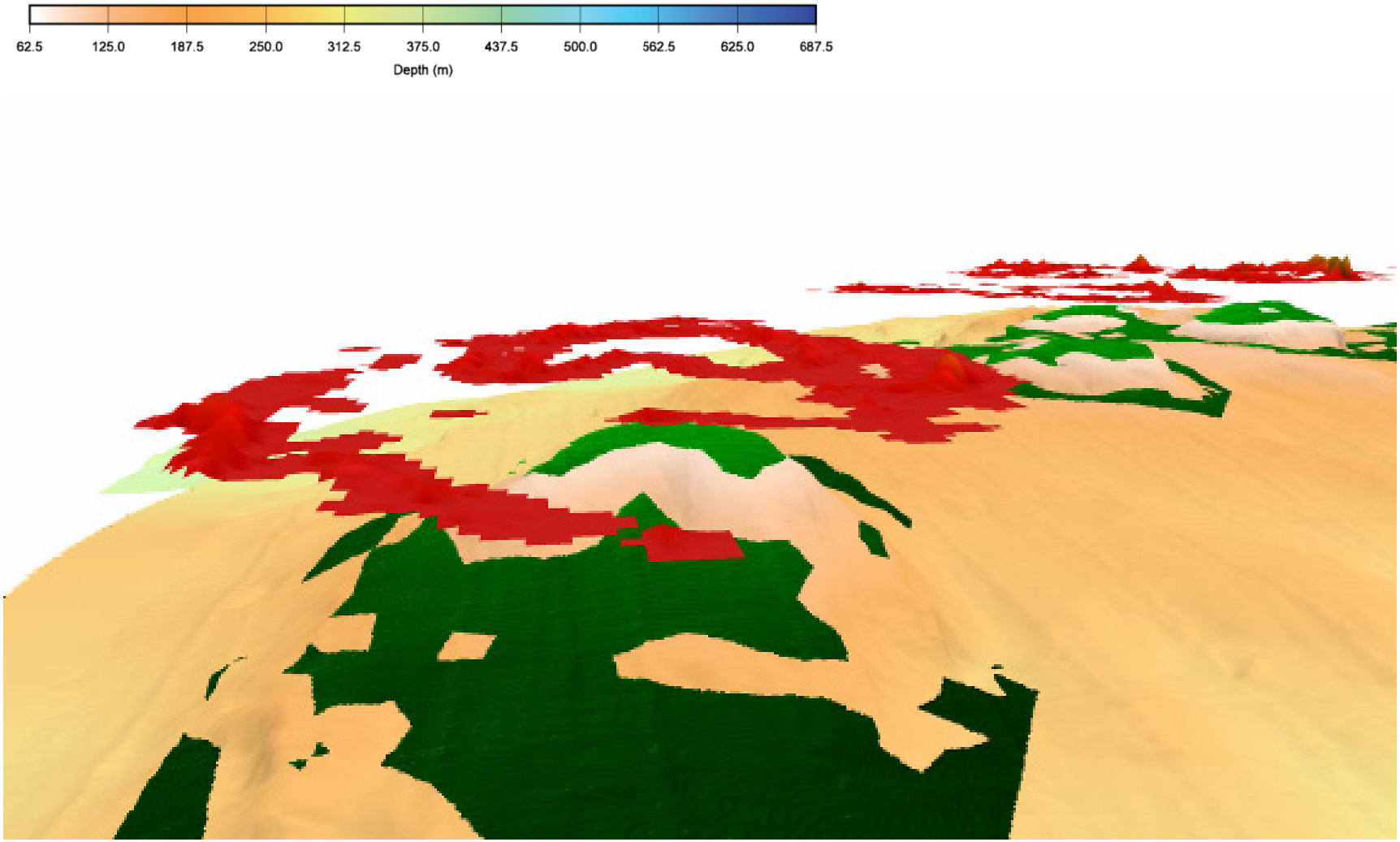

Figure 4-13

Figure 4-13 The grading of problem severity of "less problem zones" shown in 3-D. The topography of the red surface indicates the levels of failure according to the multivariate regression analysis. The orange and yellow peaks indicate the most problematic zones. Scale and depth legend as in Figure 4-7.

number of bonus features: they often lead to new insights regarding areas of the sea floor that are otherwise unreachable for direct observation. The challenges involved in interpreting bathymetric data, however, still remain, since features 'imaged' using sonar techniques are sometimes not real, but represent artifacts of 'electronic noise' (compare what has been said earlier about the problem of artifacts in the data), which can lead to 'false' interpretations of features on the sea floor.

Ideally, when one is surveying a poorly mapped or unknown area, some knowledge of the general direction of structures and major features is useful, so one may avoid paralleling the ship direction with the sea floor structures. Typically, artifacts that consistently follow the ship sail direction are likely to be a direct result of the real-time conditions (e. g. roll, pitch, heave etc., discussed earlier); these can only be identified as such in reality if they crosscut the natural features, or appear in areas where the sea floor is completely flat. In fact, data from a flat area in a survey represent perhaps the best data subset in which such artificial artifacts can be correctly identified. Acquiring redundant data over the same area and in multiple directions is also useful for identifying artificial features, but in this case the amount of data can quickly grow to an unmanageable size if too many overlaps occur. A sensible approach is to pre-survey the region of interest in low resolution, using a fast ship speed and wide swaths. This will produce a preliminary picture of the main features and will increase the quality of data by allowing the high resolution tracks to be planned in accordance with these preliminary findings.

Once noisy data and repetitious features not related to the real morphology, have been identified, several filters can be applied to the data files to successfully edit these. One typical example concerns outer pings, which are often much less reliable and randomly distributed as the angles of the ping returns of the outer part of the swaths become larger. These outer pings, sometimes referred to as 'bad tracks', can be 'flagged' by the MB-system software and collectively ignored. However, the final determination is always based on visual criteria, and corrections not identified by the filters are edited manually prior to processing and creating a survey grid. The advantage of 'flagging' is that while no data are effectively deleted or manipulated away from their original state, only data that pass the quality test will be used for a digital elevation model of the sea floor.

Once the local surveys and the subsequent editing are completed, the next challenge is that of integrating the new survey with older surveys in the nearby areas (if any such surveys exist). Most surveys, if collected on research vessels, become publicly available, but they exist typically in a range of different data formats native to the various host sonar systems with which they were collected. The MB-System has a very useful feature for adding other data to a survey in that it can identify and convert a wide range of different data formats.

As to integrating the surface models or digital elevation models, this is an even greater challenge, as these models are based on a grid calculation taking into account a geographical projection system. Such files can have their coordinates embedded in various projection systems and in different formats. Thus, latitude and longitude may either be given in degrees, minutes, and seconds (or in various

fractions of these units), or in the UTM format. Careful attention should be given to converting or standardizing these formats without loss of spatial accuracy. This, perhaps, remains the biggest challenge when merging older data with new. With regard to the data from The Shallows presented here, they stand alone at present, but will in a later study be compared to, and integrated with, newer data collected at higher resolution on a more recent cruise with the R/V Knorr (Mey et al., *in prep*). Even so, The Shallows data presented here are of a much higher quality and resolution, compared to what is readily available through the online GeoMapApp (2006) interface, despite the fact that for our purposes, the resolution of 100 meters per pixel of the GeoMapApp data still is too low, which becomes clear when one compares Figures 4-3 (GeoMapApp data) and 4-8 (our data), presented above.

CONCLUSIONS

Our spatial study of the Barbados Shallows bathymetry data has indeed proven useful for gaining insight into the main structures and identifying potential drilling targets for scientific sampling. The resolution of our new Shallows data not only exceeds that of the existing data for both DEMs available for the areas around Barbados (GeoMapApp), but it also qualitatively surpasses the space-borne SRTM DEM of the island itself. While for the purpose of positioning a small drill pod like ours (5 x 5 meters), the final resolution of our data in the ship's sail direction was not as high as desirable, our study has shown that using

the protocols set forth in this chapter, but employing higher resolution data will further aid the search for ideal pod placements for sampling targets.

ACKNOWLEDGEMENTS

I would like to thank the late Bill Haxby for introducing me to the tools necessary to study the bathymetry of the Barbados shallows. As a token of my great appreciation, I have chosen to use his "Haxby" color palette to portray The Shallows—a palette which by far, is the most aesthetical. I would like to thank Andrew Goodwyllie (Lamont Doherty Earth Observatory) for his enthusiasm and help from the very first time I walked into his office and asked about MB-System. Thanks also to Dale Chayes (who wrote MB-System together with Dave Caress) for technical assistance. I am indebted to Juliana Maantay (Lehman College) for suggestions to the manuscript in its early stages and to Gary Hemming (Queens College) for comments and fruitful conversations on the topic and to Rick Fairbanks (Columbia University) for his support and discussions. I also thank The Graduate Center (CUNY) for a University Fellowship supporting this work.

Appendix 4-1: A list of processed raw data files from the 18 October 2003, R/V Ewing cruise (leg EW0310) used for this study.

00031018023010p.mb183 183 1.000000
00031018024010p.mb183 183 1.000000
00031018025010p.mb183 183 1.000000
00031018030010p.mb183 183 1.000000
00031018031010p.mb183 183 1.000000
00031018032010p.mb183 183 1.000000
00031018033010p.mb183 183 1.000000
00031018034010p.mb183 183 1.000000
00031018035010p.mb183 183 1.000000
00031018040010p.mb183 183 1.000000
00031018041010p.mb183 183 1.000000
00031018042010p.mb183 183 1.000000
00031018043010p.mb183 183 1.000000
00031018044010p.mb183 183 1.000000
00031018045010p.mb183 183 1.000000
00031018050010p.mb183 183 1.000000
00031018051010p.mb183 183 1.000000
00031018052010p.mb183 183 1.000000
00031018053010p.mb183 183 1.000000
00031018054010p.mb183 183 1.000000
00031018055010p.mb183 183 1.000000
00031018060010p.mb183 183 1.000000
00031018061010p.mb183 183 1.000000
00031018062010p.mb183 183 1.000000
00031018063010p.mb183 183 1.000000
00031018064010p.mb183 183 1.000000
00031018065010p.mb183 183 1.000000
00031018070010p.mb183 183 1.000000
00031018071010p.mb183 183 1.000000
00031018072010p.mb183 183 1.000000
00031018073010p.mb183 183 1.000000
00031018074010p.mb183 183 1.000000
00031018075010p.mb183 183 1.000000
00031018080010p.mb183 183 1.000000
00031018081010p.mb183 183 1.000000
00031018082010p.mb183 183 1.000000
00031018083010p.mb183 183 1.000000
00031018084010p.mb183 183 1.000000
00031018085010p.mb183 183 1.000000
00031018090010p.mb183 183 1.000000
00031018091010p.mb183 183 1.000000

00031018092010p.mb183 183 1.000000
00031018093010p.mb183 183 1.000000
00031018094010p.mb183 183 1.000000
00031018095010p.mb183 183 1.000000
00031018100010p.mb183 183 1.000000
00031018101010p.mb183 183 1.000000
00031018102010p.mb183 183 1.000000
00031018103010p.mb183 183 1.000000
00031018104010p.mb183 183 1.000000
00031018105010p.mb183 183 1.000000
00031018110010p.mb183 183 1.000000
00031018111010p.mb183 183 1.000000
00031018112010p.mb183 183 1.000000
00031018113010p.mb183 183 1.000000
00031018114010p.mb183 183 1.000000
00031018115010p.mb183 183 1.000000
00031018120010p.mb183 183 1.000000
00031018121010p.mb183 183 1.000000
00031018122010p.mb183 183 1.000000
00031018123010p.mb183 183 1.000000
00031018124010p.mb183 183 1.000000
00031018125010p.mb183 183 1.000000
00031018130010p.mb183 183 1.000000
00031018131010p.mb183 183 1.000000
00031018132010p.mb183 183 1.000000
00031018133010p.mb183 183 1.000000
00031018134010p.mb183 183 1.000000
00031018135010p.mb183 183 1.000000
00031018140010p.mb183 183 1.000000
00031018141010p.mb183 183 1.000000
00031018142010p.mb183 183 1.000000
00031018143010p.mb183 183 1.000000
00031018144010p.mb183 183 1.000000
00031018145010p.mb183 183 1.000000
00031018150010p.mb183 183 1.000000
00031018151010p.mb183 183 1.000000
00031018152010p.mb183 183 1.000000
00031018153010p.mb183 183 1.000000
00031018154010p.mb183 183 1.000000

Appendix 4-2: Example of available parameters used for processing the bathymetry data for this study.

```
## MB-System processing parameter file
## Written by mb_pr_writepar version $Id: mb_process.c,v 5.34
2006/01/06 18:27:19 caress Exp $
## MB-system Version 5.0.9
## Generated by user <jacob> on cpu <TIME> at <Mon Apr 24
14:11:05 2006>
##
##
## Forces explicit reading of parameter modes.
EXPLICIT
##
## General Parameters:
FORMAT 183
INFILE 00031018050010pp.mb183
OUTFILE 00031018050010ppp.mb183
##
## Navigation Merging:
NAVMODE 0
NAVFILE
NAVFORMAT 0
NAVHEADING 0
NAVSPEED 0
NAVDRAFT 0
NAVATTITUDE 0
NAVINTERP 0
NAVTIMESHIFT 0.000000
NAVSHIFT 0
NAVOFFSETX 0.000000
NAVOFFSETY 0.000000
NAVOFFSETZ 0.000000
##
## Adjusted Navigation Merging:
NAVADJMODE 0
NAVADJFILE
NAVADJINTERP 0
##
## Attitude Merging:
ATTITUDEMODE 0
ATTITUDEFILE
ATTITUDEFORMAT 1
##
## Sonardepth Merging:
SONARDEPTHMODE 0
SONARDEPTHFILE
SONARDEPTHFORMAT 1
##
## Data cutting:
DATACUTCLEAR
##
## Bathymetry Flagging:
EDITSAVEMODE 1
```

```
EDITSAVEFILE 00031018050010pp.mb183.esf
##
## Bathymetry Recalculation:
SVPMODE 0
SVPFILE
SSVMODE 0
SSV 0.000000
TTMODE 0
TTMULTIPLY 1.000000
ANGLEMODE 1
SOUNDSPEEDREF 1
STATICMODE 0
STATICFILE
##
## Draft Correction:
DRAFTMODE 0
DRAFT 0.000000
DRAFTOFFSET 0.000000
DRAFTMULTIPLY 1.000000
##
## Heave Correction:
HEAVEMODE 0
HEAVEOFFSET 0.000000
HEAVEMULTIPLY 1.000000
##
## Lever Correction:
LEVERMODE 0
VRUOFFSETX 0.000000
VRUOFFSETY 0.000000
VRUOFFSETZ 0.000000
SONAROFFSETX 0.000000
SONAROFFSETY 0.000000
SONAROFFSETZ 0.000000
##
## Roll Correction:
ROLLBIASMODE 0
ROLLBIAS 0.000000
ROLLBIASPORT 0.000000
ROLLBIASSTBD 0.000000
##
## Pitch Correction:
PITCHBIASMODE 0
PITCHBIAS 0.000000
##
## Heading Correction:
HEADINGMODE 0
HEADINGOFFSET 0.000000
##
## Tide Correction:
TIDEMODE 0
TIDEFILE
TIDEFORMAT 1
##
## Amplitude Correction:
AMPCORRMODE 0
AMPCORRFILE
AMPCORRTYPE 0
```

```
AMPCORRSYMMETRY 1
AMPCORRANGLE 30.000000
AMPCORRSLOPE 0
##
## Sidescan Correction:
SSCORRMODE 0
SSCORRFILE
SSCORRTYPE 0
SSCORRSYMMETRY 1
SSCORRANGLE 30.000000
SSCORRSLOPE 0
##
## Sidescan Recalculation:
SSRECALCMODE 0
SSPIXELSIZE 0.000000
SSSWATHWIDTH 0.000000
SSINTERPOLATE 0
##
## Metadata Insertion:
METAVESSEL
METAINSTITUTION
METAPLATFORM
METASONAR
METASONARVERSION
METACRUISEID
METACRUISENAME
METAPI
METAPIINSTITUTION
METACLIENT
METASVCORRECTED -1
METATIDECORRECTED -1
METABATHEDITMANUAL -1
METABATHEDITAUTO -1
METAROLLBIAS 10000000.000000
METAPITCHBIAS 10000000.000000
METAHEADINGBIAS 10000000.000000
METADRAFT 10000000.000000
##
## Processing Kluges:
```

Appendix 4-3: An example of a PERL script used to generate maps for this study.

```
#! /bin/csh -f
#
# Shellscript to create Postscript plot of data in grd file
# Created by macro mbm_grdplot
#
# This shellscript created by following command line:
# mbm_grdplot -IAllShallowsData10m.grd -G1 -C -V -LFile
AllShallowsData10m.grd - Topography Grid:Topography (m)
#
# Define shell variables used in this script:
set PS_FILE         = AllShallowsData10m.grd.ps
set CPT_FILE        = AllShallowsData10m.grd.cpt
set MAP_PROJECTION  = m
set MAP_SCALE       = 55.177
set MAP_REGION      = -59.5292/-59.4333/12.9125/13.0458
set X_OFFSET        = 1.6042
set Y_OFFSET        = 2
#
# Save existing GMT defaults
echo Saving GMT defaults...
gmtdefaults -L > gmtdefaults$$
#
# Set new GMT defaults
echo Setting new GMT defaults...
gmtset MEASURE_UNIT inch
gmtset PAPER_MEDIA archA+
gmtset ANOT_FONT Helvetica
gmtset LABEL_FONT Helvetica
gmtset HEADER_FONT Helvetica
gmtset ANOT_FONT_SIZE 8
gmtset LABEL_FONT_SIZE 8
gmtset HEADER_FONT_SIZE 10
gmtset FRAME_WIDTH 0.075
gmtset TICK_LENGTH 0.075
gmtset PAGE_ORIENTATION LANDSCAPE
gmtset COLOR_BACKGROUND 0/0/0
gmtset COLOR_FOREGROUND 255/255/255
gmtset COLOR_NAN 255/255/255
gmtset DEGREE_FORMAT 3
#
# Make color pallette table file
echo Making color pallette table file...
echo   -550  37  57 175   -500  40 127 251 > $CPT_FILE
echo   -500  40 127 251   -450  50 190 255 >> $CPT_FILE
echo   -450  50 190 255   -400 106 235 255 >> $CPT_FILE
echo   -400 106 235 255   -350 138 236 174 >> $CPT_FILE
echo   -350 138 236 174   -300 205 255 162 >> $CPT_FILE
echo   -300 205 255 162   -250 240 236 121 >> $CPT_FILE
echo   -250 240 236 121   -200 255 189  87 >> $CPT_FILE
echo   -200 255 189  87   -150 255 161  68 >> $CPT_FILE
echo   -150 255 161  68   -100 255 186 133 >> $CPT_FILE
```

```
echo   -100 255 186 133    -50 255 255 255 >> $CPT_FILE
#
# Define data files to be plotted:
set DATA_FILE        = AllShallowsData10m.grd
set INTENSITY_FILE   =
#
# Make color image
echo Running grdimage...
grdimage $DATA_FILE -J$MAP_PROJECTION$MAP_SCALE \
   -R$MAP_REGION -C$CPT_FILE \
   -P -X$X_OFFSET -Y$Y_OFFSET -K -V >! $PS_FILE
#
# Make contour plot
echo Running grdcontour...
grdcontour $DATA_FILE -J$MAP_PROJECTION$MAP_SCALE \
   -R$MAP_REGION \
   -C25 \
   -L-531.044/-62.7557 -Wc1p\
   -P -K -O -V >> $PS_FILE
#
# Make color scale
echo Running psscale...
psscale -C$CPT_FILE \
   -D2.6458/-0.5000/5.2915/0.1500h \
   -B":Topography (m):" \
   -P -K -O -V >> $PS_FILE
#
# Make basemap
echo Running psbasemap...
psbasemap -J$MAP_PROJECTION$MAP_SCALE \
   -R$MAP_REGION \
   -B2m/2m:."File AllShallowsData10m.grd - Topography Grid": \
   -P -O -V >> $PS_FILE
#
# Delete surplus files
echo Deleting surplus files...
/bin/rm -f $CPT_FILE
#
# Reset GMT default fonts
echo Resetting GMT fonts...
/bin/mv gmtdefaults$$ .gmtdefaults
#
# Run ghostview
echo Running ghostview in background...
ghostview -portrait -media BBox AllShallowsData10m.grd.ps &
#
# All done!
echo All done!
```

Appendix 4-4: Example of information files for data

```
Swath Data File:      00031018123010p.mb183
MBIO Data Format ID:  183
Format name:          MBF_HSDS2LAM
Informal Description: L-DEO HSDS2 processing format
Attributes:           STN Atlas multibeam sonars,
                      Hydrosweep DS2, Hydrosweep MD,
                      Fansweep 10, Fansweep 20,
                      bathymetry, amplitude, and sidescan,
                      up to 1440 beams and 4096 pixels,
                      XDR binary, L-DEO.

Data Totals:
Number of Records:                          124
Bathymetry Data (140 beams):
  Number of Beams:            17360
  Number of Good Beams:       12425     71.57%
  Number of Zero Beams:         282      1.62%
  Number of Flagged Beams:     4653     26.80%
Amplitude Data (140 beams):
  Number of Beams:            17360
  Number of Good Beams:       12425     71.57%
  Number of Zero Beams:         282      1.62%
  Number of Flagged Beams:     4653     26.80%
Sidescan Data (4094 pixels):
  Number of Pixels:          388146
  Number of Good Pixels:     348718     89.84%
  Number of Zero Pixels:      39428     10.16%
  Number of Flagged Pixels:       0      0.00%

Navigation Totals:
Total Time:             0.1645 hours
Total Track Length:     3.0720 km
Average Speed:         18.6729 km/hr (10.0935 knots)

Start of Data:
Time:  10 18 2003 12:29:56.409999  JD291
Lon:  -59.4955     Lat:   12.9197     Depth:   339.1631 meters
Speed: 17.2000 km/hr ( 9.2973 knots)  Heading: 275.5400 degrees
Sonar Depth:    3.2600 m  Sonar Altitude:  335.9031 m

End of Data:
Time:  10 18 2003 12:39:48.671000  JD291
Lon:  -59.4969     Lat:   12.9455     Depth:   199.8282 meters
Speed: 18.4500 km/hr ( 9.9730 knots)  Heading:   5.3400 degrees
Sonar Depth:    3.7300 m  Sonar Altitude:  196.3959 m

Limits:
Minimum Longitude:     -59.5058   Maximum Longitude:     -59.4903
Minimum Latitude:       12.9130   Maximum Latitude:       12.9458
Minimum Sonar Depth:     1.9000   Maximum Sonar Depth:     4.9300
Minimum Altitude:      194.1626   Maximum Altitude:      337.2478
Minimum Depth:         196.4947   Maximum Depth:         346.7411
Minimum Amplitude:       0.0000   Maximum Amplitude:     249.0000
```

```
Minimum Sidescan:        1.0000   Maximum Sidescan:      255.0000

Data Record Type Notices:
DN: 124 MB_DATA_DATA (ID=1): survey data
DN: 93 MB_DATA_COMMENT (ID=2): comment

Nonfatal Error Notices:
EN: 93 MB_ERROR_COMMENT (ID=-5): Comment record

Problem Notices:

Coverage Mask:
CM dimensions: 10 10
CM:   0 0 1 1 1 1 1 1 1 0
CM:   0 0 1 1 1 1 1 1 1 0
CM:   0 0 1 1 1 1 1 1 1 1
CM:   0 1 1 1 1 1 1 1 1 1
CM:   0 1 1 1 1 1 1 1 1 1
CM:   1 1 1 1 1 1 1 1 1 1
CM:   1 1 1 1 1 1 1 1 1 1
CM:   1 1 1 1 1 1 1 1 1 0
CM:   0 1 1 1 1 1 1 0 0 0
CM:   0 0 1 1 1 1 1 0 0 0
```

CHAPTER 5
MORPHOLOGY OF THE BARBADOS SHALLOWS AND ITS CORAL HABITAT DURING THE LAST GLACIAL CYCLE

By

Jacob L. Mey[1, 2]

1. Lamont Doherty Earth Observatory of Columbia University, Palisades, New York 10964, USA.

2. Graduate Center, City University of New York, New York, NY 10016, USA.

ABSTRACT

Fossil corals are important proxies for studying past sea level changes and past ocean surface temperature variations. They are also essential for calibrating the radiocarbon calibration curve. Clues from reef geometry and the distribution of coral species in the old reef tracts, in combination with high accuracy U-Th and U-Pa dating techniques, contribute crucial benchmarks when we reconstruct major climatic changes in the past. However, when the reefs are brought out of the marine environment, due to either sea level drop or isostasy, they become sub-aerially exposed. As a result, they come into contact with freshwater and undergo diagenesis. This process is reflected in the uranium series open-system signatures. The alteration potential is highest the first time the reefs are exposed, which is when the freshwater vadose environment inflicts the maximum diagenetic effects on the reefs. Among the most discussed effects is the fractionation of the uranium series. Reefs that have remained in the marine environment are much better preserved and yield ample closed-system samples for dating. The plethora of processes that affect the reefs, once they are subjected to the freshwater vadose zone, are not well constrained and a clear understanding of any combination of these has so far not been achieved.

We chose to prospect for samples in the marine setting as an alternative approach to circumvent the problems related to diagenesis, primarily in order to limit the number of time-consuming analyses of samples with unreliable ages. In our offshore prospecting, we have applied new tools, including high resolution

bathymetry and GIS spatial analysis, to help us identify prospective targets in the drowned reefs around the Barbados Shallows and elsewhere. The targets are identified by comparing reef habitat zones through time, pegged both by the sea level curve derived from Caribbean *Acropora palmata* corals and by spatial data derived from reef profiles on land and off-shore drill cores. The *Acropora palmata* corals are ideal for studying past sea level, because their most massive species thrive in the high energy zones in the upper 5 meters of the ocean. We also estimated paleo-habitat zones for deeper growing species such as *Montastrea annularis*, *Porites asteroides*, *Acropora cervicornis,* and *Diploria spp.* at various stages of sea level having occurred since the last glacial low stand. These new bathymetric and geo-spatial maps will contribute to our understanding of the reef geometry of the Barbados Shallows, while increasing the chances of successful sampling.

INTRODUCTION

The collection of maps presented below form a 3-dimensional portrait of the sea-floor topography (hereafter 'digital elevation model'– DEM) and backscatter intensity of the Barbados Shallows. This area and the Island of Barbados itself are part of the 'Barbados Rise' accretionary prism, stretching north-south along the eastern side of the subduction zone where the North American plate decends under the Caribbean plate from west to east (Figure 5-1). 'The Shallows' is located 4-7 kilometers south-southeast offshore Barbados. Together they are the only local rises on the Barbados Ridge that have emerged above the sea level (see Figure 5-1 and 5-2). Neither the Shallows nor Barbados itself have a volcanic component, but are entirely covered by a coral cap. The new maps presented here are based on multi-beam echo sounder data that were collected by the R/V Maurice Ewing in October 2003. During the last of a 16-day transit from Bergen, Norway to Bridgetown, Barbados, the R/V Ewing collected data on The Shallows.[1] The Shallows study area covers 107 km^2 and stretches 10 kilometers east-west and 14 kilometers north-south. The survey area is shaped like a rhombus in order to cover several distinct shallow areas thought to be large kilometer sized banks with drowned pinnacle reefs (Figure 5-3A). The most recent additions to the reef growth occurred 21,000 – 9,000 years ago, when the ocean surface rose from 120 to 60 meters below today's sea level. During

[1] This research vessel was decommissioned in 2005 and replaced by R/V Marcus G. Langseth, also owned by the NSF and likewise operated by Lamont Doherty Earth Observatory (LDEO) of Columbia University.

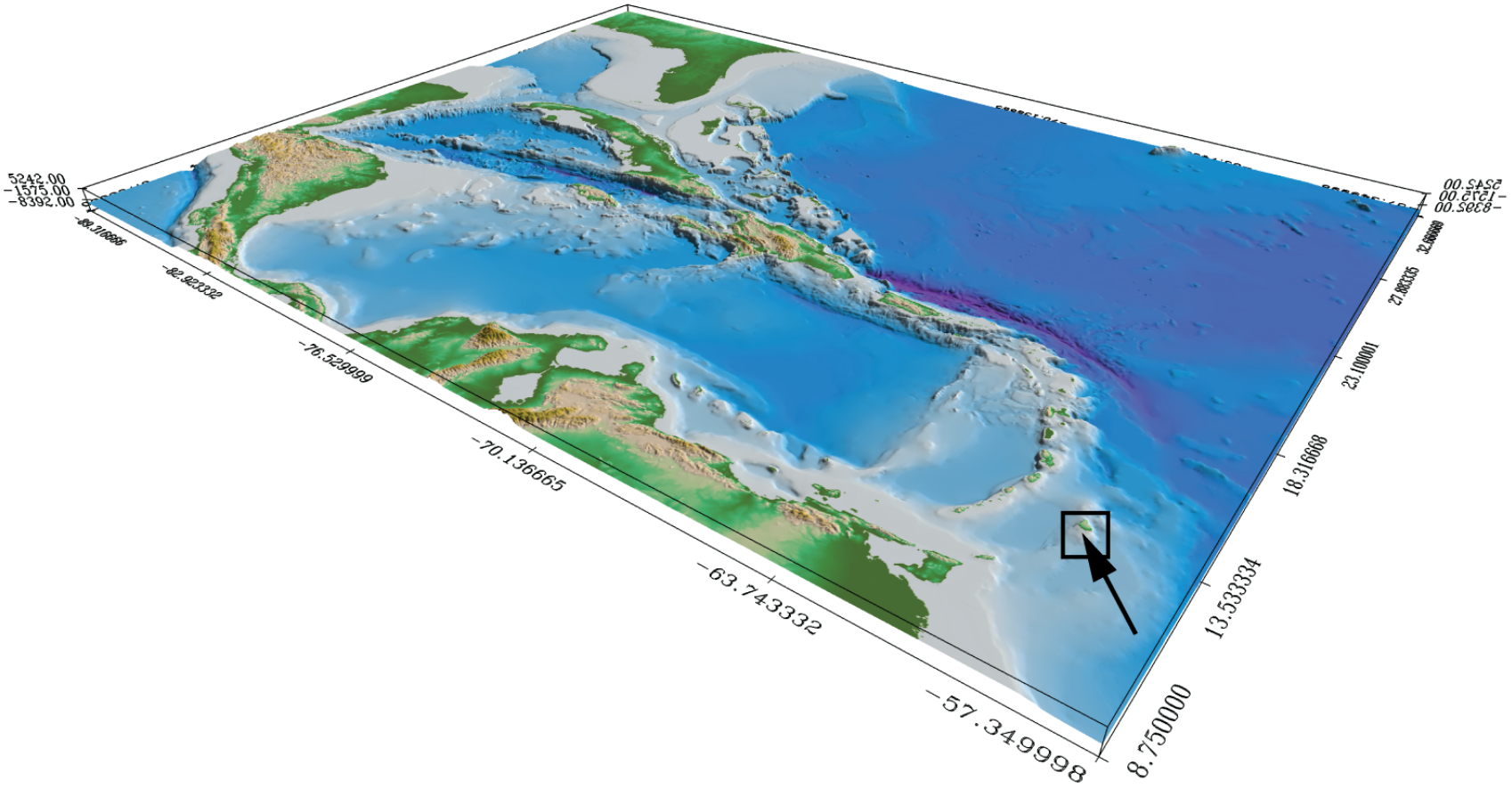
5242.00
-1575.00
-8392.00
-76.529999
-70.136665
-63.743332
-57.349998
8.750000
13.533334
18.316668
23.100001

Figure 5-1

Figure 5-1: General topographical and bathymetric maps of the Caribbean and vicinity. The small box indicates the location of Barbados in the Caribbean Sea. This map was made using 2 kilometer per pixel resolution bathymetric data from GEBCO, General Bathymetric Chart of the Oceans by the BODC (British Oceanographic Data Centre).

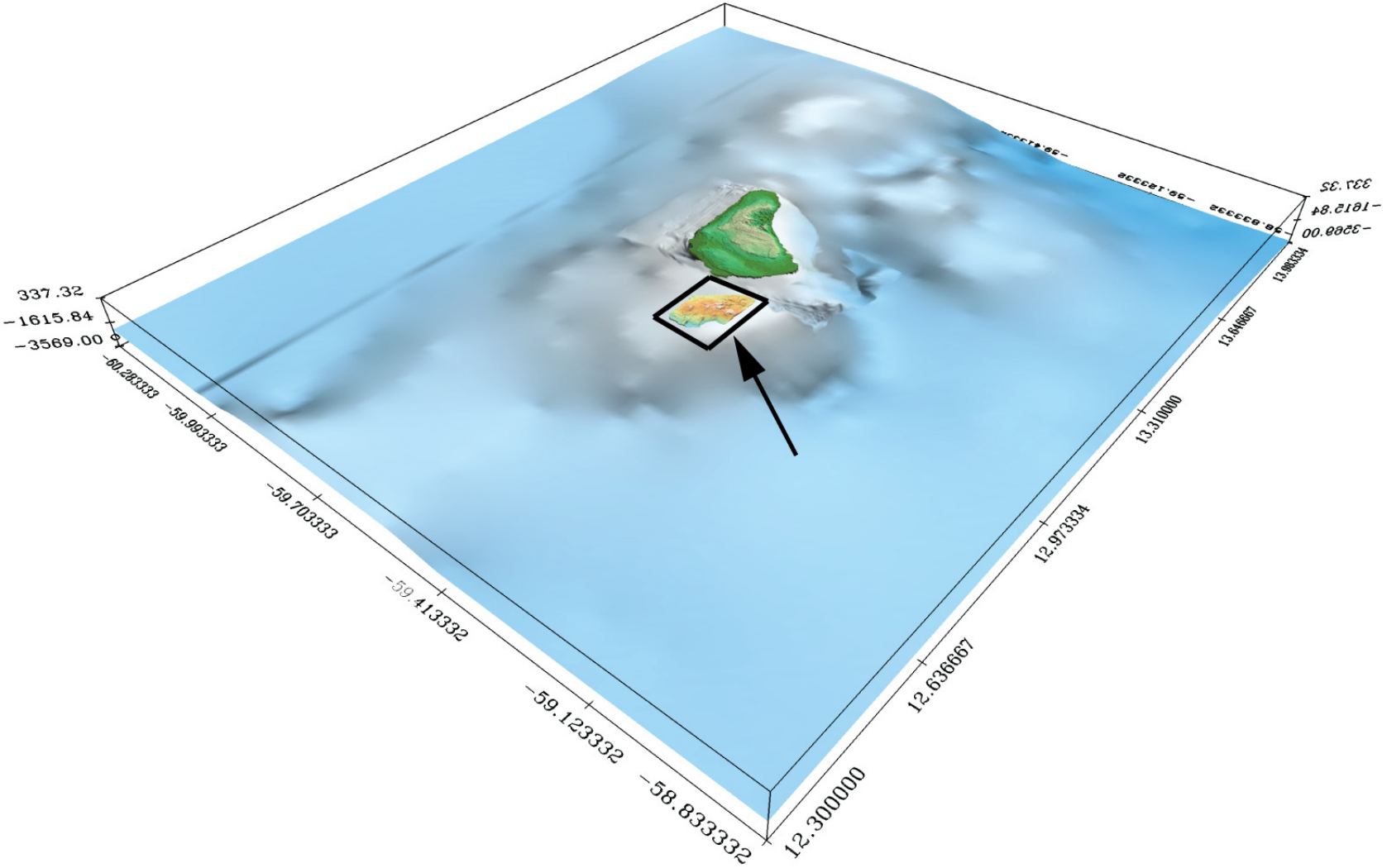
337.32
-1615.84
-3569.00
-60.283333
-59.993333
-59.703333
-59.413332
-59.123332
-58.833332
12.300000
12.636667
12.973334
13.310000
13.646667
13.983334

Figure 5-2

Figure 5-2: General topographical map of Barbados and vicinity. The small box indicates the location of the underwater Shallows, approximately 8 kilometers south-east of Barbados. This map was constructed using 2-kilometer per pixel resolution bathymetric data from GEBCO, General Bathymetric Chart of the Oceans by the BODC (British Oceanographic Data Centre), 119-meter per pixel resolution bathymetric and digital elevation model data Marine Geosciences Data System (http://www.marine-geo.org), using the Ridge 2000 and MARGINS programs' data portals of the MGDS data collection (Carbotte et al., 2000), 90-meter per pixel resolution digital elevation model data from NASA's Shuttle Radar Topography Mission (SRTM) data center and 11-meter per pixel resolution multibeam sonar swath data from and this study.

this time, the Earth was coming out of its last glacial maximum and entering the beginning of the Holocene period. Sometime during the first couple of millennia of this epoch, the highest reefs on the Shallows were drowned. The corals could not keep up with the fast sea level rise, caused by the second major melt-water pulse (MVP-2) which occurred as a result of the accelerated breakup and melting of the polar ice caps approximately 9,000 years ago (Shackleton, 1987). Consequently, the latest additions of reefs on the pinnacles of the Shallows have never been exposed to freshwater. Neither do they have an added component of older reefs, as is the case for the main island, which is constructed entirely of reefs which become successively older towards the center of the island. The factors mentioned above frame the reefs on the Shallows as excellent targets for pristine closed system samples.

At this time, only the unprocessed sonar data from the R/V Ewing, Bergen-Bridgetown, transect are available through the Marine Geosciences Data System (http://www.marine-geo.org), using the Ridge 2000 and MARGINS program data portals of the MGDS data collection (Carbotte et al., 2000). Additional processed data used for the surrounding areas were collected from NASA's Shuttle Radar Topography Mission (SRTM) data center and from the British Oceanographic Data Centre (BODC) of the General Bathymetric Chart of the Oceans (GEBCO). We have used the interpolated surface relief from the bathymetric data and the backscatter intensity draped upon this topographic relief as a prospecting tool for drowned reefs.

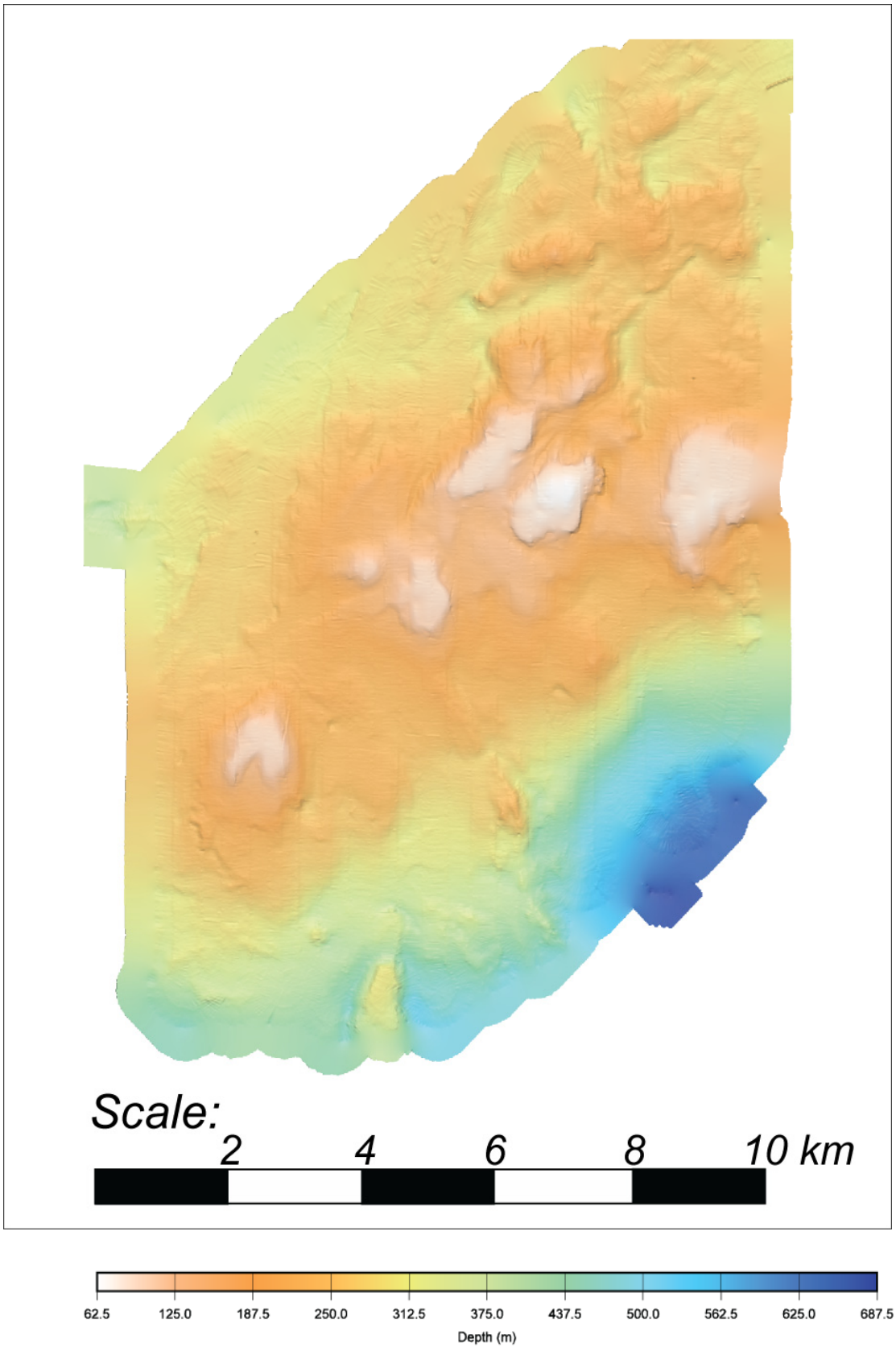
Scale:
2
4
6
8
10 km
62.5
125.0
187.5
250.0
312.5
375.0
437.5
500.0
562.5
625.0
687.5
Depth (m)

Figure 5-3A

Figure 5-3A Perpendicular non-projected map of the Barbados Shallows showing the scale of the full area. The Shallows map covers approximately 10 kilometers (east-west) and 14 kilometers (north-south). This digital elevation model was constructed of processed multibeam sonar swath data from this study.

METHODS AND MATERIALS

The survey of the Shallows was performed on 18 October 2003, using the Atlas Hydrosweep DS–2 multibeam 15.5–kHz bathymetric swath sonar and a 3.5–kHz sub-bottom profiler of the R/V Maurice Ewing. This system utilizes up to 140 electronically aimed beams spaced with 2 degree intervals on the ship hull, thus covering a swath of sea floor up to 2.5 times the water depth. The entire area over the Shallows was surveyed with averagely spaced parallel tracks approximately 200-250 meters apart (Figure 4-7, Chapter 4). A few areas of the highest pinnacles (62 meters below sea level) were only covered 90-95% by the swath, its triangular geometry limiting coverage at shallower depths. On the other hand, below 600 meters depth there was a nearly 100% swath overlap of parallel tracks. The configuration of the bathymetric sonar of this transect was run in the "deep" mode, which is not considered ideal for water depths below 100 meters. As a result, approximately 1 % of the surveyed area at the shallowest depths did not get swathed completely between parallel tracks. The ship's speed during the Shallows bathymetry survey was between 9 and 10 knots, resulting in a horizontal along-track resolution of 4-6 meters per 1 second spaced pings. However, in most cases the sea bottom ping interval was less than that, resulting in an average 3-5 meter along-track resolution, but offering a resolution of as good as 3 meters on the shallowest areas. The across-track ping return resolution depending on depth varied from less than 2.5 meters (close to the center beam and 70 meter water depth) up to 21 meters (furthest away from the center beam: this resolution

decreases with water depth and distance from the central beam according to the geometry of the ping angles of the swath.

The open-source Unix software package "MB-Systems" (Caress and Chayes, 2006) was used to edit, process, and grid the Hydrosweep raw data. The results are presented at an overall resolution of 11 meters per pixel in both the shallowest (less than 60 meters below sea level) and in the deepest areas (less 500 meters below sea level). This result is made possible via specialized processing in MB-Systems for even the low resolution areas. The MB-Systems program takes advantage of the returning pings being reflected by a 'footprint', a predictable elliptical area rather than a single point on the sea floor. The MB-Systems software then calculates a grid interpolation from the beam footprints, rather than from a weighting function tied to the grid cell spacing determined by centered grid-box points (Caress & Chayes, 2006). The beam footprints are calculated using the angular beam widths and the sonar altitude above the seafloor. For each grid cell, with a beam footprint lying fully or partially within the cell, a weighting value is determined by the fraction of the beam contained within the cell (the beam does not have to be wholly hedged by the entire cell area). This approach allows outputting data grids that have a resolution greater than that of the raw data, especially in the case of overlapping tracks. This approach was chosen for the Shallows data because in its course, the survey spans relative large depth variations. Sensible results are thus ensured in deep regions where the grid cells may be much smaller than the beam footprints, in spite of the fact that cell size originally was defined by the shallower high-density data. As to the 'footprints'

themselves, these are normally assumed to be flat, representing an average depth within which the sonar return is recorded as a single ping. With regard to the morphological characteristics of the footprint, in particular of the angles of reflection off of these features, influence on ping return may either be favorable or unfavorable. In any case, this influence does not affect the time elapsed between the ping signals leaving the transducer and their arrival in the hydrophone, but may affect the quality and intensity of the return.

Figure 5-3B shows the 3D-projection, relief-shadowing, color-coding, and contouring as these were done using Fledermaus Pro (IVS3D). The geospatial relationships, additional geo-coding, and contouring were calculated in ArcMap 9.1 (ESRI). ImageJ (a software from NIH) was used to enhance (stretch) the bit-depth range of grayscale images so as to enhance subtle backscatter variations that otherwise would be less visible.

Processing bathymetric data

A common characteristic of bathymetric data-sets is the influence of several types of artifacts in the raw data. Mostly this is caused by combinations of electronic noise, but there are also other sources. Some of these artifacts are caused by combinations of real-time variations during collection and must be dealt with extensively and carefully through both automatic processing and manual editing in MB-Systems. The research vessel, while collecting data on the

Figure 5-3B

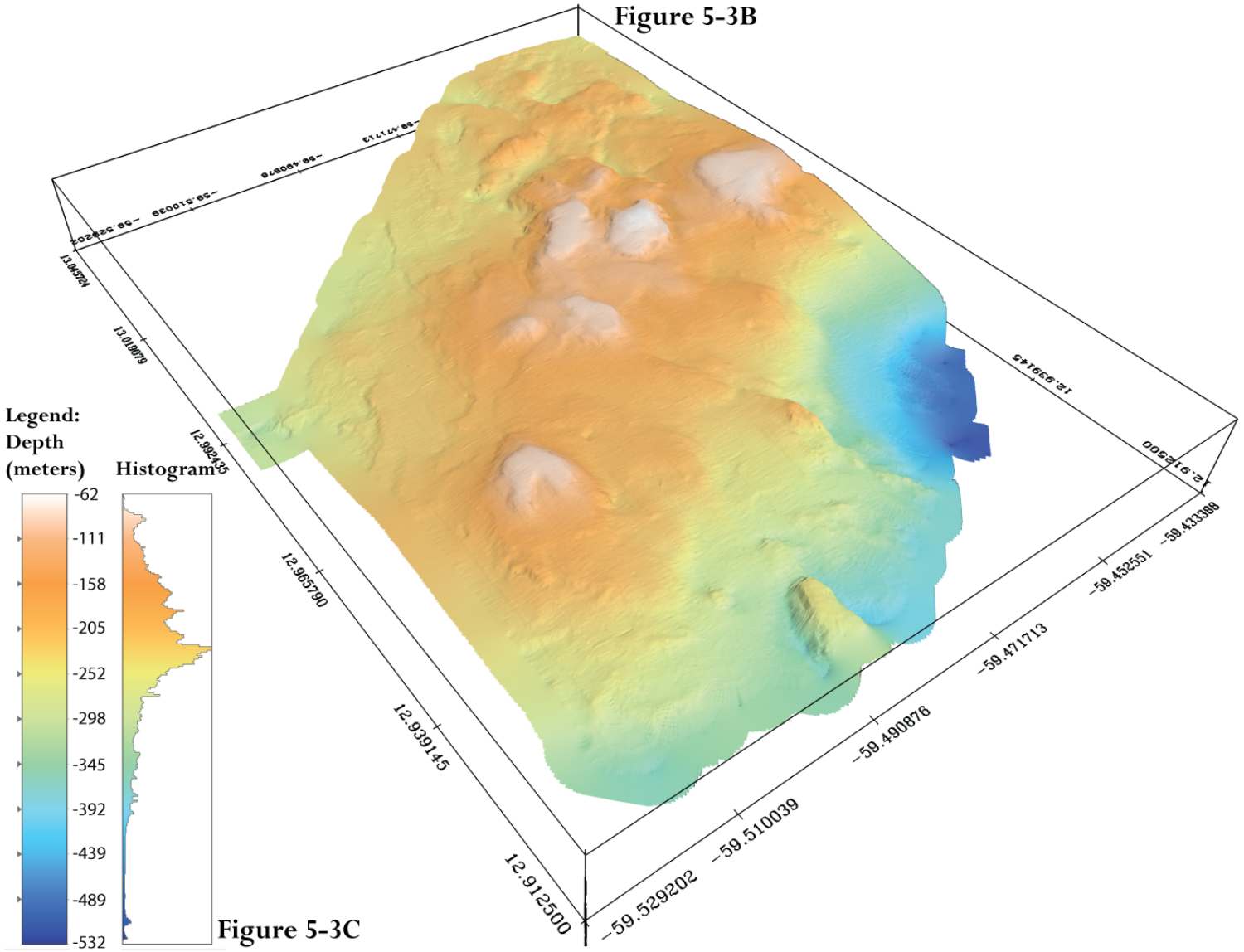

Legend:
Depth
(meters)

Histogram

Figure 5-3C

Figures 5-3B and 5-3C: Bathymetric Map of the Barbados Shallows, made from Hydrosweep 2 sonar data processed in MB-Systems and projected in Fledermaus Pro (see the text for details on data collecting, processing, and projecting). Scale as in Figure 4-7.

sea surface, is subject to a three-dimensional displacement, primarily resulting from varying sea-stands. To counter some of the problems involved here, the R/V Ewing utilized three on-board gyroscopes and GPS receivers, accurate to less than a meter, used as spatial fix points to control and correct for these various sources of real-time data variability. Data streams that may be affected by unwanted spatial and temporal variables include, but are not limited to; ship speed, spatial positioning (GPS), roll, pitch, heave, tilt, yaw, tide, water sound velocity profile, salinity, water temperature, depth, sea bottom reflection characteristics, electronic noise and gain locks etc. The real-time displacements were recorded simultaneously with the electronic data streams of the ping returns. Most newer systems are capable of applying the necessary corrections in real time, in addition to being gathered in a set of parameter files (see Appendix 4-2, Chapter 4 for an example of available parameters). These parameters are applied as corrections during the post-processing of each data file, using the MB-Systems 'mbprocess' command. Every data file must be inspected and those containing swaths with "bad" pings are flagged manually in the MB-Systems program 'mbedit'. The advantage of using the MB-Systems program is that many of the "bad" pings can be flagged automatically by defining a filter which eliminates "unrealistic" features in the data. Typical examples include excessive slope values, streaks from consistently poor performance of one or more hydrophones and excessively long or short deviations from the expected ping returns, as based on depth, temperature, and salinity profile of the sea water, all of which affect sound velocity. The center beam signal is stronger by default on most multi-beam

bathymetry systems, thereby ensuring a bench-mark for ping returns in the swath data.

RESULTS

Bathymetry data, spatial analysis, and models of the coral provenance since the last glacial maximum are shown in Figures 5-1 to 5-21. The maps vary in scale; for instance, the Shallows bathymetric map (Figure 5-3B; letter sized print) is approximately on the scale of 1:50,000 at the center of the map and varies along the north-south axis according to the perspective of the 3D-projection. This kind of projection renders the maps unsuitable for precise navigation. In contrast, our orthogonal maps (e. g. Figure 5-3A) of the same model, are precise to a couple of meters and thus excellent for navigation.

Map descriptions

Figure 5-3A show a digital elevation model (DEM) as it is viewed directly above the center area, viz., orthogonally to the average surface plane of the Shallows. Figure 5-3B shows the 3-D projection of the same digital elevation model, but viewed from a lower angle above the plane and from the south-west. Bill Haxby's color scheme (Haxby et al., 1983) was used to color code the topography based on water depth, ranging from 532 meters below sea level (dark blue) to 62 meters below sea level (white). The relief shading was done by

artificially illuminating a 10-times vertical exaggerated digital elevation model of the gridded bathymetry data and then draping the shading result on the non-exaggerated model. The enhanced shading effect allows for an appreciative advantage both in our analysis and visual inspection, but without introducing an unrealistic and visually confusing vertical exaggeration of the real relief. The orthogonally projected data are shown with a 3-times vertical exaggeration, so as to better appreciate the shadowing-effect of the sea floor relief and to further enhance the topographic details for analysis. For both maps (Figure 5-3A and 5-3B), the illumination source was set to originate at an azimuth angle of 175 degrees and 40 degrees above the horizon. The result highlights the topographical features by illuminating the southern slopes and creating shadows on the northern ones.

Contours on the bathymetric maps were chosen at 20 meter equal intervals, starting from the shallowest features at 62 meters below sea level to the deepest levels of approximately 532 meters. All contours were calculated and drawn using Fledermaus Pro and ArcMap. Figure 5-4 shows the contour information as an interpolated surface of the digital elevation model. The white and pink colors represent the possible exposures of reef structures, presumably dominated by species such as *Acropora palmata* and *Montastrea annularis* in the lightest shaded areas. In Figure 5-5, only the 10-meter contour lines with the depths are shown.

By artificially exaggerating the topographical relief for the illumination, features that are not recognizable by regular contouring become visible (compare

Figure 5-5 with Figure 5-3B) and some of the effects of the regular artifacts, such as the characteristic bathymetry swath-pattern (often called 'sushi-mat' pattern) may be reduced.

The Shallows bank structures are assumed to have been constructed by successive reef-growth at various times, the last of these during the last 31,000 years (see also the Discussion, below). However, these reefs may have had their older foundations laid during earlier glacial cycles during Termination II. We assume that the morphology, as imaged in our bathymetric survey today, shows the resulting surfaces of reefs that grew since the last glacial maximum, although these probably cap older structures reflecting the sea level changes during the previous interglacial period. The reddish colors in Figure 5-4 represent areas where the deeper growing species may have grown during the last glacial low-stand, in accordance with the sea level curve pictured in Figure 5-6, which is based on corals from other nearby areas offshore Barbados (Peltier and Fairbanks, 2006 and references there). Yellow to green areas represent possible deposits of carbonate sands and rubble from reefs which grew at higher strata. The second contoured surface in Figure 5-5 shows only the contour-lines with no surface interpolation. The curves are color-coded to match that of the 'Haxby' (Haxby et al 1983) palette used for the main bathymetric map (Figure 5-3B). For both figures the contours where smoothed, using a 2 by 2 cell median filter.

Figure 5-7A is a result of a slope analysis carried out using MB-Systems. The slope information were binned in areas of like steepness. This is also shown as a histogram of the distribution of steepness for all cell pixels (which are

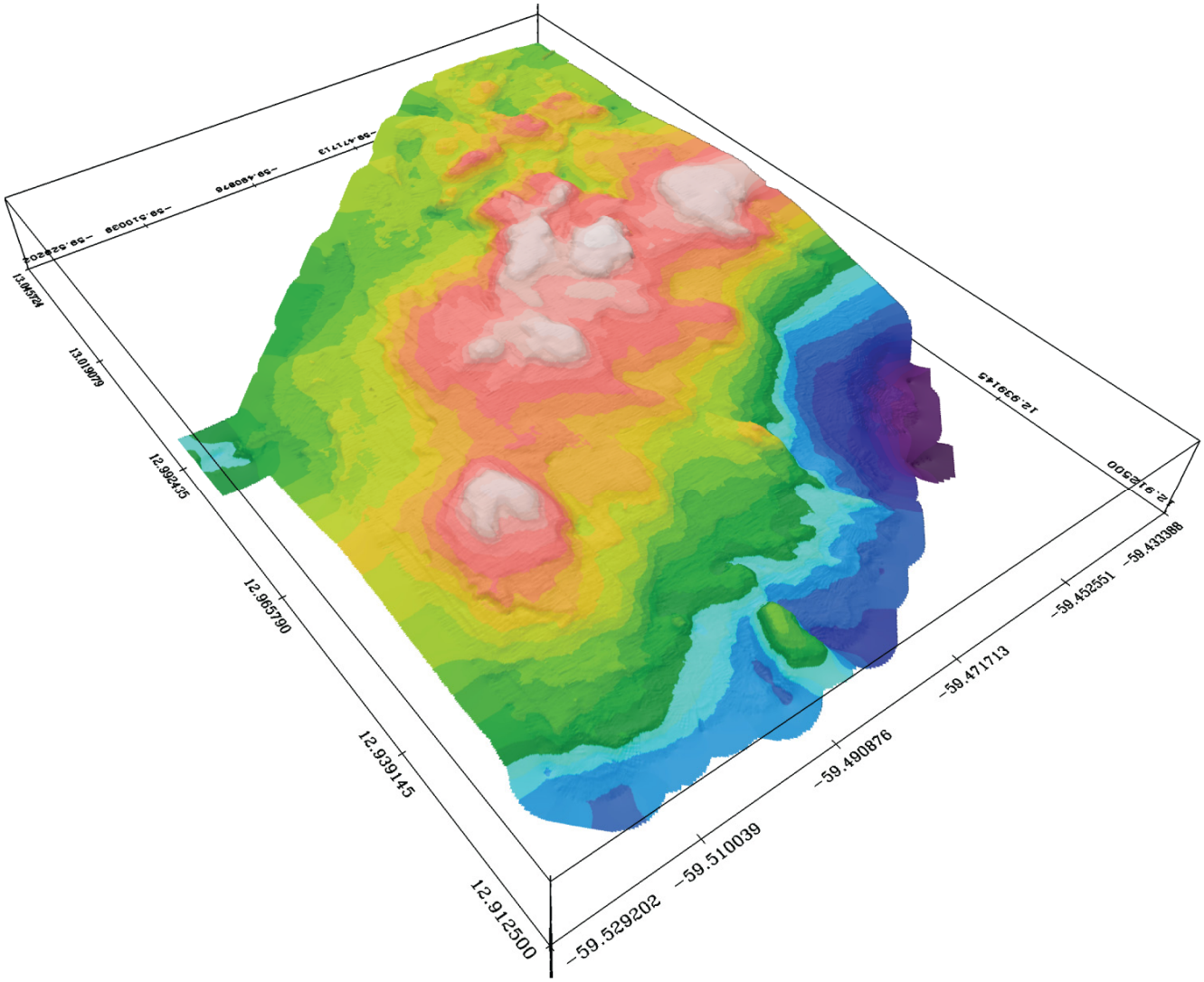
13.019079
12.992475
12.965790
12.939145
12.912500
−59.529202
−59.510039
−59.490876
−59.471713
−59.452551
−59.433388

Figure 5-4

Figure 5-4 Surface analysis of the Shallows, showing variations in elevations (color coded for clarity), as well as a rough distinction between major constructional pinnacle reefs (white shades), coral sand and rubble deposits (red shades), and Pre-Pleistocene deposits (green and blue shades). Z-heights are exaggerated 3 times. Scale as defined in Figure 4-7.

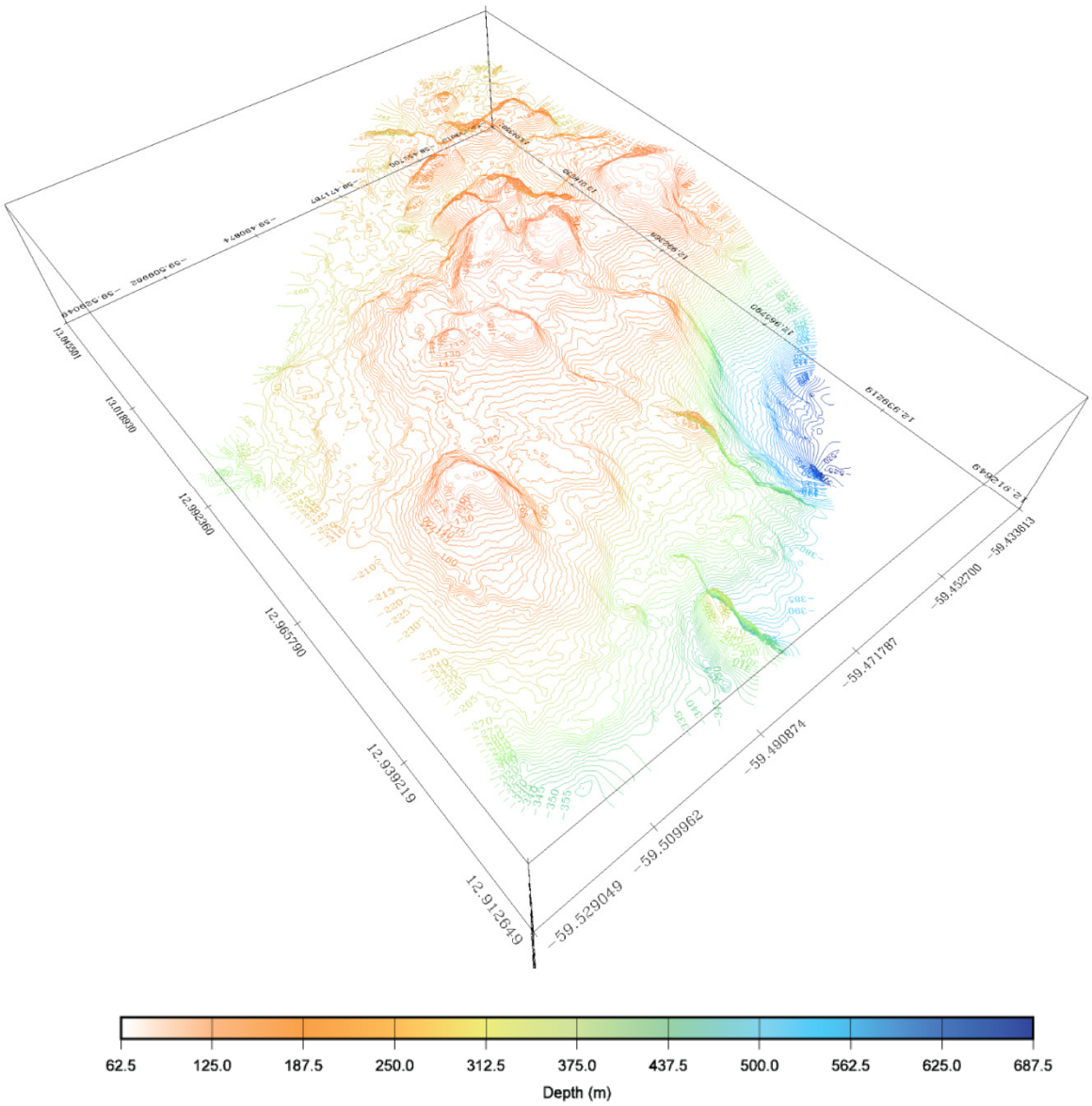
13.018000
12.992360
12.965790
12.939219
12.912649
−59.529049
−59.509962
−59.490874
−59.471787
−59.452700
−59.433613
62.5
125.0
187.5
250.0
312.5
375.0
437.5
500.0
562.5
625.0
687.5
Depth (m)

Figure 5.5

Figure 5-5 Contoured map of the Shallows used for spatial analysis. The 5 meter contour intervals are marked on the map surface. Z-heights are exaggerated 6 times. Scale as defined in Figure 4-7.

color-coded accordance with their distribution, such that the steepest areas are orange to red, whereas the flat areas are represented by green and blue hues). Generally, most of the slopes on the shallows have low angles, as indicated by the histogram distribution (Figure 5-7B). The exceptions are the cases where the corals successively built reef tracts and created steep fore-reef slopes, even though the steepest slopes, judging from their construction, were probably carved out later due to high erosion rates. (Such could be the case in areas with higher wave energy and prevailing surface currents from the east, especially on the windward (eastern) sides of the Shallows banks).

The slope data processed in MB-Systems are projected onto the model of the original bathymetry DEM (Figure 5-3B). The data-holes (some of them showing red underlying color) are large cells for which the slope data gridding (created according to the criterion established earlier) failed to provide enough nodes to feed into the algorithm. The criterion in question unambiguously determined that, in order to pass, the cell must satisfy at least a 50% equally distributed data coverage within a 50 by 50 meter area, thereby avoiding unfounded interpolation over data gaps. The final resolution of the successful slope cells is 11 by 11 meters, thus matching the resolution of the main bathymetric map in Figure 5-3B. Figure 5-8B is a drawing depicting the prevailing ocean currents in the Atlantic (after Tomczak and Godfrey, 2003). The Barbados Shallows are affected by the joining of two main warm ocean surface currents moving from east to west: The 'Southern Equatorial Warm Current' (SEWC) moves up along the eastern coast of South America until reaching the Lesser Antilles. There it meets the 'Northern

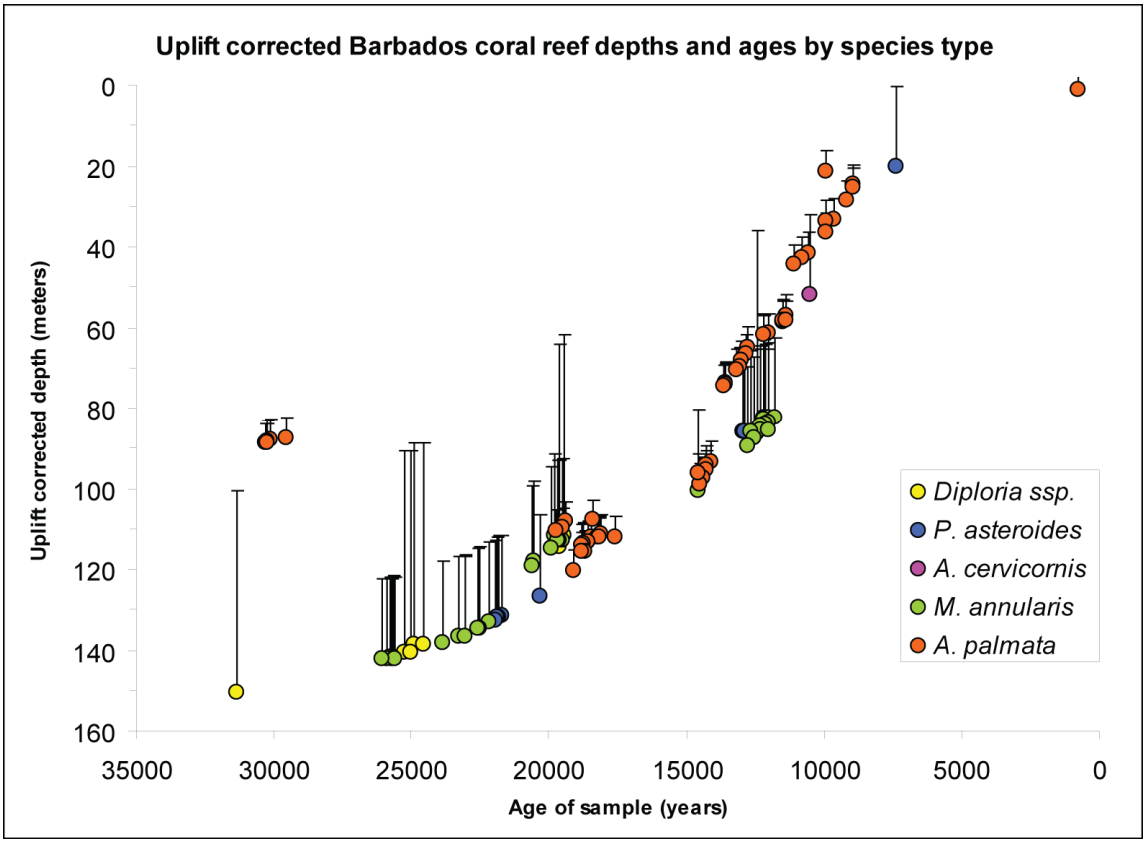
Uplift corrected Barbados coral reef depths and ages by species type
Uplift corrected depth (meters)
0
20
40
60
80
100
120
140
160
35000
30000
25000
20000
15000
10000
5000
0
Age of sample (years)
Diploria ssp.
P. asteroides
A. cervicornis
M. annularis
A. palmata

Figure 5-6

Figure 5-6 Uplift-corrected sea level data from Barbados. (Coral sea level data from Peltier and Fairbanks, 2006). P = Porites, A = Acropora, M = Montastrea. Error bars indicate the presumed maximum depth in the water column where the individual species are most likely to grow.

Figure 5-7A
Slope Analysis

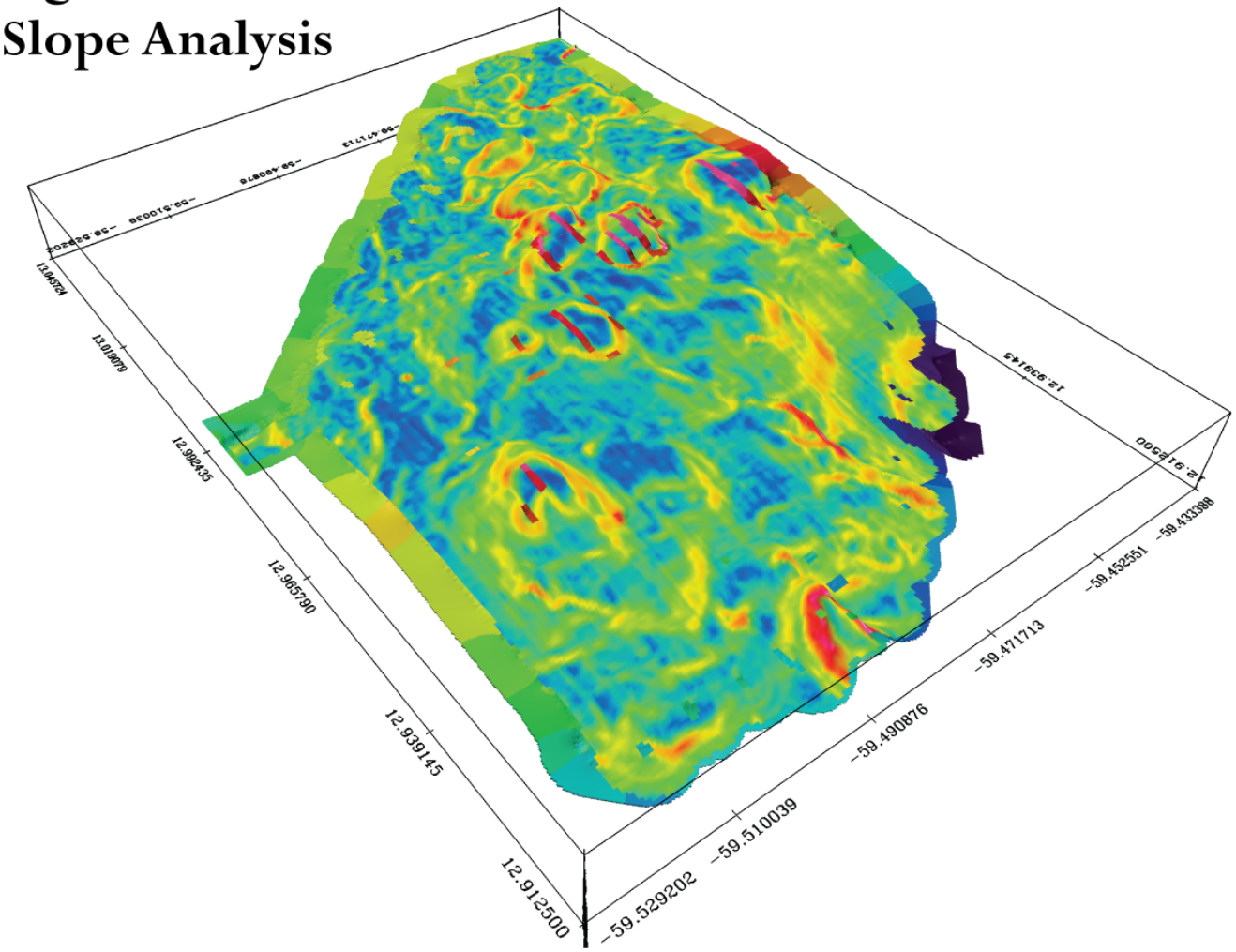

Slope legend: (degrees)

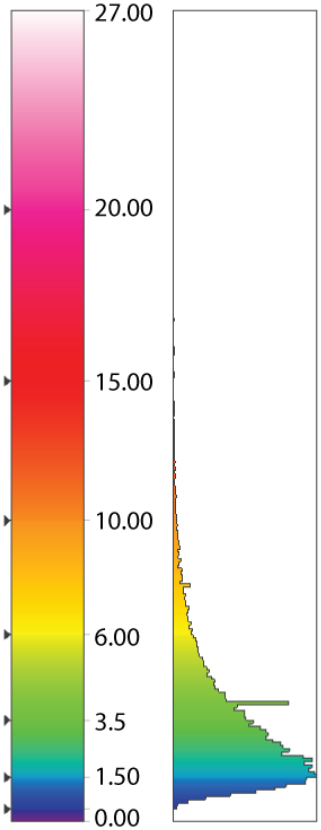

Figure 5-7B

Figures 5-7A and 5-7B Slope analysis of the Barbados Shallows, whose slopes are used in the analysis of possible reef cliffs. Dark red areas indicate the steepest slopes with an inclination of between 15 and 27 degrees. Z-heights are exaggerated 3 times. Scale as defined in Figure 4-7.

Equatorial Warm Current' (NEWC), which moves east to west from the African coast. Both the Northern and the Southern Equatorial Warm Currents flow from east to west. They meet and mingle east of the Caribbean islands on approach to Barbados. On approaching from the east, the prevailing surface currents meet the steep underwater slope on the leeward side of Barbados, which surges upwards over a couple of kilometers from below 2600 meters to the shallow waters of 200-300 meters below sea level. This geometrical layout has a profound effect on the ocean currents around the island. The ocean currents are pressed both to the north and to the south of the island, thereby creating a drag which results in the currents' predominantly south-southwesterly direction over The Shallows. The drag effect makes them carve out the main direction of sediment transportation, as well as the channels around the Shallows' north-eastern areas that may be a result of long term effects of gouging by the swift currents (Figure 5-8B). The arrows representing the prevailing currents over the Shallows were drawn, based on a visual interpretation of predominant 'gouged out' features and of the general sea floor morphology, such that the predominant arrows indicate the places where the currents are believed to have been strongest over time.

Backscatter data

Backscatter signal images reflect sea floor textures and are used to interpret types of sediments, as shown in Figures 5-9A, 5-9B, 5-10 and 5-11. As a rule of

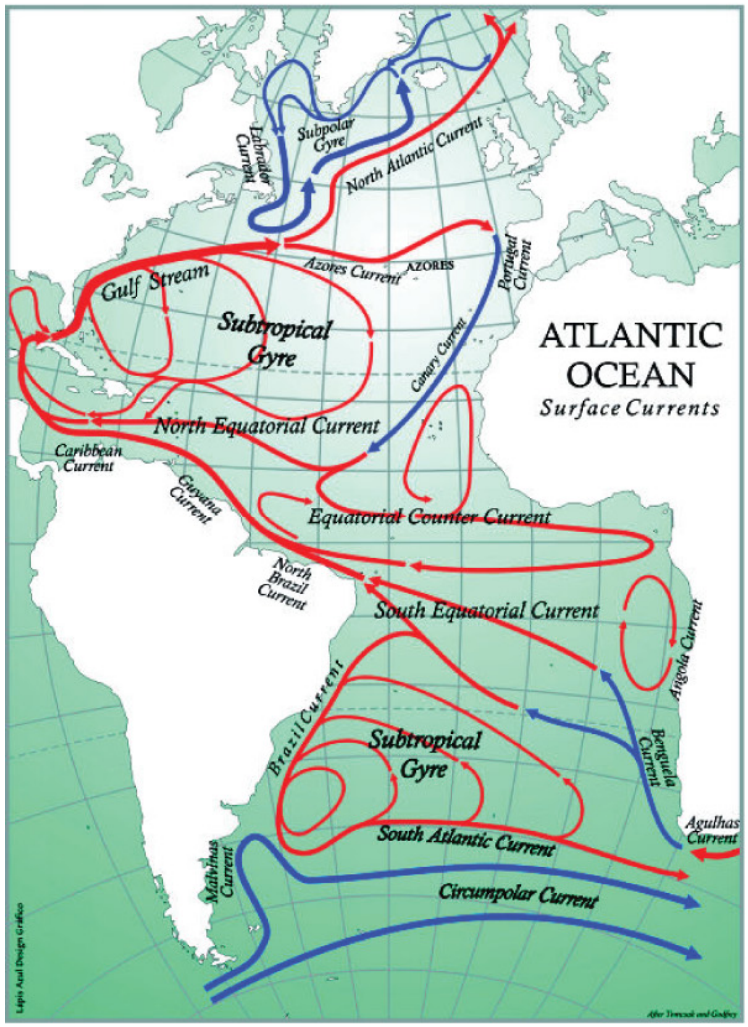

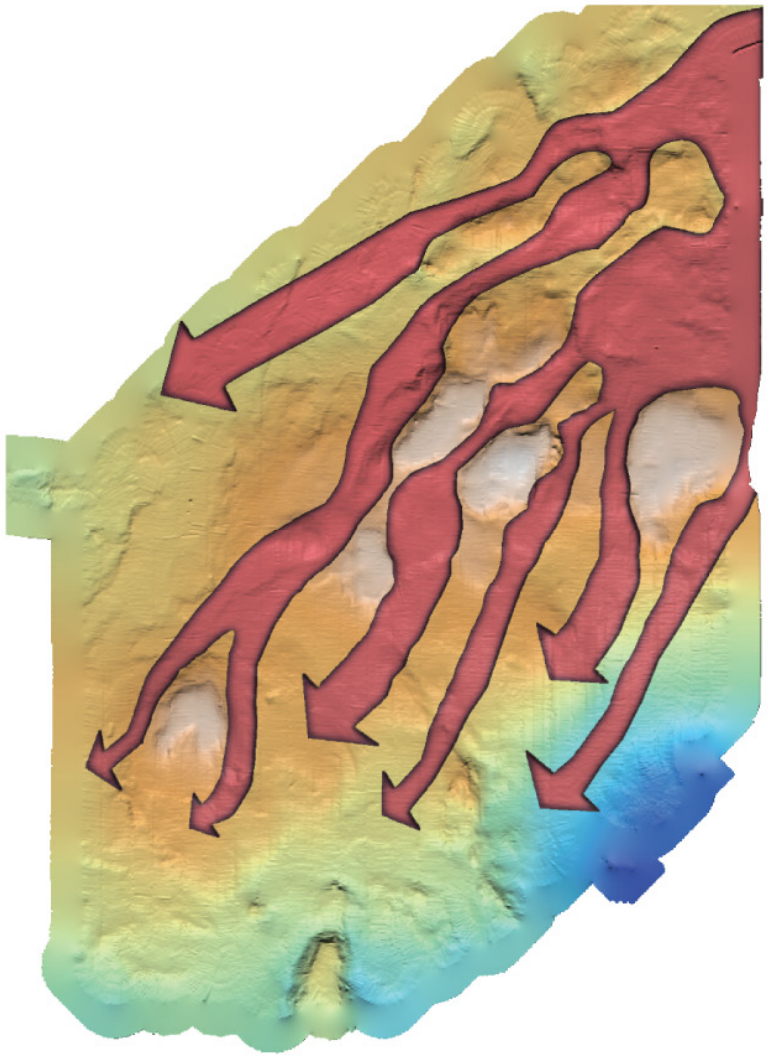

Figure 5-8A and 5-8B

Figures 5-8A (right) and **5-8B** (left) Map of the prevailing ocean currents 8A in the Atlantic Ocean (after Tomczak and Godfrey, 2003). The drawing in figure 5-8B depicts the prevailing currents around the Barbados Shallows. See text for explanation.

thumb, high return signals (shown as lighter pixels) are sound reflections from denser or harder materials, whereas low return signals (shown as darker pixels) are backscattered data from softer materials. The responses vary in accordance with the bottom's characteristic sediment textures: higher intensity signals reflect a hard, rocky bottom, whereas low intensity signals typically indicate fine sands or soft muddy deposits.

The map shown in Figure 5-9A is processed from the raw data (shown in Figure 5-9B) and was enhanced by stretching the bit-depth of the original image to span all of the 256 grays for an 8-bit image, using the open source java program ImageJ (NIH). The original 16-bit information (65528 gray levels) was reduced to an 8-bit structure (256 grays). The original image data bit-range showed a relatively narrow spectrum of responses (mainly between 156 and 186 levels of gray). Outside this range, the signal response was less than 1% for this particular dataset. The range of 156-186, covering at least 98% of the signal response, was then 'bit-stretched' to fit from 1 to 254, with any grays below 156 being set to zero (black) and any above 186 to 255 (white). The new bit-stretched image was then draped upon the digital elevation model (DEM) from the bathymetry data in the following manner: First, the image was geo-coded to match the area spatially in the Longitude and Latitude directions, using the WGS84 datum for projection. Following this, the image was processed in Fledermaus Pro to match the Z-height values for each pixel. (The slight coloration of the projected backscatter image (Figure 5-9B) is a deliberate transparent coloring effect of the Haxby color palette that was also used for the

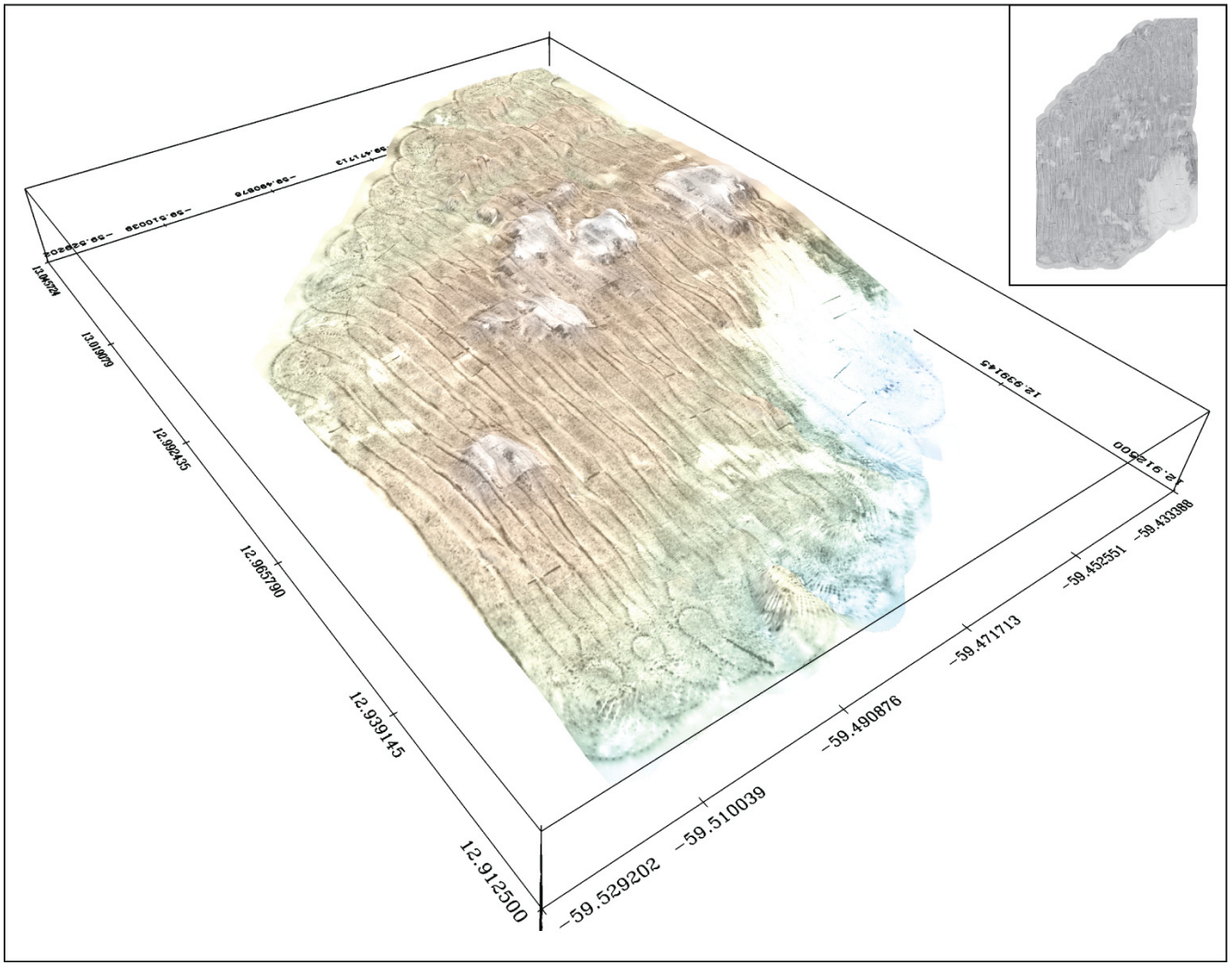

Figure 5-9A (inset) **and 5-9B**

Figure 5-9A (inset) **and 5-9B** Raw backscatter data of the Barbados Shallows. The backscatter data are draped on the digital elevation model from Figure 5-3B and colored with the Haxby et al. (1983) color palette. Z-heights are exaggerated 3 times. Scale as defined in Figure 4-7.

bathymetry data set in Figure 5-3B to enhance the visual effect). Figure 5-10 shows the bit-depth enhanced backscatter image showing three basic coloration gradients: green for rough or hard textured sediments, red for intermediate hardness/roughness, and yellow for softer and smoother textures of bottom sediments. As mentioned earlier, backscatter data are inherently noisy by nature, and artifacts of various and unknown kinds are visible as lines parallel to the ship track direction. The color-enhanced map is draped over the DEM based on the bathymetric survey; it, too, is colored using the shadow rendering technique described above. Figure 5-10 shows a slightly lighter illumination in the color shades on the southern faces and slightly darker ones on the northern ones, exactly as it was the case for the bathymetry DEM (Figure 5-3B). This effect should be interpreted differently from the backscatter data: it is merely a visual enhancement, since much of the Shallows sea floor is predominantly made up of carbonate sands and show low backscatter signals.

This interpretation of the various compositions fits in well with the lower backscatter intensity that was recorded. Compared to the typically higher signals from denser silicate rocks and sand, the hard signals in this case could come from the presumed Tertiary sandstone and the high silicate conglomerates that are known to underlie the coral cap of Barbados (Radtke and Schellmann, 2003) Other possible sea floor rocks could include older volcanic formations. However, such formations are only inferable from high backscatter signals, such as found in the deeper areas towards the south eastern section of the studied area (see Figure 5-10). Backscatter interpretations are naturally subjective and should therefore be

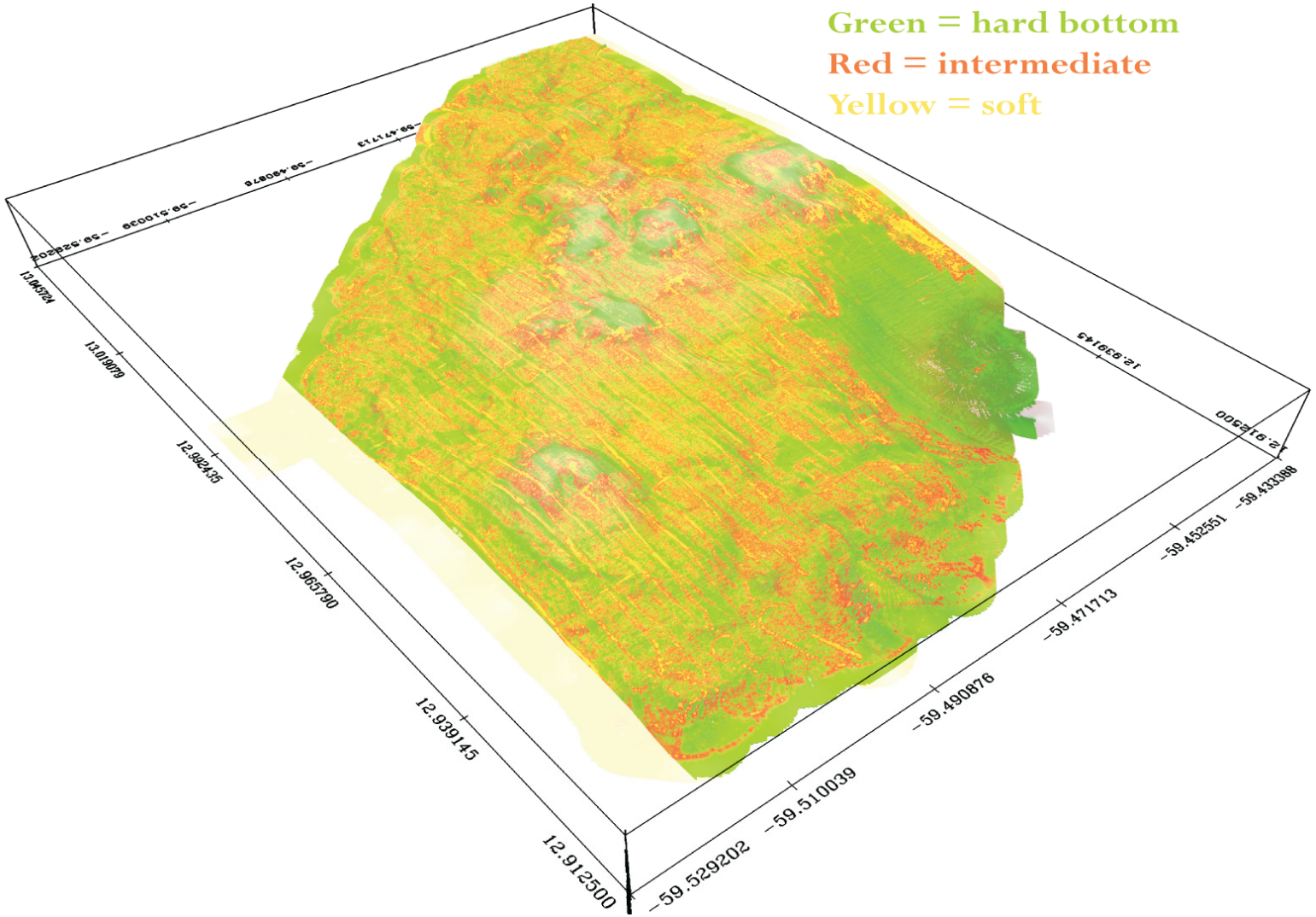
Green = hard bottom
Red = intermediate
Yellow = soft
13.045724
13.018079
12.992435
12.965790
12.939145
12.912500
-59.529202
-59.510039
-59.490876
-59.471713
-59.452551
-59.433388

Figure 5-10

Figure 5-10 Processed backscatter data of the Barbados Shallows draped upon the digital elevation model from Figure 5-3B. (See the text for explanation of the data processing and coloring). Z-heights are exaggerated 3 times. Scale as defined in Figure 4-7.

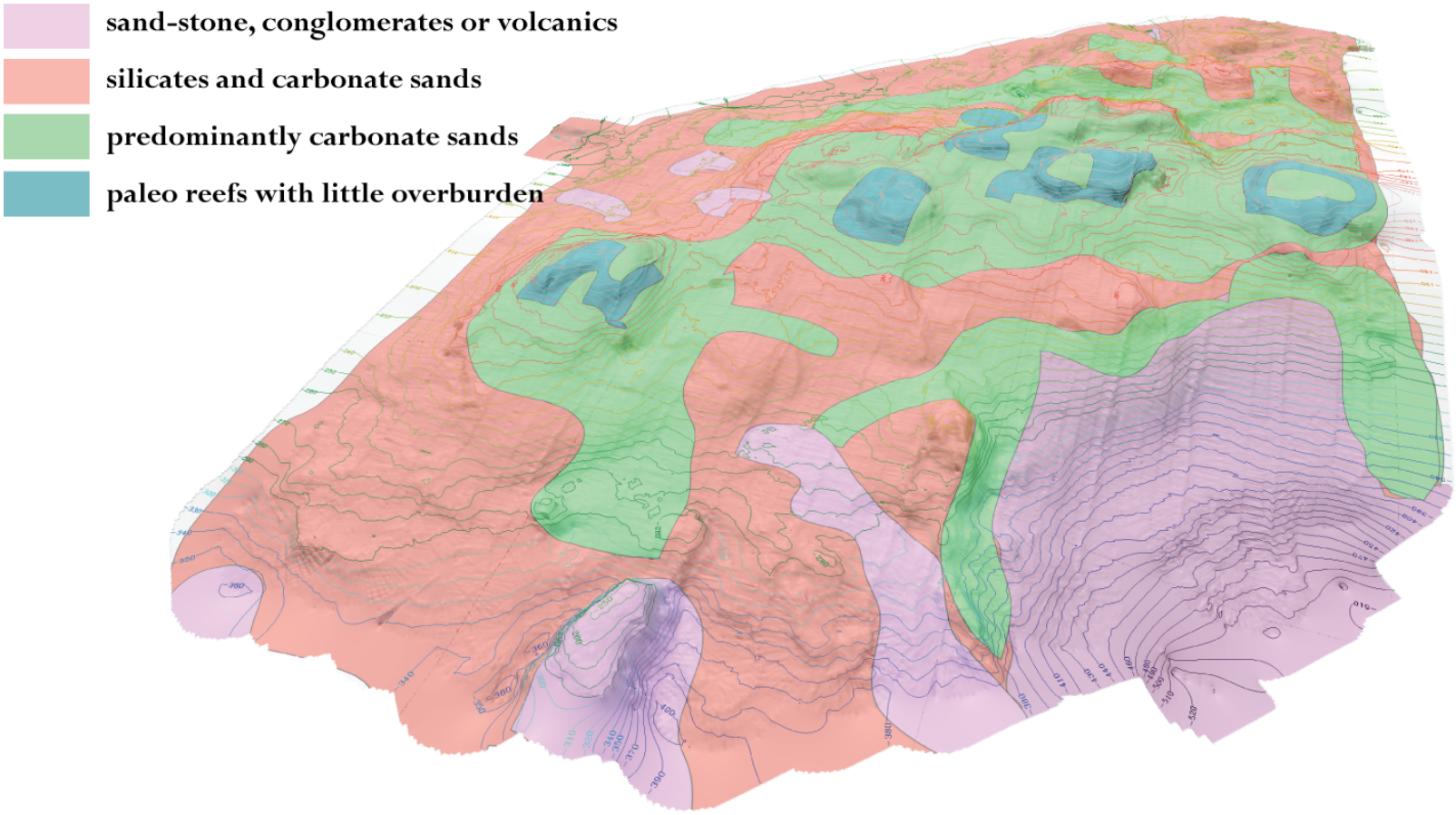
sand-stone, conglomerates or volcanics
silicates and carbonate sands
predominantly carbonate sands
paleo reefs with little overburden

Figure 5-11

Figure 5-11 Interpretation of the backscatter data on the Barbados shallows. This interpretation should not be taken too literally, as the backscatter signal is affected by electronic noise and varying sea floor vegetation. Z-heights are exaggerated 3 times. Scale as defined in Figure 4-7.

substantiated by other observations such as core logs, underwater photography, or grab and dredge samples. For example, preliminary testing (Mey et al., *in prep.*) confirm that central parts of the main plateau tops of the Shallows consist mainly of rubble and sands. A recent attempt to drill on the Shallows during a cruise undertaken with the R/V Knorr in April-May of 2007 pointed in the same direction. The backscatter data in Figure 5-10 support these observations by displaying slightly 'softer' signals around the central areas on the shallowest formations (60-80 meters). While these backscatter data clearly corroborate our survey, they are useful only as a rough guide to points of interests, and need to be followed up by higher resolution sonar surveys, and ideally, by visual inspection.

DISCUSSION

Spatial analysis of coral provenance

Coral provenance with changing sea levels was inferred by using coral dates and depth data for several species drilled elsewhere closer to the island of Barbados. The sea level data from the present and previous studies of corals drilled offshore Barbados (Fairbanks, 1989; Peltier and Fairbanks, 2006 and reference there) are shown in Figure 5-6. These data are uplift-corrected to account for the isostasy to make them directly comparable to modern sea level. This allows for direct reading of the water depth at the time of reef growth. The average reef-uplift rate used in this model is 0.36 mm per year. This would make

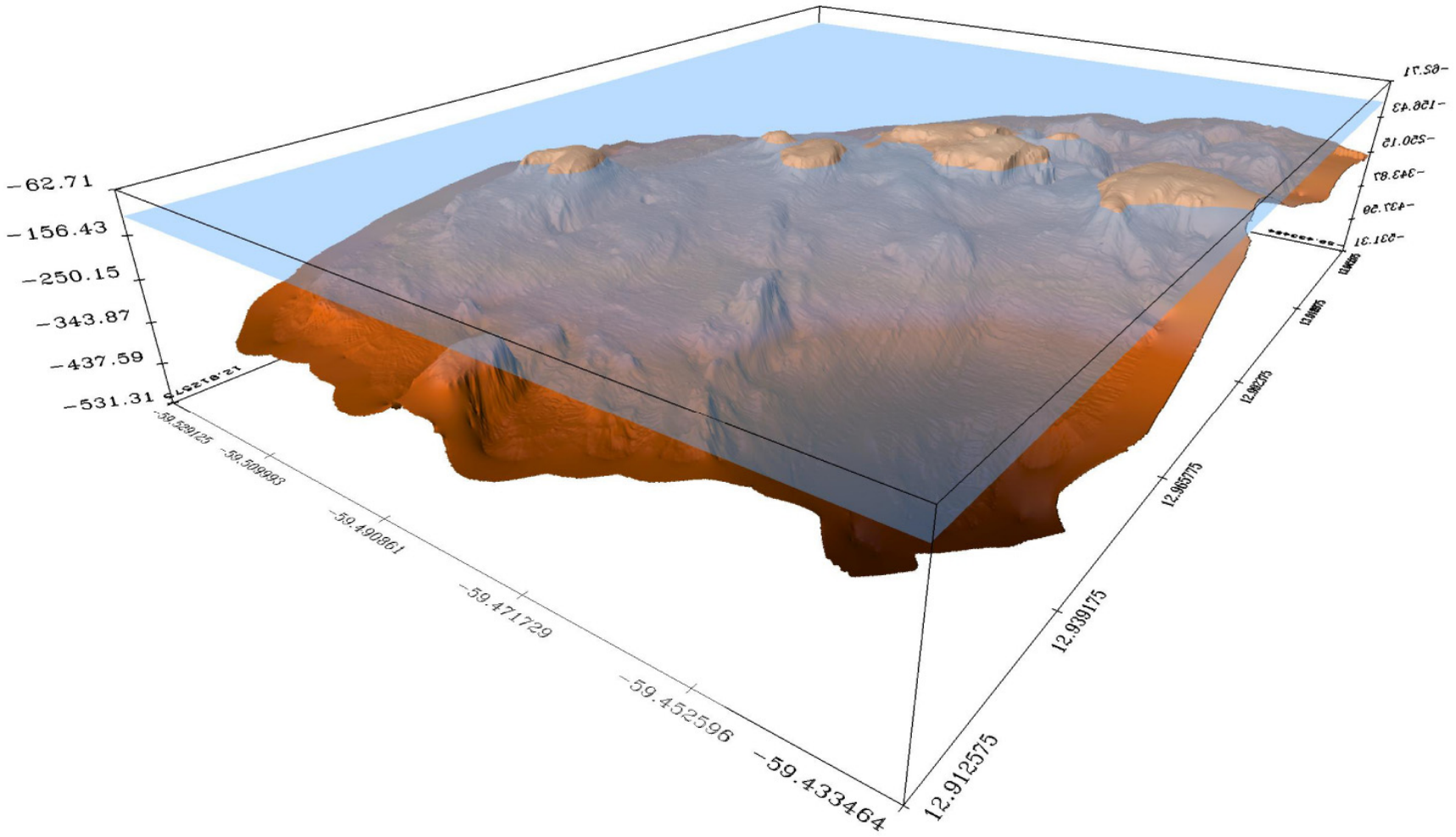
-62.71
-156.43
-250.15
-343.87
-437.59
-531.31
-59.433464
-59.452596
-59.471729
-59.490861
-59.509993
12.912575
12.939175
12.965775

Figure 5-12

Figure 5-12 The exposed areas of the Barbados Shallows 26,000 years ago, when the global sea level was approximately 120-125 meters below the present. The sea level adopted here is based on finds from corals in the Barbados reefs nearby (coral sea level data from Peltier and Fairbanks, 2006; see Figure 5-6). Z-hights are exaggerated 6 times to enhance the topographical variation. Scale as defined in Figure 4-7.

for a sea bottom level 31,000 years ago of almost 9 meters below the present. In other words, reefs that grew 31,000 years ago are nearly 9 meters higher today, relative to their original location and the sea level at that time. This correction has been applied to all the provenance intervals (Table 5-1 and Figures 5-13A to 5-21A) modeled for the various coral species, the models being based on today's sea bottom data and the core depth at which the corals were collected (Fairbanks, 1989). The spatial placements of habitat zones are inferred from these uplift-corrected sea level for five different coral species. The inferrers are based on the modern extent of habitat zones of the corals *Acropora palmata* (growing on the reef crest in the top 5 meter high energy environments), *Montastrea annularis*, *Porites asteroides,* and *Acropora cervicornis* (growing mostly on the slopes immediately adjoining the reef crests and in the lower energy reef flats and fore-reef slopes down to approximately 20 meters, and *Diploria spp.* (aka. 'brain coral'), growing mostly in the same places as mentioned above, but with a distinct preference for the lower energy environments on the reef slopes at depths down to 50 meters.

Figures 5-13A to 5-21A show the modeled and color-coded coral species habitats zone as it may have been back in time. Each color band represents the water column from surface to maximum depth of occurrence of the various species, as described above. Most species overlap in the upper waters except in the high energy zones, where *Acropora palmata* dominates the fauna. Figures 5-13B to 5-21B show profiles marked with dashed lines the reef topography. These profiles are color-coded according to what is modeled on the

Table 5-1 Paleo sea level and coral habitat zones below present sea level

Time (years)	*paleo sea level* [1]	*isostatic rise* [2]	*Acropora Palmata*	*Ma, Pa, Ac* [3]	*Diploria spp.*
9,000	-18.76 m	+3.24 m	-19 to -24 m	down to -38 m	down to -69 m
12,000	-55.68 m	+4.32 m	-56 to -61 m	down to -76 m	down to -106 m
14,000	-88.96 m	+5.04 m	-89 to -95 m	down to -108 m	down to -138 m
18,000	-101.52 m	+6.48 m	-102 to -107 m	down to -122 m	down to -152 m
26,000	-116.68 m	+9.36 m	-117 to -122 m	down to -137 m	down to -166 m
31,000	-78.84 m	+11.16 m	-79 to -84 m	down to -99 m	down to -129 m
36,000	-84.04 m	+12.96 m	-84 to -89 m	down to -104 m	down to -134 m
62,000	-72.68 m	+22.32 m	-73 to -78 m	down to - 93 m	down to -123 m
135,000	-77.40 m	+48.60 m	-75 to -84 m	down to - 98 m	down to -128 m

Table 5-1 Paleo sea level and coral habitat zones below present sea level

[1] *paleo sea level* = contour level on the present sea bottom where the water line was at the time (i. e. the paleo beach).

[2] *isostatic rise* = regional uplift since the time (years) assuming 0.36 millimeters per year.

[3] *Ma = Montastrea annularis, Pa = Porites asteroides, Ac = Acropora cervicornis.*

The habitat zones are estimated based on common occurrences of these five coral species: *Acropora palmata* grows in the high energy 0-5 meter zone from sea surface. *Montastrea annularis*, *Porites asteroides*, *Acropora cervicornis* typically grow in the 5-20 meter lower energy zones below the sea surface, but also grows below and above. *Diploria spp* is common in deeper 20-50 meter zone and also found at higher levels, but not below.

surface exposure along the dashed line, thus they do not represent depth-profiles. As it appears here they are artifacts of the Fledermaus program.

The Shallows morphology and the interpretation of coral provenance

As part of the Barbados Rise to the south of the island itself, The Shallows area included in this survey covers approximately 107 square kilometers. The Shallows is the only area on the Barbados Rise which had massive growing reefs, detached from the Barbados coastline[2]. During the last glacial maximum, it was comprised of several small islands and broad lagoons Figure 5-12. Even so, the Shallows were never land-fast with Barbados at any time during the Pleistocene. The remnants of the Shallows islands during the glacial low stand are clearly visible on the coral sea level bathymetric map as shown in Figures 5-3B and 5-12 (sea level at 120-125 meters lower than present) and is even more apparent in the results of the coral habitat zones as they are modeled through time (Figures 5-13A through 5-21A).

Geologically, the Shallows consist mainly of six large underwater banks rising 60-80 meters above the sea floor, all having relatively flat caps, varying only a few to ten meters in height from the bank edges to the centers. These plateaus very consistently plane out at 62-70 meters below sea level at their highest points.

[2] A recent survey (Mey et al., *in prep*) shows that the small Trader Bank, 2 miles south-southwest of Bridgetown, may also have been reef producing during the same time

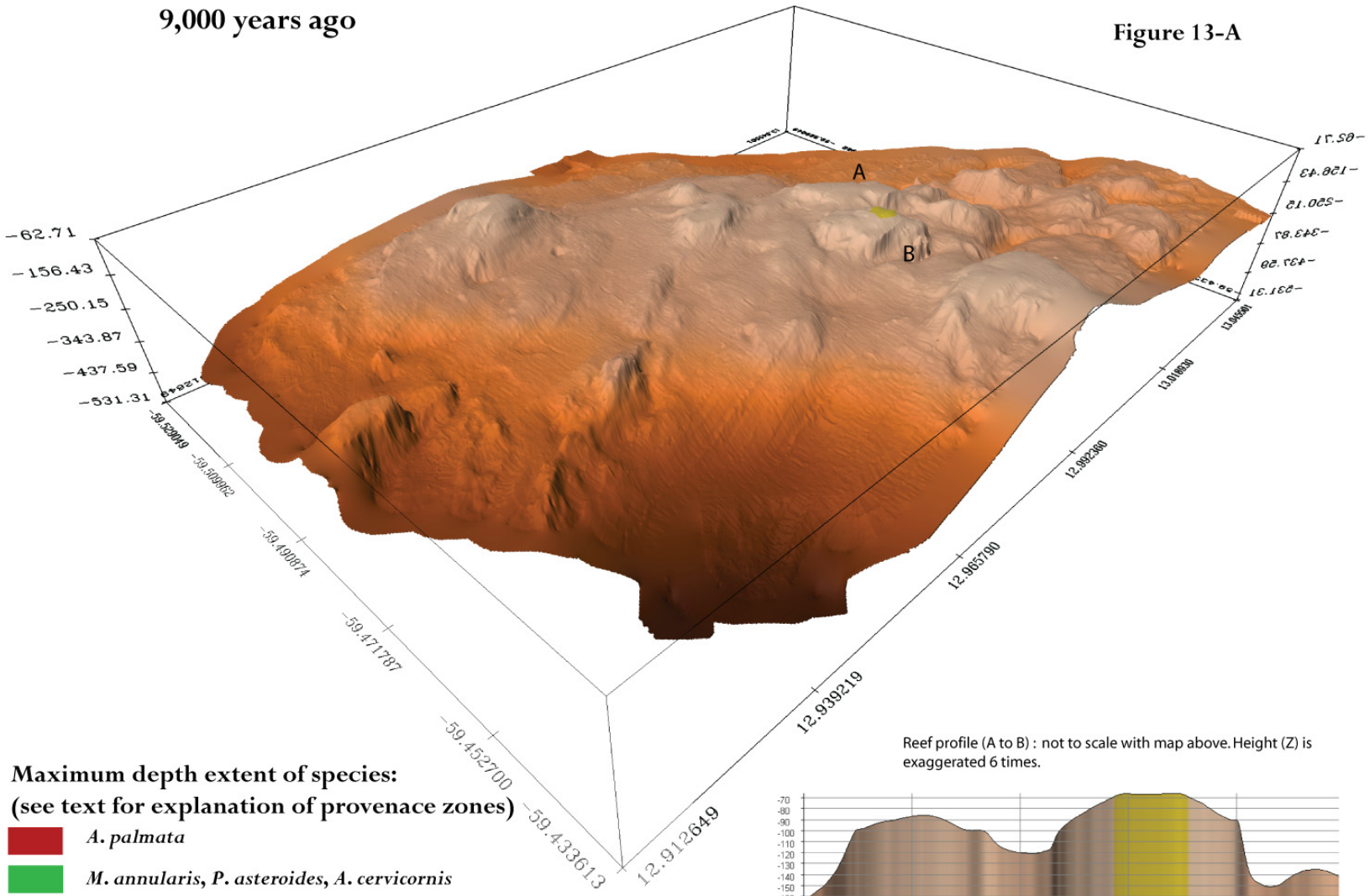

Figure 13-A

Reef profile (A to B) : not to scale with map above. Height (Z) is exaggerated 6 times.

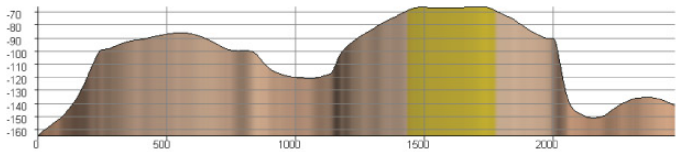

Figure 13-B

Figures 5-13A and 5-13B Modeled coral provenance on the Barbados Shallows at 9,000 years ago. The model is uplift-corrected (Bender et al., 1979; Speed et al., 2004) and is based on coral data from nearby Barbados reefs (coral sea level data from Peltier and Fairbanks, 2006, see Figure 5-6). *P.* = *Porites*, *A.* = *Acropora*, *M.* = *Montastrea*. Z-heights are exaggerated 6 times. Scale as in Figure 4-7

12,000 years ago

Figure 14-A

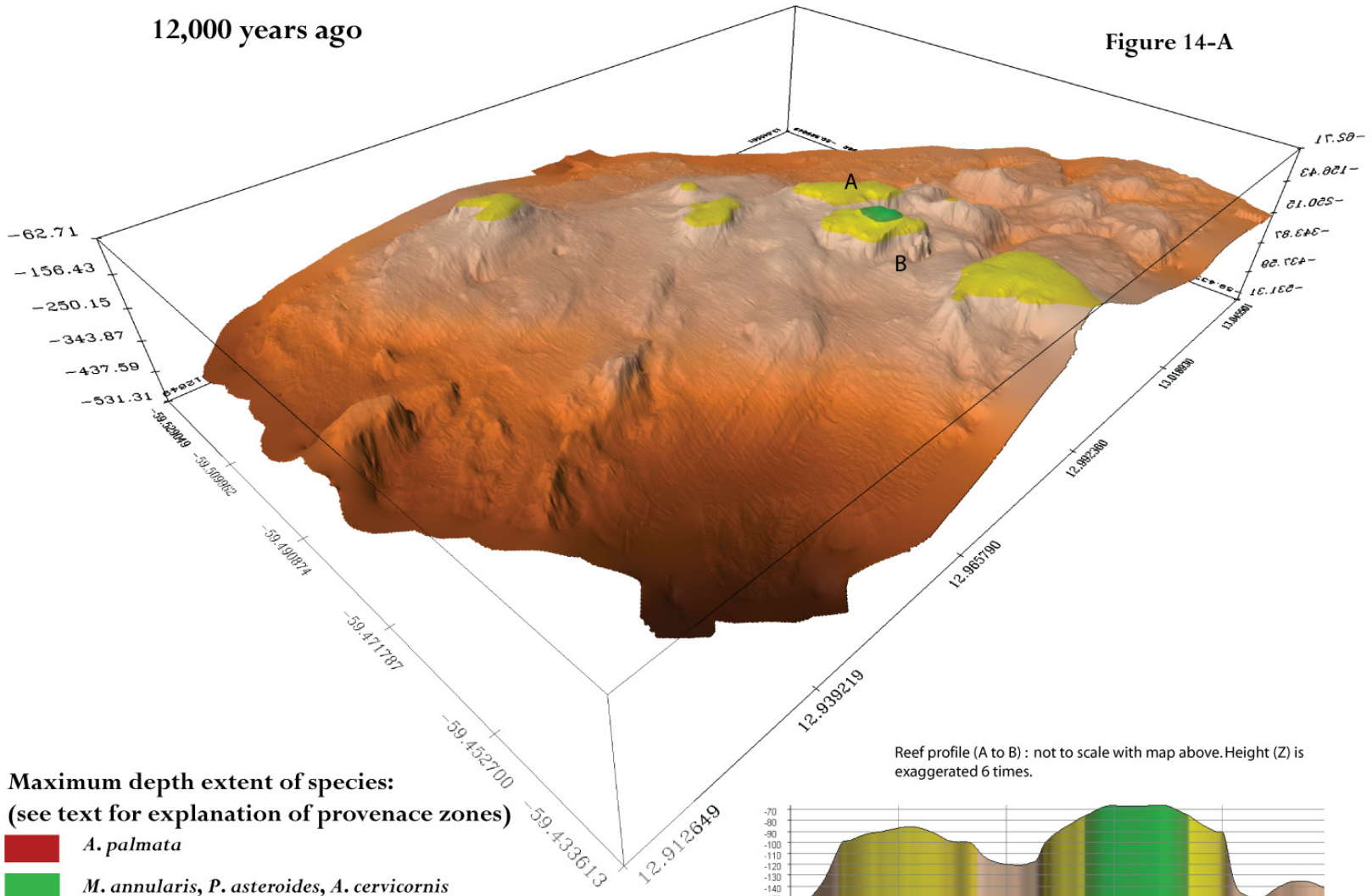

Maximum depth extent of species:
(see text for explanation of provenace zones)

- *A. palmata*
- *M. annularis, P. asteroides, A. cervicornis*
- *Diploria spp.*

Reef profile (A to B) : not to scale with map above. Height (Z) is exaggerated 6 times.

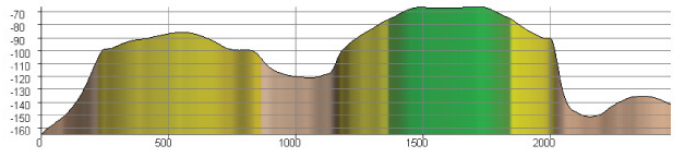

Figure 14-B

Figures 5-14A and 5-14B Modeled coral provenance on the Barbados Shallows at 12,000 years ago. The model is uplift-corrected (Bender et al., 1979; Speed et al., 2004) and is based on coral data from nearby Barbados reefs (coral sea level data from Peltier and Fairbanks, 2006, see Figure 5-6). *P.* = *Porites*, *A.* = *Acropora*, *M.* = *Montastrea*. Z-heights are exaggerated 6 times. Scale as defined in Figure 4-7.

14,000 years ago

Figure 15-A

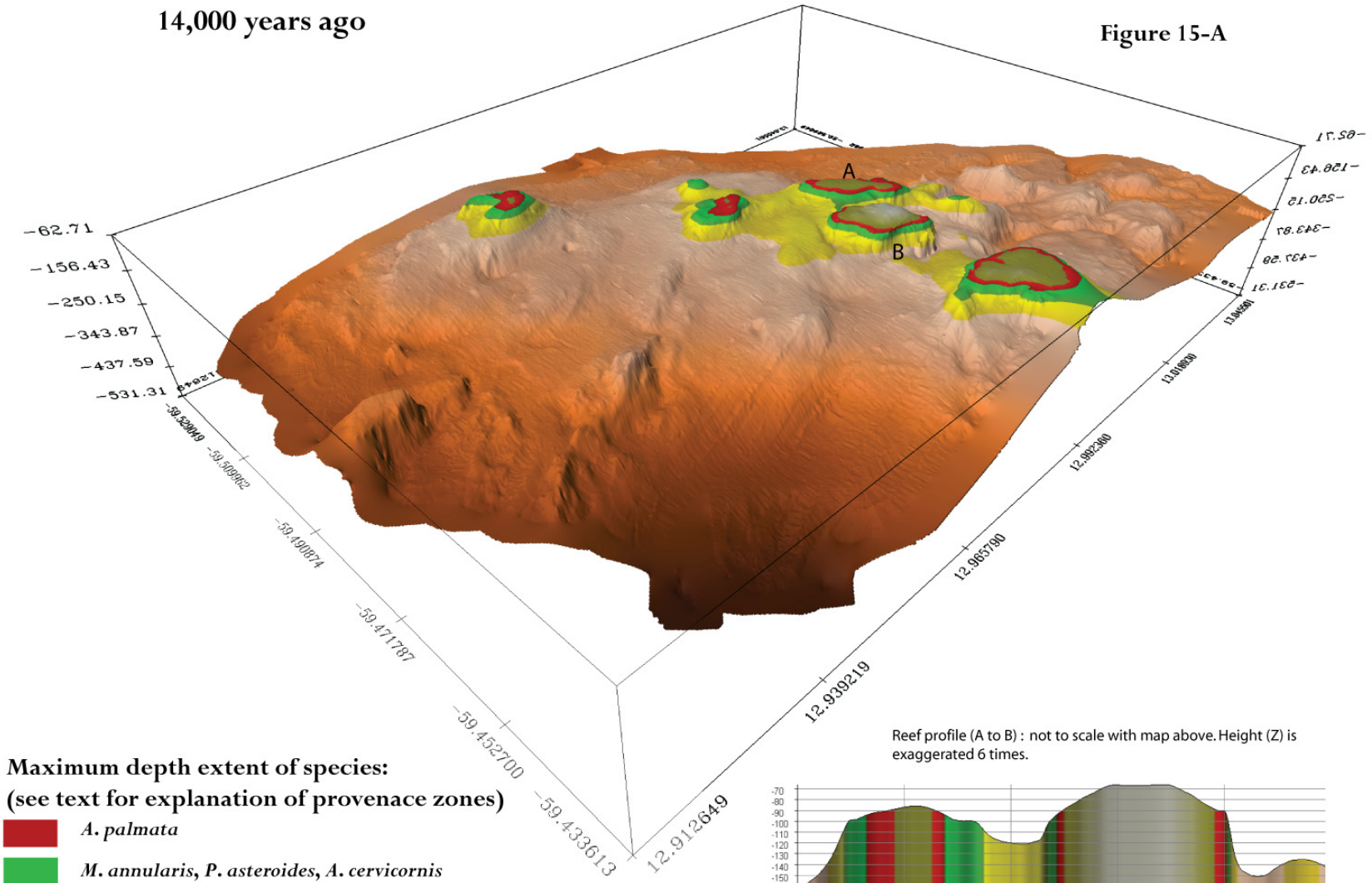

Maximum depth extent of species:
(see text for explanation of provenace zones)

- ***A. palmata***
- ***M. annularis*, *P. asteroides*, *A. cervicornis***
- ***Diploria spp.***

Reef profile (A to B) : not to scale with map above. Height (Z) is exaggerated 6 times.

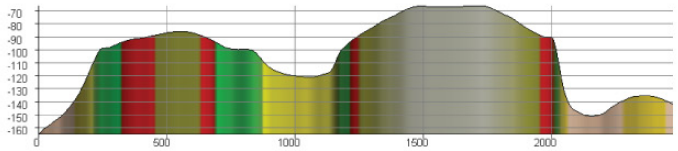

Figure 15-B

Figures 5-15A and 5-15B Modeled coral provenance on the Barbados Shallows at 14,000 years ago. The model has been uplift-corrected (Bender et al., 1979; Speed et al., 2004) and is based on coral data from nearby Barbados reefs (coral sea level data from Peltier and Fairbanks, 2006, see Figure 5-6). *P.* = *Porites*, *A.* = *Acropora*, *M.* = *Montastrea*. Z-heights are exaggerated 6 times. Scale as defined in Figure 4-7.

18,000 years ago

Figure 16-A

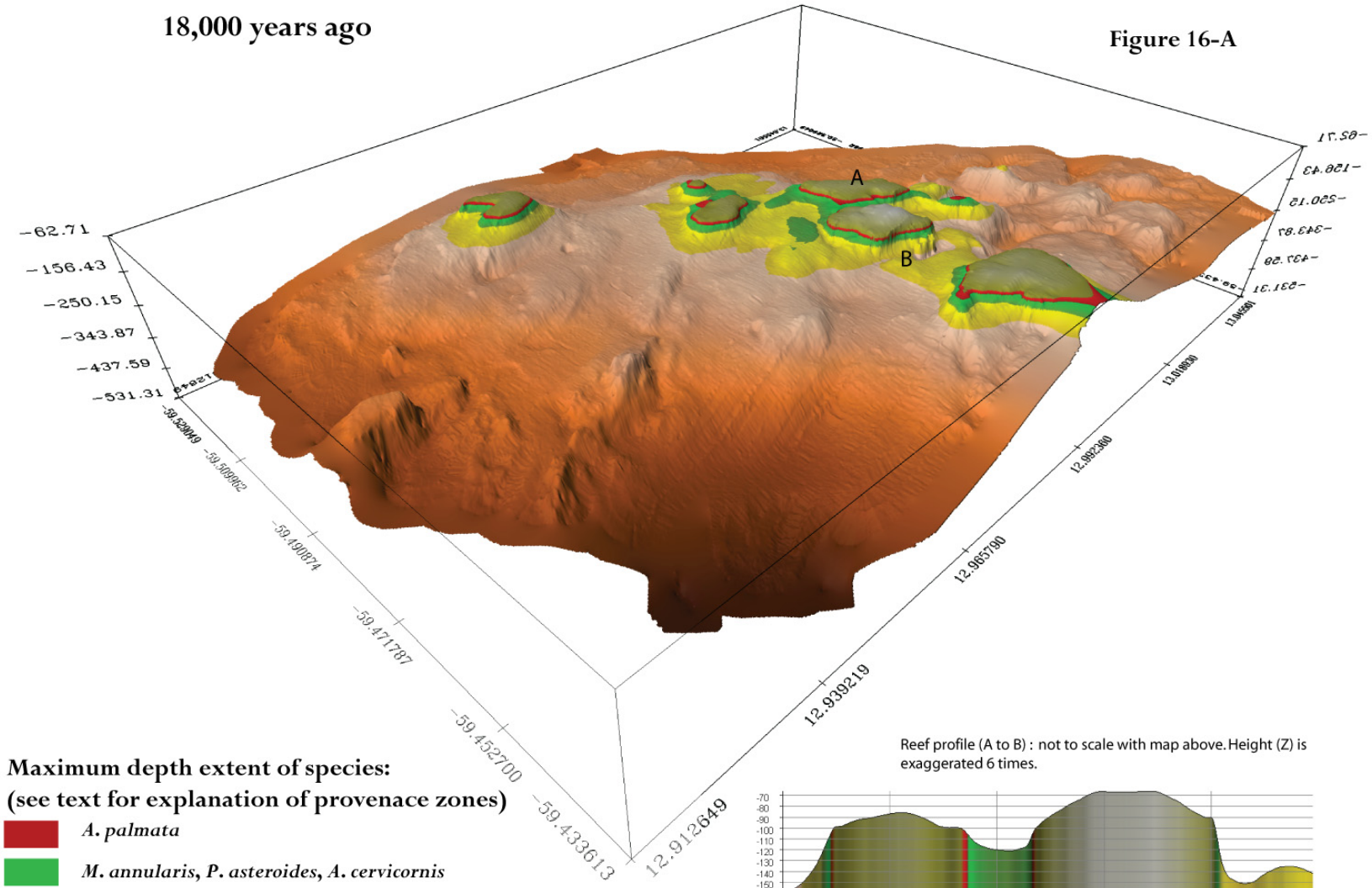

Maximum depth extent of species:
(see text for explanation of provenace zones)

- *A. palmata*
- *M. annularis, P. asteroides, A. cervicornis*
- *Diploria spp.*

Reef profile (A to B) : not to scale with map above. Height (Z) is exaggerated 6 times.

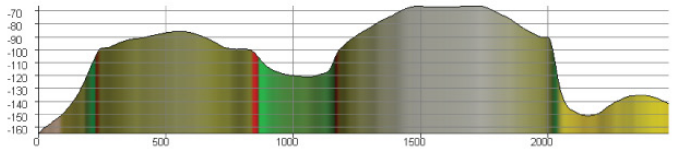

Figure 16-B

Figures 5-16A and 5-16B Modeled coral provenance on the Barbados Shallows at 18,000 years ago. The model is uplift-corrected (Bender et al., 1979; Speed et al., 2004) and is based on coral data from nearby Barbados reefs (coral sea level data from Peltier and Fairbanks, 2006, see Figure 5-6). *P.* = *Porites*, *A.* = *Acropora*, *M.* = *Montastrea*. Z-heights are exaggerated 6 times. Scale as defined in Figure 4-7.

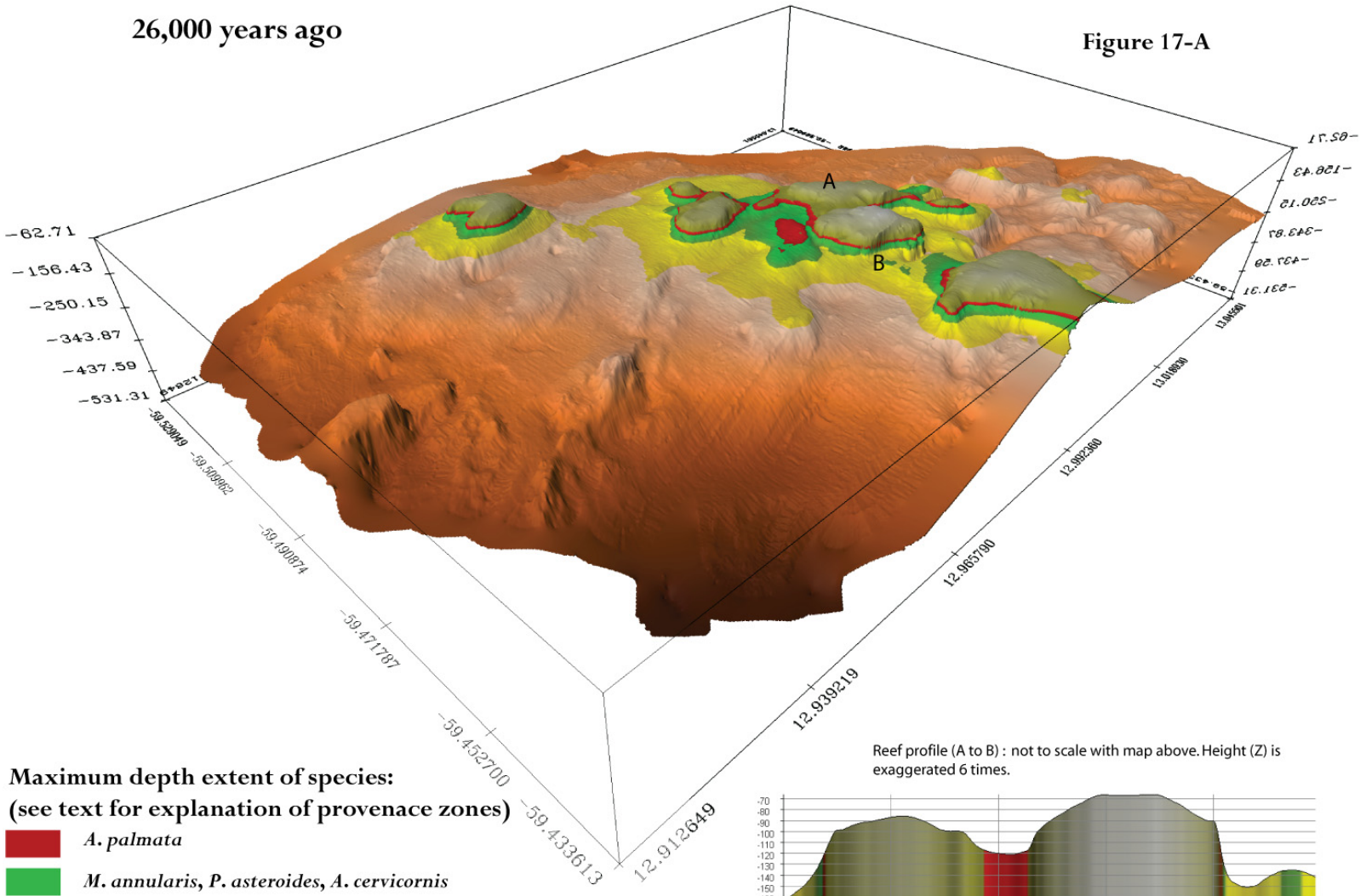

Figure 17-A

Figure 17-B

Figures 5-17A and 5-17B Modeled coral provenance on the Barbados Shallows at 26,000 years ago. The model is uplift-corrected (Bender et al., 1979; Speed et al., 2004) and is based on coral data from nearby Barbados reefs (coral sea level data from Peltier and Fairbanks, 2006, see Figure 5-6). *P.* = *Porites*, *A.* = *Acropora*, *M.* = *Montastrea*. Z-heights are exaggerated 6 times. Scale as defined in Figure 4-7.

31,000 years ago

Figure 18-A

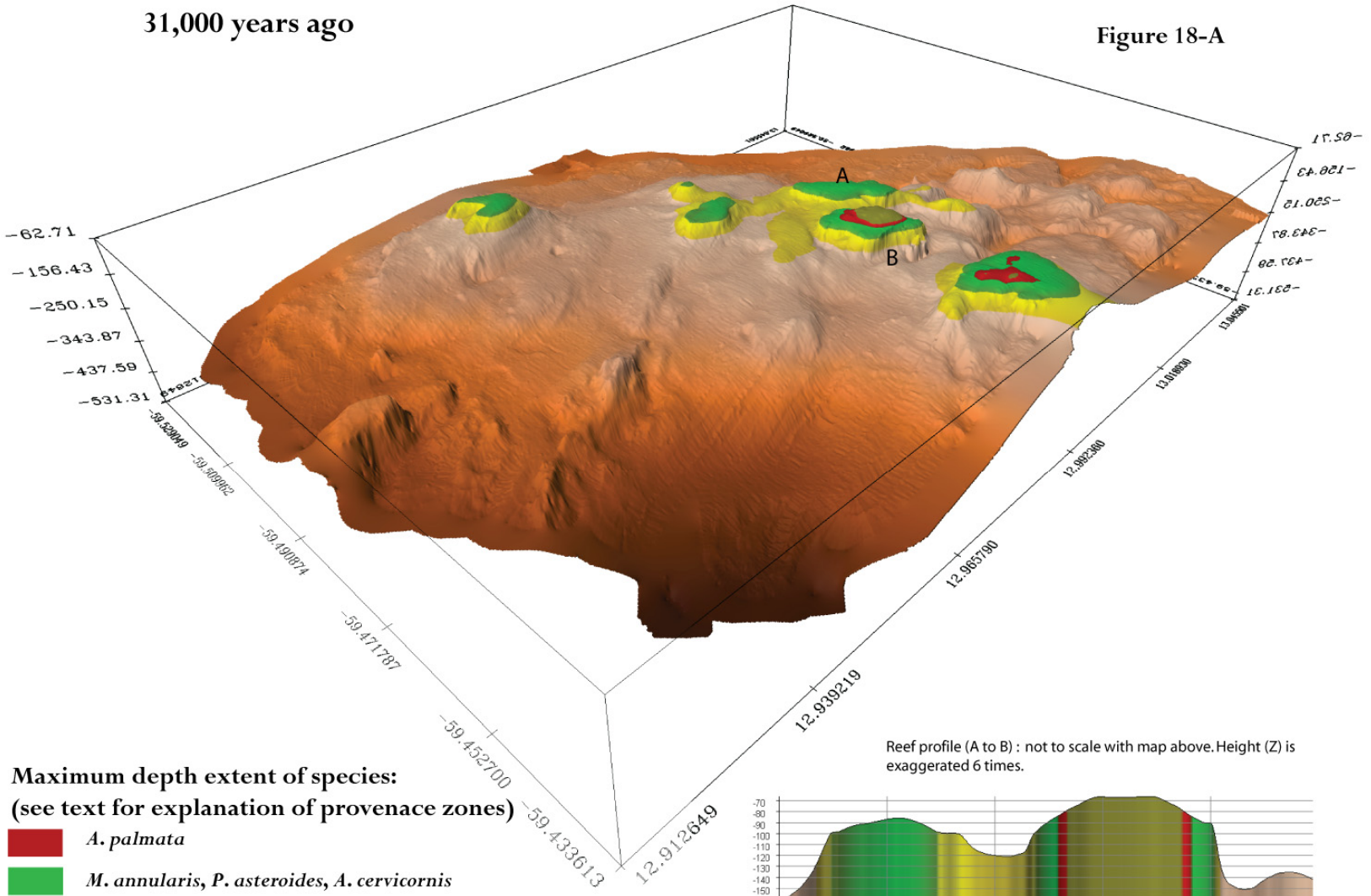

Maximum depth extent of species:
(see text for explanation of provenace zones)

- *A. palmata*
- *M. annularis, P. asteroides, A. cervicornis*
- *Diploria spp.*

Reef profile (A to B) : not to scale with map above. Height (Z) is exaggerated 6 times.

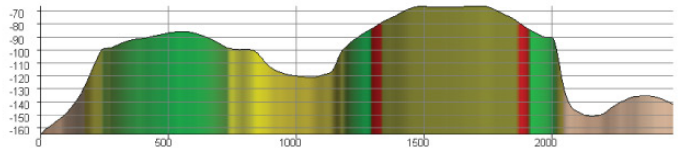

Figure 18-B

Figures 5-18A and 5-18B Modeled coral provenance on the Barbados Shallows at 31,000 years ago. The model is uplift-corrected (Bender et al., 1979; Speed et al., 2004) and is based on coral data from nearby Barbados reefs (coral sea level data from Peltier and Fairbanks, 2006, see Figure 5-6). *P.* = *Porites*, *A.* = *Acropora*, *M.* = *Montastrea*. Z-heights are exaggerated 6 times. Scale as defined in Figure 4-7.

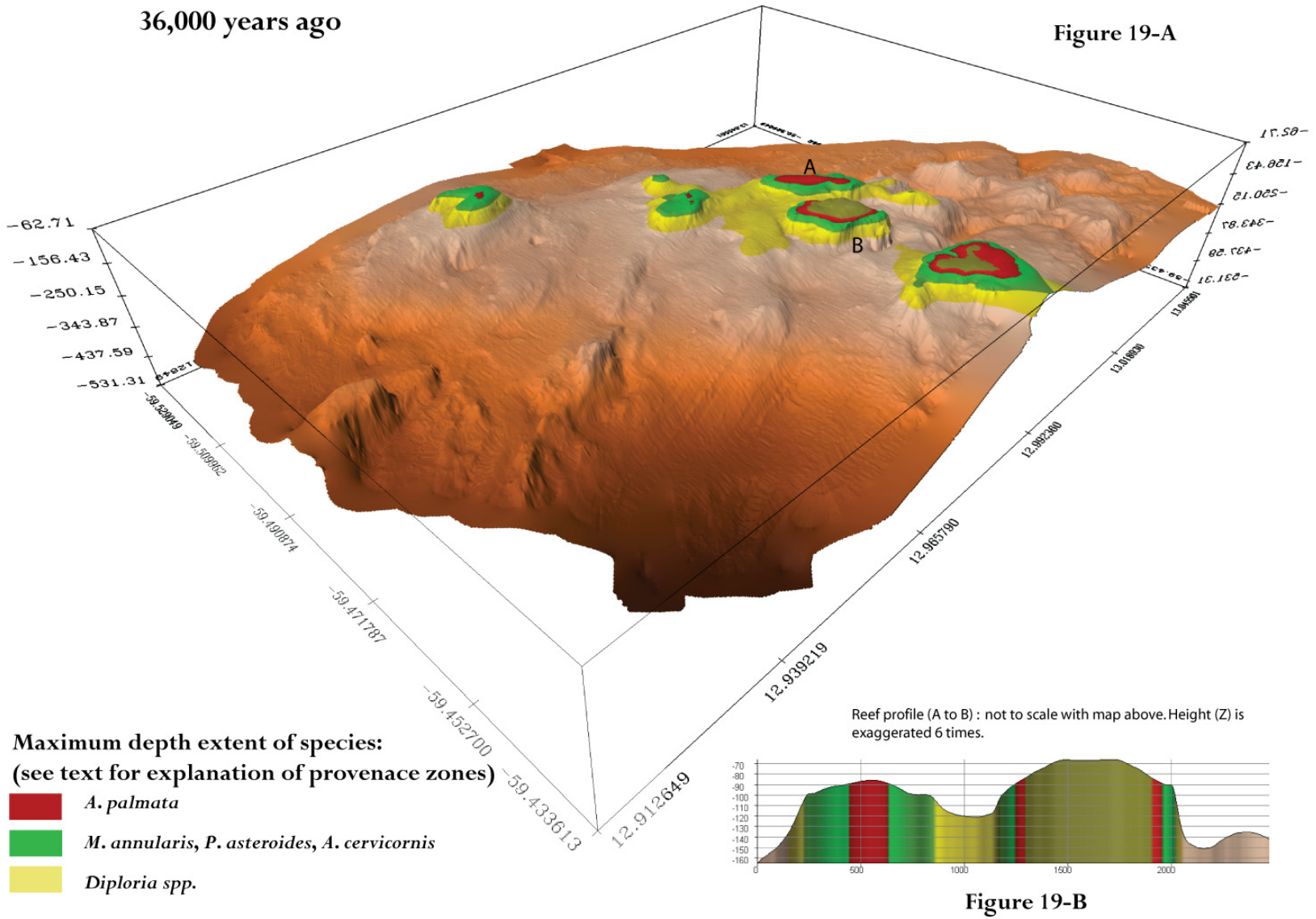
36,000 years ago
Figure 19-A
A
B
-62.71
-156.43
-250.15
-343.87
-437.59
-531.31
-59.490874
-59.471787
-59.452700
-59.433613
12.912649
12.939219
12.965790
Maximum depth extent of species:
(see text for explanation of provenace zones)
A. palmata
M. annularis, P. asteroides, A. cervicornis
Diploria spp.
Reef profile (A to B) : not to scale with map above. Height (Z) is exaggerated 6 times.
-70
-80
-90
-100
-110
-120
-130
-140
-150
-160
0
500
1000
1500
2000

Figure 19-B

Figures 5-19A and 5-19B Modeled coral provenance on the Barbados Shallows at 36,000 years ago. The model is uplift-corrected (Bender et al., 1979; Speed et al., 2004) and is based on coral data from nearby Barbados reefs (coral sea level data from Peltier and Fairbanks, 2006, see Figure 5-6). *P.* = *Porites*, *A.* = *Acropora*, *M.* = *Montastrea*. Z-heights are exaggerated 6 times. Scale as defined in Figure 4-7.

62,000 years ago

Figure 20-A

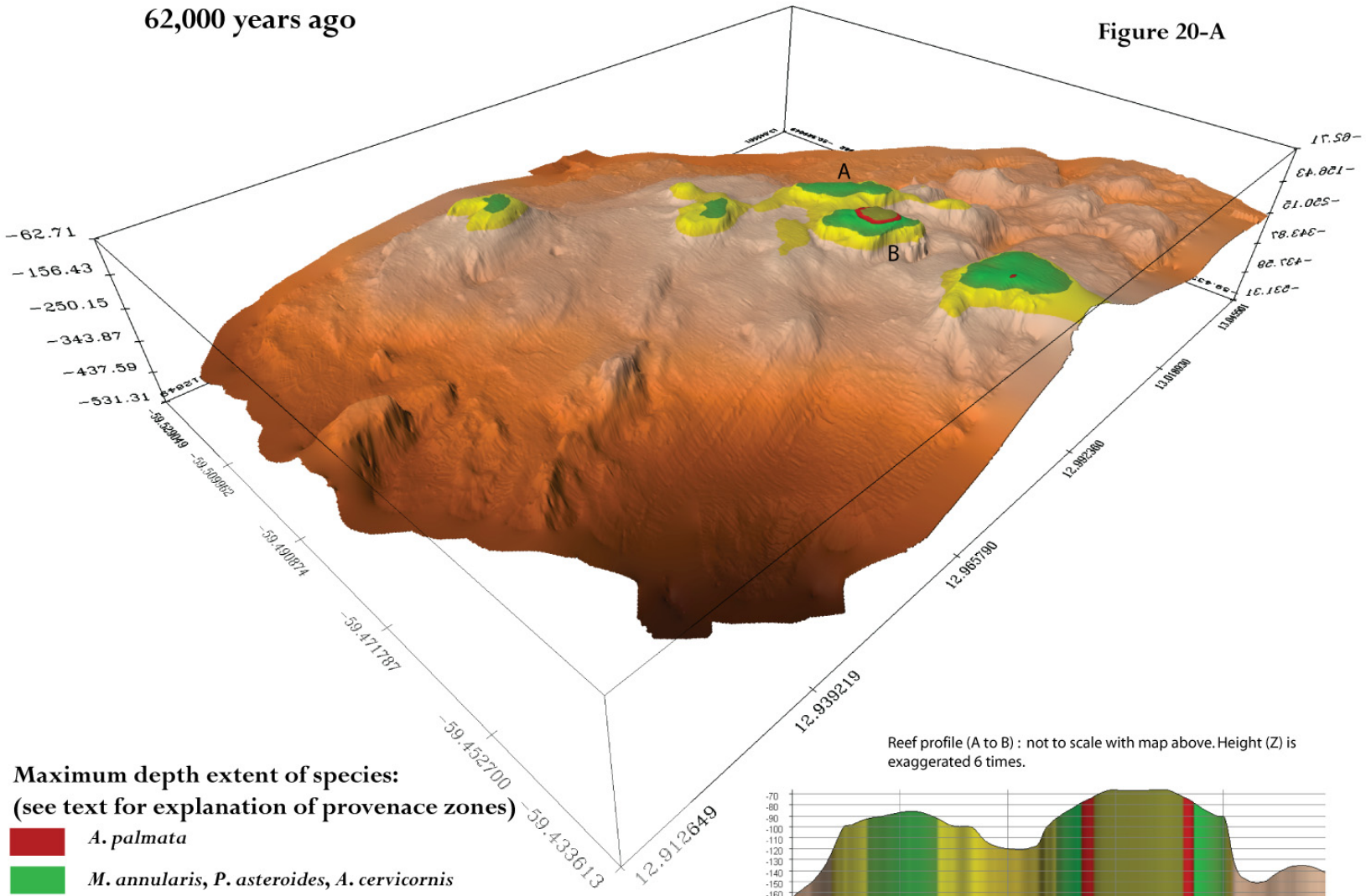

Maximum depth extent of species:
(see text for explanation of provenace zones)

- *A. palmata*
- *M. annularis, P. asteroides, A. cervicornis*
- *Diploria spp.*

Reef profile (A to B) : not to scale with map above. Height (Z) is exaggerated 6 times.

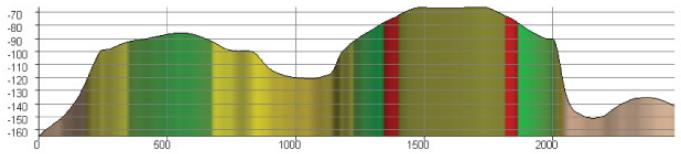

Figure 20-B

Figure 5-20A and 5-20B Modeled coral provenance on the Barbados Shallows at 62,000 years ago. The model is uplift-corrected (Bender et al., 1979; Speed et al., 2004) and is based on coral data from nearby Barbados reefs (coral sea level data from Peltier and Fairbanks, 2006, see Figure 5-6). *P.* = *Porites*, *A.* = *Acropora*, *M.* = *Montastrea*. Z-heights are exaggerated 6 times. Scale as defined in Figure 4-7.

135,000 years ago

Figure 21-A

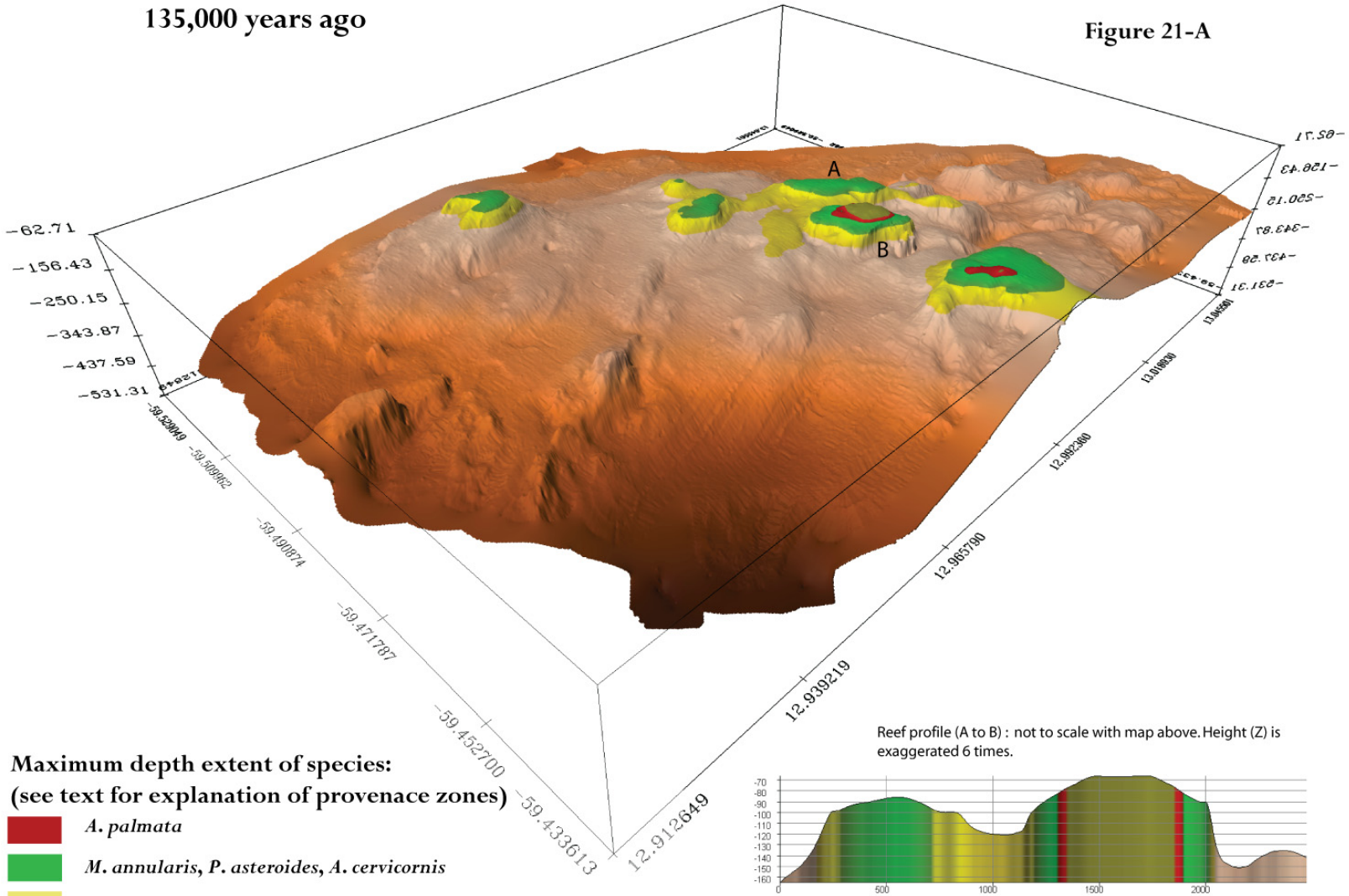

Maximum depth extent of species:
(see text for explanation of provenace zones)

- *A. palmata*
- *M. annularis, P. asteroides, A. cervicornis*
- *Diploria spp.*

Reef profile (A to B) : not to scale with map above. Height (Z) is exaggerated 6 times.

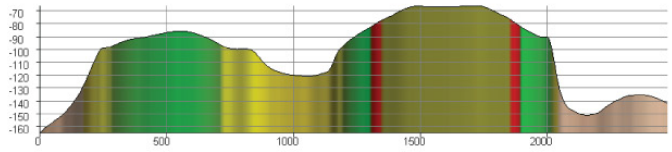

Figure 21-B

Figure 5-21A and 5-21B Modeled coral provenance on the Barbados Shallows at 135,000 years ago. The model is uplift-corrected (Bender et al., 1979; Speed et al., 2004) and is based on coral data from nearby Barbados reefs (coral sea level data from Peltier and Fairbanks, 2006, see Figure 5-6). *P.* = *Porites*, *A.* = *Acropora*, *M.* = *Montastrea*. Z-heights are exaggerated 6 times. Scale as defined in Figure 4-7.

As to size, the plateaus range from 500 meters up to several kilometers across. With regard to morphology, they show the steep edges that are characteristic of the Barbados Island paleo reefs. These sharp features are a result of forming massive reef crests that were subsequently bio- and mechanically eroded in the coastal environments creating steep escarpments as seen along the modern Barbados coast. Such dominant escarpments are also found on Barbados itself in the form of the First and Second High Cliffs, although these terraces were further eroded by weathering after they were uplifted to their present positions.

The backscatter data (Figure 5-9A, 5-9B, 5-10 and 5-11) also confirm the characteristics of the bottom textures as being comparable to coral reefs and carbonate sand or rubble. Around the shallowest areas, there are several places that show steep slopes combined with high intensity backscatter signals. These two prominent characteristics are most likely represent paleo reef cliffs that grew and were later eroded when the sea level was much lower – see Figures 5-17A – 5-17B. Erosion during the glacial maximum low stand resulted in the formation of sharp escarpments (mainly due to bio-erosion), creating deeply carved notches followed by increased mechanical breakdown and collapse. Along the modern Barbados coast, such deep nudges mark the current cliffs of the present high stand. These notches were created during long periods of bio-erosion, typically the work of snails and algae at the ocean surface level. Similar deep notches, created only in cliffs at contemporary sea level, are found inland as paleo features on the First and Second High Barbados reef cliffs (Blanchon & Eisenhauer, 2001; Radtke and Schellmann, 2003). Later, when the Shallows formations where

drowned by rising sea level, a continued directional ‘gouging’ by the prevailing surface ocean currents (see Figure 5-8B) may have carved out the sea floor to form its characteristic general south-southwest structures, as revealed by our recently constructed 3-D maps of the Barbados Shallows (Figure 5-3B).

In this study the isostatic rise on the Shallows is presumed to have been constant of 0.36 millimeters per year over the last glacial cycle. There are other estimates of uplift rates from Barbados that range from approximately 0.25 millimeters per year at Christ Church (Bender et al., 1979), 0.34 millimeters per year in Saint Georges Valley (Bender et al., 1979, Fairbanks et al. 1989), 0.44 millimeters per year on the Claremont Nose (Matthews et al., 1973), 0.51 millimeters per year on the Claremont Nose ‘Anticline’ (Radtke and Schellmann, 2006), to as high as 0.53 millimeters per year at Cave Hill (Speed et al., 2004), Results from drill core from the offshore reefs in Oistins Bay support an uplift rate of 0.34-0.36 millimeters per year (Peltier and Fairbanks, 2006; Mey et al., in prep). The estimated uplift rate of 0.34-0.36 millimeter per year would have allowed *Acropora palmata* to colonize on the top of two of the Shallows banks 135,000 years ago if the glacial low stand at this time was approx 120-125 meters below the contemporary sea level as it is estimated in the last glacial low stand. Reefs older than Termination II would not had a chance to colonize because the water would have been too deep. Since the last glacial maximum there were periods of time that were more favorable to reef growth. Especially during times when the past sea level was close to the flat areas of the banks e. g. 13-14,000 years ago (Figure 5-15), 31-62,000 years ago (Figure 5-18, 5-19, and 5-20) and

possibly, during the glacial low stand preceding Termination II, 135-138,000 years ago (Figure 5-21). During these times the *Acropora Palmata* could colonize on or near the tops of the Shallows banks. Preliminary results from high resolution bathymetric data and especially backscatter data (Mey et al., *in prep*), shows recognizable structures and high reflectance features where the corals are thought to have established reefs based on our spatial analysis. The backscatter data further indicate that these structures are similar compared to the drowned reefs that surround Barbados (Mey et al., *in prep*) and are also comparable to reef structures on Barbados. At other times, when the sea level was at the steep cliffs sides below the flat bank tops, (e.g. 18-30,000 years ago Figure 5-17 and 5-18), the corals would have difficulty establishing large constructional reefs. The last possible coral growth on the Shallows was approximately 9000 years ago (prior to melt water pulse II) when only the Diploria spp would have survived at the very top of the shallowest bank (Figure 5-13).

CONCLUSIONS

Reefs that have never been exposed to percolating freshwater have a less chance of being affected by the disequilibrium phenomena in the uranium series that are typical of open systems. Prospecting for such samples that are 'preserved' in the marine environment is desirable for obtaining reliable U-Th and U-Pa ages. Multi-beam bathymetry and geospatial analysis of underwater reef morphologies will help identify such suitable sample sites. The large kilometer

sized flat-topped bank structures of the Barbados Shallows are most likely covered by coral caps. This is inferred from the modeled reef habitat zones on the Shallows that were available to coral-growth since the glacial maximum prior to termination II. The unique combination of sea level variation and uplift rate allowed *Acropora palmata* to colonize on the Shallows banks at 138-135,000 years ago, 62-30,000 years ago and 14-13,000 years ago. There were presumed hiatuses of massive reef crest development due to the sea level either being too low or too high for significant reef growth on the bank tops from 135-62,000 years ago and 30-15,000 years ago. Prior to melt water pulse 2 around 9,000 years ago, the last corals that grew on The Shallows were probably *Diploria spp*.

ACKNOWLEDGEMENTS

I would like to thank the late Bill Haxby for introducing me to the tools necessary for studying the Barbados shallows. In great appreciation, I have chosen to use his 'Haxby' color palette (see Haxby et al., 1983) to portray the Shallows; this palette is by far the most aesthetical. I thank Andrew Goodwillie at Lamont Doherty Earth Observatory for introducing me to MB-Systems. I thank Gary Hemming (Queens College, CUNY) and Rick Fairbanks (Columbia University) for their support and discussions. I also thank The Graduate Center (CUNY) for a University Fellowship supporting this work.

CHAPTER 6
THE NERITIC EXPANSION AND THE ATMOSPHERIC pCO_2-CURVE SINCE THE LAST GLACIAL MAXIMUM: THE CORAL REEF HYPOTHESIS REVISITED WITH GIS

By

Jacob L. Mey[1, 2]

1. Lamont Doherty Earth Observatory of Columbia University, Palisades, New York 10964, USA.

2. Graduate Center, City University of New York, New York, NY 10016, USA.

ABSTRACT

The rise in atmospheric pCO_2 since the last glacial maximum was marked by two episodes when the production rate increased significantly, stalled, and dropped before continuing to rise. At the same time that these pCO_2 anomalies occurred, major polar ice cap melting (also known as melt water pulse events) took place. This resulted in a temporary, but significant acceleration of global sea level rise. The effects on the neritic environments, including coral colonies, must have been serious, even devastating. Major constructional, now drowned paleoreefs around the globe bear out evidence of an exceptionally fast sea level rise in the past. The global impact on the coral reefs and the shallow carbonate producing neritic environments in the tropics may have had a detectable effect on ocean CO_2 production and its evasion to the atmosphere. On the other hand, recent findings from the Antarctic Siple Dome ice core show that, after the major melt water events called 1A and 1B, the pCO_2 input into the atmosphere was halted and even reduced, presumably as a response to the rapid sea-level rise. The correlation between the pCO_2 curve from the ice cores and the δD record indicates the onset of the melt water events themselves was caused by a major shift in global climate caused by temperature rise in the northern and southern hemispheres. The temperature rise could therefore have been a direct effect of the increased pCO_2 production rate into the atmosphere: a 'paleo greenhouse effect'.

Prior to the 1A and 1B events, as the sea level crept up on large shelves such as the Sunda shelf and also onto the North Australian, Seychelles, and Bahamian

banks, there was a multiple-fold expansion of areas suitable for the growth of carbonate producing organisms such as corals, cocolids, and sponges. Based on the coral-based sea level curve, our geospatial analysis of the neritic expansion shows that there is a direct correlation between the melt water events and the expected rapid expansion of carbonate producing (coral reef) provinces after flooding. More surprisingly, there is also a strong correlation between the variation of the rising atmospheric pCO_2 and the neritic expansion. Our analysis of the 1st derivatives of (i) the neritic expansion, (ii) the increasing atmospheric pCO_2, and (iii) the rising sea level, suggests a direct correlation between the quick rise of atmospheric pCO_2 levels and the rapid increase in potential reef-sustaining areas in the shallow ocean. For the flat, low-lying Sunda and North Australian shelves, an amplified pCO_2 forcing may have been helped by the rapid inundation of the vast CO_2 sequestering mangrove forests on the shelves, while at the same time the CO_2 producing neritic environments expanded rapidly.

INTRODUCTION

Global sea level and atmospheric CO_2 changes since the last glacial maximum

For several decades, aspects of the Earth System that influence the carbon cycle have been a high priority topic of research. Here, variations in surface water level and in the amount of atmospheric partial pressure of CO_2 (pCO_2) on a glacial/interglacial time-scale have been of special interest. The role of the ocean, shallow and deep, is paramount to our understanding of the atmospheric CO_2 cycle. However, with several mechanisms at play, each of their extent and degree of contribution to the carbon cycle still is not, and perhaps never will be fully resolved. Some of the central questions are:

(i) Did the ocean's biological pump, which is responsible for organic carbon sequestration, use nutrients more efficiently during glacial times and thereby, sequester more carbon? (Sigman & Boyle, 2000)

(ii) How did the world oceans' nutrient reservoir size change in the period from last glacial to interglacial? Were there any changes in the terrestrial carbon storage and in ocean temperature? (Adams et al., 1990).

(iii) Did the marine calcium carbonate budget change? How did changes in ocean ventilation affect the atmospheric pCO_2 ? (Marchitto et al., 2005).

(iv) Do total carbonate equilibria (chemical, thermodynamic, and kinetic) persist on a glacial/interglacial time-scale? (Walker & Opdyke, 1995; Archer et al., 2000).

(v) How did temperature and salinity affect the CO_2 sequestration in the glacial ocean? (Keir, 1988)

(vi) To what extent did carbonate from continental weathering in the interglacial contribute to changes in pCO_2 content, and what roles did factors such as alkalinity and Dissolved Inorganic Carbon (DIC) play in this context? (Broecker & Peng, 1987).

(vii) How important are potential and poorly understood changes in the lysocline? (Broecker & Clark, 2007).

All these questions are essential for our understanding of the carbon cycle on a glacial/interglacial time-scale. The majority of these questions are beyond the scope of the present work, which aims to provide new arguments, based on some rather simplistic assumptions-cum-data concerning the contribution of shallow carbonate production (i.e. coral reef growth) to atmospheric pCO_2 variability during the last 22,000 years.

If shallow-shelf carbonate production has had a detectable or even a significant influence on atmospheric pCO_2 on a glacial/interglacial time-scale, then a comparison between rates of change in sea level compared with rates of coral habitat expansion and rates of change in atmospheric pCO_2 should provide insight into this. This reasoning is at the basis of the so-called 'coral reef hypothesis' (Berger, 1982).

Peaks on atmospheric pCO_2 curves from different ice cores may have offsets (due to varying snow accumulation rates), when they are compared to similar peaks registered for other climatic events, such as happened at the onset of the Younger Dryas epoch in the form a major MVP's (melt water pulses, aka Heinrich events). Despite this, it is possible to correlate the data by using the 1st order derivatives of the sea level and pCO_2 curves and comparing them for the last 22,000 years. Doing this, we were able to show that, since the last glacial maximum, several major expansions and subsequent massive drowning of coral reefs possibly played a role in determining the pCO_2 balance between the surface ocean water and the atmosphere.

According to Berger's (1982) coral reef hypothesis, changes in the rate of coral reef carbonate deposition may have been a key controller in Quaternary variations of atmospheric pCO_2. Coral growth is an effective means of carbonate calcification, thereby, in the process produces CO_2 in the surface ocean on shallow shelf margins. As these areas expand, they will cause a significant increase in CO_2 evasion from the shallow ocean to the atmosphere. This could happen during times of rapidly expanding accommodation of lateral and vertical space of the coral habitat zones (or carbonate producing neritic environments in general), especially when the sea level was rising at a rate that did not drown the corals completely (Opdyke & Walker, 1992). We therefore hypothesize that the lateral expansion of reef habitats on these shallow flat shelves, as they were flooded due to the rising sea level, may have caused a significant increase in reef production. However, if the sea level rise was too rapid, the corals could not

'keep up' and the reefs drowned, effectively shutting down a big part of the CO_2 production in the surface ocean over a relatively short time period. Growth resumed when the sea level rose more slowly, thereby accommodating the growth pace of the corals. Arguably, if the relative timing of the pCO_2 changes fits in with the changes in sea level, this may imply that the waxing and waning of coral reef growth and other carbonate production factors through time did indeed affect the pCO_2 rate in the atmosphere. According to Vecsei & Berger (2004), carbonate production was high from 14,000 years before present (BP) to a peak in the early Holocene (approximately from 9,000-6,000 years BP). In their study, they concluded that coral reef production was low in the early stages of deglaciation (approximately 18,000-16,000 years BP), and thus, its contribution to the increase in atmospheric pCO_2 was small.

The question now is, how exactly would coral reef growth affect the change in the carbonate chemistry of the ocean and effectively contribute to the atmospheric pCO_2? To answer this question, we have to consider the mechanisms of continental weathering and carbonate deposition on the ocean shelves (Figure 6-1). The balance between the two processes is governed by the reaction:

(6.1) $$Ca^{2+} + 2HCO_3^- = CaCO_3 + CO_2 + H_2O$$

As normal in a balanced equation, if the $CaCO_3$ burial (i.e. deposition from shelf production; right side) is larger than the carbonate input occasioned by weathering (left side), a decrease in alkalinity will occur, and the amount of

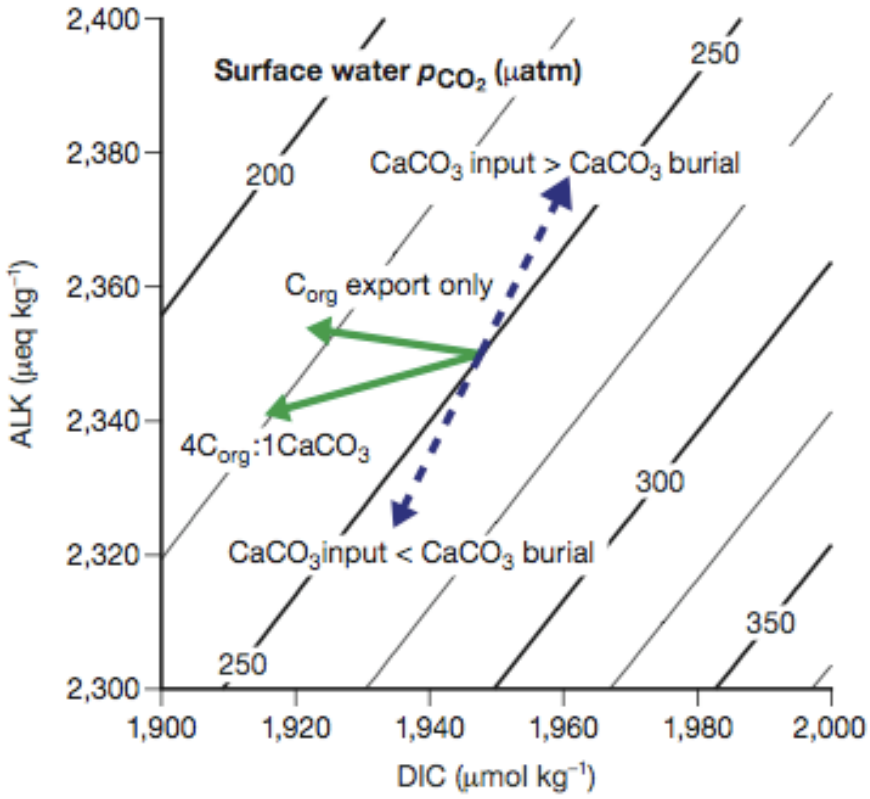
Surface water p_{CO_2} (µatm)
200
250
300
350
$CaCO_3$ input > $CaCO_3$ burial
C_{org} export only
$4C_{org}$:1$CaCO_3$
$CaCO_3$input < $CaCO_3$ burial
ALK (µeq kg^{-1})
2,400
2,380
2,360
2,340
2,320
2,300
1,900
1,920
1,940
1,960
1,980
2,000
DIC (µmol kg^{-1})

Figure 6-1

Figure 6-1 Relationship between alkalinity, dissolved inorganic carbon (DIC), and surface water pCO_2. Blue dashed arrows show how the balance between continental weathering input and the $CaCO_3$ burial on shelves would affect surface water pCO_2, as alkalinity and DIC change (Sigman & Boyle, 2000).

inorganic carbon dissolved in the shallow oceans (the DIC) will diminish. As a direct result, the surface water pCO_2 increases, thereby shifting the gas exchange balance towards evasion into the atmosphere, thereby raising the pCO_2.in the atmosphere. In the opposite scenario, when the weathering outpaces the burial, the ocean's alkalinity and the amount of DIC go up, thereby decreasing the pCO_2 surface water. This then allows CO_2 to invade the ocean from the atmosphere (Opdyke & Walker, 1992; Sigman & Boyle, 2000).

Fig. 6-1 illustrates how the carbonate production on the shallow shelves may increase the release of CO_2 into the atmosphere. When the rising sea flooded the large areas of the Sunda and North Australian shelves (totaling nearly 5 million square km – more than half the size of the US), the enormous and very flat plains of the shallow shelves were able to accommodate a tremendous expansion of reef habitats and shallow neritic zones. During the last glacial maximum, these vast plains were laid bare, thereby also potentially contributing to the increased release of carbonate weathering products into the ocean. In the present study, we investigate the relationship between the atmospheric CO_2 variation and the vast expansion of coral habitats and shallow carbonate producing neritic environments during the sea level rise that has occurred since the last glacial maximum.

MATERIALS AND METHODS

Estimates of Coral reef habitat and shallow neritic environment expansions during sea level rise since the last glacial maximum

The coral habitat zones were defined to occupy the top 30 meters of the ocean. The area covered by this water column (known as the shallow neritic zone) is defined as the likely habitat for corals and other carbonate producing organisms on the shelves. The total area of the 30 meter shallow neritic zone was calculated for every 5 meters of sea level rise, as indicated in the region's low resolution (3.5 minutes per pixel) and higher resolution (1 minute per pixel) bathymetric maps shown in Figure 6-2 (Plate 1-26). Estimates of coral reef habitat extensions at rising sea levels were calculated using geospatial techniques based on the software ArcGIS (ESRI) and Fledermaus Pro (IVS-3D).

Data sources

Three-dimensional maps of the Sunda and North Australian shelves were created from processed raw data downloaded from two sources:

(i) the low resolution 3.5 minute (7 km meters per pixel) digital elevation models of the regional bathymetry that are available through the GeoMapApp (2006) portal. The processed data were downloaded from the GeoAppMap portal in a special "geo-tiff" format (GeoMapApp, 2006) and imported into ArcGIS and

Fledermaus Pro. The advantage of this format is its full attribute table, containing pixel depths for any region of interest for which such data exist. The land-based data are from the 1998 Shuttle Radar Topography Mission (Shuttle Radar Topography Mission, 1998; http://www2.jpl.nasa.gov/srtm/). These data have a much higher resolution (90 meters per pixel), but when they are downloaded from the GeoMapApp portal, the resolution for the large region is likewise 7 km pr pixel. The full resolution digital elevation model data are available from the US Geological Survey (USGS; http://seamless.usgs.gov/Website/Seamless/viewer.php) in USGS-DEM formats (Digital Elevation Model) for any area of interest.

(ii) the higher resolution 1 minute (2 km per pixel at the Equator and 1 km per pixel at the Poles) digital elevation models were downloaded from the General Bathymetric Chart of the Oceans (GEBCO) portal of the British Oceanographic Data Centre (BODC). These 2 km per pixel data proved more precise than the above mentioned 7.5 km resolution data, nevertheless the variable rate of expansion for shallow neritic habitats since last glacial maximum was duplicated. These higher resolution processed data were downloaded from the BODC's GEBCO portal in a special Generic Mapping Tool (GMT) gridded (.grd) format and imported directly into ArcGis and Fledermaus Pro. The advantage of this format, referred to above, is its full attribute table, containing pixel depths and Cartesian information for any region of interest for which such data exist. The land data are likewise based on the 1998 Shuttle Radar Topography Mission, as

described above, with the exception that, when they were downloaded from the GEBCO portal, the resolution for the large region is 2 km per pixel (Figure 6-2).

The data showing the rate of change in the expanding habitat zones were extracted and calculated in ArcGIS using a raster calculator. Each raster data set was analyzed for cells meeting the criteria for the 30 meter water depth at various sea levels in the past (i.e. at 5 meter intervals, from -120 to 0 meters below present sea level). The data were output as a gray scale image, representing the 30 meter levels by 256 shades of gray (where 1 = black, 255 = white). The areas of interest were then re-binned to stretch from 20 to 200 in order to avoid overlap with noise and other disturbing factors; below and above these values, everything was set to pure white (255). These data were output from ArcGIS as tiff images and imported into ImageJ (the java version of the National Institute of Health's image analysis program 'NIH Image'). The numerical values of a histogram for each image (representing a particular sea level), with the distribution of grays binned in thirty separate 1 meter zones, were output to Excel and plotted as area changes per 1 meter of sea level change (interpolated from the 10 meter and the 5 meter intervals). The neritic expansion per meter of sea level rise was normalized to the known sea level change curve and plotted as area change versus time in years, thereby ensuring an important direct comparison with other climatic datasets plotted versus time. The rates of change (i. e. the 1st derivatives) in the total 30 meter surface ocean zone were calculated from the area changes versus time (year) curves.

Atmospheric CO_2 variation and sea level rise curves since the last glacial maximum

We have used the high resolution relative atmospheric pCO_2 data, obtained from the ice core drilled at the Antarctic SIPLE Dome (Ahn et al., 2004), to estimate the atmospheric pCO_2 change rate. The pCO_2 data were filtered with a 4-point moving average, so as to reduce higher frequencies and noise, and ensure a smoother calculation of the 1st derivative curve.

For sea level rise, we have used the curve based on data from Barbados and multiple other localities (Fairbanks, 1989; Peltier & Fairbanks, 2006). We used the statistically constrained version of the sea level curve (as published in Peltier and Fairbanks, 2006) to calculate the 1st derivative which in this case represents the rate change of sea level rise through time since the last glacial maximum.

RESULTS

Figure 6-2 (Plates 1 through 26) are the results of our geospatial analysis of the 30 meter surface neritic zone over the Sunda shelf, the North Australian shelf, and the surrounding region, which covers over 40 million square km (8 percent of Earth's total surface). The data shown here are the higher resolution bathymetric maps (offering a 1 minute resolution, which translates to 2 km per pixel at the Equator and 1 km per pixel at the Poles). The data comprise the areal distribution of the 30 meter shallow neritic zones (shown in red in Figure 6-2, Plates 1 through 26) for every 5 meters of sea level rise since the last glacial maximum. In Figure

6-2 (Plate 1), the light green areas represent the bare shelves during the last glacial maximum, when sea levels where 120 meters below present. The total exposed shelf area here is nearly 5 million square km. Visual inspection of Figure 6-2 (Plates 1 through 26) clearly indicates how the shallow water areas on the Sunda shelf changed quite significantly as the sea level rose. This change is plotted in Figure 6-3 and 6-4, where it is shown for the total shallow area (in millions of square km) underlying the 0-30 meters deep water column, with the change plotted versus time. The 1st derivative for the low resolution parent curve and the higher resolution parent curve are plotted in Figures 6-3 and 6-4, respectively. The 1st derivative of the curve representing the areal rate of change in the 30 meter neritic zone is similar to the low resolution (7 km per pixel) data compared to the higher resolution (2 km per pixel) data. This effectively confirms the reproducibility of the trends on the two scales. We will only treat the higher (2 km per pixel) resolution data set in the following.

The 1st derivative for the 30 meter neritic zone (Figure 6-4) shows three distinct peaks: a major peak occurring approximately 14,500 -14,000 years ago, another major peak occurring 11,400 -10,800 years ago, and a smaller, broader peak occurring 10,200-9,400 years ago (the three peaks are marked with translucent bars in Figure 6-4). During the peak episodes, the area of the 0-30 meter deep neritic zone increased drastically (this phenomenon is henceforth referred to as the 'neritic expansion'). Phrased in another way, increasingly larger areas on the shelf were flooded with each meter of sea level rise (compare Figure 6-2, Plate 14 (60 meters below present sea level) to Figure 6-2, Plate 17 (45

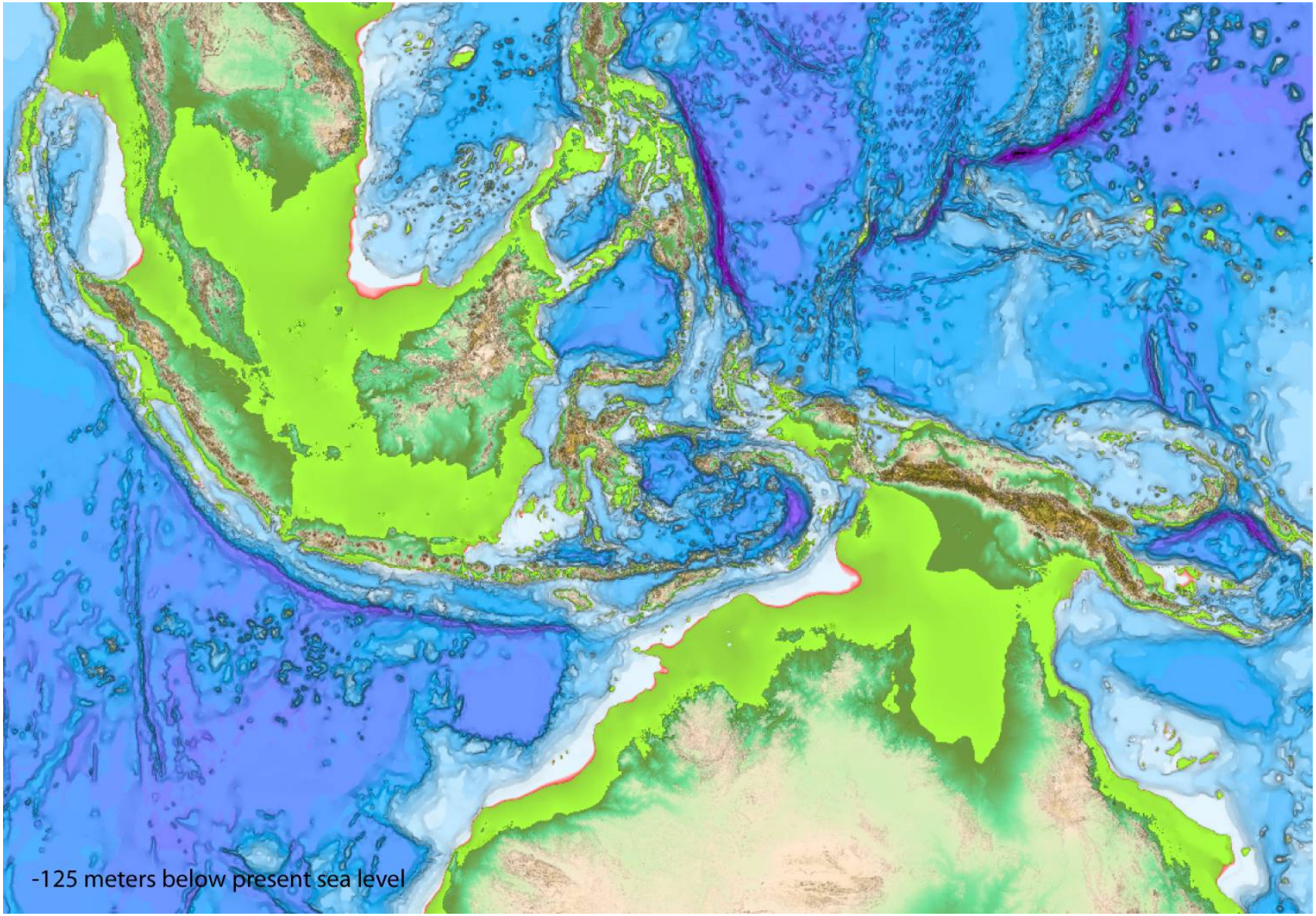

Figure 6-2 (plate 1)

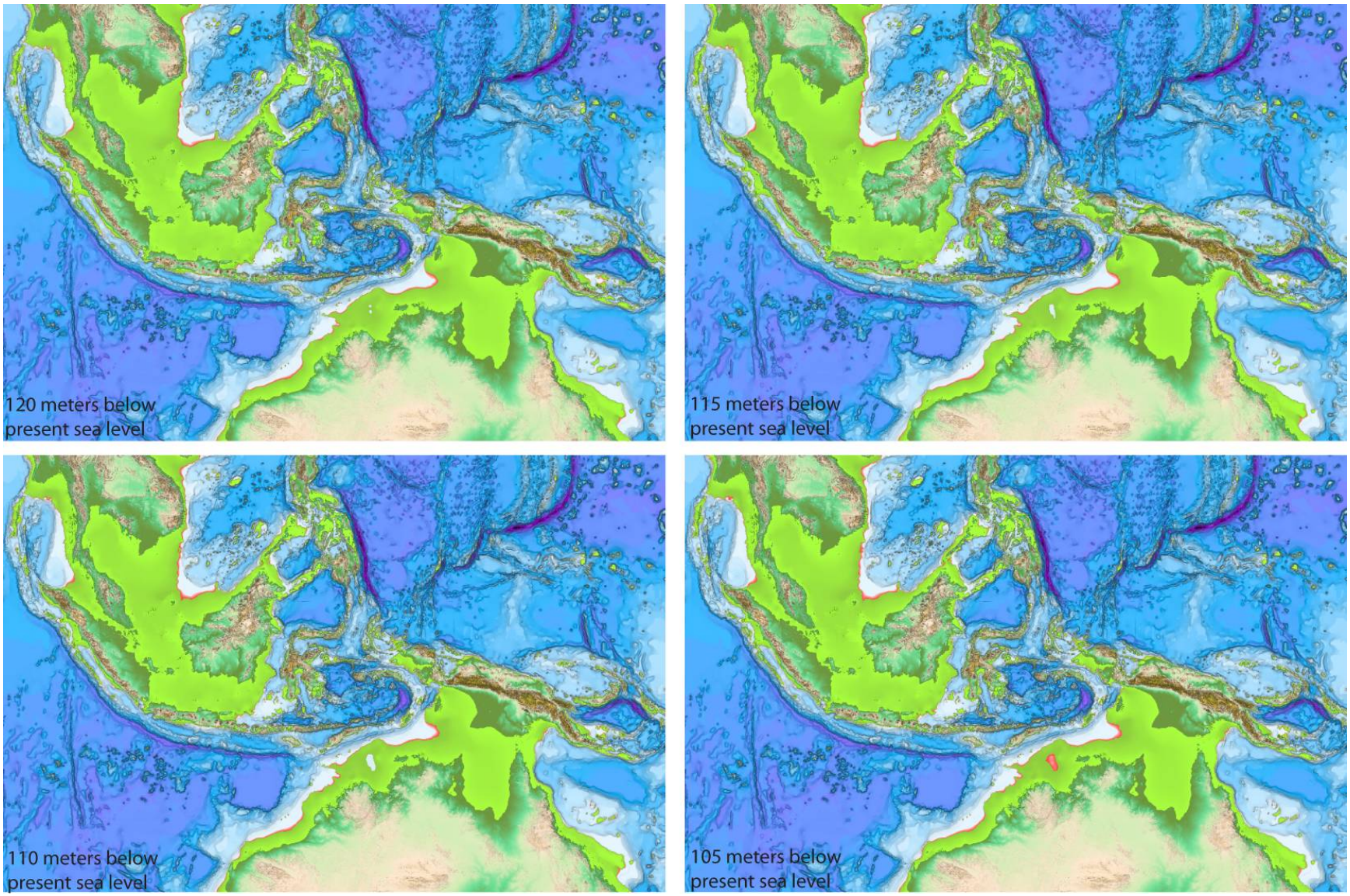

Figure 6-2 (plate 2 through 5)

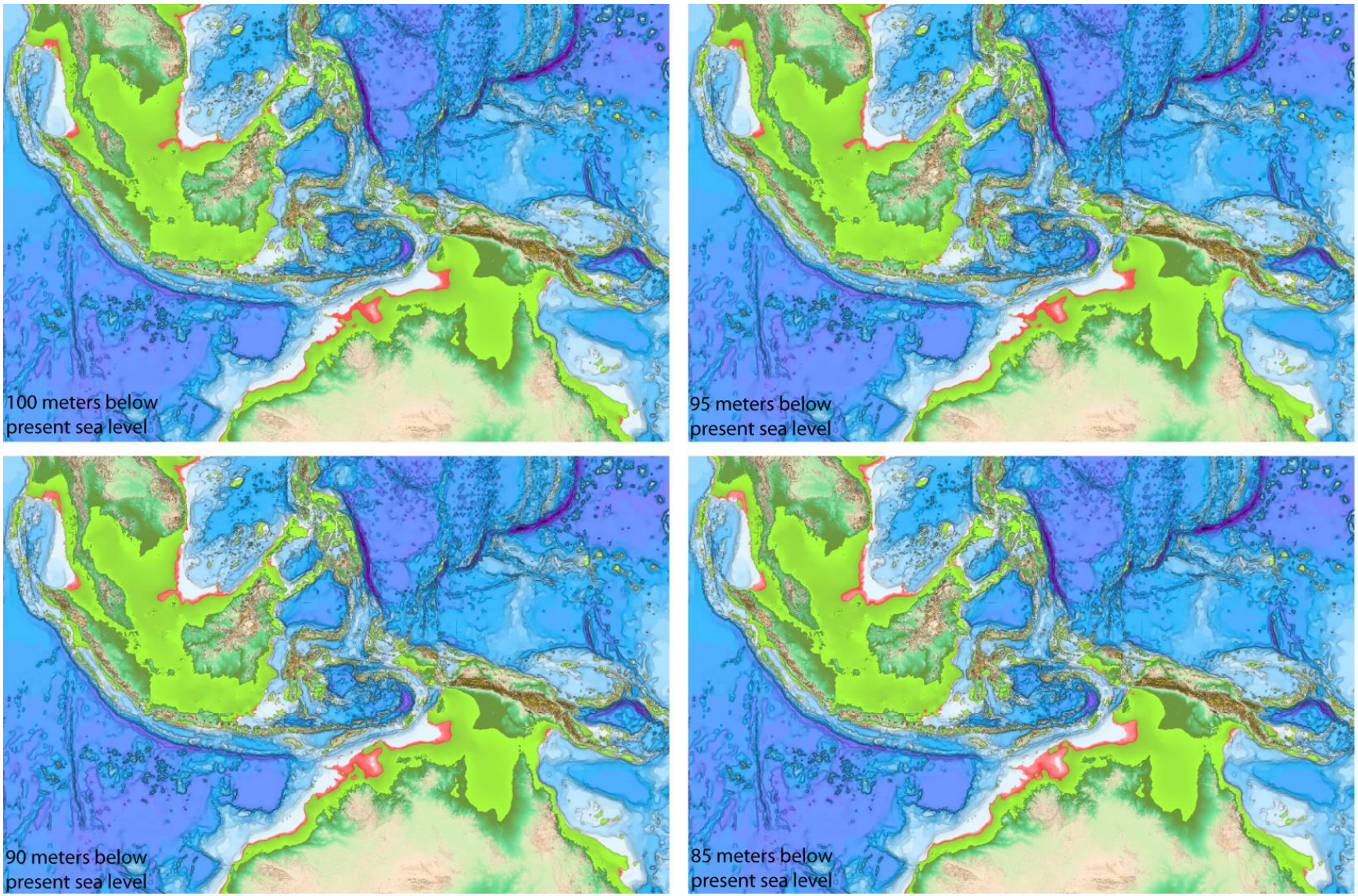

Figure 6-2 (plate 5 through 9)

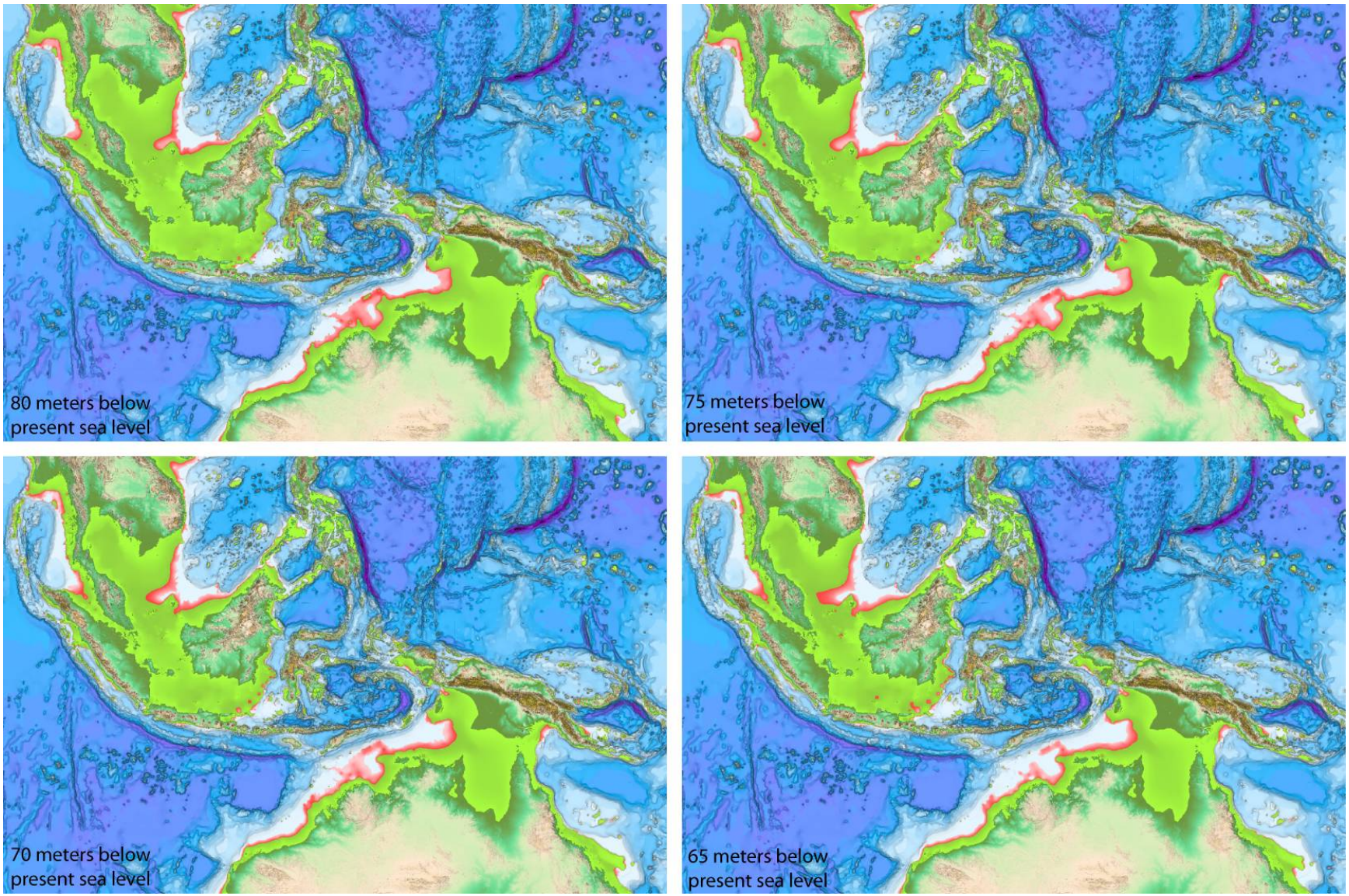

Figure 6-2 (plate 10 through 13)

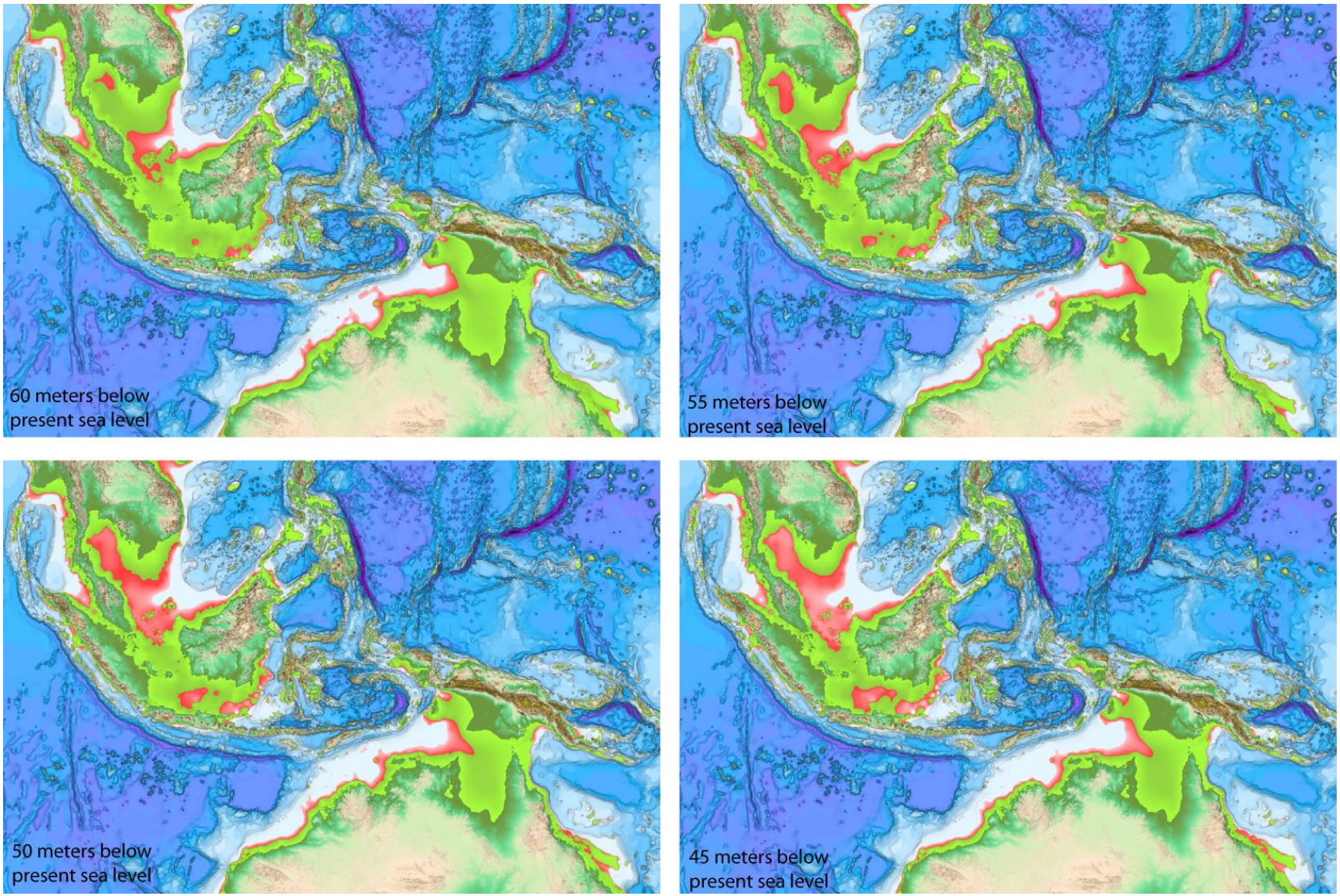

Figure 6-2 (plate 14 through 17)

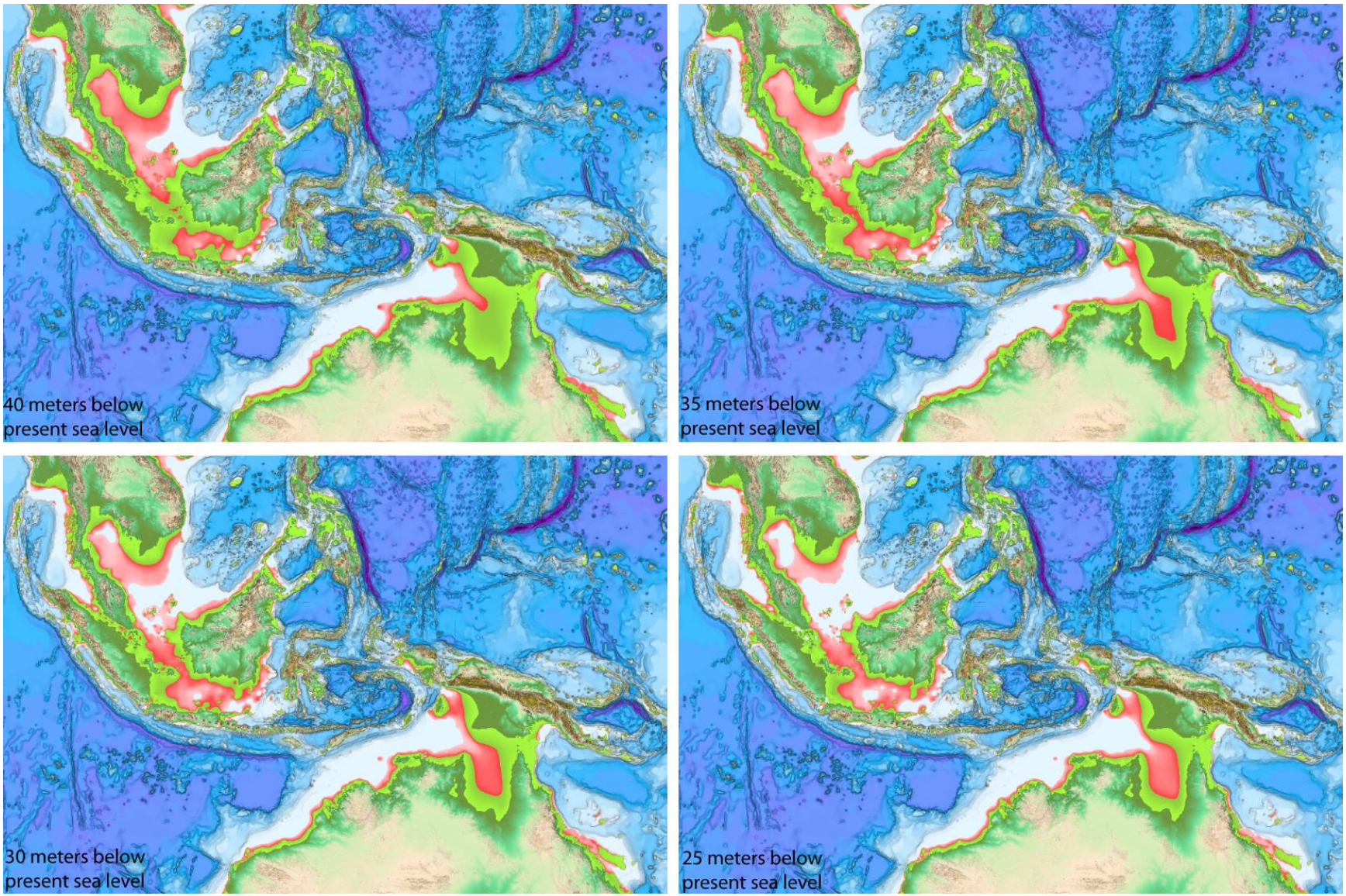

Figure 6-2 (plate 18 through 21)

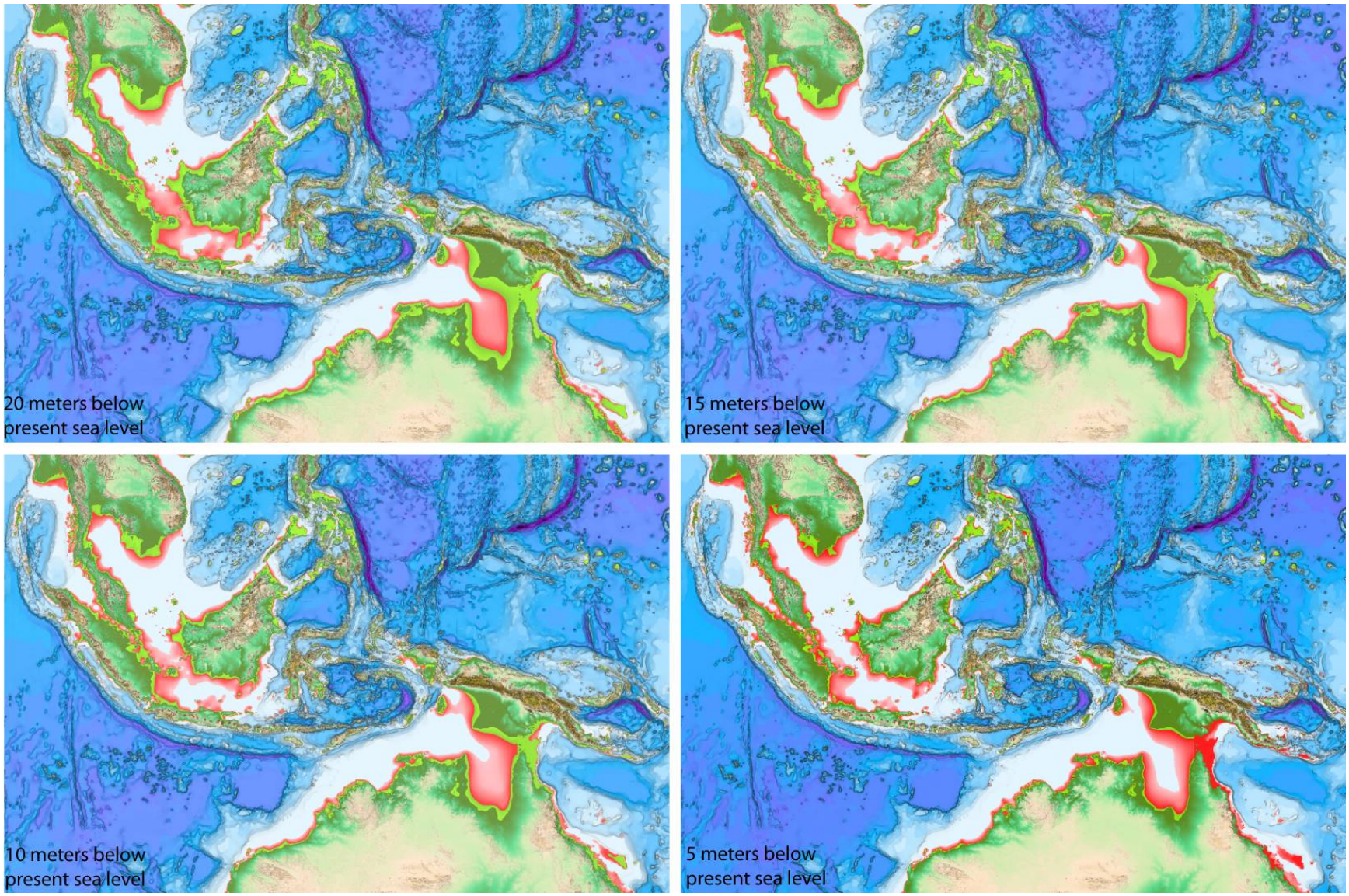

Figure 6-2 (plate 22 through 25)

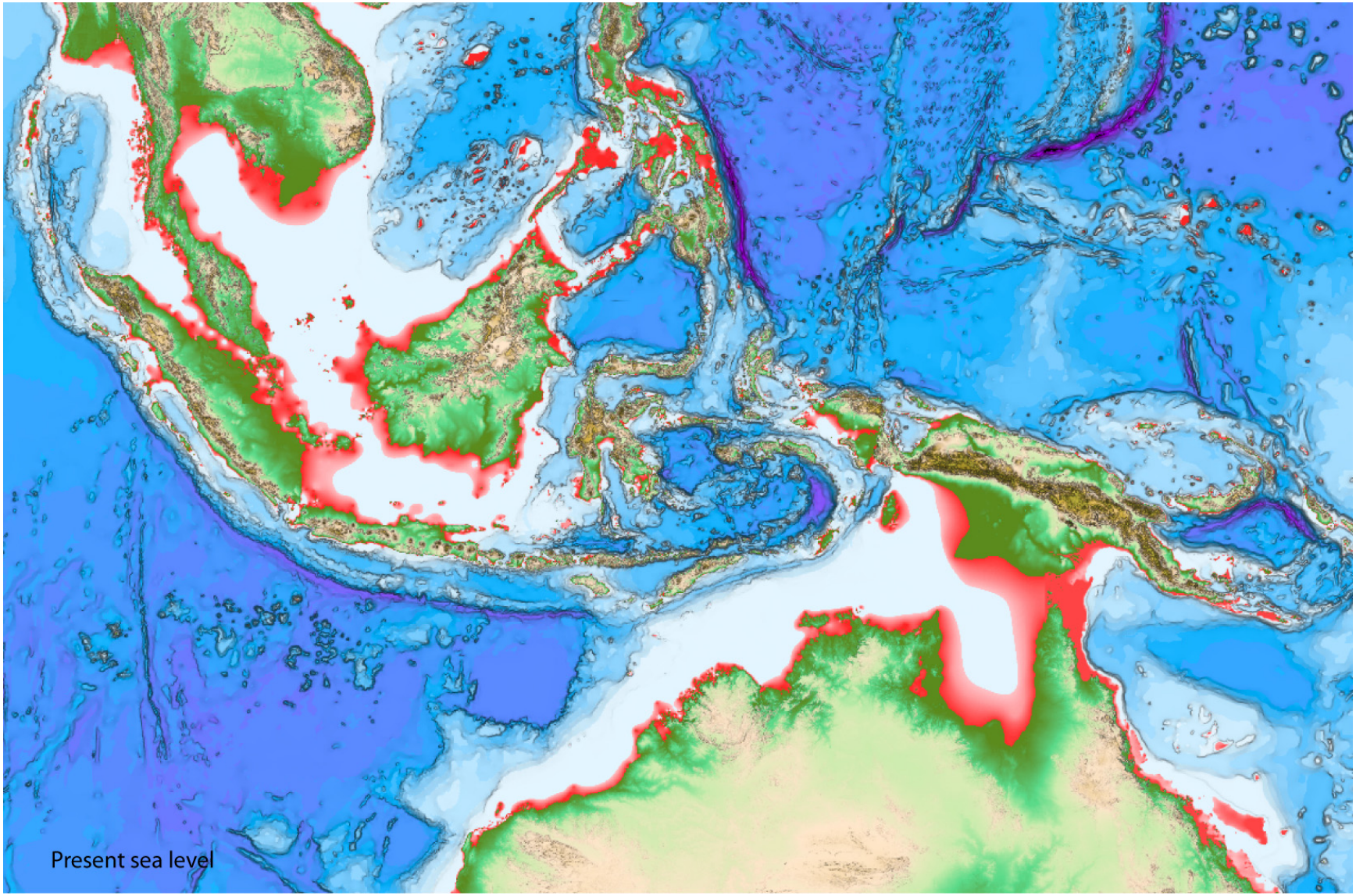

Figure 6-2 (plate 26)

Figure 6-2 (Plates 1 through 26) Results of a 1 minute per pixel resolution geospatial analysis delineating the areas covered by an arbitrary 30 meter deep neritic zone. The Plates also show how these zones progressively expanded on the Sunda and North Australian shelves, as the sea level rose ever since the last glacial maximum. The neritic zones (in red tones) were calculated for every 5 meters of sea level rise. The results of the area calculations of the neritic expansion are plotted in Figure 6-3 and 6-4 (data from DEM's of low and higher resolution, respectively).

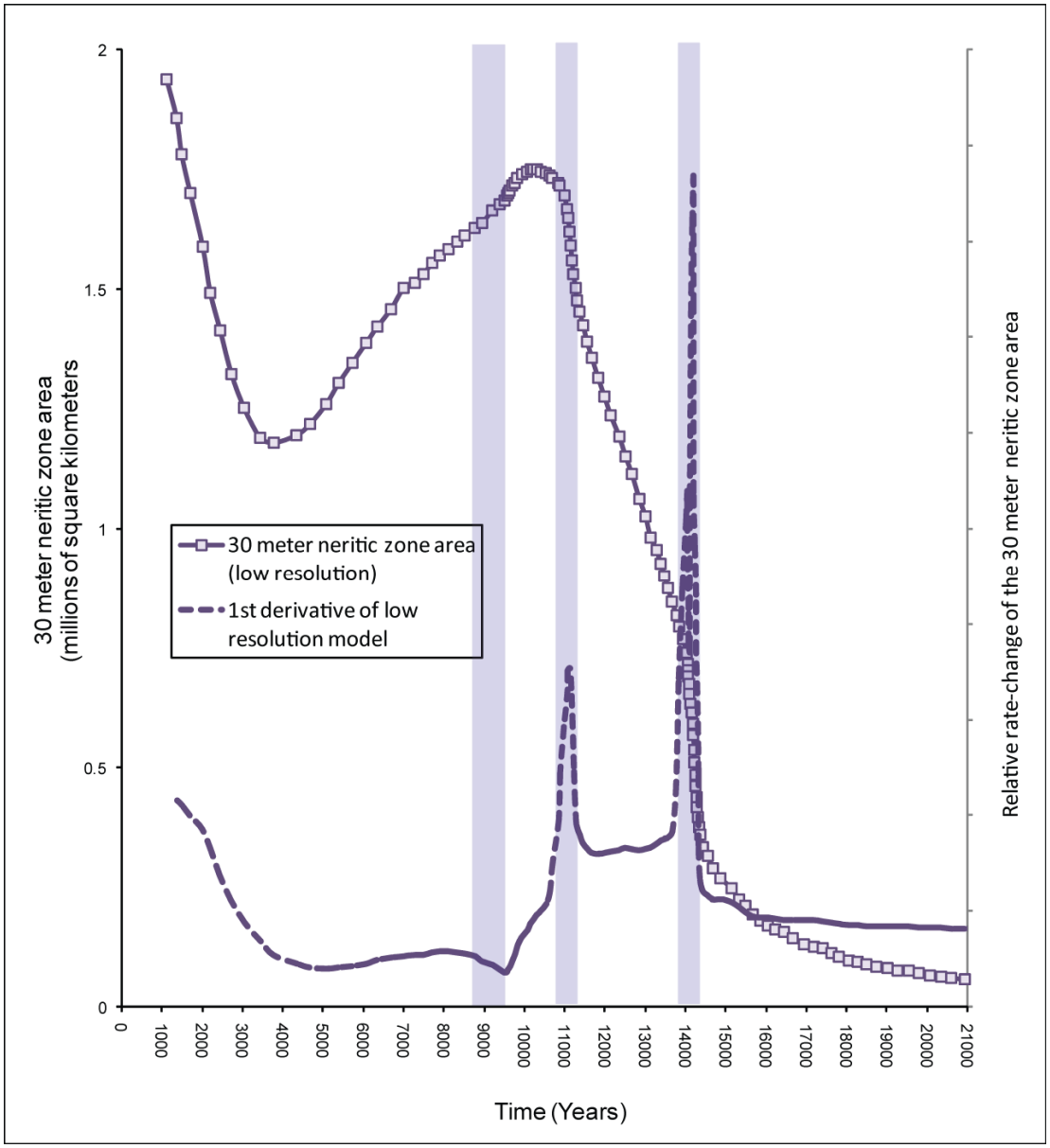
30 meter neritic zone area
(millions of square kilometers
Relative rate-change of the 30 meter neritic zone area
Time (Years)
30 meter neritic zone area (low resolution)
1st derivative of low resolution model
0
0.5
1
1.5
2
0
1000
2000
3000
4000
5000
6000
7000
8000
9000
10000
11000
12000
13000
14000
15000
16000
17000
18000
19000
20000
21000

Figure 6-3

Figure 6-3 The low resolution curve (3.5 minute per pixel) for the expansion of the 30 meter deep neritic zone that covers the sea floor. The 1st derivative is scaled up artificially to fit the range of the parent curve.

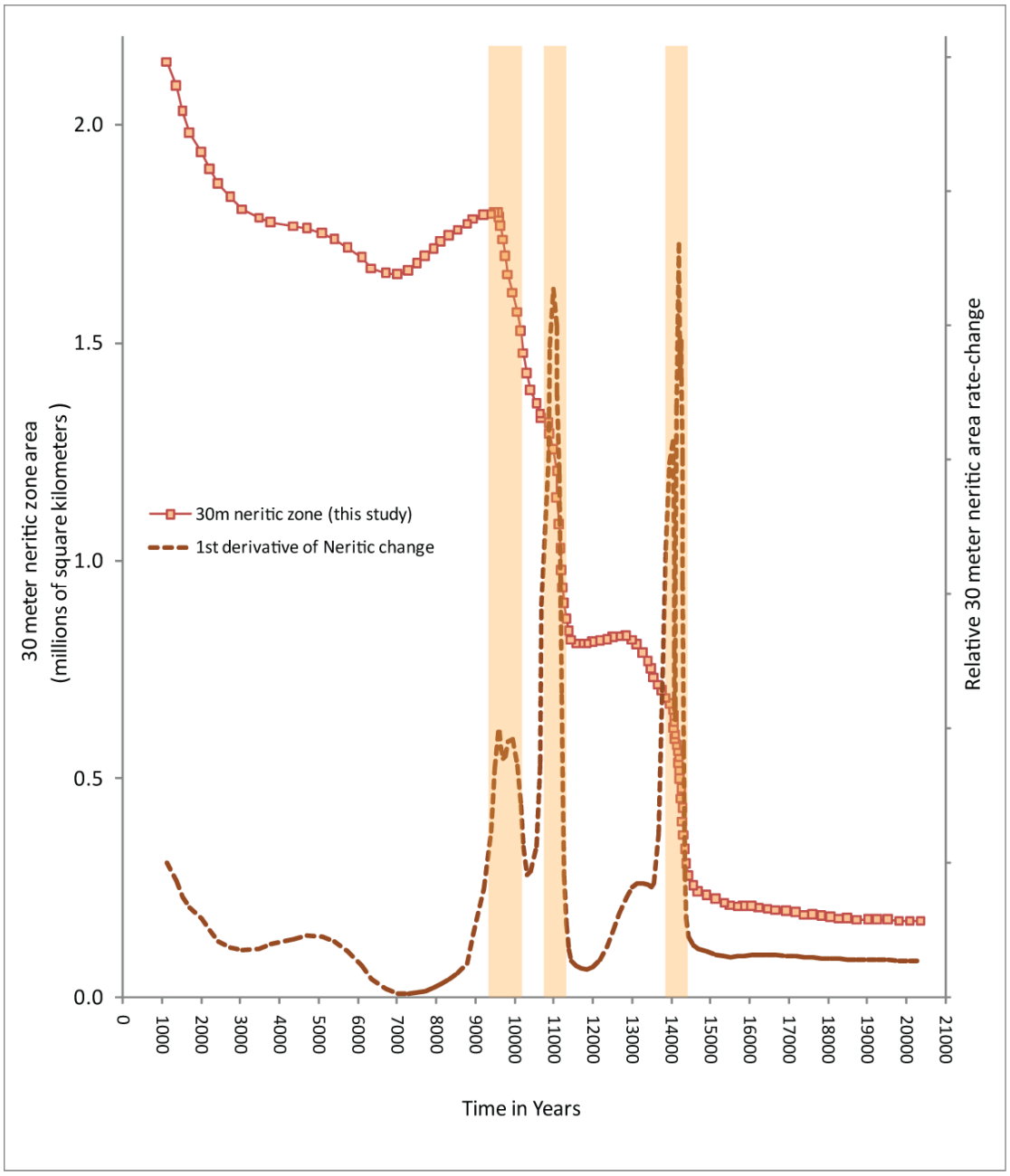
30 meter neritic zone area
(millions of square kilometers)
Relative 30 meter neritic area rate-change
30m neritic zone (this study)
1st derivative of Neritic change
Time in Years
0.0
0.5
1.0
1.5
2.0
0
1000
2000
3000
4000
5000
6000
7000
8000
9000
10000
11000
12000
13000
14000
15000
16000
17000
18000
19000
20000
21000

Figure 6-4

Figure 6-4 The higher resolution curve (1 minute per pixel) for the expansion of the 30 meter deep neritic zone that covers the sea floor. The 1st derivative is scaled up artificially to fit the range of the parent curve.

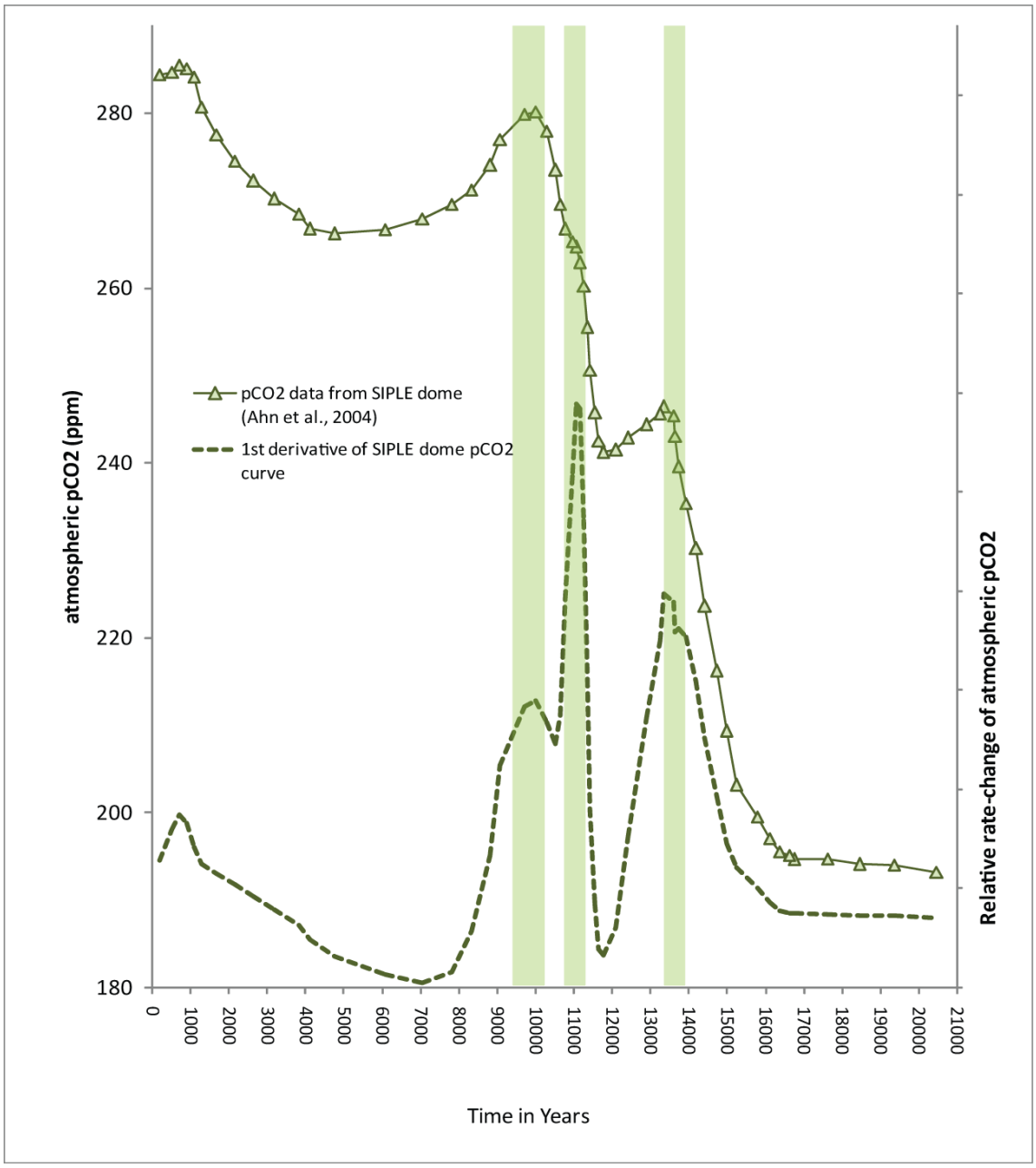
280
260
240
220
200
180
atmospheric pCO2 (ppm)
pCO2 data from SIPLE dome (Ahn et al., 2004)
1st derivative of SIPLE dome pCO2 curve
Relative rate-change of atmospheric pCO2
0
1000
2000
3000
4000
5000
6000
7000
8000
9000
10000
11000
12000
13000
14000
15000
16000
17000
18000
19000
20000
21000
Time in Years

Figure 6-5

Figure 6-5 Relative pCO_2 of the atmosphere since the last glacial maximum, as measured in the Antarctic ice core from the SIPLE dome (Data from Ahn et al., 2004) and its 1st derivative curve. The original data was smoothed with a 4-point running average.

meters below present sea level). During times when the neritic expansion waned (negative 1st derivative), the water depths of the already flooded flat areas on the shelf began to exceed the maximum depth (as defined above) of 30 meters for the shallow neritic zone, without adding an equal amount of new shallow areas as a result of new flooding. In other words, the geometry of the shoreline changed from flat to steep.

Figure 6-5 shows the relative atmospheric pCO_2 curve (Ahn et al., 2004) and its 1st derivative. The original pCO_2 data set was smoothed with a 4-point running average to filter out the minor noise from the major trends and produce a smooth 1st derivative curve. Likewise, as shown by the 1st derivatives for the neritic expansion curve in Figure 6-5, we see the 1st derivative of the atmospheric pCO_2 curve also showing three distinct peaks which are marked with translucent bars. The 1st derivative *p*CO2 has a major peak occurring approximately 14,000-13,000 years ago, another major peak from 11,400-10,800 years ago and a minor peak occurs from 10,200-9,400 years ago. The three episodes are marked with translucent bars on Figure 6-5. During the times when the pCO_2 level peaked, the evasion of CO_2 from the ocean into the atmosphere must have risen distinctly, and at an accelerated rate, compared to the overall average during the time elapsed since the last glacial maximum.

Figure 6-6 shows the coral-based sea level curve (Peltier and Fairbanks, 2006) and its 1st derivative. As is the case for the two 1st derivative curves (the neritic expansion and the atmospheric pCO_2, curves, respectively), shown previously, the 1st derivative curve for the sea level also displays distinct peaks: A minor peak

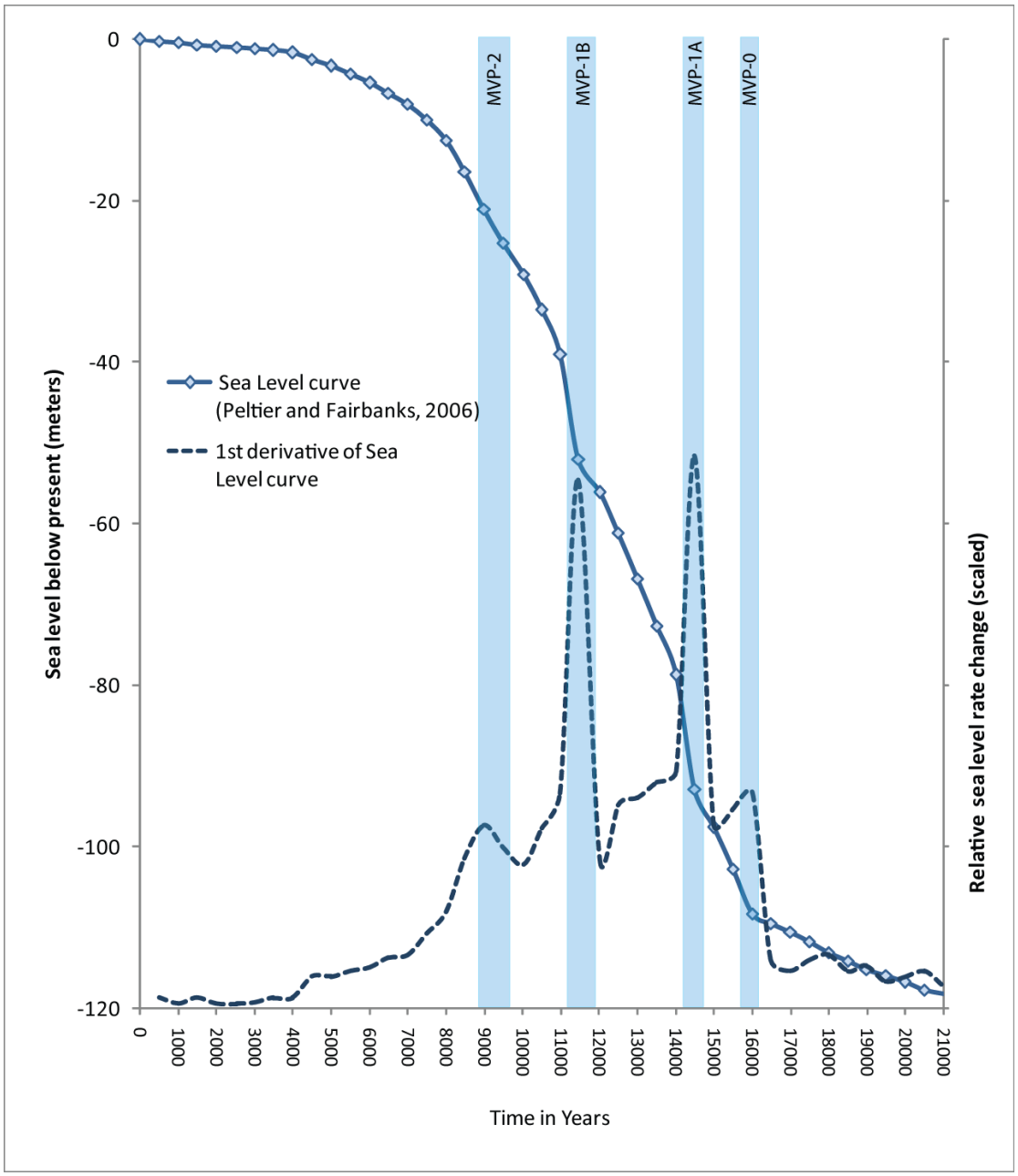
MVP-2
MVP-1B
MVP-1A
MVP-0
Sea Level curve
(Peltier and Fairbanks, 2006)
1st derivative of Sea
Level curve
Sea level below present (meters)
Relative sea level rate change (scaled)
Time in Years
0
-20
-40
-60
-80
-100
-120
0
1000
2000
3000
4000
5000
6000
7000
8000
9000
10000
11000
12000
13000
14000
15000
16000
17000
18000
19000
20000
21000

Figure 6-6

Figure 6-6 Sea level rise and its 1st derivative curve from the last glacial maximum to present, based on coral data from a variety of localities (see Peltier and Fairbanks, 2006). The melt water pulses (MVPs) are marked, in accordance with the rates of change in the new sea level curve, as MVP-0 (~16,200 years ago), MVP-1A (~14,700 years ago), MVP-1B (~11,800 years ago) and MVP-2 (~9,500 years ago).

(16,200-15,500 years ago), a major one (14,800-14,200 years ago), another major one (11,900-11,200 years ago), and a minor peak (9,600-8,700 years ago). The four 'peak episodes' are marked with translucent bars in Figure 6-6. During peak times, the sea level rose faster than average (i.e. a 'melt water pulse' - MVP). The two major 1st derivative peaks in Figure 6-6 represent a first melt water pulse (MVP-1A, approximately 14,700 years ago) and a second melt water pulse (MVP-1B, approximately 11,500 years ago).

We have chosen to compare the 1st derivative curves for (i) the neritic expansion on the flooded areas of the shelves, (ii) rising relative atmospheric pCO_2 and(iii) the sea level rise, in order to compare and correlate these significant episodes of change in their rise since the last glacial maximum. If there is a connection between the anomalous (the above average) rise of atmospheric pCO_2 and the expansion of reef habitats (possibly in combination with shrinking (flooding) of effective CO_2 sequestering mangroves and swamps thought to have occupied much of the vast areas on the flat shallow shelves), the rate changes of these three environmental variables may shed light on such a connection.

DISCUSSION

Between the last glacial maximum and the early Holocene, both the EPICA Dome C (data not shown here – see Monnin et al., 2004) and the SIPLE Dome (Ahn et al., 2004) Antarctic ice cores show two episodes of a coupled, sharp increase, followed by a decrease, in relative atmospheric pCO_2 (Figure 6-5). The decrease occurring between the two episodes marks the brief Antarctic Cold

Reversal (and simultaneously, the Bølling-Allerød warm period in the Northern Hemisphere). The two curves are slightly offset from each other. This is best explained by the ambiguous lag times from when the snow fell on the domes until it was compacted enough to trap and seal the CO_2 within the air bubbles (Monnin et al., 2004). Since we are interested in episodes of significant rates of change in both atmospheric pCO_2 and sea level, we calculated and compared the 1st derivatives of the pCO_2 curve from the SIPLE Dome data and the coral-based sea level curve since the last glacial maximum. Using this method greatly reduced our dependency on the exact matching of the curves. It also reduced the significance of the lag, as we were able to rely more importantly on our matching of simultaneous rate changes in atmospheric pCO_2, in sea level rise, and (as included in this study) in the relative neritic expansion (i.e. the expansion of coral habitats) during the flooding of the shallow Sunda and North Australian shelves as the last ice age ended.

We chose the Sunda and North Australian shelves as study areas, because they constitute the largest shallow continental shelf system outside the Polar areas. The waxing and waning of ice ages forced an area of nearly 5 million square km to switch from being completely flooded during interglacial periods to being exposed a few tens of meters above sea level during glacial maxima, and back again during the next flooding. As to the regional shelf, it is tectonically stable and extremely flat, which facilitated significant and rapid environmental changes for very large areas as a result of only a few meters of increase or decrease in sea level.

Figure 6-7 shows the combined records for neritic expansion, increasing atmospheric pCO_2, and sea level rise. Figure 6-8 shows the 1st derivatives of the three parent curves from Figure 6-7. Observing the parent curves, one notices a clear connection between the flooding of the shelves (and subsequent neritic expansion), the sea level, and the atmospheric CO_2 curve. For the derivative curves in Figure 6-8, the match is even more remarkable. This relationship between the sea level and the flooding (neritic expansion) does not come as a surprise. However, what needs to be scrutinized in more depth is how the geometry of the global shelves 'regulates' this rate of change on a vertical scale. Another question deals with the ways the corals may be thought to regulate the CO_2 content of the atmosphere. In the study of past sea levels, corals from present stratigraphic levels are typically dated by U-Th or ^{14}C methods, corrected for any isostatic component, and evaluated as marking the sea level corresponding to the age of the coral in question. In this way, several stratigraphic hiatuses in the coral record have been discovered. One explanation is that sea levels must at times have risen too fast for the living corals to accommodate the vertical growth. As a consequence, they were drowned. It seems reasonable to assume that such a global drowning with rising sea level would have some effect on the CO_2 balance between the ocean and the atmosphere. The question is how much? By way of the same argument, would not a massive lateral expansion of the reef habitats be able to shift the CO_2 balance between the ocean and the atmosphere, resulting in higher CO_2 levels for the latter? These questions are central when we attempt to evaluate the coral reef hypothesis and the phenomena that led to its formulation.

The almost perfect synchronicity of the 1st derivatives, as shown in Figure 6-8, clearly confirms the existence of a relationship between the flooding of the shelves and the rising atmospheric pCO_2, but is this relationship exclusively controlled by calcification in the upper 30 meter water column?

As we have seen above, the 1st derivative of the sea level curve (Peltier and Fairbanks, 1989) shows two significant peaks and two smaller ones. The larger peaks confirm the timing and extent of the rapid sea level changes that occurred as 'melt water pulses' 1-A and 1-B (see Fig. 6-3). The 1st derivative of the SIPLE dome pCO_2 curve matches our hypothetical evaluation of the response of CO_2 to sea level change, assuming coral reef growth to be a significant contributor to the atmospheric pCO_2 variability. The match may be explained if we assume that the maximum pCO_2 rate change coincides with the inflection point of the 1st derivative of the sea level curve (i. e., at the inception of the melt water pulse in question which would also allow for the rapid neritic expansion on the flat shelves). Following this reasoning, when the coral reefs drowned and further growth diminished during a too rapid sea level rise, the atmospheric pCO_2 would decrease in return, because much less CO_2 was produced from the calcification of coral skeletons and other organisms. On the other hand, such a rapid sea level rise would have flooded vast areas on the Sunda and North Australian shelves, home to hundreds of thousands square km of low-lying mangrove forests, as well.

Hence, the geometry of these flat shelves prompted a double punch to the CO_2 curve, in that the vast lateral expansion of the CO_2-producing reef habitats was

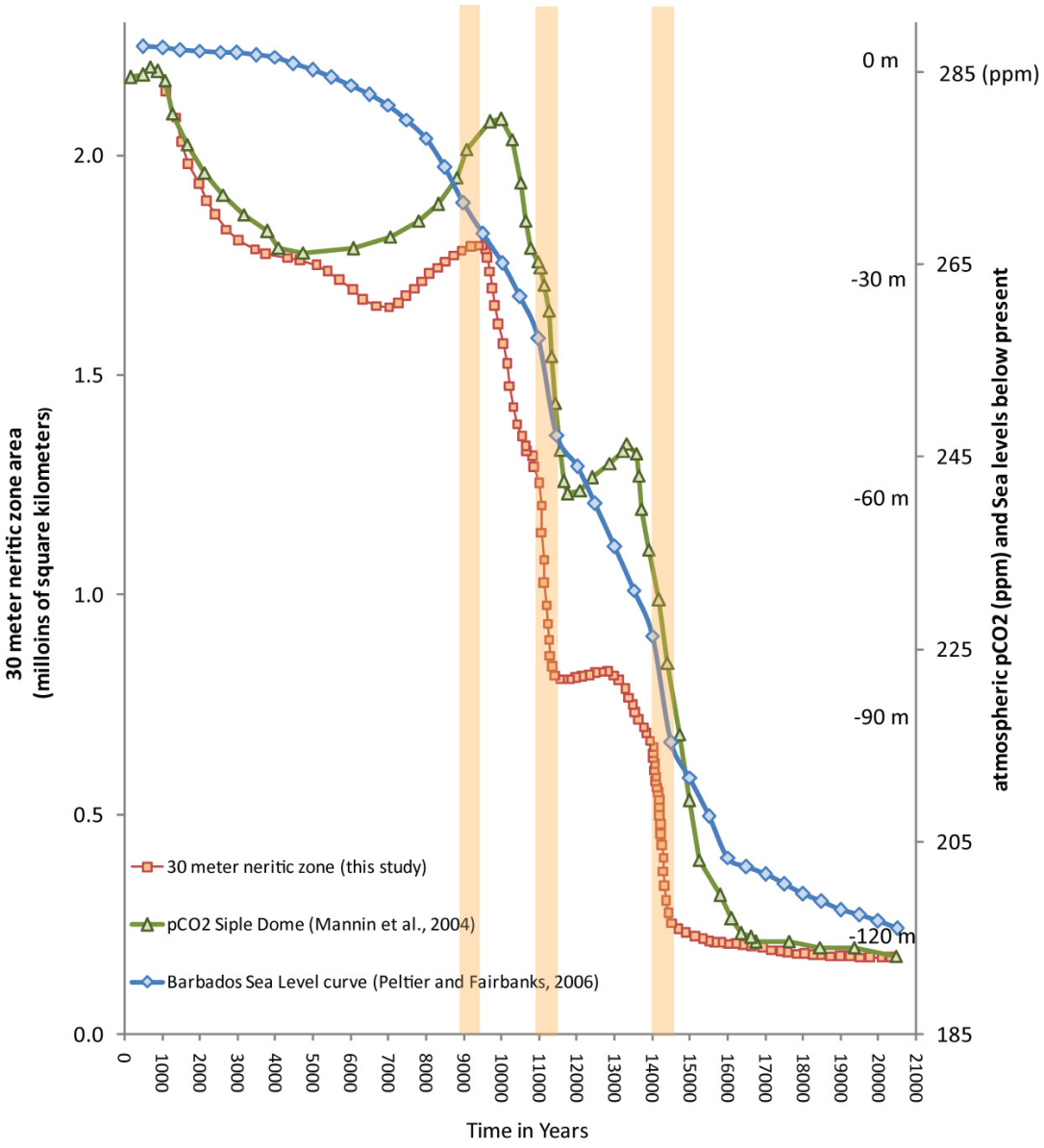
30 meter neritic zone area
(milloins of square kilometers)
atmospheric pCO2 (ppm) and Sea levels below present
0 m
-30 m
-60 m
-90 m
-120 m
285 (ppm)
265
245
225
205
185
2.0
1.5
1.0
0.5
0.0
0
1000
2000
3000
4000
5000
6000
7000
8000
9000
10000
11000
12000
13000
14000
15000
16000
17000
18000
19000
20000
21000
Time in Years
30 meter neritic zone (this study)
pCO2 Siple Dome (Mannin et al., 2004)
Barbados Sea Level curve (Peltier and Fairbanks, 2006)

Figure 6-7

Figure 6-7 The three curves showing the evolution, since the last glacial maximum, of (i) neritic expansion (red), (ii) atmospheric pCO_2 (green), and (iii) the coral-based sea level (blue).

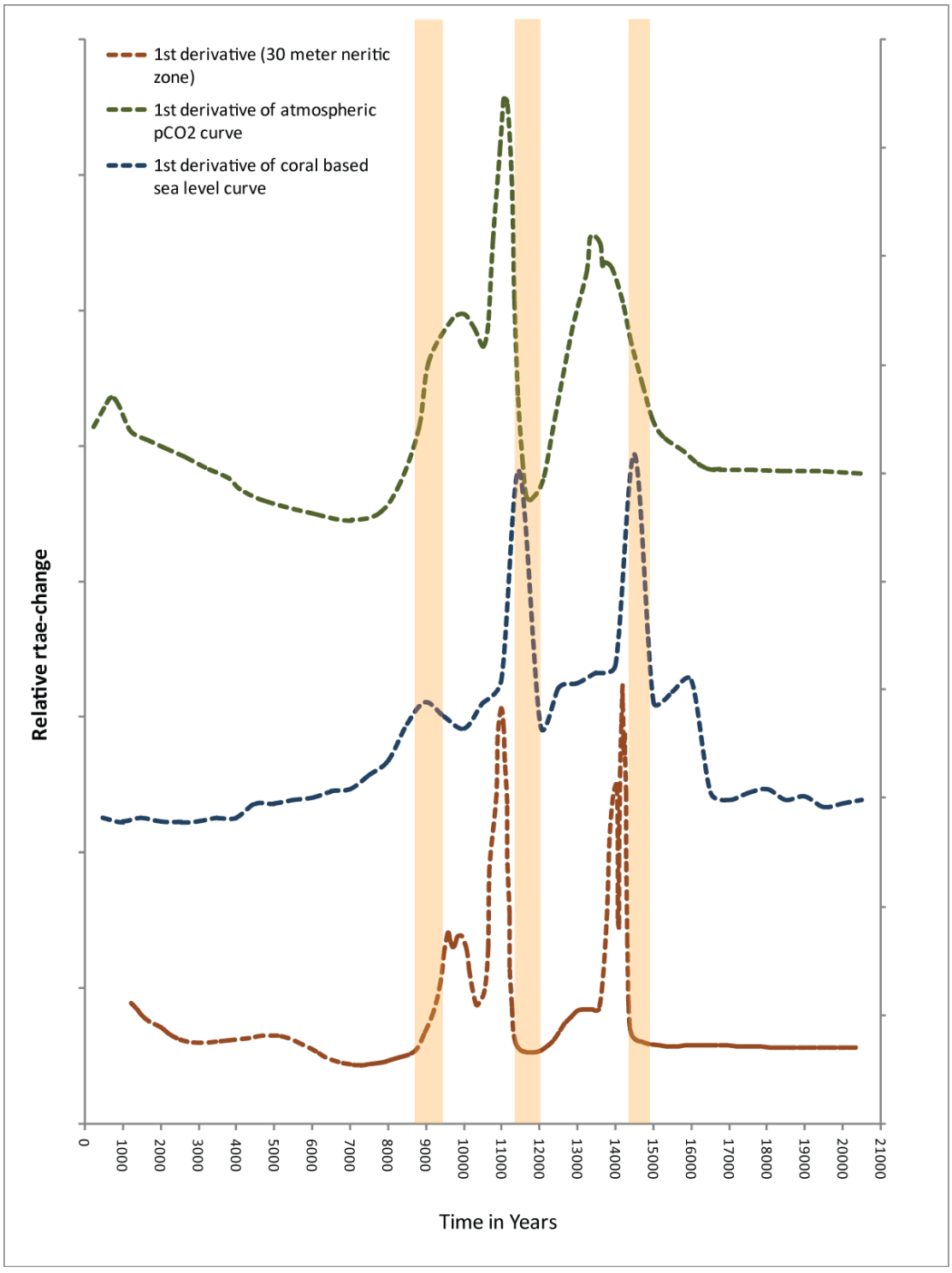
1st derivative (30 meter neritic zone)
1st derivative of atmospheric pCO2 curve
1st derivative of coral based sea level curve
Relative rtae-change
0
1000
2000
3000
4000
5000
6000
7000
8000
9000
10000
11000
12000
13000
14000
15000
16000
17000
18000
19000
20000
21000
Time in Years

Figure 6-8

Figure 6-8 The 1st derivatives of the parent curves from Figure 6-7) of (i) neritic expansion (red), (ii) atmospheric pCO_2 (green), and (iii) the coral data based sea level (blue) since the last glacial maximum.

combined with the vast inundation of the CO_2 sequestering mangroves and low-lying forests and jungles. In both cases, the results of these processes would help drive up the CO_2 content in the atmosphere. In terms of the coupled derivatives shown in Figure 6-8, this is indeed a viable explanation. When the Earth exited the last glacial, the sea level was below the shelves rim and there were no vast flat areas where the corals could colonize. On the contrary, they were confined, as our analysis shows, to small slivers of sea floor beneath the slope shoulder (See Figure 6-2, Plate 1). Later, when the sea level crept up on the flat shelves, the neritic environments could increase laterally. They did this at a tremendous rate and increased their habitat multiple-fold (compare Figure 6-2, Plate 1 with Figure 6-2 Plate 10, and the neritic expansion curve in Figure 6-4). During this latter flooding, the vast mangrove forests on the shelves were inundated by the marine transgression. However, as the sea level rose further, the large, flat, newly colonized areas became too deep for the corals and other fauna to continue sunlight dependent growth. The lateral expansion of reef habitat was not only slowed down, but even reduced, with loss of the flat bottom below 30 meters and with no significant expansion at the top, as the new shore line gradually became steeper. Judging from our geospatial analysis, this seems to have happened twice on the Sunda and North Australian Shelves since the last glacial maximum. Remarkably, during both episodes the atmospheric rise in pCO_2 showed a similar evolution. The fact that the two events happened when the sea level was approximately at 85 meters and at 30 meters below present corresponds well with the overall geometry of the Sunda and the North Australian shelves. These

shelves have two plateaus at these levels that are flatter and larger than the rest of the shelves (see Figure 6-2, Plates 1 through 26).

CONCLUSIONS

Based on the above data and hypotheses, a link is seen between the neritic expansion on the Sunda and North Australian shallow continental shelves and the rise of the atmospheric pCO_2 (as shown by the characteristic shape of its derivative curve in Fig. 6-8). Our considerations are backed up by the following conclusions:

1) The variable sea level rise following the last glacial maximum, coupled with an increasingly expanding neritic zone on the shallow shelves, allowed for accelerated growth of coral reefs and other carbonate producing organisms. Consequently, this increased the surface water pCO_2, and caused CO_2 to evade into the atmosphere. This development may have been further exacerbated by the flooding and inundating of vast CO_2-sequestering mangrove and forest areas, as the sea level crept up on the flat parts of the shelves.

2) The onset of the first melt water pulse (MWP-1A) was occasioned by the accelerated rise of CO_2 into the atmosphere, causing surface warming and the breaking down of ice sheets. The accelerated rise in sea level compounded this effect by first allowing the neritic areas to expand, and later (as evidenced by the 'kink' of the CO_2 curve in Figure 6-8), by causing a massive drowning of reefs and the carbonate producing fauna that could not keep up with the fast seawater rise. Consequently, the CO_2 output from the ocean to the atmosphere dropped.

Notice also that the massive carbonate producing fauna die-off at this time is concurrent with possible increased continental carbonate and silicate weathering, likewise associated with this pulse of rapid sea level rise, as the weather became warmer and wetter in the north and in the south. The net effect of this process could effectively have lowered surface water pCO_2, by drawing down CO_2 from the atmosphere into the ocean.

3) After the MVPs, sea level rise returned to average rates, and the carbonate producing neritic zone resumed and continued its contribution to the increase in atmospheric pCO_2, as long as ample accommodation space for reef development continued to increase with rising sea levels.

4) A similar trend was to repeat itself right after the second melt water pulse (MWP-1B). However, the increase in atmospheric pCO_2 that followed the return of average sea level rise after the MVP-1B, did not occur to the same extent after MWP-1A. By the same token, immediately following MVP-1B, the neritic expansion dropped, because the defined 30 meter neritic zone had lost the large flat areas at approximately 35 meters on the shelves, when the sea level rose above the shelves and the new coastline became steeper. As shown in our geospatial analysis, in the Holocene, the neritic expansion at first dropped because of this loss, but increased again after 5,000 years, to reach today's levels. The remarkable correlation in the Holocene between the shallow neritic zone waning and its increase to today's extent, which so closely matches the fluctuations in the atmospheric pCO_2, further strengthens our claim that there exists a close relationship between them.

REFERENCES

Adams, J.M., Faure, H., Faure-Denard, L., McGlade, J.M., and Woodward, F.I. (1990) Increases in terrestrial carbon storage from the Last Glacial Maximum to the present. *Nature,* **348**, 711-714

Adloff, J. P., and Rössler, K. (1991). Recoil and transmutation effect in migration behavior of actinides. *Radiochimica Acta,* **52/53,** 269-274.

Ahn, J., Wahlen, M., Deck, B., Brook, E., Mayewski, P., Taylor, K., White, J. (2004) A record of atmospheric CO_2 during the last 40,000 years from the Siple dome, Antarctica ice core. *Journal of Geophysical Research (Atmospheres)* –available at: http://nsidc.org/data/docs/agdc/nsidc0202_wahlen/

Allan, J. R., and Matthews, R. K. (1977). Carbon and oxygen isotopes as diagenetic and stratigraphic tools: surface and subsurface data, Barbados, West Indies. *Geology* **5,** 16-20.

Andersen, M. B., Stirling, C. H., Potter, E.-K., Halliday, A. N., Blake, S. G., McCulloch, M. T., Ayling, B. F. and O'Leary, M. (2008) High-precision U-series measurements of more than 500,000 year old fossil corals, *Earth and Planetary Science Letters* **265** (1-2), 229-245.

Anderson, T. F., Bender, M. L.., and Broecker, W. S. (1973). Surface areas of biogenic carbonates and their relation to fossil ultra structure and diagenesis. *Journal of Sedimentary Petrology* **43,** 471-477.

Archer, D., Winguth, A., Lea, D., and Mahowald, N. (2000) What caused the glacial/interglacial atmospheric pCO_2 cycles. *Reviews of Geophysics*, **38** (2), 159-189

Banner, J. L., Wasserburg, G. J., Chen, J. H., and Humphrey, J. D. (1991). Uranium-series evidence on diagenesis and hydrology in Pleistocene carbonates of Barbados, West Indies. *Earth and Planetary Science Letters* **107,** 129-137.

Banner, J. L., Wasserburg, G. J., Chen, J. H., Humphrey John, D., and Anonymous. (1990). Carbonate deposition, diagenesis and hydrology on Barbados, West Indies; uranium-series evidence.; Geological Society of America, 1990 annual meeting. *Abstracts with Programs Geological Society of America* **22,** 88.

Bar-Matthews, M., Wasserburg, G. J., and Chen, J. H. (1993). Diagenesis of fossil coral skeletons; correlation between trace elements, textures, and $^{234}U/^{238}U$. *Geochimica et Cosmochimica Acta* **57,** 257-276.

Bard, E., Hamelin, B., and Fairbanks, R. G. (1990). U-Th ages obtained by mass spectrometry in corals from Barbados; sea level during the past 130,000 years. *Nature (London)* **346,** 456-458.

Barnett, M. O., Jardine, P. M., Brooks, S. C., and Selim, H. M. (2000). Adsorption and transport of uranium (VI) in subsurface media. *Soil Science Society of America Journal* **64,** 908-917.

Bender, M. L., Fairbanks, R. G., Taylor, F. W., Matthews, R. K., Goddard, J. G., and Broecker, W. S. (1979). Uranium-series dating of the Pleistocene reef tracts of Barbados, West Indies. *Geological Society of America Bulletin* **90,** I 577-I 594.

Berger, A. (1978) Long-term variations of caloric insolation resulting from the Earth's orbital elements. *Quat. Res.* **9,** 139–167

Berger, W.H. (1982) Increase in carbon dioxide in the atmosphere during deglaciation: The coral reef hypothesis. *Naturwissenschaften,* **69**, 87-88

Bischoff, J. L., and Fitzpatrick, J. A. (1991). U-series dating of impure carbonates; an isochron technique using total-sample dissolution. *Geochimica et Cosmochimica Acta* **55,** 543-554.

Blanchon, P. and Eisenhauer, A. (2001) Multi-Stage reef development on Barbados during the last interglaciation. *Quat. Sci. Rev.* **20**, 1093-1112.

Broecker, W. S. (1973). The marine chemistry of carbon and its role in oceanographic research.; *Oceanography; the Last Frontier*. 56-66.

Broecker, W.S. and Peng, T.-H. (1987) The role of CaCO3 compensation in the glacial to interglacial atmospheric CO2 change? *Global Biogeochemical Cycles* **1**, 16-29

Broecker and Clark (2007) Is the magnitude of the carbonate ion decrease in the abyssal ocean over the last 8 kr consistent with the 20 ppm rise in atmospheric CO2 content? *Paleoceanography*, **22**, PA1202

Caress, D. W. and Chayes, D. N. (2006) MB-System: Mapping the Seafloor *http://www.mbari.org/data/MB-System and http://www.ldeo.columbia.edu/res/pi/MB-System*

Carbotte, S. M., Arko, R., Chayes, D. N., Haxby, W., Lehnert, K., O'Hara, S., Ryan, W. B. F., Weissel, R. A.; Shipley, T., Gahagan, L., and Johnson, K. and Shank, T. (2000) New Integrated Data Management System for Ridge2000 and MARGINS Research, *Eos*, **85**, (51, 21)

Chen, J. H., Curran, H. A., White, B., and Wasserburg, G. J. (1991). Precise chronology of the last interglacial period; ^{234}U- ^{230}Th data from fossil coral reefs in the Bahamas; with Suppl. Data 91-01. *Geological Society of America Bulletin* **103,** 82-97.

Cherdyntsev, V. V., Kazachevskiy, I. V., and Kuz'mina-Ye, A. (1965). Dating of Pleistocene carbonate formations by the uranium and thorium isotopes. *Geochem. Int.* **2,** 794-801

Chiu, T-C, Fairbanks, R.G., Mortlock, R.A.and A.L. Bloom, (2005) Extending the radiocarbon calibration beyond 26000 years before present using fossil corals. *Quaternary Science Reviews*, **24**, 1797-1808

Chiu, T-C, Fairbanks, R.G., Mortlock, R.A., Cao, L., Fairbanks, T.W. and Bloom, A.L. (2006). Redundant 230Th/234U/238U and 231Pa/235U dating of fossil corals: verification of U-series ages for radiocarbon calibration. *Quaternary Science Reviews*, **25**, 2431-2440.

Cutler, K. B., Edwards, R. L., Taylor, F. W., Cheng, H., Adkins ,J., Gallup, C. D., Cutler, P. M.,. Burr, G. S and Bloom, A. L. (2003). Rapid sea-level fall and deep ocean temperature change since the last interglacial period. *Earth and Planet. Sci. Lett.* **206**, 253-271.

Dickin, A. P. (2005). Radiogenic isotope geology. 2 ed. Cambridge University Press, 470 pp.

Eggins, S. M., Grün, R., McCulloch, M. T., Pike, A. W. G., Chappell, J., Kinsley, L., Mortimer, G., Shelley, M., Murray-Wallace, C. V., Spötl, C., and Taylor, L. (2005). In situ U-series dating by laser-ablation multi-collector ICPMS: new prospects for Quaternary geochronology. *Quaternary Science Reviews* **24,** 2523-2538.

Esat, T. M., and Yokohama, Y. (2006) Variability in the uranium isotopic composition of the oceans over glacial-interglacial timescales. *Geochimica et Cosmochimica Acta.* **70**(16), 4140-4150.

Esat, T. M., M. T. McCulloch, J. Chappell, B. Pillans and A. Omura (1999). Rapid fluctuations in sea level recorded at Huon Peninsula during the penultimate deglaciation. *Science* **283**, 197-201.

Fairbanks, R.G. (1988) Barbados off shore drilling program cruise report. *R/V Ranger Cruise 88-13 Cruise report, Lamont Doherty Earth Observatory.* (Filed under NSF grant# OCE87-17172)

Fairbanks, R.G., (1989) A 17,000 year glacio-eustatic sea level record: influence of glacial melting rates on the Younger Dryas event and deep ocean circulation. *Nature*, **342**, 637-642.

Fairbanks, R. G., Mortlock, R. A., Chiu, T., Cao, L., Kaplan, A., Guilderson, T. P., Fairbanks, T. W., Bloom, A. L., Grootes, P. M., and Nadeau, M. J. (2005). Radiocarbon calibration curve spanning 0 to 50,000 years BP based on paired (super 230) Th/ (super 234) U/ (super 238) U and (super 14) C dates on pristine corals. *Quaternary Science Reviews* **24,** 1781-1796.

GEBCO, General Bathymetric Chart of the Oceans by the BODC (British Oceanographic Data Centre)

Gallup, C. D., Edwards, R. L., and Johnson, R. G. (1994). The timing of high sea levels over the past 200,000 years. *Science* **263,** 796-800.

GeoMapApp (2006) *Lamont Doherty Earth Observatory* http://www.marine-geo.org/geomapapp/

Hamelin, B., Bard, E., Zindler, A., and Fairbanks, R. G. (1991). $^{234}U/^{238}U$ mass spectrometry of corals; how accurate is the U-Th age of the last interglacial period? *Earth and Planetary Science Letters* **106,** 169-180.

Hays, J. D., Imbrie, J. and Shackleton, N. J. (1976). "Variations in the Earth's orbit: pacemaker of the ice ages." Science 194: 1121-1131.

Haxby, W. F., Karner, G. D., LaBrecque, J. L. and Weissel, J. K. (1983) Digital images of combined Oceanic and Continental data sets and their use in tectonic studies, *EOS Trans*. **64**, 995-1003.

Henderson, G. M., Cohen, A. S., and O-Nions, R. K. (1993). $^{234}U/^{238}U$ ratios and ^{230}Th ages for Hateruma Atoll corals; implications for coral diagenesis and seawater $^{234}U/^{238}U$ ratios. *Earth and Planetary Science Letters* **115,** 65-73.

Henderson, G. M., Slowey, N. C., and Fleisher, M. Q. (2001). U-Th dating of carbonate platform and slope sediments. *Geochimica et Cosmochimica Acta* **65,** 2757-2770.

Henderson, G. M., (2002) . Seawater ($^{234}U/^{230}Th$) during the last 800.000 years. *Earth and Planetary Science Letters*, **199** (1-2), 97-110.

ImageJ – *http://rsb.info.nih.gov/ij/*

Imbrie, J., Hays, J. D., Martinson, D. G., McIntyre, A., Mix, A. C., Morley, J. J., Pisias, N. G., Prell, W. L. and Shackleton, N. J. (1984) The orbital theory of Pleistocene climate: support from a revised chronology of the marine $\delta^{18}O$

record. *Milankovitch and Climate. A. L. Berger. Norwell, MA, D. Reidel Publishing Company.* 1, 269-305.

Ivanovich, M., and Harmon, R. S. (1992). Uranium-series disequilibrium; applications to Earth, marine, and environmental sciences. 2 ed. *Oxford University Press, Oxford***,** 911 pp.

Ivanovich, M., Latham, A. G., and Ku, T. L. (1992a). Uranium-series disequilibrium applications in geochronology.; in: "*Uranium-series Disequilibrium; Applications to Earth, Marine, and Environmental Sciences"* (M. Ivanovich, and R. S. Harmon, Eds.), 62-94, Clarendon Press, Oxford, United Kingdom.

Ivanovich, M., Latham, A. G., Longworth, G., and Gascoyne, M. (1992b). Applications to radioactive waste disposal studies.; 2. *In "Uranium-series disequilibrium; applications to Earth, marine, and environmental sciences."* (M. Ivanovich, and R. S. Harmon, Eds.), pp. 583-630. Clarendon Press, Oxford, United Kingdom.

Kaufman, A. (1993). An evaluation of several methods for determining 230Th/U ages in impure carbonates. *Geochimica et Cosmochimica Acta* **57,** 2303-2317.

Kaufman, A., Broecker, W. S., Ku, T. L., and Thurber, D. L. (1971). The status of U-series methods of mollusk dating. *Geochimica et Cosmochimica Acta* **35,** 1155-1183.

Keir, R.S. (1988) On the late Pleistocene ocean geochemistry and circulation. *Paleoceanography* **3**, 413-445

Kigoshi, K. (1971). α-recoil thorium-234; dissolution into water and the uranium-234/ uranium-238 disequilibrium in nature. *Science* **173,** 47-48.

Kronfeld, J. (1974). Uranium deposition and Th-234 α-recoil; an explanation for extreme U-234/U-238 fractionation within the Trinity Aquifer. *Earth and Planetary Science Letters* **21,** 327-330.

Kronfeld, J., Vogel, J. C., and Talma, A. S. (1994). A new explanation for extreme $^{234}U/^{238}U$ disequilibria in a dolomitic aquifer. *Earth and Planetary Science Letters* **123,** 81-93.

Ku, T. L., Ivanovich, M., and Luo, S. (1990). U-series dating of last interglacial high sea stands; Barbados revisited. *Quaternary Research (New York)* **33,** 129-147.

Langmuir, D., and Herman, J. S. (1980). The mobility of thorium in natural waters at low temperatures. *Geochimica et Cosmochimica Acta* **44,** 1753-1766.

Langmuir, D. (1997) Aqueous Environmental Geochemistry, Prentice-Hall, Upper Saddle River, NJ, 600 pp.

Liang, Z., and Ku, T. L. (1984). The U-series dating of detritus-laden carbonate deposits. *Diqiu Huaxue Geochimica, Science Press. Bejing, China* **1984,** 10-21

Luo, S., and Ku, T. L. (1991). U-series isochron dating; a generalized method employing total-sample dissolution. *Geochimica et Cosmochimica Acta* **55,** 555-564.

Luo, S., Ku, T. L., Roback, R., Murrell, M. T., and McLing, T. L. (2000). In-situ radionuclide transport and preferential groundwater flows at INEEL (Idaho): Decay-series disequilibrium studies. *Geochimica et Cosmochimica Acta* **64,** 867-881.

Marchitto, T.M., Lynch-Stieglitz, J., Hemming, S.R. (2005). Deep Pacific CaCO3 compensation and glacial-interglacial atmospheric CO_2. *Earth and Planetary Science Letters,* **231**, 317-336

Matthews, R.K., (1973) Relative elevation of later Pleistocene high sea level stands, Barbados, *Quaternary Research* **3**, 147–153.

MB-system (2006) *Lamont Doherty Earth Observatory Data repository* http://www.ldeo.columbia.edu/res/pi/MB-System/html/mbsystem_how_to_get.html

Mesolella, K. J., Matthews, R. K., Broecker, W. S. and Thurber, D. L. (1969). "The astronomical theory of climatic change: Barbados data." J. Geology 77: 250-274.

Mesolella, K. J., Sealy, H. A., and Matthews, R. K. (1970) Facies Geometries within Pleistocene reefs of Barbados, West Indies. *American Association of Petroleum Geologists Bulletin* **54**, 1899-1917.

Mey, J. L., Fairbanks, R. G., Mortlock, R., Bradtmiller L., (2005): Uranium Series Diagenesis in Corals Exposed to Fresh Water: Toward Better Prospecting for Closed System Samples for High Accuracy Dating. *Eos Trans. AGU*, **86**(52)

Mey, J. L., Fairbanks, R. G., Mortlock, R., (2008) (*in prep.*) The diagenesis of Barbadian coral paleoreefs: uranium series disequilibria systematics and the effects of repeated emergence histories *(planned submission to Earth and Planetary Science Letters- April 2008)*

Mey, J. L., Fairbanks, R. G., Mortlock, R. A. (*in prep*). The drowned Pleistocene paleoreefs of Barbados.

Milankovitch, M. M. (1941) Canon of insolation and the ice age problem (English translation by the Israel Program for Science Translations,Washington, D.C.). *Serb. Acad. Beorg. Spec Publ.* **132.**

Monnin, E., Steig, E.J., Siegenthaler, U., Kawamura, K., Schwander, J., Stauffer, B., Stocker, T.F., Morse, D.L., Barnola, J.-M., Bellier, B., Raynaud, D., and Fischer, H. (2004) Evidence for substantial accumulation rate variability in Antarctica during the Holocene, through synchronization of CO_2 in the Taylor Dome, Dome C, and DML ice cores. *Earth and Planetary Science Letters,* **224**, 45-54

Morse, J. W., Shanbhag, P. M., Saito, A., and Choppin, G. R. (1984). Interaction of uranyl ions in carbonate media. *Chemical Geology* **42,** 85-99.

Mortlock, R., A., Fairbanks, R., G., Chiu, T. C., and Rubenstone, J. (2005). $^{230}Th/^{234}U/^{238}U$ and $^{231}Pa/^{235}U$ ages from a single fossil coral fragment by multi-collector magnetic-sector inductively coupled plasma mass spectrometry. *Geochimica et Cosmochimica Acta* **69,** 649-657.

Opdyke, B.N., and Walker, J.C.G. (1992) Return of the coral reef hypothesis: Basin to shelf partitioning of $CaCO_3$ and its effect on atmospheric CO_2. *Geology,* **20**, 733-736

Ordonez-Regil, E., Schleiffer, J. J., and Adloff, J. P. (1989). Chemical effects of α-recoil in uranium minerals. *Radiochimica Acta* **47,** 177-185.

Osmond, J. K., and Cowart, J. B. (1976). Uranium isotopes in ground-water as a clue to palaeohydrology and palaeoclimatology. *International Geological Congress, Abstracts--Congres Geologique Internationale, Resumes.* **25**, (2-11**),** 478.

Osmond, J. K., and Cowart, J. B. (1980). ^{230}Th, ^{234}U, and ^{238}U disequilibria in secondary uranium deposits. *International Geological Congress, Abstracts--Congres Geologique Internationale*, **26** (3), 982

Osmond, J. K., and Cowart, J. B. (1985). Mass balances by uranium-series disequilibria in natural phosphate deposits and mine products.; The Geological Society of America, 98th annual meeting. *Abstracts with Programs Geological Society of America* **17,** 683.

Osmond, J. K., and Cowart, J. B. (1992). Ground water.; 2. *In* "Uranium-series disequilibrium; applications to Earth, marine, and environmental sciences." (M. Ivanovich, and R. S. Harmon, Eds.), pp. 290-333. Clarendon Press, Oxford, United Kingdom.

Osmond, S. K., Cowart, J. B., and Ivanovich, M. (1983). Uranium isotopic disequilibrium in ground water as an indicator of anomalies.; Nuclear geophysics; applications of nuclear techniques in minerals exploration, mining and process control. *International Journal of Applied Radiation and Isotopes* **34,** 283-308.

Peltier, W. R. and Fairbanks, R. G. (2006) Global glacial ice volume and Last Glacial Maximum duration from an extended Barbados sea level record. *Quaternary Science Reviews*, **25**, 3322-3337

Petit, J. C., Langevin, Y., and Dran, J. C. (1985). $^{234}U/^{238}U$ disequilibrium in nature: theroretical reassesment of the various proposed models. *Bulletin Mineralogie* **108,** 745-753.

Pingitore, N. E. Jr. (1976) Vadose and phreatic diagenesis; processes, products and their recognition in corals. *Journal of Sedimentary Petrology* **46** (4), 985-1006.

Porter, S. C., (1989) Some geological implications of average Quaternary glacial conditions. *Quaternary Research* **32**(3), 245-261.

Radtke, U. and Schellmann, G. (2003) ESR dating of Quaternary corals from Barbados; implications for sea-level reconstruction. In: XVI INQUA congress; Shaping the Earth; a Quaternary perspective. *Congress of the International Union for Quaternary Research*. **16**, 161.

Radtke, U and Schellmann G. (2006) Uplift history along the Clermont Nose traverse on the west coast of Barbados during the last 500,000 years; implications for paleo-sea level reconstructions. *Journal of Coastal Research*. **22**, (2), 350-357.

Rasilainen, K., Suksi, J., Ruskeeniemi, T., Pitkanen, P., and Poteri, A. (2003). Release of uranium from rock matrix--a record of glacial meltwater intrusions? *Journal of Contaminant Hydrology* **61,** 235-246.

Reeder, R. J., Nugent,M., Tait C. D., Morris, D. E.; Heald S. M.; Beck, K. M.; Hess W. P.; Lanzirotti, A. (2001) Coprecipitation of uranium(VI) with calcite; XAFS, micro-XAS, and luminescence characterization. *Geochimica et Cosmochimica Acta*. **65**(20), 3491-3503

Rose, A. W. and Wright, R. J., (1980). Gechemical Exploration Models for Sedimentary Uranium Deposits. *Journal of Geochemical Exploration*, **13**, 153-179

Rosholt, J. N., Shields, W. R., and Garner, E. L. (1963). Isotopic fractionation of uranium in sandstone. *Science* **139,** 224-226.

Rössler, K. (1983). Uranium recoil reactions. *In* "Gmelin Handbook of Inorganic Chemistry." pp. 135-164. Springer Verlag, Berlin.

R/V Ewing 03-08 Cruise data (2003) *Lamont Doherty Earth Observatory (Columbia University) data repository*: http://www.marine-geo.org/link/entry.php?id=EW0308

Schellmann, G. and Radtke, U. (2002) The Coral Reef Terraces of Barbados – A Guide. Fourth Annual meeting of IGCP Project 437. *Internal Publication, University of Bamberg*, 160 Pages.

Schmidt, V., Chayes, D., Caress, D. (2006) *MB-system Cookbook and Manual Pages*
http://www.ldeo.columbia.edu/res/pi/MB-System/html/mbsystem_cookbook.html
http://www.ldeo.columbia.edu/res/pi/MB-System/html/mbsystem_manpages.html

Scholz, D., Mangani, A., and Felis, T. (2004). U-series dating of diagenetically altered fossil corals. *Earth and Planetary Science Letters* **218,** 163-178.

Scholz, D. and Mangini, A. (2007) How Precise are U-series coral ages? *Geochimica et Cosmochimaica Acta* **71**, 1935-1948

Scholz D., Mangini A., and Meischner D. (2006) U-redistribution in fossil reef corals from Barbados, West Indies, and sea level reconstruction for MIS 6.5. In *The Climate of Past Interglacials* (eds. F. Sirocko, M. Claussen, M.F. Sanchez-Goni and T. Litt). Elsevier, Amsterdam Heidelberg New York, pp. 119–140.

Schwarcz, H. P., and Latham, A. G. (1989). Dirty calcites; 1, Uranium-series dating of contaminated calcite using leachates alone. *Chemical Geology: Isotope Geoscience Section* **80,** 35-43.

Shackleton, N. J. (1987). Oxygen isotopes, ice volume and sea level. *Quat. Sci. Rev.* **6**(3-4), 183-190.

Shackleton, N. J., Imbrie, J., Hall, M. A. (1983) Oxygen and carbon isotope record of East Pacific core V19-30: implications for the formation of deep water in the late Pleistocene North Atlantic. *Earth and Planetary Science Letters* **65**(2), 233-244

Shuttle Radar Topography Mission (SRTM) (2003) http://www2.jpl.nasa.gov/srtm/).

Sigman, D.M., and Boyle, E.A. (2000) Glacial/interglacial variations in atmospheric carbon dioxide. *Nature*, **407**, 859-869

Speed, R. C. (1990) Volume loss and defluidization history of Barbados. *Journal of Geophysical Research*, **95** (B6) 8983-8996.

Speed, R. C. and Cheng, H. (2004) Evolution of marine terraces and sea level in the last interglacial, Cave Hill, Barbados. *GSA Bull.* **116**(1/2), 219-232.

Stein M., Wasserburg G. J., Aharon P. J., Chen H., Zhu Z. R., Bloom A., and Chappell J. (1993) TIMS U-series dating and stable isotopes of the last interglacial event in Papua New Guinea. *Geochim. Cosmochim. Acta* **57**, 2541-2554.

Stirling, C. H., Esat T. M., Lambeck K., McCulloch M. T., Blake S. G., Lee D.-C. and Halliday A. N. (2001) Orbital forcing of the marine isotope stage 9 interglacial. *Science* **291**, 290-293.

Stirling, C. H., Esat T. M., McCulloch M. T. and Lambeck K. (1995) High precision U-series dating of corals from Western Australia and implications for the timing and duration of the last interglacial. *Earth and Planet. Sci. Lett.* **135**, 115-130.

Sturchio, N. C.; Antonio, M. R.; Soderholm, L.; Sutton, S. R.; Brannon, J. C. (1998), *Science* **281**, 971-973.

Suksi, J., and Rasilainen, K. (2001a). Isotopic Fractionation of U in Rocks Reflecting Redox Conditions Around a Groundwater Flow Route. *Materials Research Society Symposium Proceedings (Scientific Basis for Nuclear Waste Management XXIV)* **663,** 11/11_5.

Suksi, J., and Rasilainen, K. (2001b). Isotopic fractionation of U in rocks reflecting redox conditions around a groundwater flow route. *Scientific Basis for Nuclear Waste Management XXIV Symposium, Materials Research Society Proceedings* **663,** 961-969.

Suksi, J., Rasilainen, K., and Pitkanen, P. (2006) Variations in $^{234}U/^{238}U$ activity ratios in groundwater--A key to flow system characterisation? *Physics and Chemistry of the Earth, Parts A/B/C* **31**(10-14) 556-571. *In: MIGRATION 2005, the 10th international conference on the Chemistry and migration of actinides and fission products in the geosphere. Geckeis-Horst (editor)* Elsevier. Kidlington, United Kingdom. 2006.

Thompson, W. G., and Goldstein, S. L. (2005). Open-System Coral Ages Reveal Persistent Suborbital Sea-Level Cycles. *Science* **308,** 401-404.

Thompson, W. G. (2004). A 250,000-Year Record of Sea Level and Climate from Open-System Coral Ages. Ph.D. Thesis, 133 pages, Columbia University, New York.

Thompson, W. G., Spiegelman, M. W., Goldstein, S. L., and Speed, R. C. (2003). An open-system model for U-series age determinations of fossil corals. *Earth and Planetary Science Letters* **210,** 365-381.

Tomczak, M. and Godfrey, J. S. (2003) Regional Oceanography: an Introduction 2nd edition, xi+390 Pages. Daya Publishing House, Delhi

US Geological Survey digital elevation model (USGS-DEM) (2003) http://seamless.usgs.gov/Website/Seamless/viewer.php

van Calsteren, P., and Thomas, L. (2006). Uranium-series dating applications in natural environmental science. *Earth-Science Reviews* **75,** 155-175.

Vecsei, A., and Berger, W.H. (2004) Increase of atmospheric CO2 during deglaciation: constraints on the coral reef hypothesis from patterns of deposition. *Global Biogeochemical Cycles,* **18**, doi:=10.1029/2003GB002147

Villemant, B., and Feuillet, N. (2003). Dating open systems by the ^{238}U-^{234}U-^{230}Th method: application to Quaternary reef terraces. *Earth and Planetary Science Letters* **210,** 105-118.

von Gunten, H. R., Surbeck, H., and Roessler, E. (1996). Uranium-series disequilibrium and high thorium and radium enrichments in karst formations. *Environmental Science and Technology,* **30,** 1268-1274.

Waelbroeck, C., Labeyrie L., Michel E., Duplessey J. C., McManus J. F., Lambeck K., Balbon E.and Labracherie M. (2002) Sea-level and deep water temperature changes derived from benthic foraminifera isotopic changes. Quaternary Science Reviews, **21**, 295-305.

Walker, J.C.G., and Opdyke, B.C. 1995. Influence of variable rates of neritic deposition on atmospheric carbon dioxide and pelagic sediments. *Paleocenography,* **10**, 415-427

Wessel, P. and Smith, W. H. F. (2006) GMT (Generic Mapping Tools) Cookbook and Manual pages: http://gmt.soest.hawaii.edu/gmt/gmt_services.html

Winland, H. D. (1971). "Diagenesis of Carbonate Grains in Marine and Meteoric Waters." Unpublished Ph. D. Thesis, 320 Pages, Brown University.

CURRICULUM VITAE

JACOB LOUIS MEY, IV

SENIOR STAFF ASSOCIATE
LAMONT DOHERTY EARTH OBSERVATORY
OF COLUMBIA UNIVERSITY
NEW CORE LABORATORY – BLDG 207
ROUTE 9W
PALISADES, NY 10964
PHONE: (845) 365 8649 FAX: (845) 365 8154

MEY@LDEO.COLUMBIA.EDU

RESEARCH ASSOCIATE
DEPARTMENT OF ASTROPHYSICS
AMERICAN MUSEUM OF NATURAL HISTORY
CENTRAL PARK WEST AT 79TH STREET
NEW YORK, NY 10024

http://research.amnh.org/users/mey
http://lyot.org/team

MEY@AMNH.ORG

EDUCATION:

2008 Ph.D, The Graduate Center, City University of New York, Dissertation: The Uranium Series Diagenesis And The Morphology Of Drowned Barbadian Paleo-Reefs Advisors: Professor R. G. Fairbanks (Columbia University) and Professor N. G. Hemming (Queens College).

2005-2008. Doctoral Student in geochemistry, EES at the Graduate Center, City University of New York (CUNY). Graduate Coursework completed Spring 2007 (GPA= 4.0). Advanced to PhD candidacy April 20th, 2007. Dissertation defense April 14th, 2008.

2005-2006 Visiting Scholar, Lamont-Doherty Earth Observatory, Columbia University. Courtesy Appointment by Professor R. G. Fairbanks.

2001-2003 Continuing Education, Earth and Environmental Sciences, Columbia University

1999 Cand. Scient. (M.S.) Thesis in Geology, Department of Earth Sciences, University of Aarhus, Denmark. "Mineralogy and Petrology of the Bekkestul Lamprophyre, Telemark, SE Norway" (Advisor: Prof. C. Tegner).

1993 B. Sc., Thesis in Geology, Department of Earth Sciences, University of Aarhus, Denmark.

FELLOWSHIPS, GRANTS AND AWARDS:

2007-2008 Graduate Center Fellowship, City University of New York (CUNY).

2006-2007 Graduate Center Fellowship, City University of New York (CUNY).

2006-2007 Graduate Center Research Stipend, City University of New York (CUNY).

2006-2007 Graduate Center Fellowship, City University of New York (CUNY).

2006-2009 Co-Pi on NSF DBI Major Research Instrumentation (MRI) grant # 06-19559, "Acquisition of a Variable Pressure Scanning Electron Microscope (VP-SEM) at the American Museum of Natural History, New York. Successful award $386,563.00

2006 Award for "Best Micrograph" – second place, Microscopy Society of America.

2005-2006 Graduate Center Fellowship, City University of New York (CUNY).

2004-pres. Supported by NSF grant OCE99-11637 and ATM03-27722 (Principal Investigator, Prof. R. G. Fairbanks, Columbia University).

2005 Award for "Best Micrograph" - runner up, Microscopy Society of America.

2001-2004 Supported by NSF Grant EAR 0160750 (Principal Investigator, Curator E. A. Mathez).

1993-1999 University Stipend, Danish Educational Ministry, Denmark.

EMPLOYMENT:

2007-pres Senior Staff Associate, Lamont Doherty Earth Observatory of Columbia University, New York.

2007-pres	Research Associate, Department of Astrophysics, American Museum of Natural History, New York
2003-2007.	Laboratory Manager, Microscopy and Imaging Facility, American Museum of Natural History (AMNH), New York.
2000-2003	Scientific Assistant II, Earth and Planetary Sciences, American Museum of Natural History (AMNH), New York.
1996-1998	Teachers Assistant, Department of Earth Sciences, University of Aarhus, Denmark.
1991	Field Assistant and Helicopter Navigator, Nunaoil A/S, West Greenland
1991	Summer position at the State of Israel Geological Survey.
1990	Field Assistant, NGU (Norwegian Geological Survey).
1986-1987	Laboratory Technician, Metabolism Associates, New Haven, Conn., USA.

INSTRUMENTATION AND ANALYTICAL EXPERIENCE:

2007-pres.	VG Elemental AXIOM: Single Collector High Resolution Inductively Coupled Plasma Mass Spectrometer (HR-ICP-MS) Lamont Doherty Earth Observatory, CU.(months)
2005-pres.	Philips PW-3040-MPD X'pert X-ray Diffractometer (XRD), Lamont Doherty Earth Observatory, Columbia University (days).
2005-pres.	Rigaku DMAX/rapid X-ray Micro-diffractometer (XRD), Earth and Planetary Science, AMNH (months).
2003-pres.	FISONS Plasma 54, Multi-Collector-Magnetic-Sector Double-Focusing-Inductively Coupled Plasma Mass Spectrometer (MC-MSDF-ICPMS) Lamont Doherty Earth Observatory, Columbia University (weeks).
2003-pres.	Gatan MonoCL cathodoluminescence (CL) imaging, Microscopy and Imaging Facility, AMNH (years).

2003-pres.	Zeiss Axiovert 100 M and LSM 510, Laser Scanning Confocal Microscopy, AMNH (years).
2000-pres.	Hitachi S-4700 "Cold Field Emission" Scanning Electron Microscope (SEM),AMNH (years).
2000-pres.	Cameca SX-100, 5-spectrometer (WDS & EDS) Microprobe, Earth and Planetary Science, AMNH (years).
1996-pres.	Princeton Gamma Tech (PGT- Now Bruker AXS) Energy Dispersive Spectrum (EDS) X-ray microanalysis and mapping, University of Aarhus ('96-'99); Earth and Planetary Science, AMNH ('00 –'03); Microscopy and Imaging Facility, AMNH ('03-present) (years).
1993-pres.	Back Scatter Electron (BSE) imaging and mapping: Department of Earth Sciences, University of Aarhus ('93 –'99); Earth and Planetary Science, AMNH ('00 –'03); Microscopy and Imaging Facility, AMNH ('03-present) (years).
1990-pres.	Chemical lab experience including general chemical labs, clean workbenches, class 10000 to class 1000 clean labs. Sample preparation experience for chemical analysis includes isotope separation (column chemistry), acid digestion, spiking, isotope dilution and other techniques: Department of Earth Sciences, University of Aarhus ('92 –'99)(years); Earth and Planetary Science, AMNH ('00 – '03)(years); Lamont Doherty Earth Observatory, Columbia University ('02 - pres.)(months); Microscopy and Imaging Facility, AMNH ('03 - pres.)(years)
2004	Cameca IMS 3f Ion Microprobe, Woods Hole Oceanographic Institution (WHOI) (days).
2003	Finnigan MAT-251 with Carousel-48 for carbonates, stable isotope spectrometer, Lamont Doherty Earth Observatory, Columbia University (weeks).
2001-2003	Nicolet 20-SXB Fourier Transform Infra Red (FTIR) spectroscopy, Earth and Planetary Science, AMNH (weeks).
1993-1999	JEOL JXA-8600 Microprobe, Department of Earth Sciences, University of Aarhus, Denmark (years).

1994-1995 Perkin Elmer 3300 with automated sample feeder, Atomic Absorption Spectroscopy (AAS), Department of Chemistry, University of Aarhus, Denmark (months).

1994-1996 Deltech Vertical tube furnace DT-31, High Temperature furnace, Department of Earth Sciences, University of Aarhus, Denmark (months).

1992-1993 Philips PW-2400 X-ray fluorescence (XRF), Department of Earth Sciences, University of Aarhus, Denmark (months).

1992-1993 Philips PW-3710 X-ray diffraction (XRD), Department of Earth Sciences, University of Aarhus, Denmark (months).

1992 Aarhus STM, Scanning Tunneling Microscopy (STM) microanalysis and electron back scatter diffraction (EBSD) imaging, Department of Physics and Astronomy, University of Aarhus, Denmark (days).

HARDWARE AND SOFTWARE EXPERIENCE:

Since 1998, I have built an array of custom high end computers solving the need to process very large data sets. At AMNH, I have recently built 3 such systems; the latest is a 64-bit dual-core (upgradeable to octa-core) system with 8 gigabytes of memory and 1.5 terabytes of storage space. These systems are built to process and visualize 3D-tomographic data-sets acquired from Laser Confocal (LSCM), Cat Scan (CT), Syncotron hard X-ray source or Magnetic Resonance (MRI) instruments and also high resolution topographical models from sonar bathymetry and satellite imagery and elevation modal data. In my previous job at AMNH, I managed 30 computer systems including 11 specialized instrument servers, 8 data processing stations, 3 file sharing and data servers, 6 workstations (MAC and PC), 2 Linux systems and 8 various printers including a large format poster printer. I managed the MIF department website, which I started to migrate to 'Plone' - online content management system.

Software fluency:

Programs: Fledermaus (PC); Imaris (PC), IMIX (PC); ArcMAP & ArcView (PC); MatLAB (PC); OriginLAB (PC); ImageJ (Linux, PC & Mac); MB-System (UNIX); Generic Mapping Tools (UNIX), Photoshop (PC & Mac); Illustrator (PC & Mac); Acrobat Pro (PC & Mac); Excel (PC & Mac); Word (PC & Mac); PowerPoint (PC & Mac); html-code (various programs); Designer (PC); CorelDraw (PC); Quark (Mac); FileMakerPro (PC & Mac); Access (PC & Mac) EndNote (PC); DesignCad (PC); ImagePro (PC); ScionImage (PC);

Operating systems: DOS (PC); Windows (PC – ver. 3.0, 3.1, NT, 95, 98, 2000, Me, XP and XP64-bit); System (Mac – ver. 8, 9 and OSX), Cygwin (UNIX PC emulator) and Debian and Ubuntu (Linux flavors).

CURRENT RESEARCH PURSUITS:

As a geologist/geochemist I am primarily interested in the geochemistry of both stable and radiogenic isotopes. I study Oxygen, Carbon, and mainly Uranium series (U-Th-Pa) isotopes in fossilized coral skeletons, in an effort to model paleo ocean sea-level, ultimately used to proxy past climate variations. The primary focus of my Ph.D. is investigating the timing and extent of element redistribution, isotopic fractionation and micro textural modifications in 10,000-600.000 year old corals from Barbados. The goal of this research is to enhance the resolution and quality of past climate proxy data in paleo coral reefs. Another aspect of my project is to incorporate spatial data into 3-dimensional topographical models using software such as MB-System, Generic Mapping Tools (GMT) and Fledermaus Pro. I have recently computed such a model of the sea-bottom of the "Shallows" SE of Barbados and also of the island itself to identify reef structures and other morphological features to aid sampling and study of the preservation conditions. On a recent cruise I collected a 42 GB bathymetry data set of the drowned reefs around Barbados. My project is advised by Prof. N. G. Hemming and R.G. Fairbanks and, so far, all my lab-work has been at Lamont Doherty Earth Observatory, mainly in Fairbanks' ICP-MS facilities in the New Core Lab.

My background is also in igneous petrology, studying geochemical characteristics and secondary texture modifications in rocks from layered intrusions. My focus has been on the petrogenesis of the UG2-chromitite and its silicate host rocks in the eastern section of the Bushveld Complex, Republic of South Africa.

Collaborating with the Microscopy and Imaging Facility at AMNH, my main research endeavor is imaging micro-textures and structures using various sophisticated microscopes, such as scanning electron (SEM), cathodoluminescence spectrography (CL), and laser confocal scanning (CLSM) microscopes. I develop new applications for visualizing tomography data in 3D-reconstructions and portray these images in ways, which make them scientifically informative and educational.

I collaborate with the Lyot project (http://lyot.org)at the Astrophysics department at the American Museum of Natural History . We use the laser confocal scanning microscope to image micro-features on several crucial components used in the coronagraph, to aid the understanding of such sub-micron structures and their effects on exoplanet and star images.

FIELDWORK, EXCURSIONS AND CRUISES:

2008	Araihazar, Bangladesh (planned 2 weeks in May) Member of drilling and sediment sampling for mitigation of Arsenic in groundwater
2008	Araihazar, Bangladesh (2 weeks in January) Member of drilling and sediment sampling for mitigation of Arsenic in groundwater
2007	Soledad Basin, Pacific Ocean (1 week in Oct. 2007, expedition member)
2007	Barbados, Caribbean Ocean (5 weeks, expedition member in charge of bathymetry survey – 1 day field trip on Barbados)
2005	Oahu, Hawaii, USA (1 week – field work and conference).
2002	Barbados, Caribbean (1 week – field trip/work).
2000	Bushveld layered intrusion, Transvaal, Republic of South Africa (5 weeks – field work).
1998	Cornwall, England and Ireland (2 weeks – field trip and workshop).
1996	Alps in Switzerland and Italy (2 weeks – field trip and workshop).
1992	Hjartdal area, Central Telemark, Norway (7 weeks – fieldwork).
1991	Negev Desert, Golan Heights and West Bank, Israel (4 weeks – summer position, field work and workshop).
1991	Nordre Strømfjord and Lersletten regions, Western Greenland (9 weeks – field work).
1990	Hjartdal and Tinnsjø, Central Telemark, Norway (8 weeks – field work).

PROFESSIONAL DEVELOPMENT:

2005	Gatan MonoCL cathodoluminescence advanced workshop at Hitachi Demo Headquarters, Pleasanton, CA, USA.

2004 Lehigh University Microscopy School: Problem Solving with SEM and X-Ray Microanalysis.

2003 FDNY (Fire Department of New York), Category C14 Certificate of Fitness for managing a Chemical Laboratory.

1986 Renatron™ Technical Seminar, Boston, Mass., USA.

US PATENTS:

2006 Inventor of "Method for Marking Crystalline Materials Using Cathodoluminescence" Sponsored by the American Museum of Natural Hisory. Patent Application prepared by "Davidson, Davidson & Kappel, LLC, New York" and formally submitted on July 28, 2006.

MEMBERSHIPS:

American Geophysical Union (AGU)
American Microscopy Society (MSA)
International Society for Optical Engineering (SPIE)
Geochemical Society (GS)

SEMINARS, TALKS AND PRESENTATIONS:

2008 Graduate Center, City University of New York, *The Uranium Series Diagenesis and the Morphology of Drowned Barbadian Paleo-Reefs. (Public PhD dissertation defence)*

2007 Lamont Doherty Earth Observatory, CU: *Uranium Series Diagenesis in Corals: Toward Better Prospecting techniques for Closed System samples for High Accuracy Dating (diary of a climate proxy hunter) (Public Second Exam Presentation and defense)*

2007 DEES, Columbia University: *The provenance of coral reef growth and the Atmospheric CO_2-curve since the last glacial maximum: The Coral reef hypothesis revisited with GIS. Presentation with Lida Teneva.*

2007 Lamont Doherty Earth Observatory (LDEO): *"Determining Likely Provenance of* Acropora *palmata and* Acropora *cervicornis Corals on the Barbados Shallows during Pleistocene Sea Level from 10-30 ka using GIS and Multibeam Sonar Bathymetry* (*2 posters on display in New Core Lab, LDEO*).

2007 Graduate Center, CUNY: Sixth Annual Nature, Ecology and Society Colloquium: Research and Action for a Green Future. *Optimal Drill Pod Placement for Scientific Drilling on the Shallows South of Barbados (poster presentation).*

2007 New York Microscopy Society February Meeting, American Museum of Natural History: *Microscopy Applied to Studies of the Cosmos (invited presentation).*

2006 Graduate center, CUNY and LDEO: *"Determining Likely Provenance of* Acropora *palmata and* Acropora *cervicornis Corals on the Barbados Shallows during Pleistocene Sea Level Low Stands from 10-30 ka using GIS and Sonar Bathymetry* (*independent research presentation and 2 posters*).

2006 Microscopy and Microanalysis 2006, Chicago: *"Optimal Conditions for Acquiring Cathodoluminescence (CL) Images Using a Cold-Field Emission Scanning Electron Microscope" (conference talk).*

2006 Microscopy and Microanalysis Conference 2006, Chicago: *"When Searching for Planets orbiting distant Stars: Why Would You Look Through a Microscope" (poster presentation).*

2006 Graduate Center Science Fair 2006, CUNY: *"Uranium Series Diagenesis in Corals Exposed to Fresh Water: Toward Better Prospecting for Closed System Samples for High Accuracy Dating (poster presentation).*

2006 Lehman College, CUNY: *Optimal Drill Pod Placement for Scientific Drilling on the Shallows South of Barbados Using Bathymetric Data and Spatial Analysis in GIS. (GIS certificate presentation).*

2006 Lehman College, CUNY: *Optimal Drill Pod Placement for Scientific Drilling on the Shallows South of Barbados (poster presentation).*

2006 Graduate Center, CUNY: *"Uranium Series Diagenesis in Corals Exposed to Fresh Water: Toward Better Prospecting for Closed System Samples for High Accuracy Dating (course presentation).*

2005 AGU Joint Assembly, Fall 2005, San Francisco: "*Uranium Series Diagenesis in Corals Exposed to Fresh Water: Toward Better Prospecting for Closed System Samples for High Accuracy Dating" (poster presentation).*

2005 Microscopy and Microanalysis 2005, Honolulu, Hawaii: "*Quantifying Errors of Particle Size Distributions Using Flatbed Scanner Images" (poster presentation)*

2005 Microscopy and Microanalysis 2005, Honolulu, Hawaii: "*Characterization of Epitaxial Bands and Beam Damage of Natural Zircon Using Cathodoluminescence" (poster presentation).*

2005 Graduate Center, CUNY: "*Coral Proxy Reconstruction of Equatorial Pacific ENSO Events through the Holocene" (course presentation)*

2005 SEES, Queens College: "*Optimal Double and Triple Spiking for High Precision Lead Isotope Measurements" (course presentation)*

2004 AGU Joint Assembly, Spring 2004: *"A Mixed Unit beneath the UG2 Chromitite, Bushveld Complex, and the Evolution of Partially Molten Layered Intrusions" (poster presentation).*

2003 Lamont-Doherty Earth Observatory: "*The Paleo Coral Reef Terraces of Barbados: A walk Through Sea Level Changes in the Last Interglacial" (course presentation).*

2003 American Museum of Natural History: "*The Paleo Reefs of Barbados" (seminar.)*

2002 Lamont-Doherty Earth Observatory: "*Os-Re isotope systematics in the Bushveld Layered Intrusion, Transvaal, Republic of South Africa" (course presentation).*

2002 American Museum of Natural History: "*Introduction to U-Pb, U-Th Isotope Systematics in Geochronology Studies" (seminar).*

2002 American Museum of Natural History: "*Os-Re Isotope Systematics in the Bushveld Layered Intrusion, Transvaal, Republic of South Africa" (seminar).*

2001 American Museum of Natural History: "*A Trip to the Bushveld Intrusion" (seminar).*

2000 American Museum of Natural History: "*Reverse Zoned High Ti-Phlogopite of the Bekkestul Ultramafic Lamprophyre, Fen Province, Southern Norway: Evidence for Substitution Mechanism Control" (seminar).*

1999 EUG Conf. X, Strasbourg, France: "*Reverse Zoned High Ti-Phlogopite Phenocrysts of the Bekkestul Ultramafic Lamprophyre, Fen Province, Southern Norway: Evidence for Substitution Mechanism Control" (poster presentation).*

1999 University of Lund, Sweden: "*Reverse Zoned High Ti-Phlogopite of the Bekkestul Ultramafic Lamprophyre, Fen Province, Southern Norway: Evidence for Volatile Loss or Magma Mixing?" (conference talk).*

1999 University of Aarhus, Denmark: *"Biotite Geothermobarometry of the Alkaline Igneous Rocks" (Cand. Scient (M.S.) thesis talk).*

1998 University of Aarhus, Denmark: *"Mineralogy and Petrology of the Bekkestul Ultramafic Lamprophyre, -Initial Results" (seminar).*

1998 University of Aarhus, Denmark: "*A New Discovery of an Ultramafic Lamprophyre in the Eastern Part of the Hjartdal Sector, Telemark Norway" (seminar).*

1996 University of Aarhus, Denmark: "*Geology of the Eastern Hjartdal Sector, Telemark, Norway" (seminar).*

SUPERVISED ASSISTANTS, STUDENTS AND VOLUNTEERS:

2008 Accepted one REU student and one Summer Intern.

2008-pres **Emily Hickey**, Laboratory Assistant, Lamont Doherty Earth Observatory

2007 **Laura Siden,** Research for Undergraduates intern, Lamont Doherty Earth Observatory

2007-2008 **Qing Jia (Mary)** Laboratory Assistant, Lamont Doherty Earth Observatory

2003-2006 **Sonali Shukla**: Physics major at NYU, New York, AMNH volunteer, Co-Author (Now in Earth and Environmental Sciences graduate school at Columbia University).

2005 **Nathaniel Greenstein**: Physics Major at Carnegie Mellon University, PA., Summer AMNH volunteer intern, Co- Author.

2003-2005 **Pia Ramchandani**: Senior at Greenwich High School, CT. 2004 and 2005 Science Award Projects, Co-Author.

2003 **Diane Lyons**: Summer volunteer intern at AMNH, Geosciences major at Franklin & Marshall College, PA.

2000-2004 **Sheldon Gross**: Retiree, Volunteer at AMNH.

PUBLICATIONS AND WORK IN PROGRESS:

Mey, J. L., 2008: (invited papers/notes- in prep) Museum Microscopy Applications – (a series of short 1-page notes for "Microscopy Today" on microscopy applications at The American Museum of Natural History, *Microscopy Today XX-XXXX*

Mey, J. L., and Oppenheimer, B. R., Soummer, R., Sivaramakrishnan, A., 2008: (invited paper – in prep.) Aiding Astronomers in Finding Planets around Distant Stars: Resolving and Modeling Feature Effects on the Optics Using Laser Confocal Scanning Microscopy. *Microscopy Today, XX-XXXX*

Shara, M., and Mey, J. L. 2008: (in prep.) Morphology of Nanometer Cracks in Diamond. (shall be submitted to Journal of Gemology)

Mey, J. L., 2007: (invited paper- in prep.) Calibration and Errors of Particle Analysis Using Flatbed Scanner Imaging. *Microscopy Today XX-XXXX*

Mey, J. L., Fairbanks, R. G., Mortlock, R., 2008: (submitted) Uranium Series Diagenesis in Corals Exposed to Fresh Water: Prospecting Techniques for Closed System Samples for High Accuracy Dating (will be submitted to Earth and Planetary Science Letters, Spring 2007).

Sivaramakrishnan, Anand; Oppenheimer, Ben R.; Hinkley, Sasha; Brenner, Douglas; Soummer, Rémi; Mey, Jacob L.; Lloyd, James P.; Perrin, Marshall D.; Graham, James R.; Makidon, Russell B.; Roberts, Lewis C., Jr.; Kuhn, Jeffrey R., 2007: The Lyot Project: status and results. *Comptes Rendus Physique, Vol. 8, p. 355-364 (April 2007)*

Ebel, D. S., Mey, J. L., Rivers, M. L., 2007: Nondestructive laser confocal scanning microscopy and synchrotron micro-tomography of single stardust and analog tracks in aerogel keystones**.** *Lunar Planetary Science XXXVIII, Abstract #1977.*

Mey, J. L., and Sacha, B., 2006: Five high resolution color enhanced scanning electron microscopy (SEM) images in "Nothing To Sneeze At:"*, Readers Digest, August 2006, pp. 152-155.*

Mey, J. L., Oppenheimer, B. R., Soummer, R., Sivaramakrishnan, A., 2006: Searching for Planets Orbiting Distant Suns: Why Would You Look Through a Microscope? *Microscopy and Microanalysis, Proceedings Vol. 12, Nr. 708.*

Mey, J. L. and Klaus, A., 2006. Optimal Conditions for Acquiring Cathodoluminescence (CL) Images Using a Cold-Field Emission Scanning Electron Microscope. *Microscopy and Microanalysis, Proceedings, Vol. 12, Nr. 81.*

Mey, J. L., and Sacha, B., 2006: 5 high resolution color enhanced scanning electron microscopy(SEM) images in "Misery for all seasons – allergies: a modern epidemic"*, National Geographic Magazine, May 2006, pp.120, 128-129.*

Mey, J. L., Shukla, S., Mathez, E. A., 2006. Possible and Impossible Errors in Size Distribution Analysis of Particles Using Flatbed Scanner Images. *NIST Particle Workshop 2006, Proceedings and Programme, pp. 22-23.*

Mey, J. L., Fairbanks, R. G., Mortlock, R., Bradtmiller L., 2005: Uranium Series Diagenesis in Corals Exposed to Fresh Water: Toward Better Prospecting for Closed System Samples for High Accuracy Dating. *Eos Trans. AGU,* 86(52), Fall Meet. Suppl., Abstract PP21C-1572.

Mathez, E. A. and Mey, J. L., 2005: Character of the UG2 chromitite and petrogenesis of its Pegmatoidal Footwall, Northeastern Bushveld Complex. *Economic Geology, Vol. 100, pp. 1617-1630*

Mey, J. L. and Klaus, A., 2005. Characterization of Epitaxial Bands and Electron Beam Damage in Natural Zircon Using Cathodoluminescence. *Microscopy and Microanalysis, Proceedings Vol. 11, Nr. 267*

Mey, J. L., Shukla, S., Mathez, E. A., 2005. Quantifying Size Errors of Particle Distribution Analysis Using Flatbed Scanner Images. *Microscopy and Microanalysis, Proceedings, Vol. 11, Nr. 612.*

Oppenheimer, Ben R.; Digby, Andrew P.; Newburgh, Laura; Brenner, Douglas; Shara, Michael; Mey, Jacob; Mandeville, Charles; Makidon, Russell B.; Sivaramakrishnan, Anand; Soummer, Remi; Graham, James R.; Kalas, Paul; Perrin, Marshall D.; Roberts, Lewis C., Jr.; Kuhn, Jeffrey R.; Whitman, Kathryn; Lloyd, James P., 2004. The Lyot project: toward exoplanet imaging and spectroscopy. *In: Advancements Adaptive Optics, Calia, D.B., B. Ellerbroek and R. Ragazzoni (editors), Proceedings of the SPIE, Vol. 5490: p. 433-442.*

Mey, J. L. and Mathez, E.A., 2004. A Mixed Unit beneath the UG-2 Chromitite, Bushveld Complex, and the Evolution of Partially Molten Layered Intrusions. *AGU Joint Assembly, Spring, 2004, V51B-09.*

Mey, J. L. and Tegner, C., 1999. Reverse Zoned High Ti-Phlogopite Phenocrysts of the Bekkestul Ultramafic Lamprophyre, Fen Province, Southern Norway: Evidence for Substitution Mechanism. *EUG 10, J. Conf. Abs. 4, (1999). No. 008: 5P/29, p. 796.*

Mey, J. L., 1999. Reverse Zoned High Ti-Phlogopite Phenocrysts of the Bekkestul Ultramafic Lamprophyre, Fen Province, Southern Norway: Evidence for Volatile Loss or Magma Mixing? In: *Steno '99 (12-14 March 1999) Geology Symposium Abstracts*, *lecture 9*, *Geologiska Institutionen, University of Lund, Sweden.*

Mey, J. L., 1999. Mineralogy and Petrology of the Bekkestul Lamprophyre, Telemark, SE Norway. *M. Sc. Thesis. Department of Earth Sciences, Aarhus University, Denmark, 119 pages.*

Mey, J. L., 1998. Meteor over Grønland. *GeologiskNyt* **1,** 7-9. [In Danish]

Mey, J. L., 1998. Evidence of a triplet meteorite impact in Greenland: A preliminary study of a prolonged bolide "flash", recorded by a stationary security video camera, Nuuk,

Greenland. *Internal Report, Dept. of Earth Sciences, Aarhus University, Denmark, 34 pages.*

Mey, J. L., 1992: Field reports for the Skårset-Råstulli area, Hjartdal region, Telemark, SE Norway. *NGU Internal Report, 25 pages.*

OTHER RESEARCH ACTIVITIES AND PAST PURSUITS:

2006 Working with National Geographic Magazine on a story on Biomemetics. I will produce high quality color-enhanced SEM and confocal images of natural microstructures mimicked by humans and used in everyday life, science and engineering. Story will run in National Geographic Magazine in 2007-8.

2006 Working with the AMNH exhibitions department on creating a virtual three-dimensional model of "Rusinga", a small island in Lake Victoria, Kenya. Rusinga holds a unique geologic environment, which preserved many human and animal fossils. In my model I have created an interactive three dimensional environment of the island using satellite data and ArcGIS. I have added spatial data and draped geology and other important locality features to follow the topography of the model. The interactive "Rusinga" will be on permanent AMNH-display in the new "Hall of Human Origin" which opened in February 2007.

2006 Working with exhibitions in producing color-enhanced SEM images of pollen assemblages. Two of these images are on permanent display in the "Hall of Human Origin", AMNH.

2006 Working with Randy Mercurio (AMNH) in making species distribution maps of centipedes in central US-states using ArcMAP 9.1. This work will be portrayed in a book and catalog on centipede distribution.

2003-pres Collaborating with The Lyot project (http://lyot.org). Using my knowledge of image analysis techniques, my contribution is producing high-resolution micro imaging of the sub-micron features on the gold plated coronagraph focal plane masks and how they affect images of stars and exoplanets. Principal Investigator: Dr. B. Oppenheimer.

2004-2005 Collaboration with Bob Sacha on SEM imaging of allergens. Bob is a free lance professional photographer for The National Geographic Magazine. One of my images from this work has won an award with the Microscopy Society of America in category "MSA Best Micrograph – 2005".
Four of our images were published in National Geographic, May 2006 issue and one is published on the National Geographic website. Five of our images were published in Readers Digest, August 2006 issue.

1997-1999 Participated in a project concerning the December 9, 1997 Greenland meteor event (Principal Investigator: Professor H. Pedersen, Space Research Institute, University of Copenhagen).

1994-1998 Working full time as a professional musician while studying part time at the Department of Earth Sciences, University of Aarhus, Denmark, in anticipation of pursuing further studies towards an advanced graduate degree.

1992-1998 Member of the "Telemark group", a group of geology professors and students from the University of Aarhus). The group was established to survey and investigate the precious metal potentials of the Hjartdal and Tinnsjø regions, Central Telemark, Norway (Principal Investigators: Professors J. S. Petersen and T. Falkum, Department of Earth Sciences, University of Aarhus, Denmark).

1987-1994 Working as a part time musician.

1987-1989 Chairman of the Student Academic Committee, Department of Earth Sciences, University of Aarhus, Denmark.